Science Innovation
INTERNATIONAL SCIENTIFIC JOURNAL

ISSN: 2181-3337

SCIENCE & INNOVATION

INTERNATIONAL SCIENTIFIC JOURNAL

VOLUME 5 | ISSUE 8 | 2026
Series A: Technical Sciences

Science Innovation
INTERNATIONAL SCIENTIFIC JOURNAL

International Scientific Journal
SCIENCE AND INNOVATION
Series A
Volume 5 Issue 8
August 2026

Tashkent 2026

INTERNATIONAL SCIENTIFIC JOURNAL

SCIENCE & INNOVATION

Series A: Technical Sciences

VOLUME	ISSUE	PUBLICATION DATE	PLACE
5	8	31 AUGUST 2026	TASHKENT

ISSUE IDENTIFICATION

RECOMMENDED ISSUE CITATION

Science and Innovation. Series A: Technical Sciences. Volume 5, Issue 8, August 2026. Tashkent: Science and Innovation LLC.
ISSN 2181-3337.

Individual article DOIs are registered through Crossref under prefix 10.67620.

JOURNAL INFORMATION

Volume / issue	Volume 5 · Issue 8	**Publication date**	31 August 2026
ISSN	2181-3337	**Publisher**	Science and Innovation LLC
Established	2022	**Publication language**	English
Frequency	Monthly	**Publication format**	Electronic · Open Access
Peer review	Double-blind peer review	**License**	Creative Commons Attribution 4.0
DOI registration	Crossref · Prefix 10.67620	**Official website**	https://scientists.uz

AIMS AND SCOPE

Series A publishes original research and reviews in engineering, technology, computer and information sciences, energy, architecture and construction, materials science, applied physics and mathematics, industrial systems, automation, environmental engineering, and related interdisciplinary innovations.

EDITORIAL AND PUBLICATION STANDARDS

PEER REVIEW

Editorial screening, integrity checks, independent double-blind review, and a documented editorial decision.

ETHICS & CORRECTIONS

Conflicts of interest, authorship, misconduct, corrections, retractions, complaints, and appeals are handled under published journal policies.

AI TRANSPARENCY

Authors must disclose substantive use of generative AI. AI tools cannot be credited as authors; responsibility remains with the human authors.

EDITORIAL OFFICE

Bakhtiyor Rustamov	CEO Science and innovation LLC	**Kozim Ergashov**	Academic Editor
Gulira'no Rakhmatullayeva	Responsible Secretary	**Feruzabonu Mannonova**	Language Editor
Feruza Ollomurodova	Manuscript Coordinator	**Jahongir Bekmuradov**	Language Editor
Farangiz Sagdullaeva	Technical Editor	**Anvar Ergashev**	Digital Media Designer
Dilnoza Narzullayeva	Editorial Manager	**Asila Khaydaralieva**	Academic Editor
Sevara O'rinboyeva	Editorial Manager	**Bakhrom Qurbonov**	Digital Media Designer

PUBLISHER AND CONTACT

Science and Innovation LLC · Mass Media License No. 1597 (27 April 2022) · Publishing License No. 455168 (21 November 2024)
150 Shota Rustaveli Street, Vega Business Center, 6th floor, Room 2, Tashkent 100121, Uzbekistan
info@scientists.uz · +998 90 125 96 54 · https://scientists.uz · https://science-innovation.org

© 2026 Authors. Published by Science and Innovation LLC under CC BY 4.0.

SCIENTIFIC EDITORIAL BOARD

Series A: Technical Sciences

EDITOR-IN-CHIEF: ABDURAKHMONOVA NILUFAR ZAYNOBIDDIN QIZI - DOCTOR OF PHILOLOGICAL SCIENCES, PROFESSOR

33 BOARD MEMBERS	**INTERNATIONAL REPRESENTATION** Uzbekistan · South Korea · Cameroon · Russian Federation · Kyrgyzstan · Malaysia · India · United States · Iran · France

Members are listed by academic standing and editorial responsibility. Current institutional profiles and contact details are maintained on the journal website.

Yusupbekov Nodirbek Rustambekovich DSc, Technical Sciences, Academician, Academy of Sciences of Uzbekistan, Honored Scientist *Tashkent State Technical University named after Islam Karimov · Uzbekistan*	**Mirsaidov Mirziyod Mirsaidovich** DSc, Technical Sciences, Professor, Academician, Academy of Sciences of Uzbekistan *TIIAME" National Research University · Uzbekistan*	**Allayev Qahramon Rahimovich** DSc, Technical Sciences, Professor, Academician, Academy of Sciences of Uzbekistan, Honored Youth Mentor of Uzbekistan *Academy of Sciences of the Republic of Uzbekistan · Uzbekistan*
Mirzaev Bahodir Suyunovich DSc, Technical Sciences, Professor, Rector *"Tashkent Institute of Irrigation and Agricultural Mechanization Engineers" National Research University · Uzbekistan*	**Gorbachyov Oleg Anatolyevich** DSc, Technical Sciences, Professor, Director of the Irkutsk Branch *Moscow State Technical University of Civil Aviation, Irkutsk Branch · Russia*	**Erokhin Vyacheslav Vladimirovich** DSc, Technical Sciences, Associate Professor, Dean of the Faculty of Aviation Systems and Complexes *Moscow State Technical University of Civil Aviation, Irkutsk Branch · Russia*
Yo'ldoshev Shukurullo Ubaydullayevich DSc, Technical Sciences, Professor, Academician, Academy of Sciences of Uzbekistan *TIIAME" National Research University · Uzbekistan*	**Bakiyev Masharif Ro'zmetovich** DSc, Technical Sciences, Professor *TIIAME" National Research University · Uzbekistan*	**Uon Don Yon** DSc, Technical Sciences, Professor *South Korea National Council for Future Education · South Korea*
Jimbo H. Claver PhD in Applied Mathematics and Statistics, Professor *Samarkand International University of Technology (SIUT) · Cameroon / Uzbekistan*	**Borisyuk Petr Viktorovich** DSc, Physical and Mathematical Sciences *National Research Nuclear University MEPhI (Russian Federation) · Russian Federation*	**Nishonov Mirkozimjon** Candidate of Technical Sciences, Professor *Fergana State University · Uzbekistan*
Sanayev Ermat Shermatovich PhD in Technical Sciences, Assoc. Professor *Tashkent Institute of Chemical Technology · Uzbekistan*	**Eshmuradov Dilshod Elmuradovich** Candidate of Technical Sciences, Assoc. Professor *Tashkent University of Information Technologies named after Muhammad al-Khwarizmi · Uzbekistan*	**Musayeva Shoira** Candidate of Economic Sciences, Professor *Samarkand Institute of Economics and Service · Uzbekistan*
Usmonov Ilkhom Achilovich Candidate of Technical Sciences, Professor *Samarkand State Institute of Architecture and Construction · Uzbekistan*	**Kamolov Ikhtiyor Ramazonovich** Candidate of Technical Sciences, Professor *Navoi State University · Uzbekistan*	**Abdazimov Anvar Daniyarovich** DSc, Technical Sciences, Professor *Tashkent State Technical University · Uzbekistan*
Akhatov Jasurjon Saidovich DSc, Technical Sciences, Professor *S.A. Azimov Institute of Physics and Technology of the Academy of Sciences of the Republic of Uzbekistan · Uzbekistan*	**Bazarov Dilshod Rayimovich** DSc, Technical Sciences, Professor *TIIAME" National Research University · Uzbekistan*	**Dodakho'jayev Abdulla Tursunovich** DSc, Technical Sciences, Professor *Tashkent State Technical University named after Islam Karimov · Uzbekistan*
Fayzullayev Normurot Ibodullayevich DSc, Technical Sciences, Professor *Samarkand State University · Uzbekistan*	**Ibadullayev Akhmadjon Sobirovich** DSc, Technical Sciences, Professor *Tashkent State Transport University · Uzbekistan*	**Attokurov Urmat Tologonovich** Candidate of Technical Sciences, Assoc. Professor, Professor *M.M. Adyshev Osh Technological University · Kyrgyzstan*
Che Zalina binti Zulkifli PhD in Electrical and Electronic Engineering, Professor *Universiti Pendidikan Sultan Idris (UPSI) · Malaysia*	**Sreekumara Ganapathy** PhD in Civil Engineering, Professor *Ajou University in Tashkent · India / Uzbekistan*	**Hwang Myeon-Eun** Professor of Electrical and Computer Engineering *Ajou University in Tashkent · South Korea / Uzbekistan*
Dr. Danish Ather PhD in Information Technology, Professor *Amity University · India*	**Seungjik Lee** PhD in Information Technology, Professor *Tashkent University of Information Technologies named after Muhammad al-Khwarizmi · South Korea / Uzbekistan*	**Olimov Bakhshillo Amrillayevich** Candidate of Physical and Mathematical Sciences, Assoc. Professor, Professor *Editor of the journal "Physics · Uzbekistan*
Bradley Fitzgerald Jacob Professor of Electrical and Computer Engineering *Samarkand International University of Technology (SIUT) · USA / Uzbekistan*	**Mohammad Reza Bahrami** PhD in Mechanical Engineering, Professor *Samarkand International University of Technology (SIUT) · Iran / Uzbekistan*	**Florence Dujjarik Sandrine** PhD, Professor *Samarkand International University of Technology (SIUT) · France / Uzbekistan*
Kamalova Dilnavoz Ikhtiyorovna DSc, Technical Sciences, Professor *Navoi State University · Uzbekistan*	**Yunusov Mirdjalil Yusupovich** DSc, Technical Sciences, Professor *Tashkent Institute of Chemical Technology · Uzbekistan*	**Safarov Toyir Tursunovich** DSc, Technical Sciences, Professor *Tashkent Institute of Chemical Technology · Uzbekistan*

ISSN: 2181-3337 | SCIENTISTS.UZ

ISSN: 2181-3337 | SCIENTISTS.UZ VOLUME 5 ISSUE 8 | AUGUST 2026

DEVELOPMENT OF AN OPTIMIZED PERFORMANCE-GRADED (PG) ASPHALT BINDER FOR UZBEKISTAN'S ROAD-CLIMATIC CONDITIONS AND TRAFFIC LOADS: RHEOLOGICAL CHARACTERIZATION AND HYBRID POLYMER MODIFICATION

Kurbonov Salohiddin
Tashkent State Transport University, Tashkent, Uzbekistan

DOI: 10.67620/sai.58a0001

ABSTRACT

This study characterized a BND 50/70 paving-grade asphalt binder used in Uzbekistan and evaluated four polymer-modification strategies designed to achieve a PG 76-28 performance grade. The testing program included rotational viscosity, flash point, dynamic shear rheometer testing of unaged and rolling thin-film oven-aged binders, multiple stress creep recovery (MSCR), pressure aging vessel aging, and bending beam rheometer (BBR) testing. The modifiers were TITAN 7686 plastomer, LG501S styrene-butadiene-styrene elastomer, their hybrid combination, and a hybrid formulation containing 1.0% Reclamite® plasticizer. For base-binder measurements with available duplicates, means, sample standard deviations, and coefficients of variation were calculated. The base binder had a mean viscosity of 0.625 ± 0.038 Pa·s at 135 °C and a mean flash point of 270.0 ± 8.49 °C. Polymer modification increased the reported critical high temperature to 77.62 °C with TITAN 7686, 83.30 °C with 3.0% LG501S, 83.10 °C with the LG501S/TITAN hybrid, and 79.30 °C with the LG501S/TITAN/Reclamite® hybrid. The optimized formulation had an S(60) value of 170 MPa and an m-value of 0.305 at −18 °C, with a reported critical low temperature of approximately −29.1 °C. It was therefore classified as PG 76-28. Because replicate-level observations were unavailable for every modified formulation, inferential statistics were not applied. The results support hybrid elastomeric-plastomeric modification with controlled plasticization, while additional replicate MSCR and mixture-level validation remain necessary before field implementation.

ACCEPTED

25.08.26

Keywords: *asphalt binder, performance grade, polymer modification, MSCR, BBR, Uzbekistan.*

CC BY

Introduction

Asphalt pavement performance is governed by interactions among binder properties, aggregate structure, environmental conditions, traffic loading, and aging. Pavement temperature and repeated traffic loading are particularly important because asphalt binders exhibit strongly temperature- and time-dependent viscoelastic behavior. At elevated temperatures, reduced binder stiffness and viscosity can promote permanent deformation and rutting, whereas excessive stiffness and inadequate stress relaxation at low temperatures can increase susceptibility to thermal cracking.

The Performance Grade (PG) system developed through the Strategic Highway Research Program provides a performance-related framework for selecting asphalt binders according to expected pavement temperatures. Unlike conventional penetration- or viscosity-based classifications, PG grading relates binder properties to maximum and minimum pavement design temperatures and applies rheological criteria to high-, intermediate-, and low-temperature performance (American Association of State Highway and Transportation Officials [AASHTO], 2023; ASTM International, 2023a).

The Superpave approach is particularly relevant where high pavement temperatures coincide with substantial traffic loading. Binder selection should therefore consider both environmental conditions and traffic characteristics. NCHRP research has emphasized the importance of incorporating traffic loading into performance-based asphalt-binder and mixture evaluation, particularly for heavily trafficked pavements (Bahia et al., 2001; West et al., 2018).

Uzbekistan has a predominantly continental climate characterized by hot, dry summers, substantial seasonal temperature variation, and marked spatial variability. Previous investigations applying Superpave principles to long-term meteorological observations have demonstrated the feasibility of estimating pavement-temperature extremes and corresponding PG classes for different regions of Uzbekistan (Sadikov et al., 2021). Road-climatic zoning research has likewise identified substantial regional differences in environmental conditions that affect pavement performance (Urakov et al., 2022).

Selection of BND 50/70 binder on the basis of penetration and other conventional physical properties does not explicitly account for the combined effects of high pavement temperatures and heavy or slow-moving traffic. Polymer modification is therefore a potentially effective strategy for increasing high-temperature stiffness, elastic recovery, resistance to permanent deformation, and rheological stability.

Among polymer modifiers, SBS elastomers are widely used because they can form an elastomeric network within the asphalt phase, increasing elastic response and resistance to repeated deformation. Plastomeric modifiers can increase stiffness and deformation resistance at elevated temperatures, but excessive stiffening may impair low-temperature relaxation. Compatibility, dosage, morphology, aging behavior, and interactions among modifiers must therefore be considered (Behnood & Gharehveran, 2019; Yang et al., 2024).

The dynamic shear rheometer (DSR) is a principal instrument for characterizing the temperature-dependent viscoelastic behavior of asphalt binders. The complex shear modulus, $|G^*|$, and phase angle, δ, describe binder stiffness and viscoelastic response. The parameter $|G^*|/\sin\delta$ is used in conventional high-temperature PG criteria (ASTM International, 2025b).

The multiple stress creep recovery (MSCR) test provides additional information on nonrecoverable creep compliance (Jnr) and elastic recovery under repeated loading. It is particularly relevant for polymer-modified binders subjected to heavy or slow-moving traffic because it captures response characteristics that are not fully represented by the conventional $|G^*|/\sin\delta$ parameter (ASTM International, 2024; Liu et al., 2021).

At low temperatures, the bending beam rheometer (BBR) is used to determine creep stiffness, S, and the m-value. These parameters characterize the binder's ability to relax thermally induced stresses and are therefore associated with low-temperature cracking susceptibility (ASTM International, 2025a).

Although polymer modification of asphalt binders has been widely studied, comparatively little research has examined the combined use of SBS, plastomeric, and plasticizing modifiers for BND 50/70 binders under Uzbekistan's hot continental climate and traffic conditions. This study therefore characterized a BND 50/70 asphalt binder used in Uzbekistan and evaluated four polymer-modification strategies aimed at achieving PG 76-28 performance. Particular attention was given to the balance between high-temperature rutting resistance and low-temperature flexibility. The study's principal contribution is the experimental evaluation of an SBS-plastomer-plasticizer hybrid system for a BND 50/70 binder used

in Uzbekistan, with the final formulation selected on the basis of high- and low-temperature rheological performance.

Materials and Methods

Base Asphalt Binder

The base binder was BND 50/70 paving-grade petroleum asphalt supplied from the Russian Federation by JSC Gazpromneft-Moscow Oil Refinery (Gazpromneft-MNPZ) for road-construction applications in Uzbekistan. It was characterized using rotational viscosity, flash point, DSR, RTFO, PAV, BBR, and MSCR procedures, and the measured properties were compared with applicable PG requirements.

Polymer Modifiers and Formulations

Four modification strategies were investigated:

1. Modification I: BND 50/70 + 2.0% TITAN 7686
2. Modification II: BND 50/70 + 3.0% LG501S
3. Modification III: BND 50/70 + 2.5% LG501S + 0.7% TITAN 7686
4. Modification IV: BND 50/70 + 2.5% LG501S + 0.7% TITAN 7686 + 1.0% Reclamite®

LG501S was used as the SBS elastomeric modifier, TITAN 7686 as the plastomeric modifier, and Reclamite® as the plasticizing component.

Table 1

Composition of the Optimized Binder Formulation

Component	Content, % of base binder	Approximate content, % of total formulation
BND 50/70	100.0	95.97
LG501S (SBS elastomer)	2.5	2.40
TITAN 7686 (plastomer)	0.7	0.67
Reclamite® plasticizer	1.0	0.96

Binder Modification Procedure

The BND 50/70 binder was heated to a temperature suitable for polymer incorporation and homogenization. The selected modifiers were gradually introduced under mechanical mixing. For the hybrid formulation, LG501S and TITAN 7686 were incorporated together, followed by Reclamite®. The resulting polymer-bitumen systems were conditioned before rheological testing. Preparation and conditioning procedures were kept as consistent as possible across formulations, and mixtures were visually checked for homogeneity and phase separation.

Experimental Testing Program

The experimental program consisted of:

1. Rotational viscosity measurement at 135 °C
2. Flash-point determination
3. DSR testing of the unaged binder
4. RTFO aging
5. DSR testing after RTFO aging
6. MSCR testing
7. PAV aging
8. DSR testing after PAV aging
9. BBR testing at low temperatures
10. Determination of the final PG classification

The testing program was based on applicable ASTM, AASHTO, and GOST procedures.

Rotational viscosity testing followed ASTM D4402/D4402M-23 and GOST 33137-2014 (ASTM International, 2023b; GOST 33137-2014, 2014). Short-term aging used the rolling thin-film oven test in

ISSN: 2181-3337 | SCIENTISTS.UZ

accordance with ASTM D2872-22 and GOST 33140-2014 (ASTM International, 2022; GOST 33140-2014, 2014). DSR testing followed ASTM D7175-25 and GOST R 58400.10-2019 (ASTM International, 2025b; GOST R 58400.10-2019, 2019), MSCR testing followed ASTM D7405-24 and GOST R 58400.6-2019 (ASTM International, 2024; GOST R 58400.6-2019, 2019), PAV aging followed GOST R 58400.5-2019 (GOST R 58400.5-2019, 2019), and BBR testing followed ASTM D6648-25a and GOST R 58400.8-2019 (ASTM International, 2025a; GOST R 58400.8-2019, 2019). PG classification was interpreted using ASTM D6373-23, AASHTO M 320-23, and GOST R 58400.1-2019 (AASHTO, 2023; ASTM International, 2023a; GOST R 58400.1-2019, 2019). Flash-point testing followed GOST 33141-2014 (GOST 33141-2014, 2014).

Replicate Measurements and Statistical Analysis

To improve transparency and reliability, individual replicate measurements were evaluated statistically wherever raw replicate data were available.

The arithmetic mean was calculated as:

$$\bar{x} = (1/n) \sum_{i=1}^{n} x_i$$

The sample standard deviation was calculated as:

$$SD = \sqrt{[\sum_{i=1}^{n} (x_i - \bar{x})^2 / (n - 1)]}$$

The coefficient of variation was calculated as:

$$CV = (SD / \bar{x}) \times 100$$

For the original BND 50/70 binder, duplicate measurements were available for dynamic viscosity, flash point, RTFOT mass change, BBR creep stiffness, and BBR m-value. These measurements are reported as mean ± SD together with CV. For the polymer-modified binders, the available dataset consisted primarily of final measured values for each formulation and test condition; replicate-level observations were not available for every parameter. Consequently, SD and CV were not assigned to those values, and inferential tests such as ANOVA and post hoc comparisons were not performed. Comparisons among modified binders are therefore based on measured rheological response and compliance with relevant PG criteria rather than statistical ranking of treatment means.

Performance Grade Determination

The high-temperature PG was determined from the critical temperature at which the binder satisfied the specified $|G^*|/\sin\delta$ criteria for unaged and RTFO-aged conditions. The low-temperature PG was determined from BBR creep stiffness and m-value criteria. Final grades were assigned in standard 6 °C increments. Accordingly, a reported critical high temperature of 79.3 °C and a reported critical low temperature of approximately −29.1 °C correspond to the discrete PG 76-28 classification.

Results

Statistical Characterization of the Unmodified BND 50/70 Binder

The individual replicate results and calculated descriptive statistics are presented in Table 2.

Table 2

Replicate Measurements and Statistical Characteristics of the BND 50/70 Binder

Parameter	Individual measurements	n	Mean	SD	CV, %
Dynamic viscosity at 135 °C, Pa·s	0.652; 0.598	2	0.625	0.038	6.11
Flash point, °C	276; 264	2	270.0	8.49	3.14
RTFOT mass change, %	0.42; 0.58	2	0.500	0.113	22.63
Reported BBR S(60), MPa	170; 208	2	189.0	26.87	14.22
Reported BBR m-value	0.302; 0.318	2	0.310	0.011	3.65

The dynamic viscosity measurements were 0.652 and 0.598 Pa·s, yielding a mean of 0.625 ± 0.038 Pa·s and a CV of 6.11%. This value was well below the specified maximum of 3 Pa·s.

Flash-point measurements were 276 and 264 °C, yielding a mean of 270.0 ± 8.49 °C and a CV of 3.14%. The mean flash point exceeded the specified minimum of 230 °C.

RTFOT mass changes were 0.42% and 0.58%, yielding a mean of 0.50 ± 0.11%. Although the CV was relatively high (22.63%), the mean mass change remained within the specified limit.

The available BBR duplicate measurements yielded a mean creep stiffness of 189 ± 26.87 MPa and a mean m-value of 0.310 ± 0.011. Because the comparative low-temperature table uses a different set of reported test temperatures and values, the original BBR grading worksheet should be consulted before publication to confirm the test-temperature labels.

The relatively low CV for the m-value (3.65%) indicates good repeatability for this parameter, whereas the higher CV for RTFOT mass change reflects the small absolute magnitude of the measured changes.

High-Temperature Performance of the Investigated Binders

The high-temperature performance of the five investigated binder systems is summarized in Table 3.

Table 3

High-Temperature Rheological Performance of the Investigated Binders

Binder formulation	Reported critical high temperature, °C	Discrete high PG
BND 50/70	69.90	PG 64
BND 50/70 + 2.0% TITAN 7686	77.62	PG 76
BND 50/70 + 3.0% LG501S	83.30	PG 82
BND 50/70 + 2.5% LG501S + 0.7% TITAN 7686	83.10	PG 82
BND 50/70 + 2.5% LG501S + 0.7% TITAN 7686 + 1.0% Reclamite®	79.30	PG 76

The unmodified BND 50/70 binder had a reported critical high temperature of approximately 69.9 °C. Addition of 2.0% TITAN 7686 increased the reported critical temperature to 77.62 °C, an increase of 7.72 °C. The 3.0% LG501S formulation reached 83.30 °C, while the SBS/plastomer hybrid reached 83.10 °C. Addition of 1.0% Reclamite® reduced the reported critical temperature from 83.10 to 79.30 °C, but the value remained above the 76 °C threshold for the PG 76 high-temperature class. Because replicate observations were unavailable for all modified formulations, these values are presented as measured critical temperatures rather than statistically tested treatment means.

RTFO-Aged Binder Performance

RTFO aging increased the rheological stiffness of the investigated binders.

For the original BND 50/70 binder, the reported $|G^*|/\sin\delta$ values after RTFO aging were:

- 2.30 kPa at 64 °C
- 1.23 kPa at 70 °C

A critical high-temperature value of approximately 69.9 °C was reported for the RTFO-aged base binder. For the modified binders, reported RTFO-aged critical temperatures ranged from approximately 77.97 to 83.30 °C, while the final SBS/TITAN/Reclamite® formulation retained a reported critical temperature of approximately 79.3 °C. These results indicate that the polymer-modified binders maintained improved high-temperature deformation resistance after simulated short-term aging. The critical-temperature interpolation should be checked against the original DSR worksheet before publication.

PAV-Aged Binder Performance

For the unmodified BND 50/70 binder, the reported PAV-aged $|G^*|/\sin\delta$ values were:

- 1,700 kPa at 25 °C
- 6,160 kPa at 13 °C

ISSN: 2181-3337 | SCIENTISTS.UZ

The intermediate critical temperature was reported as approximately 16 °C. The value at 25 °C remained below the 5,000 kPa criterion, whereas the value at 13 °C exceeded it. These results were used to characterize intermediate-temperature performance. For the optimized formulation, PAV-aged response should be interpreted together with the low-temperature BBR results to ensure that increased high-temperature stiffness does not create unacceptable thermal-cracking susceptibility.

Low-Temperature Performance

The low-temperature properties of the investigated binders are summarized in Table 4.

Table 4

Low-Temperature Performance of the Investigated Binders

Binder	S(60), −12 °C, MPa	S(60), −18 °C, MPa	m-value, −18 °C	Reported critical low temperature, °C	Discrete low PG
BND 50/70	94.5	208	0.310	−26.62*	−28
+2.0% TITAN 7686	136	241	0.257	−22.94	−22
+3.0% LG501S	158	264	0.255	−24.10	−24
+2.5% LG501S + 0.7% TITAN 7686	179	217	0.257	−23.10	−22
+2.5% LG501S + 0.7% TITAN 7686 + 1.0% Reclamite®	119	170	0.305	−29.10	−28

Note. The base-binder discrete low PG is reported as −28 in the source dataset. Because the tabulated critical value (−26.62 °C) and the separate duplicate BBR results are not fully aligned, the original BBR grading worksheet should be checked before publication. The remaining values are presented as reported.

MSCR Performance and Traffic Considerations

The available MSCR results are presented in Table 5.

Table 5

MSCR Parameters of the Investigated Binder Formulations

Binder	Jnr,0.1, kPa^{-1}	Jnr,3.2, kPa^{-1}	Recovery, %
BND 50/70	1.157	1.553	34.23
+2.0% TITAN 7686	0.3703	1.173	216.8*
+3.0% LG501S	1.121	2.208	67.05
SBS/TITAN hybrid	0.401	1.250	211.8*
SBS/TITAN/Reclamite® hybrid	0.626	1.015	62.1

Note. Recovery values marked with an asterisk exceed 100%, which is physically unusual for conventional percent recovery. These values should be verified against the original MSCR calculation sheet and unit convention before publication. The optimized hybrid formulation had a reported Jnr,3.2 of 1.015 kPa^{-1} and recovery of 62.1%, indicating lower nonrecoverable compliance than the unmodified BND 50/70 binder. Final traffic classification should be assigned using the applicable MSCR specification and traffic category.

Discussion

Effect of Polymer Modification

Polymer modification substantially altered the high-temperature rheological behavior of BND 50/70. TITAN 7686 increased the reported critical high temperature from 69.90 to 77.62 °C. The 3.0% LG501S formulation produced a reported critical temperature of 83.30 °C, and the hybrid LG501S/TITAN system produced 83.10 °C. The similarity of these values suggests that the SBS component was a major contributor to the high-temperature improvement, while the hybrid system may provide a useful balance of elastomeric and plastomeric behavior.

ISSN: 2181-3337 | SCIENTISTS.UZ

Role of Reclamite® in the Optimized Formulation

Addition of Reclamite® reduced the reported critical high temperature from 83.10 to 79.30 °C. Although this reduction may appear adverse, the BBR results indicate improved low-temperature response. The S(60) value of the final formulation was 119 MPa at −12 °C, compared with 179 MPa for the binary SBS/TITAN formulation. At −18 °C, the final formulation had an m-value of 0.305, compared with 0.257 for the binary SBS/TITAN system. Reclamite® therefore appears to have moderated polymer-network stiffness and improved low-temperature stress relaxation. The optimized formulation represents a compromise between high-temperature rutting resistance and low-temperature flexibility.

Balance Between High- and Low-Temperature Performance

Maximizing high-temperature stiffness did not produce the best overall rheological balance. The SBS/TITAN formulation had a reported critical high temperature of approximately 83.1 °C but less favorable low-temperature behavior. By contrast, the SBS/TITAN/Reclamite® formulation had a lower reported critical high temperature of 79.3 °C but improved low-temperature characteristics. This finding underscores the need to select binders on the basis of the full rheological response rather than a single high-temperature parameter. The optimized formulation achieved:

- Critical high temperature: 79.3 °C
- Discrete high PG: 76
- BBR stiffness at −18 °C: 170 MPa
- m-value at −18 °C: 0.305
- Critical low temperature: approximately −29.1 °C
- Discrete low PG: −28

Accordingly, the final binder was classified as PG 76-28.

Relevance to Uzbekistan Climate Conditions

Selection of a PG 76-28 binder is relevant for road sections exposed to high pavement temperatures and sufficiently low winter pavement temperatures. The PG 76 high-temperature grade indicates compliance with the rheological requirements associated with the 76 °C class, while the −28 low-temperature grade indicates compliance with the corresponding low-temperature class. PG classification, however, should not be interpreted as a direct guarantee of pavement performance under every traffic condition. Pavement structure, aggregate gradation, air voids, layer thickness, axle loading, traffic speed, and environmental exposure can substantially affect rutting and cracking performance.

Effect of Traffic Loading and MSCR

The conventional $|G^*|/\sin\delta$ parameter is useful for high-temperature PG grading but does not fully characterize recoverable and nonrecoverable response under repeated loading. MSCR testing provides additional information through Jnr and percent recovery. Lower Jnr generally indicates lower susceptibility to permanent deformation, whereas higher recovery indicates a larger elastic contribution. The optimized formulation had a reported Jnr,3.2 of 1.015 kPa^{-1}, compared with 1.553 kPa^{-1} for the base BND 50/70 binder. This reduction indicates improved resistance to nonrecoverable creep at the higher stress level. Nevertheless, the MSCR dataset should be expanded through replicate testing and verification of the recovery calculations before a traffic category is assigned.

Comparison of the Investigated Formulations

The investigated formulations can be grouped by their rheological balance. The unmodified BND 50/70 had a reported critical high temperature of approximately 69.9 °C and was reported as PG 64-28. TITAN 7686 increased the high-temperature grade to PG 76, while LG501S and the SBS/TITAN hybrid produced reported critical temperatures above 82 °C. The SBS/TITAN/Reclamite® hybrid had a lower high-temperature critical value than the binary SBS/TITAN system but substantially improved low-temperature behavior. It was therefore selected as the most balanced formulation for the target PG 76-28 classification. Because replicate measurements were unavailable for all modified formulations, this

ISSN: 2181-3337 | SCIENTISTS.UZ

comparison should be interpreted as a performance-based evaluation rather than a statistical ranking of treatment means.

Optimized PG 76-28 Binder Formulation

Based on the laboratory results, the recommended PG 76-28 composition is summarized in Table 1.

The proposed binder can therefore be designated PG 76-28 for road applications in which calculated pavement temperatures and traffic conditions justify this performance level.

Conclusions

The experimental investigation supports the following conclusions:

1. The original BND 50/70 binder had a mean dynamic viscosity of 0.625 ± 0.038 Pa·s at 135 °C (CV = 6.11%, n = 2), satisfying the applicable viscosity requirement.
2. The mean flash point was 270.0 ± 8.49 °C (CV = 3.14%, n = 2), exceeding the specified minimum.
3. The mean RTFOT mass change was 0.50 ± 0.11%, remaining within the specified limit.
4. The unmodified binder had a reported critical high temperature of approximately 69.9 °C, corresponding to the discrete high-temperature class PG 64.
5. The available duplicate BBR measurements yielded a mean creep stiffness of 189 ± 26.87 MPa and a mean m-value of 0.310 ± 0.011. The original BBR grading worksheet should be checked to reconcile the test-temperature labels used across the manuscript.
6. TITAN 7686 increased the reported critical high temperature from 69.90 to 77.62 °C.
7. The 3.0% LG501S formulation and the 2.5% LG501S + 0.7% TITAN 7686 hybrid had reported critical high temperatures of 83.30 and 83.10 °C, respectively.
8. Addition of 1.0% Reclamite® reduced the reported critical high temperature to 79.30 °C while improving low-temperature rheological performance.
9. The optimized formulation had an S(60) value of 170 MPa and an m-value of 0.305 at −18 °C, satisfying the stated low-temperature criteria.
10. The reported critical low temperature of approximately −29.1 °C corresponds to the discrete −28 PG class.
11. The combination of 2.5% LG501S, 0.7% TITAN 7686, and 1.0% Reclamite® produced the most balanced high- and low-temperature rheological response among the investigated formulations.
12. The optimized binder was classified as PG 76-28.
13. The available MSCR results indicate lower nonrecoverable creep compliance for the optimized hybrid formulation than for the unmodified BND 50/70 binder, although the dataset requires replicate verification.
14. PG classification alone is insufficient for final pavement design under severe traffic conditions. MSCR traffic classification and asphalt-mixture testing for rutting, fatigue, moisture susceptibility, and low-temperature cracking should also be considered.
15. The statistical analysis underscores the importance of replicate measurements. Mean, SD, and CV were calculated only where duplicate observations were available; statistical significance was not inferred for modified-binder parameters lacking replicate-level data.

Limitations and Recommendations for Further Research

Several limitations should be acknowledged. First, the investigation used one source of BND 50/70 binder. Binder chemistry and rheological response can vary among refineries, crude-oil sources, production batches, and storage conditions; additional source binders should therefore be evaluated.

Second, replicate-level observations were available only for selected measurements of the original BND 50/70 binder. Although descriptive statistics were calculated for those measurements, complete replicate datasets were not available for all polymer-modified formulations, so inferential statistical tests were not performed.

ISSN: 2181-3337 | SCIENTISTS.UZ

Future studies should use at least three independent replicate specimens for each formulation and test condition where technically appropriate. Reporting means, SDs, CVs, confidence intervals, and inferential comparisons would permit more rigorous evaluation of modification strategies.

Third, the MSCR results should be expanded through repeated testing at 0.1 and 3.2 kPa, with verified Jnr and percent-recovery calculations. The original DSR and BBR worksheets should also be checked to reconcile the critical-temperature interpolation and test-temperature labels reported across the manuscript.

Further research should include:

- Replicate MSCR testing
- Jnr,0.1 and Jnr,3.2 determination
- Percent recovery
- Frequency-sweep testing
- Temperature-sweep testing
- Fluorescence microscopy for polymer morphology
- FTIR spectroscopy for chemical-interaction analysis
- Storage-stability testing
- Extended PAV aging
- Intermediate-temperature fatigue testing
- Thermal stress restrained specimen testing
- Wheel-tracking and rutting tests
- Repeated-load permanent-deformation tests
- Moisture-susceptibility testing
- Low-temperature cracking tests
- Asphalt-mixture performance testing
- Field validation using measured pavement-temperature and traffic data from different regions of Uzbekistan

Future research should establish direct relationships between binder-level rheological indicators, including Jnr, $|G^*|/\sin\delta$, BBR stiffness, and m-value, and asphalt-mixture performance. Such a program would allow the proposed PG 76-28 binder to be validated at the binder, mixture, and pavement-performance levels.

REFERENCES

1. American Association of State Highway and Transportation Officials. (2023). *Standard specification for performance-graded asphalt binder (AASHTO M 320-23).*
2. ASTM International. (2022). *Standard test method for effect of heat and air on a moving film of asphalt binder (rolling thin-film oven test) (ASTM D2872-22).* https://doi.org/10.1520/D2872-22
3. ASTM International. (2023a). *Standard specification for performance-graded asphalt binder (ASTM D6373-23).* https://doi.org/10.1520/D6373-23
4. ASTM International. (2023b). *Standard test method for viscosity determination of asphalt at elevated temperatures using a rotational viscometer (ASTM D4402/D4402M-23).* https://doi.org/10.1520/D4402_D4402M-23
5. ASTM International. (2024). *Standard test method for multiple stress creep recovery (MSCR) of asphalt binder using a dynamic shear rheometer (ASTM D7405-24).*
6. ASTM International. (2025a). *Standard test method for determining the flexural creep stiffness of asphalt binder using the bending beam rheometer (BBR) (ASTM D6648-25a).* https://doi.org/10.1520/D6648-25A

ISSN: 2181-3337 | SCIENTISTS.UZ

7. ASTM International. (2025b). *Standard test method for determining the rheological properties of asphalt binder using a dynamic shear rheometer (ASTM D7175-25).* https://doi.org/10.1520/D7175-25
8. Bahia, H. U., Hanson, D. I., Zeng, M., Zhai, H., Khatri, M. A., & Anderson, R. M. (2001). *Characterization of modified asphalt binders in Superpave mix design* (NCHRP Report 459). Transportation Research Board.
9. Behnood, A., & Gharehveran, M. M. (2019). Morphology, rheology, and physical properties of polymer-modified asphalt binders. *European Polymer Journal, 112,* 766–791. https://doi.org/10.1016/j.eurpolymj.2018.10.049
10. *GOST 33137-2014. Motor roads of general use. Viscous petroleum road bitumens. Method for determination of dynamic viscosity using a rotational viscometer.* (2014).
11. *GOST 33140-2014. Motor roads of general use. Viscous petroleum road bitumens. Method for determining aging under the influence of high temperature and air (RTFOT method).* (2014).
12. *GOST 33141-2014. Motor roads of general use. Viscous petroleum road bitumens. Method for determination of flash point using the Cleveland open cup method.* (2014).
13. *GOST R 58400.1-2019. General automobile roads. Petroleum-based bitumen binders. Specifications taking into account the temperature range of operation.* (2019).
14. *GOST R 58400.10-2019. Automobile roads of general use. Petroleum-based bitumen binders. Method for determination of properties using a dynamic shear rheometer (DSR).* (2019).
15. *GOST R 58400.5-2019. Automobile roads of general use. Petroleum-based bitumen binders. Method of aging under the action of pressure and temperature (PAV).* (2019).
16. *GOST R 58400.6-2019. Automobile roads of general use. Petroleum-based bitumen binders. Method of determining elastic properties at multiple shear loads (MSCR) using a dynamic shear rheometer (DSR).* (2019).
17. *GOST R 58400.8-2019. Automobile roads of general use. Petroleum-based bitumen binders. Method of determining flexural creep stiffness at subzero temperatures using the bending beam rheometer (BBR).* (2019).
18. Liu, H., Zeiada, W., Al-Khateeb, G. G., Shanableh, A., & Samarai, M. (2021). Use of the multiple stress creep recovery (MSCR) test to characterize the rutting potential of asphalt binders: A literature review. *Construction and Building Materials, 269,* 121320. https://doi.org/10.1016/j.conbuildmat.2020.121320
19. Sadikov, I. S., Karabaev, A. M., & Ashurov, F. B. (2021). Results of evaluation of extreme temperatures in different territories of the Republic of Uzbekistan with the “Superpave” method. *Journal of Academic Research and Trends in Educational Sciences, 1*(1), 56–64. https://doi.org/10.5281/zenodo.5753294
20. Urakov, A., Tashev, D., Xametov, Z., & Soataliev, R. (2022). Road maintenance and climate zoning of the territory of the Republic of Uzbekistan. In A. Manakov & A. Edigarian (Eds.), *International Scientific Siberian Transport Forum TransSiberia 2021* (Lecture Notes in Networks and Systems, Vol. 402, pp. 1213–1224). Springer. https://doi.org/10.1007/978-3-030-96380-4_133
21. West, R., Rodezno, C., Leiva, F., & Yin, F. (2018). *Development of a framework for balanced mix design* (NCHRP Project 20-07/Task 406 Final Report). Transportation Research Board.
22. Yang, Q., Lin, J., Wang, X., Wang, D., Xie, N., & Shi, X. (2024). A review of polymer-modified asphalt binder: Modification mechanisms and mechanical properties. *Cleaner Materials, 12,* 100255. https://doi.org/10.1016/j.clema.2024.100255

ISSN: 2181-3337 | SCIENTISTS.UZ VOLUME 5 ISSUE 8 | AUGUST 2026

DEFORMATION-DECOUPLED CONNECTIONS BETWEEN A PULTRUDED GFRP FRAME AND THREE-LAYER 3D-PRINTED WALLS

Analytical design methodology and a reproducible benchmark study

Akbarov Dilshod[1], **Akramov Khusnitdin**[2]

[1]Tashgiprogor LLC, Tashkent, Uzbekistan; Chief Project Engineer;
M.Sc. in Production of Building Materials, Products and Structures;
[2]Department of Technology of Building Materials and Structures,
Tashkent University of Architecture and Civil Engineering, Tashkent, Uzbekistan;
Doctor of Technical Sciences, Professor; e-mail: x.akromov@taqu.uz;
* Corresponding author: dilshodakbarov0@gmail.com

DOI: 10.67620/sai.58a0002

ABSTRACT

Pultruded glass-fiber-reinforced polymer (GFRP) frames and additively manufactured wall panels respond differently to temperature, shrinkage, and interstory drift. A rigid link between them can make a nominally non-load-bearing wall participate in the lateral system and can initiate brittle damage around fasteners or printed interlayers. This paper develops an analytical design procedure for a deformation-decoupled interface in which wall weight, out-of-plane restraint, and in-plane movement are assigned to separate components. The study is deliberately numerical; no laboratory results are reported. A reproducible two-story benchmark building in Tashkent is used to demonstrate the procedure. Loads are derived from stated geometry, densities, and design combinations rather than introduced as free numerical inputs. The original four-bolt U1 detail is reassessed against bearing, net-section tension, shear-out, cleavage, block-shear, bolt-shear, and local interlaminar-screening limit states. With EN 13706 E23 minimum properties and ASCE/SEI 74-23 resistance factors, a conventional hollow-wall through-bolt arrangement is inadequate because the tube-wall bearing reduction governs. A revised seated cleat with internal backing plates, spacer sleeves, and two M16 bolts on each of two symmetric side plates satisfies the short-duration 35.0 kN reaction and the sustained-load check; the highest sustained-load utilization is 0.94. For a 3.6 × 3.0 m wall module, the factored weight is 22.95 kN and the reaction at each of four lower supports is 7.46 kN. A stated wind-load envelope gives 1.20 kPa and 3.24 kN per side anchor. The required one-sided travel is 37.52 mm when no unverified elastic allowance is deducted, leading to a 95 mm slot. A 10% wall-participation limit is derived from a 5% cap on period reduction rather than adopted as an unexplained constant. The paper separates analytical conclusions from the tests still required before construction use.

ACCEPTED

03.09.26

Keywords: *pultruded GFRP; concrete 3D printing; bolted connection; sliding anchor; interstory drift; deformation compatibility; non-load-bearing wall; limit-state design.*

CC BY

Introduction

Pultruded GFRP profiles and additively manufactured cementitious walls are attractive for low-rise construction for different reasons. The frame offers a high strength-to-weight ratio and resistance to corrosion, whereas layer-wise printing reduces formwork and allows service channels or local thickening to be integrated into the wall geometry. These advantages do not automatically make the two subsystems compatible. The frame is expected to resist gravity and lateral actions; the exterior wall is expected to carry its own weight, remain stable out of plane, and keep the envelope weather-tight. If a rigid bracket inadvertently couples their in-plane movements, the wall can behave as an unintended diagonal strut and the structural model changes after construction (Bos et al., 2022; Erdem et al., 2021; Federal Emergency Management Agency, 2012; International Organization for Standardization & ASTM International, 2023; Wolfs et al., 2023).

The local mechanics are also dissimilar. A pultruded profile is orthotropic and has little capacity for plastic redistribution around a hole. Bearing, net-section rupture, shear-out, cleavage, block shear, washer pull-through, and local wall collapse may compete in the same joint (American Society of Civil Engineers, 2023; Eskenati et al., 2022; European Committee for Standardization, 2002, 2022; Girão Coelho & Mottram, 2015; Martins et al., 2021a, 2021b, 2023; Matharu & Mottram, 2017; Pirchio et al., 2024; Qureshi, 2022; Qureshi et al., 2020). A printed shell has directional interfaces between beads and layers; a concentrated anchor force may initiate local crushing, splitting, or interlayer separation. A polystyrene-concrete core can distribute load only if the embedded component is deliberately connected to it. Treating the assembly as a conventional steel bracket fixed to an ordinary concrete wall therefore conceals the governing links in the load path.

The scope of the paper is deliberately limited to a completed analytical study and one fully specified benchmark case. No laboratory test, raw measurement, repeated specimen, or statistical result is claimed. The quantities used in the calculations are fixed in the benchmark definition, and each numerical action is derived from stated geometry, material class, and design assumptions. The experimental program is reported only as the verification still required before a prototype can be used in construction.

The work has five objectives: (1) separate the transfer of wall weight, out-of-plane force, and in-plane movement; (2) re-check connection U1 against the relevant brittle failure modes rather than bearing alone; (3) derive the actions used to size U2-U4; (4) express accidental wall engagement through a gap law and a transparent stiffness criterion; and (5) define construction controls and the tests that remain necessary before the system can be used in a building. The outcome is a design procedure, not a certificate for a particular product.

2. Connection system and benchmark definition

2.1. Functional separation of the interface

The connection system follows one organizing rule: support separately, restrain separately, and allow movement separately. U1 joins the frame members; U2 carries the wall module at its lower edge; U3 and U4 restrain the wall normal to its plane but contain a geometric free-travel zone in the direction of interstory movement; U5 maintains movement and sealing at panel joints, corners, and openings; U6 provides dedicated attachment points for services and façade accessories. The classification prevents one concealed fastener from being assigned mutually incompatible tasks.

ISSN: 2181-3337 | SCIENTISTS.UZ

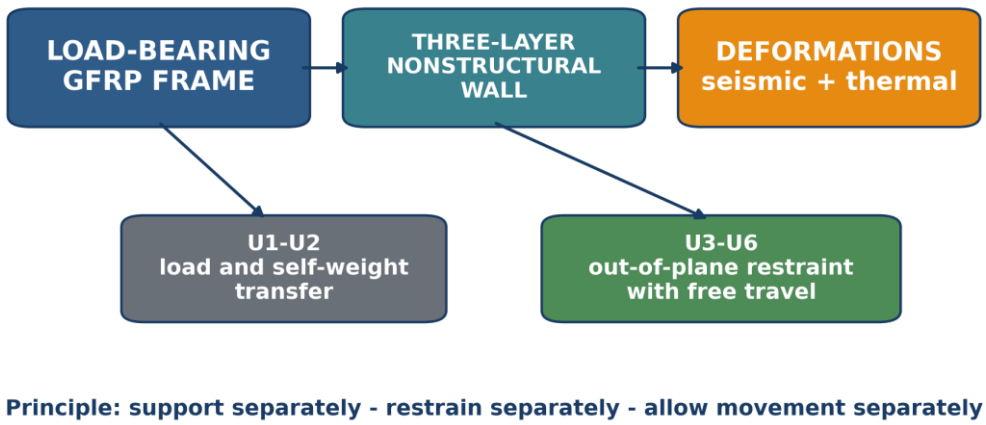


Figure 1. Functional separation of the load paths at the GFRP frame-to-wall interface.

Code	Primary function	Transferred action	Required freedom / control
U1	Beam-to-column frame joint	Beam reaction and erection forces	Predictable strength hierarchy; replaceable steel seat
U2	Lower wall support	Wall self-weight	Independent level adjustment and drainage
U3	Top sliding restraint	Out-of-plane force	Horizontal in-plane travel
U4	Side sliding restraint	Out-of-plane force	Travel parallel to interstory movement
U5	Panel joint, corner, opening	Local façade forces and sealing	Movement joint; two-stage weather seal
U6	Services and secondary attachments	Equipment / façade loads	No intersection with the U3-U5 movement path

Table 1. Functional classification of connections U1-U6.

2.2. Geometry and material data of the worked benchmark

The benchmark is a two-story building with a 10.8 × 7.2 m plan, 3.6 m framing bays, and a 3.0 m story height. It is not presented as an as-built project. Its purpose is to make the analytical sequence reproducible. The wall module is 3.6 m wide and 3.0 m high. Two 30 mm printed shells enclose a 190 mm D350 polystyrene-concrete core. The shell density is set at 1900 kg/m³ and the core density at 350 kg/m³; consequently, the areal mass is $2(0.03)(1900) + 0.19(350) = 180.5$ kg/m².

The GFRP calculations use the minimum characteristic values of EN 13706 class E23 rather than an unreferenced material strength. The chosen values are deliberately conservative: longitudinal tensile strength 240 MPa, transverse tensile strength 50 MPa, longitudinal pin-bearing strength 150 MPa, transverse pin-bearing strength 70 MPa, and in-plane shear strength 25 MPa (European Committee for Standardization, 2002). These class minima describe the benchmark material; they are not a substitute for the certificate and batch tests of a future manufacturer.

ISSN: 2181-3337 | SCIENTISTS.UZ

Parameter	Symbol	Benchmark value	Role in the analysis
Plan dimensions	L × B	10.8 × 7.2 m	Global seismic weight and bay layout
Story height	h	3.0 m	Interstory displacement
Bay / panel width	b	3.6 m	Tributary area and wall module
GFRP column	-	200 × 200 × 12 mm	U1 support member
GFRP beam	-	300 × 150 × 12 mm	Benchmark floor beam
Wall layers	$t_1/tc/t_2$	30/190/30 mm	Mass and local anchorage layout
Printed-shell density	ρs	1900 kg/m³	Declared benchmark input
Core density	ρc	350 kg/m³	D350 benchmark core
Wall areal mass	mA	180.5 kg/m²	Derived from layer thicknesses and densities
GFRP property class	-	EN 13706 E23 minima	Reference strengths for U1
Bolts	-	M16, class 8.8	U1 fasteners; threads excluded from bearing zone

Table 2. Fixed inputs of the reproducible benchmark.

3. Analytical method

3.1. Derivation of the design actions

The U1 beam reaction is obtained from the floor geometry and a stated load combination. The tributary area of one end reaction is one-half of a 3.6 × 3.6 m bay. The characteristic permanent and variable floor loads are 2.5 and 1.5 kPa, respectively. With the LRFD combination 1.2G + 1.6Q, which is consistent with the resistance format used for ASCE/SEI 74-23, the reaction is:

$$VEd = [1.2(2.5) + 1.6(1.5)](3.6 \times 3.6)/2 = 34.99 \approx 35.0\ kN \quad (1)$$

The dead-load-only combination used for the sustained-load check is 1.4G, giving VD = 22.68 kN. Two symmetric U1 seat side plates are assumed to share these reactions equally; each plate and each connected column face is therefore checked for 17.50 kN under the short-duration combination and 11.34 kN under sustained loading.

The wall weight follows directly from the derived areal mass. The design value uses a factor of 1.20, while the lower-support reaction includes a 1.30 non-uniformity factor to cover initial level differences among four adjustable shoes:

$$Gd = 1.20\ mA\ b\ h\ g = 1.20(180.5)(3.6)(3.0)(9.81)/1000 = 22.95\ kN \quad (2)$$

$$RU2,Ed = 1.30\ Gd / 4 = 7.46\ kN\ per\ lower\ support \quad (3)$$

For the façade anchor example, the site basic pressure is fixed at w0 = 0.38 kPa. The product of the design factor, exposure factor, and net pressure coefficient is 1.4 × 1.25 × 1.80. This stated envelope gives q⊥ = 1.197 kPa, rounded to 1.20 kPa. The result is not a universal pressure for Tashkent; it applies to the coefficient set defined here and must be recalculated for another height, exposure, or wall zone (American Society of Civil Engineers, 2022; Republic of Uzbekistan, 2025). Six side anchors are used, and a 1.50 distribution factor accounts for unequal engagement:

ISSN: 2181-3337 | SCIENTISTS.UZ

$$RU4,Ed = 1.50\, q_{\perp}\, b\, h / 6 = 1.50(1.20)(3.6)(3.0)/6 = 3.24\ kN \quad (4)$$

The 28 kN story shear is likewise derived. A 3.0 kPa seismic weight over the 10.8 × 7.2 m floor gives Wstory = 233.28 kN. A benchmark lateral coefficient Cs = 0.12 produces Vstory = 27.99 kN, rounded to 28.0 kN. This value is used only to illustrate the wall-participation criterion; it is not offered as a substitute for a project-specific modal response-spectrum analysis.

Quantity	Derivation	Result
U1 short-duration beam reaction	[1.2(2.5) + 1.6(1.5)] × 12.96 / 2	35.0 kN
U1 sustained dead-load reaction	1.4(2.5) × 12.96 / 2	22.68 kN
Factored wall weight	1.20 × 180.5 × 10.8 × 9.81 / 1000	22.95 kN
One U2 support reaction	1.30 × 22.95 / 4	7.46 kN
Out-of-plane pressure	1.4 × 0.38 × 1.25 × 1.80	1.20 kPa
One U4 anchor action	1.50 × 1.20 × 10.8 / 6	3.24 kN
Benchmark story shear	0.12 × 3.0 × 10.8 × 7.2	28.0 kN

Table 3. Traceable derivation of the numerical actions used in the study.

3.2. U1 limit-state equations and reduction factors

U1 is checked in accordance with the bearing-type connection provisions summarized in ASCE/SEI 74-23 and the accompanying reliability study (American Society of Civil Engineers, 2023; Pirchio et al., 2024). For a connection force parallel to the column pultrusion direction, the benchmark uses Fbr = 150 MPa, Ft = 240 MPa, and Fsh = 25 MPa. The resistance factors are 0.60 for bearing, 0.50 for longitudinal net tension in a multi-row group, 0.45 for two-row shear-out, 0.50 for cleavage, and 0.45 for block shear. A time-effect factor λ = 0.40 is applied to the dead-load-only check. Moisture, temperature, and chemical factors are taken as 1.0 because the benchmark assumes an internal, dry, temperature-controlled connection; a real exterior detail may require lower values.

The revised side-plate geometry on one column face has two M16 bolts in the load direction, 18 mm holes, wall thickness t = 12 mm, end distance e1 = 90 mm, pitch s = 80 mm, side distance e2 = 70 mm, and effective width w = 140 mm. The nominal resistances used in the numerical check are:

$$R_{br} = n_b\, t\, d\, F_{br} \quad (5)$$

$$R_{nt} = 0.2\, w\, t\, F_t \quad (6)$$

$$R_{sh} = 1.4(e_1 + s - d_n/2)\, t F_{sh} \quad (7)$$

$$R_{cl,a} = 0.15[(2e_2 - d_n)F_t + 2e_1 F_{sh}]\, t \quad (8)$$

$$R_{cl,b} = (10/9 - 4d_n/9e_1)^2\, R_{br,bolt} \quad (9)$$

$$R_{bs} = 0.5(A_{ns}F_{sh} + A_{nt}F_t) \quad (10)$$

The design resistance is Rd = φλCRn, where λ = 1.0 for the short-duration combination and 0.40 for the sustained combination. The original hollow-tube detail had washers only on the exterior side of each wall. ASCE/SEI 74-23 requires a 50% bearing reduction for that condition. The revised detail places an internal backing plate against the column wall and uses machined spacer sleeves, so the wall is clamped between two load-distribution surfaces. Omission of the one-sided-wall reduction is therefore an explicit feature of the revised detail, not an unspoken assumption. It still has to be confirmed by a full-scale connection test.

ISSN: 2181-3337 | SCIENTISTS.UZ

3.3. Kinematic model of U3-U4

The sliding restraint is represented by a geometric gap, not by an arbitrarily soft spring. The one-sided travel g contains the interstory displacement, thermal movement, wall shortening, and erection tolerance. No beneficial bracket elasticity is deducted because it has not been measured:

$$g = \theta d\, h + \alpha \Delta T L + \varepsilon sh L + \Delta tol \quad (11)$$

For θd = 1.0%, h = 3000 mm, α = 10 × 10⁻⁶/K, ΔT = 30 K, L = 3600 mm, εsh = 0.0004, and Δtol = 5 mm, the components are 30.00, 1.08, 1.44, and 5.00 mm. Thus g = 37.52 mm. With a 14 mm slot width for an M12 sliding bolt, the calculated symmetric length is 14 + 2(37.52) = 89.04 mm. A 95 mm slot is adopted to provide a manufacturing and rounding reserve.

The global model uses a piecewise law. In-plane force is zero, apart from separately calibrated friction, while $|\Delta| \le g$. After contact with a slot end, the bracket and embedded cassette are mobilized. This distinction matters because a flexible strip that acts from zero displacement can still attract a large part of the story shear.

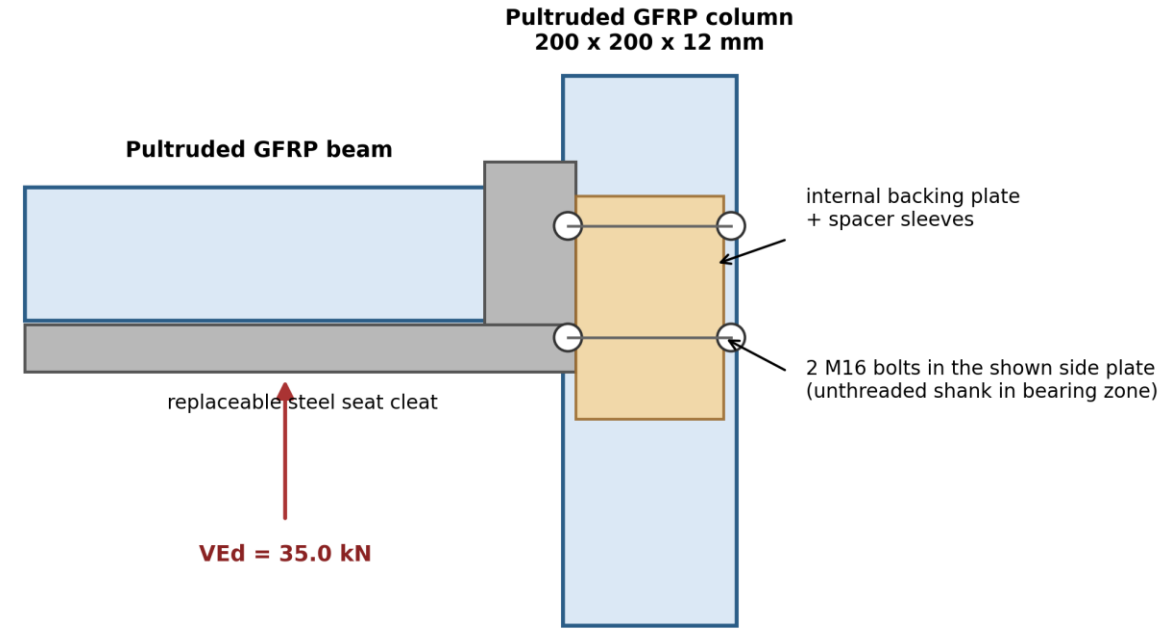
$$F(\Delta) = 0 \text{ for } |\Delta| \le g;\ \ F(\Delta) = sign(\Delta)\, min[Kc(|\Delta| - g), Rcap] \text{ for } |\Delta| > g \quad (12)$$

4. Results of the worked benchmark

4.1. U1 beam-to-column seat connection

A bearing-only calculation indicates a utilization below unity, but the complete limit-state check changes that conclusion. For four M16 bolts in a hollow column with exterior washers only, the ASCE tube-wall reduction gives a total short-duration bearing resistance of 34.56 kN, slightly less than the 35.0 kN demand. More importantly, the λ = 0.40 sustained resistance is 13.82 kN, compared with 22.68 kN. The unbacked arrangement is therefore rejected.

Figure 2 shows the revised seat. The vertical reaction is carried by the replaceable steel seat, two symmetric side plates share the force, and every bolt has an unthreaded shank through the bearing zone. An internal backing plate and exact-length sleeve are installed before tightening. The connection is thus not dependent on local compression of an unsupported tube wall.



One of two symmetric seat side plates is shown. Each plate carries one-half of the beam reaction.

ISSN: 2181-3337 | SCIENTISTS.UZ

Figure 2. Revised U1 seat detail; one of two symmetric side plates is shown.

Parameter	Value
Demand per column face, short-duration	17.50 kN
Demand per column face, sustained	11.34 kN
Bolts per side plate	2 × M16
Hole diameter dn	18 mm
Wall thickness t	12 mm
End distance e1	90 mm
Pitch s	80 mm
Side distance e2	70 mm
Effective width w	140 mm
Backing-plate diameter / width used for local screening	80 mm

Table 4. Geometry and actions for one U1 side plate and connected column face.

Limit state	Basis	Rd short, kN	Util. short	Rd sustained, kN	Util. sustained
Bearing	Per face	34.56	0.51	13.82	0.82
Net-section tension	Per face	40.32	0.43	16.13	0.70
Shear-out / longitudinal splitting	Per face	30.43	0.57	12.17	0.93
Cleavage, Eq. (8)	Per face	30.40	0.58	12.16	0.93
Cleavage at leading bolt, Eq. (9)	Per bolt	15.05	0.58	6.02	0.94
Block shear	Per face	99.58	0.18	39.83	0.28
Bolt shear, class 8.8	Per face	120.58	0.15	120.58	0.09

Table 5. Complete strength screening of U1. Utilization is demand divided by design resistance.

The sustained-load check governs. The highest utilization is 0.94 for the cleavage expression applied to the leading bolt; shear-out and the alternative cleavage expression follow closely at 0.93. This outcome is materially different from the bearing-only result: edge distance, pitch, and the time-effect factor control the detail. A reduction of e1 or s, omission of the internal plate, or allowing threads to enter the bearing zone would invalidate the stated capacity.

Interlaminar separation is not represented by a complete fracture-mechanics model because the benchmark does not specify the laminate lay-up or a measured interlaminar toughness. It is nevertheless screened quantitatively. The average ring shear around an 80 mm backing plate is $\tau_{ring} = V_{bolt}/(\pi D_{pt}) = 2.90$ MPa under the short-duration action and 1.88 MPa under sustained action. Against $0.5F_{sh} = 12.5$ MPa and $\lambda 0.5F_{sh} = 5.0$ MPa, the corresponding ratios are 0.23 and 0.38. These low average values support

ISSN: 2181-3337 | SCIENTISTS.UZ

the plate size, but they do not capture peak stresses or washer pull-through. Qualification to ASTM D7332 and a full-scale U1 test therefore remain mandatory (ASTM International, 2023b).

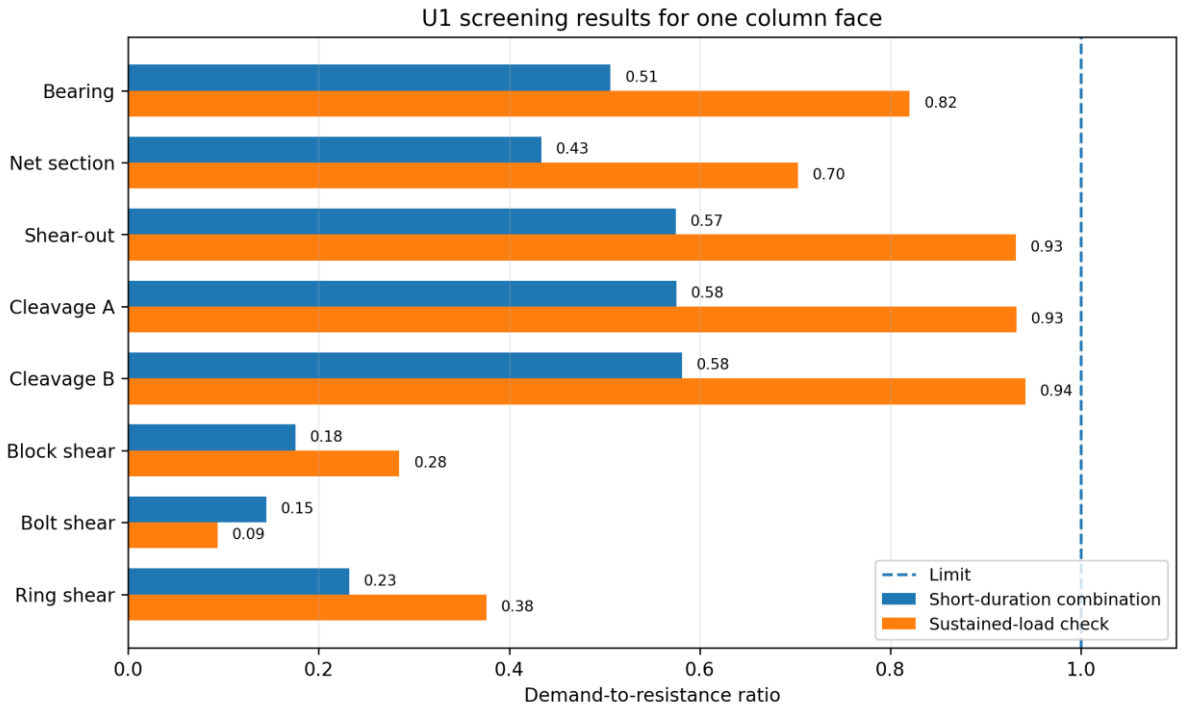


Figure 3. Demand-to-resistance ratios for the revised U1 detail.

4.2. U2 lower supports

The wall module is carried by four adjustable shoes. Side anchors do not carry permanent vertical force, which avoids frictional binding in their slots. The 7.46 kN design reaction is the input for the shoe plate, anchorage, and local wall cassette. With a nominal 120 × 80 mm contact area, the mean pressure is 7.46/0.0096 = 0.78 MPa. The bearing cassette must engage both printed shells or a locally densified core zone; transferring this pressure through one 30 mm shell is not permitted.

Drainage is part of the structural detail. The shoe is separated from the printed material by a waterproof, non-creeping pad; the lower edge drains outward; and the adjustment screw remains accessible. The façade sealant is not used as a bearing material. These measures prevent water accumulation at a point where repeated wetting, freezing, and local pressure would otherwise act together.

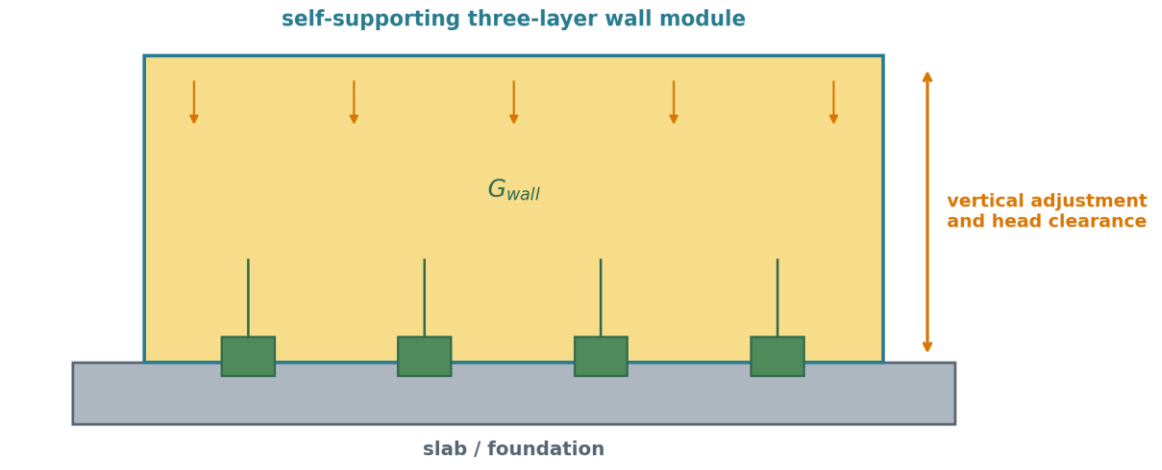


Figure 4. Separate transfer of wall self-weight through four U2 supports.

ISSN: 2181-3337 | SCIENTISTS.UZ

4.3. U3-U4 sliding restraints

The total out-of-plane force on one wall module is 12.96 kN. With six side anchors and the 1.50 distribution factor, one anchor is designed for 3.24 kN in either pressure direction. The embedded cassette must distribute this force over several printed beads and must engage the core mechanically; an adhesive film may improve contact but is not treated as the sole pull-out mechanism.

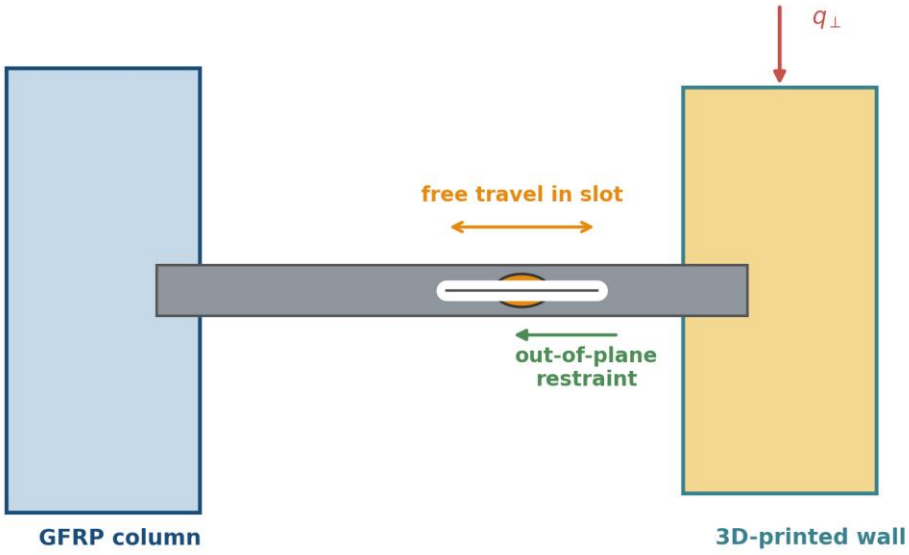


Figure 5. Sliding restraint: out-of-plane stiffness is retained while in-plane movement occurs in the slot.

Travel component	Value, mm	Basis
Interstory drift	30.00	1.0% × 3000 mm
Thermal movement	1.08	10×10^{-6}/K × 30 K × 3600 mm
Wall shortening allowance	1.44	0.0004 × 3600 mm
Erection tolerance	5.00	Printing, cassette, drilling, and frame alignment
Elastic-compliance credit	0.00	No unverified deduction
Required one-sided travel g	37.52	Sum of the above
Calculated slot length	89.04	14 + 2g
Adopted slot length	95	Rounded manufacturing reserve

Table 6. Derivation of the sliding-anchor free travel and slot length.

ISSN: 2181-3337 | SCIENTISTS.UZ

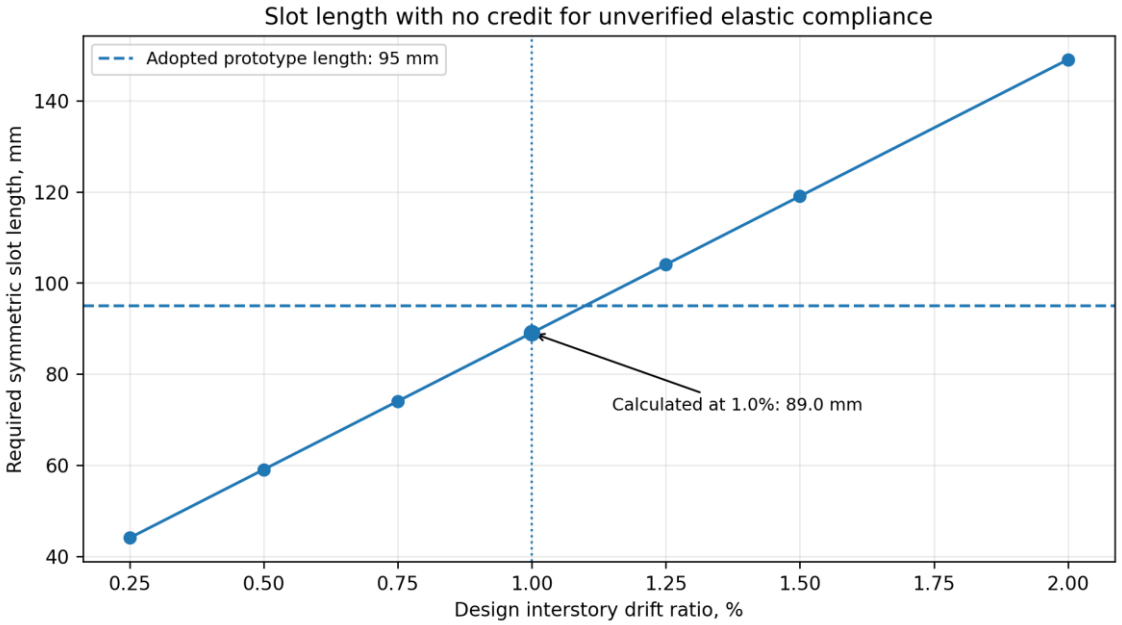


Figure 6. Required slot length as a function of the design drift ratio.

A drawing dimension alone does not guarantee movement capacity. After installation, the bolt position is measured from both slot ends and the actual positive and negative travel is recorded at the installation temperature. Mortar, sealant, a distorted washer, or a rotated cassette can consume the reserve even when the nominal slot is 95 mm. The acceptance quantity is therefore residual travel, not slot length by itself.

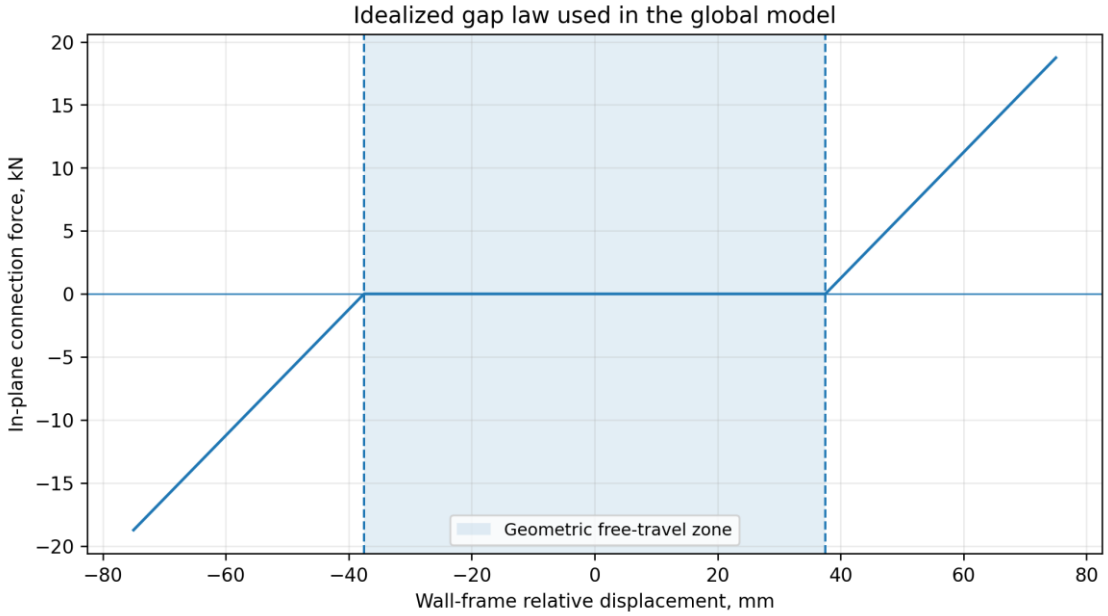


Figure 7. Piecewise force-displacement law used for the in-plane connection response.

4.4. Limit on unintended wall participation

The 10% criterion is not treated as a code limit. It is derived from a modeling tolerance. If the bare frame has stiffness Kf and the wall adds Kw before the gap is exhausted, the period ratio is $T_{coupled}/T_{frame} = 1/\sqrt{(1 + K_w/K_f)}$. Limiting the reduction of the fundamental period to 5% gives $K_w/K_f \leq 1/0.95^2 - 1 = 0.108$. A rounded limit $\beta = 0.10$ is used in the benchmark.

ISSN: 2181-3337 | SCIENTISTS.UZ

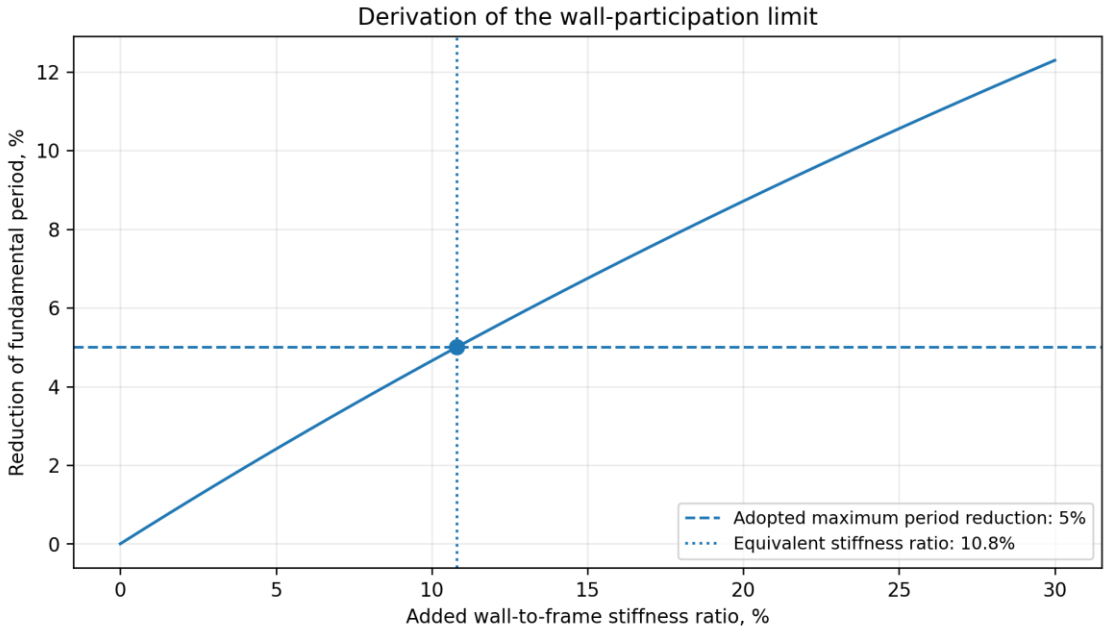


Figure 8. Relationship between unintended added stiffness and the reduction of the frame period.

For Vstory = 28.0 kN and Δd = 30 mm, the equivalent initial stiffness permitted before the design state is:

$$Kallow = \beta Vstory/\Delta d = 0.10(28.0)/30 = 0.093\ kN/mm \quad (13)$$

This small value explains why a nominally flexible bracket is not enough. A bracket with K = 0.20 kN/mm would transfer 6.0 kN at 30 mm, or 21.4% of the story shear. The geometric gap makes the pre-contact stiffness essentially zero and is therefore the controlling design feature.

4.5. Connection-option screening without subjective weights

Comparative test data, life-cycle cost data, and an agreed expert-elicitation procedure are not available; consequently, a weighted numerical score would suggest a precision that the evidence does not support. Connection concepts are therefore screened by mandatory pass/fail constraints. An option is retained only if it provides the required geometric travel, carries out-of-plane force independently of wall weight, permits inspection, and does not rely on an unverified adhesive path.

Concept	Geometric free travel ≥ g	Separate self-weight path	Inspection / repair	Screening decision
Rigid steel bracket	No	Possible	Good	Excluded: engages wall from zero displacement
Slotted GFRP bracket	Yes	Yes	Conditional	Candidate; slot wear and creep require testing
Adhesively bonded tie	No controlled gap	No	Poor	Excluded as the primary movement detail
Hybrid bonded-bolted tie	Limited / uncertain	Possible	Moderate	Conditional; not selected for benchmark
Sliding cassette with replaceable bracket	Yes	Yes	Good	Retained for prototype evaluation

Table 7. Deterministic screening of connection concepts. No claim of universal superiority is made.

ISSN: 2181-3337 | SCIENTISTS.UZ

5. Detailing, construction control, and serviceability

5.1. Installation sequence

Installation begins with a geodetic survey of the frame and the U2 support elevations. The wall is placed on the four shoes, adjusted to line and level, and temporarily restrained. U3-U4 bolts are then placed at their temperature-corrected initial positions in the slots. Only after positive and negative travel has been measured are the movement joints sealed. This order prevents finishes from hiding a blocked slot.

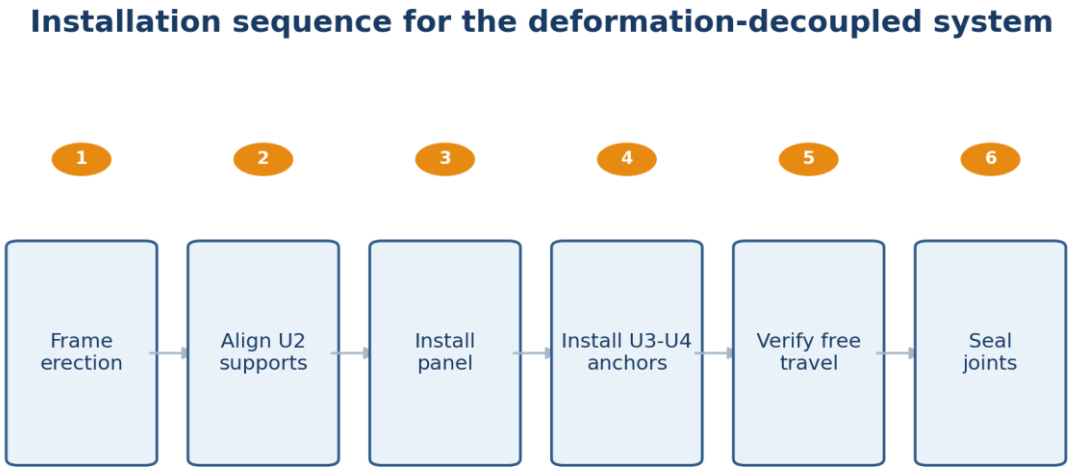


Figure 9. Recommended installation sequence for the deformation-decoupled interface.

Stage	Controlled quantity	Acceptance record
GFRP profile and U1 drilling	Batch, orientation, hole diameter, ovality, edge distances, visible delamination	Profile ID, measured geometry, photographs
U1 backing plates and sleeves	Plate dimensions; full contact; sleeve length equal to clear internal dimension	Actual plate and sleeve dimensions
U1 bolt installation	Unthreaded shank in bearing zone; calibrated tightening; no wall indentation	Bolt batch, method, torque / tension value
U2 supports	Elevation, engaged contact area, drainage, pad condition	Four support levels and final wall verticality
U3-U4 slots	Length, width, orientation, bolt position, washer clearance	Actual + and - residual travel at recorded temperature
U5 joints	Joint width, backing rod, primer, two-sided adhesion, drainage	Joint geometry and product batch
Final acceptance	Manual proof of travel, out-of-plane restraint, air/water test where required	Panel passport and acceptance sheet

Table 8. Minimum production-control plan for the benchmark connection system.

ISSN: 2181-3337 | SCIENTISTS.UZ

5.2. Thermal, moisture, and fire limitations

Metal components that cross the insulating core create local thermal bridges. The present paper does not assign a numerical U-value increment because the final cassette geometry and contact resistances are not known. A project detail must be checked with a two- or three-dimensional model in accordance with ISO 10211; the minimum internal surface temperature and condensation risk are assessed together with the point or linear transmittance (International Organization for Standardization, 2012, 2017a, 2017b). Massive through-plates should be avoided where a compact component or a GFRP thermal break can transfer the same force.

Moisture control is equally important. Exposed fibers at drilled holes are sealed; the lower support drains; dissimilar metals are isolated; and inspection covers do not create water traps. Low-friction pads in U3-U4 are selected for low creep and compatibility with the expected temperature range. None of these measures is credited as strength without product data.

No fire-resistance rating is claimed. GFRP stiffness and strength can decline at temperatures well below steel melting temperature (Correia et al., 2015). Any rated wall-frame detail requires a continuous protection system and either a validated thermomechanical model or a representative fire test under ISO 834-1 or the applicable national method (International Organization for Standardization, 1999). Fire stopping at a movement joint must preserve the specified travel.

6. Discussion

6.1. Consequences of the complete U1 check

A bearing-only calculation hides two important effects. First, a hollow profile with a washer on only one side of each wall is not equivalent to a laterally restrained coupon. Applying the tube-wall reduction changes the four-bolt detail from apparently adequate to inadequate. Second, the dead-load time-effect factor moves the governing condition from immediate bearing to the edge-sensitive shear-out and cleavage modes. The revised detail is therefore controlled by geometry and load duration rather than by bolt diameter alone.

This result also clarifies the role of the steel seat. The seat transfers the beam reaction through a replaceable component, while the internal plates and sleeves protect the primary composite profile from local crushing. A designer who simply increases bolt torque or adds a larger exterior washer does not create the same load path. The inside face of the tube wall must be engaged.

6.2. Significance of geometric decoupling

The required slot is long because interstory drift dominates the movement budget. Thermal movement and wall shortening contribute only 2.52 mm, yet they cannot be omitted because the installation tolerance acts in the same direction. Assigning no elastic-compliance credit increases the calculated requirement and eliminates dependence on an unmeasured bracket property. The detail is intentionally conservative: compliance may reduce contact force after the gap closes, but it is not used to justify a shorter gap.

The period-based derivation of β provides a rational meaning for the 10% limit. A different project can select another permitted period change and obtain its own β. The method therefore separates a transparent performance choice from the mechanics of the connection. It also makes clear that a low linear spring stiffness is not interchangeable with a true clearance.

6.3. Scope of the analytical result

The benchmark demonstrates a calculation sequence and identifies a buildable prototype. It does not establish characteristic resistance for a commercial profile, a printed mixture, or an embedded cassette. EN 13706 minima are used to avoid invented material properties, but a manufacturer may have different orthotropy, resin, veil, wall architecture, and coefficient of variation. The internal backing-plate assumption, the local interlaminar screening, slot friction, cassette pull-out, and sealing performance are all test-sensitive.

ISSN: 2181-3337 | SCIENTISTS.UZ

The analysis also uses a regular wall without an opening. Corners, windows, doors, and multiple panels can change the local anchor distribution and the global torsional response. The 1.20 kPa pressure and 0.12 lateral coefficient belong only to the stated benchmark. The method remains applicable when those values change, but the numerical results do not.

7. Limitations and planned verification

No experiment has been completed for this paper. Consequently, there are no measured load-displacement curves, repeated specimens, raw data, coefficients of variation, or statistical confidence intervals. The analytical resistances in Table 5 are code-based screening values. They must not be described as experimentally verified, and they are not sufficient for construction approval.

Before a design application, the following program is required. The list is reported as future work and is not part of the present results:

Level	Minimum series	Loading / measurement	Purpose
GFRP material and holes	At least 5 specimens per direction and condition	Tension, pin bearing, short-beam shear; dry and conditioned	Characteristic strengths, scatter, failure mode
U1 subassembly	At least 3 full-scale joints plus geometry variants	Monotonic and reversed cyclic loading; sustained hold	Capacity, slip, cleavage / splitting, sleeve and backing performance
U3-U4 anchor	At least 5 assemblies	3.24 kN out-of-plane action combined with cyclic travel to ±2% drift	Friction, binding, wear, residual travel, cassette pull-out
Wall fragment	At least 3 fragments with a joint and one opening	Cyclic in-plane drift plus pressure and air/water exposure	Cracking, leakage, unintended engagement
Conditioning	Matched conditioned and unconditioned sets	Moisture, temperature cycling, and sustained load	Durability and long-term deformation

Table 9. Planned verification program; no results from these tests are reported in this article.

Statistical treatment should be defined before testing. For each material configuration, the characteristic value, mean, standard deviation, and coefficient of variation are to be reported. For full-scale joints, the complete force-displacement response, residual deformation, failure sequence, and photographs of concealed damage are required. Acceptance criteria cannot be changed retrospectively after an unfavorable result.

8. Conclusions

1. The frame-to-wall interface can be analyzed more clearly when wall weight, out-of-plane restraint, and in-plane movement are assigned to U2, U3-U4, and the movement joints rather than combined in a universal rigid anchor.
2. The key design values are derived from a fixed benchmark. The 35.0 kN U1 reaction follows from a stated tributary area and LRFD combination; 1.20 kPa follows from the declared wind envelope; 28.0 kN follows from the benchmark story weight and lateral coefficient; and the 10% participation limit follows from a 5% cap on period reduction.

ISSN: 2181-3337 | SCIENTISTS.UZ

3. A conventional four-bolt through-connection in an unsupported hollow GFRP wall is inadequate when the ASCE/SEI 74-23 tube-wall and time-effect reductions are applied. The revised seat detail uses internal backing plates, sleeves, and an unthreaded bolt shank in the bearing zone.
4. For one revised U1 side plate, bearing, net-section tension, shear-out, cleavage, block shear, bolt shear, and a local interlaminar-stress screening were evaluated. The maximum short-duration utilization is 0.58; the maximum sustained-load utilization is 0.94 and occurs at the leading-bolt cleavage check.
5. The 3.6 × 3.0 m wall module has a factored weight of 22.95 kN. Four lower supports are designed for 7.46 kN each, while six side restraints are designed for 3.24 kN each under the stated 1.20 kPa envelope.
6. With no credit for unverified elastic compliance, the required one-sided in-plane travel is 37.52 mm. A 14 mm wide slot requires 89.04 mm analytically; 95 mm is adopted, and actual positive and negative residual travel must be measured after installation.
7. The study reports an analytical result only. Product certification, full-scale U1 testing, combined U3-U4 cycling, wall-fragment testing, and statistical evaluation remain necessary before the system can be used in a construction project.

Declarations

Author contributions. D.B.A.: conceptualization, analytical methodology, calculations, visualization, and preparation of the original manuscript. K.A.A.: scientific supervision, methodological review, interpretation of the structural results, and review and editing of the manuscript.

Funding. This research received no external funding.

Conflicts of interest. The authors declare no conflict of interest.

Data availability. No experimental dataset was generated. All benchmark inputs, equations, intermediate quantities, and analytical results used in the paper are reported in Tables 2-9.

Ethics statement. Not applicable.

REFERENCES

1. American Society of Civil Engineers. (2022). *Minimum design loads and associated criteria for buildings and other structures* (ASCE/SEI 7-22). https://doi.org/10.1061/9780784415788
2. American Society of Civil Engineers. (2023). *Load and resistance factor design (LRFD) for pultruded fiber reinforced polymer (FRP) structures* (ASCE/SEI 74-23). https://doi.org/10.1061/9780784415771
3. ASTM International. (2023a). *Standard test method for bearing response of polymer matrix composite laminates* (ASTM D5961/D5961M-23).
4. ASTM International. (2023b). *Standard test method for measuring the fastener pull-through resistance of a fiber-reinforced polymer matrix composite* (ASTM D7332/D7332M-23).
5. Bank, L. C. (2006). *Composites for construction: Structural design with FRP materials*. John Wiley & Sons.
6. Bos, F. P., Menna, C., Pradena, M., et al. (2022). The realities of additively manufactured concrete structures in practice. *Cement and Concrete Research, 156*, 106746. https://doi.org/10.1016/j.cemconres.2022.106746
7. Correia, J. R., Bai, Y., & Keller, T. (2015). A review of the fire behaviour of pultruded GFRP structural profiles for civil engineering applications. *Composite Structures, 127*, 267–287. https://doi.org/10.1016/j.compstruct.2015.03.006
8. Erdem, M. M., Emsen, E., & Bikçe, M. (2021). Experimental and numerical investigation of new flexible connection elements between infill walls and reinforced-concrete frames. *Construction and Building Materials, 296*, 123605. https://doi.org/10.1016/j.conbuildmat.2021.123605

ISSN: 2181-3337 | SCIENTISTS.UZ

9. Eskenati, A. R., Mahboob, A., Bernat-Maso, E., & Gil, L. (2022). Experimental and numerical study of adhesively and bolted connections of pultruded GFRP I-shape profiles. *Polymers, 14*, 894. https://doi.org/10.3390/polym14050894
10. European Committee for Standardization. (2002). *Reinforced plastics composites—Specifications for pultruded profiles* (EN 13706-1/-2/-3).
11. European Committee for Standardization. (2005). *Eurocode 3: Design of steel structures—Part 1-8: Design of joints* (EN 1993-1-8:2005).
12. European Committee for Standardization. (2022). *Design of fibre-polymer composite structures* (CEN/TS 19101:2022).
13. Federal Emergency Management Agency. (2012). *Reducing the risks of nonstructural earthquake damage: A practical guide* (FEMA E-74).
14. Girão Coelho, A. M., & Mottram, J. T. (2015). A review of the behaviour and analysis of bolted connections and joints in pultruded fibre reinforced polymers. *Materials & Design, 74*, 86–107. https://doi.org/10.1016/j.matdes.2015.02.011
15. International Organization for Standardization. (1999). *Fire-resistance tests—Elements of building construction—Part 1: General requirements* (ISO 834-1:1999).
16. International Organization for Standardization. (2012). *Hygrothermal performance of building components and building elements—Internal surface temperature to avoid critical surface humidity and interstitial condensation* (ISO 13788:2012).
17. International Organization for Standardization. (2017a). *Building components and building elements—Thermal resistance and thermal transmittance—Calculation methods* (ISO 6946:2017).
18. International Organization for Standardization. (2017b). *Thermal bridges in building construction—Heat flows and surface temperatures—Detailed calculations* (ISO 10211:2017).
19. International Organization for Standardization & ASTM International. (2023). *Additive manufacturing for construction—Qualification principles—Structural and infrastructure elements* (ISO/ASTM 52939:2023).
20. Martins, D., Gonilha, J., Correia, J. R., & Silvestre, N. (2021a). Exterior beam-to-column bolted connections between GFRP I-shaped pultruded profiles using stainless steel cleats. Part 1: Experimental study. *Thin-Walled Structures, 163*, 107719. https://doi.org/10.1016/j.tws.2021.107719
21. Martins, D., Gonilha, J., Correia, J. R., & Silvestre, N. (2021b). Exterior beam-to-column bolted connections between GFRP I-shaped pultruded profiles using stainless steel cleats. Part 2: Prediction of initial stiffness and strength. *Thin-Walled Structures, 164*, 107762. https://doi.org/10.1016/j.tws.2021.107762
22. Martins, D., Gonilha, J., Correia, J. R., Silvestre, N., Guerreiro, L., & Branco, F. (2023). Monotonic and cyclic sway behaviour of two-dimensional frames made of pultruded GFRP I-section profiles. *Structures*, *55*, 2461–2477. https://doi.org/10.1016/j.istruc.2023.07.035
23. Matharu, N. S., & Mottram, J. T. (2017). Plain and threaded bearing strengths for the design of bolted connections with pultruded FRP material. *Engineering Structures, 152*, 878–887. https://doi.org/10.1016/j.engstruct.2017.10.003
24. Pirchio, D., Althouse, J. A., Madlem, T. A., Denavit, M. D., & Walsh, K. Q. (2024). Assessment of resistance factors for LRFD of steel-bolted connections in pultruded FRP frames. *Journal of Composites for Construction*. https://doi.org/10.1061/JCCOF2.CCENG-4104
25. Qureshi, J. (2022). A review of fibre reinforced polymer structures. *Fibers, 10*, 27. https://doi.org/10.3390/fib10030027
26. Qureshi, J., Nadir, Y., & John, S. K. (2020). Bolted and bonded FRP beam-column joints with semi-rigid end conditions. *Composite Structures, 247*, 112500. https://doi.org/10.1016/j.compstruct.2020.112500

ISSN: 2181-3337 | SCIENTISTS.UZ VOLUME 5 ISSUE 8 | AUGUST 2026

MAXWELL–WAGNER OBSERVABILITY ANALYSIS IN TWO-FREQUENCY CAPACITIVE MEASUREMENT OF WATER CONTENT AND DENSITY IN HYDROCARBON EMULSIONS

Eshmuradov Dilshod[1], **Ismailov Otabek**[2], **Nizomov Norkhuja**[3]
Tashkent University of Information Technologies
named after Muhammad al-Khwarizmi, Tashkent, Uzbekistan[1,2,3]

DOI: 10.67620/sai.58a0003

ABSTRACT
Capacitive transducers are widely used for in-line control of fuels and other hydrocarbon media, but a single-frequency reading of effective permittivity cannot separate the water content of an emulsion from the density of the hydrocarbon phase because both quantities shift the same scalar output. This study formulates the separation task as a parameter-observability problem and shows that Maxwell–Wagner interfacial polarization provides the physical mechanism required to resolve it. A Maxwell–Garnett mixture model with complex phase permittivities was combined with the Clausius–Mossotti relation linking hydrocarbon density to permittivity, and the Jacobian of the two-frequency measurement map was analysed over a five-decade band. The determinant of the Jacobian vanishes identically when the two probing frequencies coincide, demonstrating that a second frequency is a necessary condition for observability rather than merely an accuracy refinement. Numerical analysis places the practical optimum at a low frequency below 0.05 of the relaxation frequency and a high frequency above ten times it; beyond this separation, the gain saturates within 1%. With a channel resolution of $1\cdot10^{-4}$ in relative permittivity, the propagated standard uncertainties are 0.033% for water volume fraction and 1.07 kg/m³ for density; Monte Carlo inversion reproduced these values and revealed negligible bias. The scheme was tolerant to salinity: a 50% error in the assumed water conductivity displaced the density estimate by only 0.11 kg/m³.

ACCEPTED

03.09.26

Keywords: *Maxwell–Wagner polarization; capacitive transducer; water content; observability; measurement uncertainty.*

CC BY

Introduction

In-line quality control of liquid hydrocarbons requires two quantities to be known simultaneously: the water content of the medium and the density of the hydrocarbon phase. The first governs the commercial and operational acceptability of the product; the second provides information on composition and on the presence of lighter or heavier fractions. Capacitive transducers are attractive for this task because they are non-intrusive, inexpensive, and directly sensitive to the dielectric properties of the medium (Sihvola, 1999).

The difficulty is structural rather than technological. A capacitive cell filled with a water-in-oil emulsion returns a single scalar: the effective relative permittivity of the mixture. Water raises this value because the permittivity of water exceeds that of a hydrocarbon by nearly two orders of magnitude; density

raises it as well because a denser hydrocarbon is more polarizable per unit volume. Two independent causes therefore act on one observable, and no improvement in the electronics can remove that ambiguity. The problem is one of observability in the sense used in system theory (Kalman, 1963): the map from parameters to measurements must be locally invertible before any estimation procedure can be meaningful.

Interfacial polarization offers a way out. When a heterogeneous medium contains phases with different conductivities, charge accumulates at internal interfaces and produces dielectric dispersion with a characteristic relaxation frequency. The effect was described by Maxwell (1873), given a dispersive formulation by Wagner (1914), extended to non-spherical inclusions by Sillars (1937), and extended to concentrated systems by Hanai (1960). Its central feature for the present purpose is that the dispersion is governed by the conductivity and volume fraction of the dispersed phase, whereas the permittivity of the continuous phase enters the response in a different functional form. The frequency axis therefore carries information that a single reading discards.

Interfacial polarization in emulsions and composites remains an active field. Asami (2002) surveyed the theory for two-, three-, and multiphase systems; Adohi et al. (2009) applied the Maxwell–Wagner–Hanai effective-medium description to conducting composite films; Samet et al. (2022) established scaling laws relating the characteristic frequency to the conductivity of the dispersed phase; and Qian et al. (2022) proposed an integral modification of the Maxwell–Wagner model for emulsions at higher volume fractions. These works establish the forward problem, that is, the prediction of permittivity from composition. The inverse problem relevant to measurement practice—whether and under what conditions composition can be recovered from permittivity readings—has received much less attention. In parallel, the metrological aspects of related measurement tasks have been addressed; for example, radio-transparency measurements of composite (i.e., structurally heterogeneous) materials have been placed on a metrological basis (Jumamuratov et al., 2024). Those studies, however, address the forward measurement task and do not consider the recovery of several composition parameters from one channel.

This paper addresses that gap. The aim is not to propose another mixture formula but to establish, for a two-frequency capacitive channel, the condition under which water content and hydrocarbon density become separable and to convert that condition into engineering requirements: which frequencies to choose and what resolution the measurement channel must achieve. Three questions are addressed. First, is a second frequency merely helpful or strictly necessary? Second, where should the two frequencies be placed relative to the relaxation frequency? Third, what uncertainty in the recovered quantities follows from a given uncertainty in the permittivity reading?

Methods

Dielectric model of the medium

The medium is treated as a water-in-oil emulsion of spherical droplets dispersed in a continuous hydrocarbon phase. For volume fractions below about 0.15, the Maxwell–Garnett mixing rule with complex phase permittivities describes the effective response adequately (Asami, 2002; Sihvola, 1999):

$$\varepsilon_{mix}^{*} = \varepsilon_{h}^{*}\frac{2\varepsilon_{h}^{*}+\varepsilon_{i}^{*}+2\varphi\left(\varepsilon_{i}^{*}-\varepsilon_{h}^{*}\right)}{2\varepsilon_{h}^{*}+\varepsilon_{i}^{*}\left(\varepsilon_{i}^{*}-\varepsilon_{h}^{*}\right)} \quad (1)$$

where φ is the volume fraction of the dispersed phase, and the complex permittivity of each phase is written as

$$\varepsilon^{*} = \varepsilon - j\frac{\sigma}{\omega\varepsilon_{0}} \quad (2)$$

where σ is the conductivity, ω is the angular frequency, and ε_0 is the electric constant. Subscript h denotes the host hydrocarbon, and subscript i denotes the water inclusions.

The link between the density of the hydrocarbon phase and its permittivity is supplied by the Clausius–Mossotti relation, which, for a given hydrocarbon class, uses a constant specific refraction, A (Böttcher, 1973):

ISSN: 2181-3337 | SCIENTISTS.UZ

$$\frac{\varepsilon_h-1}{\varepsilon_h+2}=A\rho,\quad \varepsilon_h=\frac{1+2A\rho}{1-2A\rho} \tag{3}$$

Calibrating A at the reference point $\rho=840\,kg/m^3$ and $\varepsilon_h=2.10$ gives $A=3.194\cdot 10^{-4}\,m^3/kg$, which maps the density interval $800-880\,kg/m^3$ to the permittivity interval 2.030–2.173. This narrow interval is the origin of the conditioning problem examined below.

In the dilute limit, the interfacial-polarization relaxation frequency follows from the conductivity of the dispersed phase and the permittivities of both phases:

$$f_{\mathrm{MW}}=\frac{\sigma_i}{2\pi\varepsilon_0(\varepsilon_i+2\varepsilon_h)} \tag{4}$$

Formulation of the observability problem

Let the parameter vector be $\mathrm{x}=(\varphi,\rho)$ and the measurement vector $y=\left(\varepsilon'(f_1),\varepsilon'(f_2)\right)$, where ε' denotes the real part of the effective permittivity. Only the real part is used because a capacitance reading is the quantity delivered directly by a charge-transfer front end. The measurement map is $y=h(x)$, and local observability requires the Jacobian

$$J=\frac{\partial\left(\varepsilon'(f_1),\varepsilon'(f_2)\right)}{\partial(\varphi,\rho)} \tag{5}$$

to be non-singular at the operating point. If $f_1=f_2$, the two rows of J are identical and $detJ=0$ for every x. Therefore, the parameters cannot be separated at any single frequency, irrespective of measurement quality. This is the formal statement of the necessity of a second frequency. The magnitude of $\det J$ then measures how far the configuration is from that degenerate case, whereas the condition number of J governs how measurement noise is amplified in the estimates.

Uncertainty is propagated in accordance with the Guide to the Expression of Uncertainty in Measurement (Joint Committee for Guides in Metrology [JCGM], 2008). For uncorrelated readings of equal standard uncertainty $u\varepsilon'$, the standard uncertainties of the estimated parameters follow from the rows of the inverse Jacobian:

$$u(\mathrm{x_k})=u(\varepsilon')\sqrt{(J^{-1})_{k1}^2+(J^{-1})_{k2}^2} \tag{6}$$

Uncertainty alone, however, does not exhaust the metrological description of an adaptive channel: the interval over which the stated uncertainty remains valid is itself an object of analysis, and criteria of metrological reliability are required to justify that interval (Sharipov et al., 2022).

Measurement scheme

Figure 1 shows the arrangement assumed throughout. A coaxial measuring cell is excited alternately at the two frequencies; a charge-transfer front end converts the cell capacitance into a code; a reference capacitor outside the cell supports periodic autocalibration of the conversion scale; and an inversion unit recovers the pair (φ,ρ) from the two permittivity readings. The inversion is performed using Newton iteration on the residuals of Equations (1)–(3), with the Jacobian evaluated by central differences at each step.

ISSN: 2181-3337 | SCIENTISTS.UZ

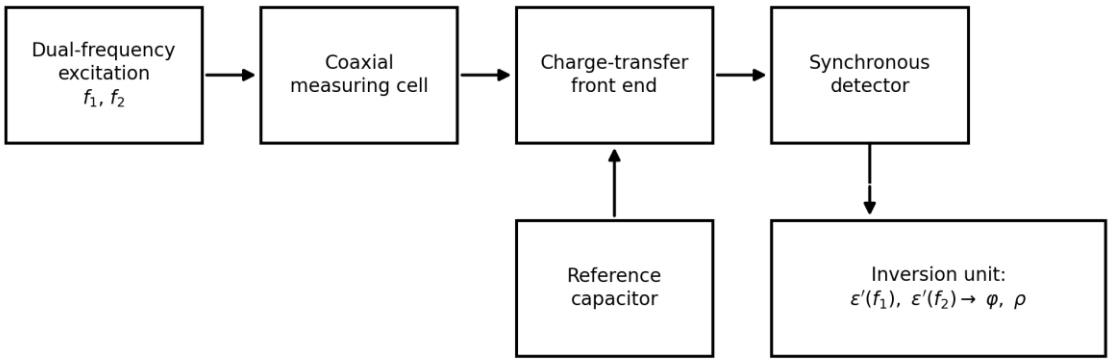


Figure 1. Functional diagram of the two-frequency capacitive measurement channel

Numerical experiment

The phase parameters used in the computations are listed in Table 1. The adopted water relative permittivity is consistent with dielectric-property data reported by Kaatze (1989). The water conductivity corresponds to weakly mineralized water, which places the relaxation frequency in the megahertz region and therefore within reach of a practical capacitive front end.

Table 1. *Parameters of the phases adopted in the computations*

Quantity	**Symbol**	**Value**	**Unit**
Water relative permittivity	ε_i	80.1	—
Water conductivity	σ_i	$1 \cdot 10^{-2}$	S/m
Hydrocarbon conductivity	σ_h	$1 \cdot 10^{-10}$	S/m
Specific refraction	A	$3.194 \cdot 10^{-4}$	m³/kg
Density range	ρ	800 … 880	kg/m³
Water volume fraction range	φ	0.005 … 0.12	—
Operating point	φ_0, ρ_0	0.05; 840	—; kg/m³
Relaxation frequency at ρ_0	f_{MW}	$2.13 \cdot 10^6$	Hz

Four computations were carried out. The dispersion curve $\varepsilon'(f)$ was evaluated over six decades for several water fractions. The determinant of the Jacobian was mapped over a grid of frequency pairs spanning five decades. Propagated uncertainties were computed from equation (6) for selected frequency pairs and for a range of channel resolutions. Finally, a Monte Carlo experiment with 500 realizations per operating point verified the propagated values and tested the inversion for bias.

Results

Dielectric dispersion of the medium

Figure 2 shows the computed dispersion. Below the relaxation frequency the water droplets behave as conducting inclusions and the effective permittivity approaches the limit $\varepsilon_h\,(1 + 2\varphi)/(1 - \varphi)$; above it the droplets act as high-permittivity dielectric inclusions and the mixture value falls. For $\varphi = 0.05$ the total dispersion depth is 0.026 units of relative permittivity, that is 1.1% of the level, and the transition is centred at 2.13 MHz. The dispersion depth grows with water content, which is precisely the behaviour that makes the frequency axis informative.

ISSN: 2181-3337 | SCIENTISTS.UZ

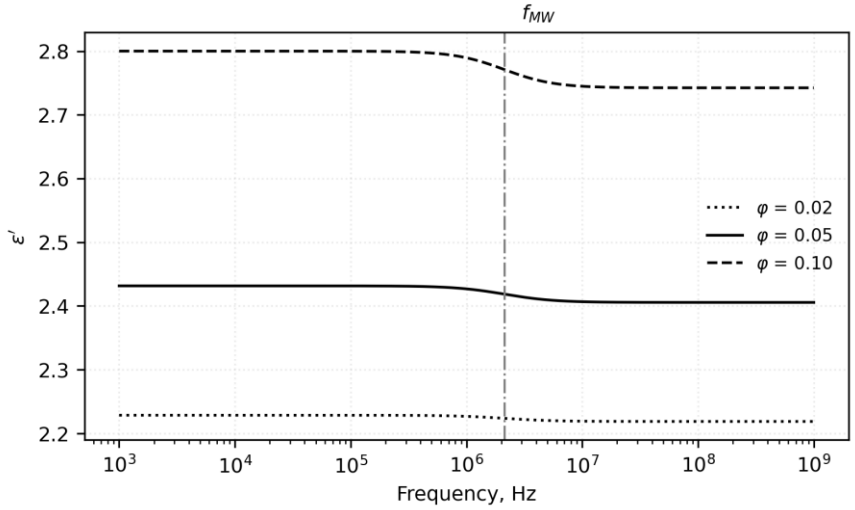


Figure 2. Effective permittivity against frequency for three water volume fractions at $\rho = 840\ kg/m^3$

Single-frequency ambiguity

The ambiguity anticipated on theoretical grounds is complete rather than partial. At 1 MHz the value $\varepsilon' = 2.42686$ is reproduced exactly by every pair listed in Table 2, which traces a continuous locus across the whole plausible range of both parameters. A single-frequency instrument cannot distinguish 2% water in a heavy hydrocarbon from 9% water in a light hydrocarbon.

Table 2. *Parameter pairs producing an identical permittivity reading at 1 MHz*

Water volume fraction φ, %	2.0	3.0	4.0	5.0	6.0	7.0	8.0	9.0
Density $\rho, kg/m^3$	940.9	907.0	873.4	840.0	806.8	773.8	741.0	708.4

Figure 3 shows the same result geometrically. Each frequency defines a locus of constant reading in the (φ, ρ) parameter plane; two frequencies define two loci whose intersection is the solution. The loci intersect at a single point, confirming observability, but they cross at a small angle. That small angle is the geometric expression of the ill-conditioning quantified below.

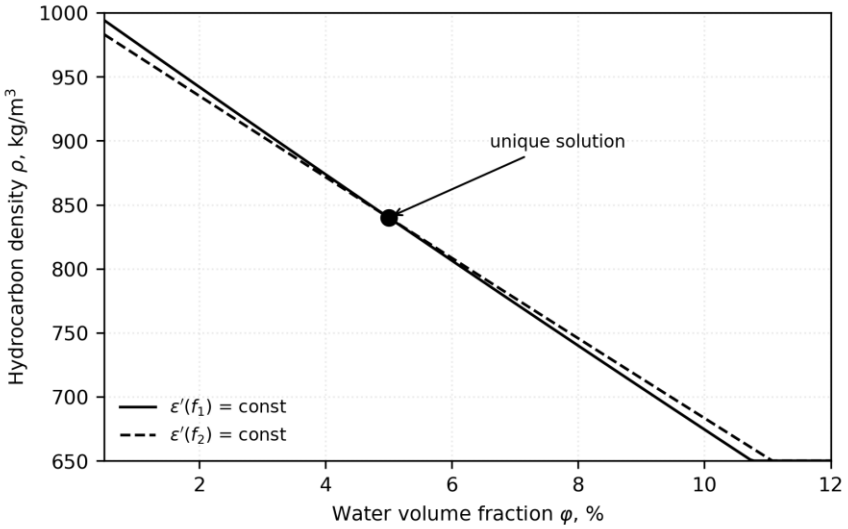


Figure 3. Loci of constant permittivity at the two probing frequencies in the parameter plane

Observability map

Figure 4 maps the determinant of the Jacobian over the plane of frequency pairs. The diagonal $f_1 = f_2$ appears as a line of exact singularity, in agreement with the analytical argument. Observability rises monotonically as the pair straddles the relaxation frequency and reaches its maximum when one frequency

ISSN: 2181-3337 | SCIENTISTS.UZ

lies far below f_{MW} and the other far above it. Over the grid examined, the maximum determinant was $8.85 \cdot 10^{-4}$, attained at $f_1 = 1.5 \cdot 10^{-3} f_{\mathrm{MW}}$ and $f_2 = 148 f_{\mathrm{MW}}$, with a condition number of $1.02 \cdot 10^{5}$.

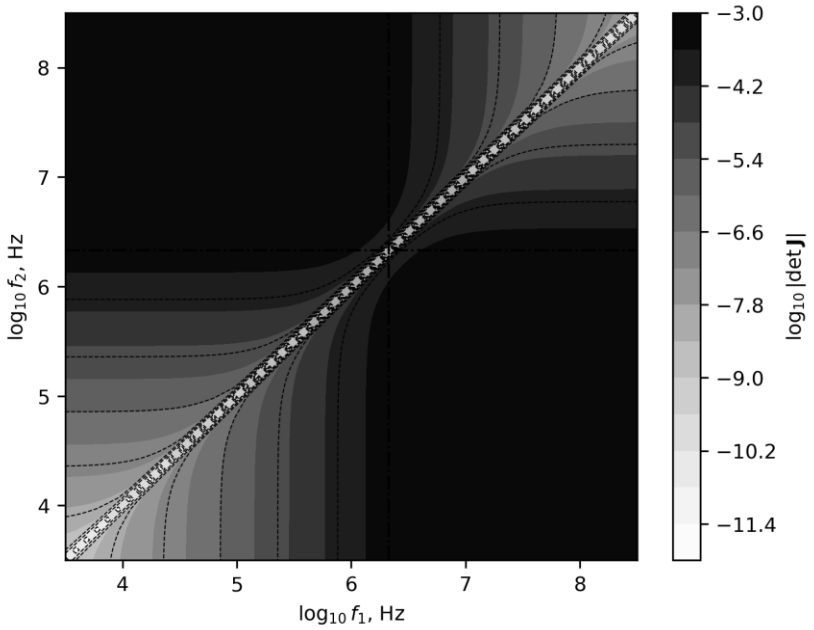


Figure 4. Decimal logarithm of the Jacobian determinant against the two probing frequencies; dash-dotted lines mark f_{MW}

The practical consequence is milder than the location of the formal optimum suggests. Table 3 lists the propagated uncertainties for frequency pairs expressed as multiples of f_{MW}. Once the low frequency is at or below $0.05 f_{\mathrm{MW}}$ and the high frequency at or above $10 f_{\mathrm{MW}}$, further separation improves the result by less than 1%. This yields a simple design rule that does not demand extreme frequencies.

Table 3. *Propagated standard uncertainties for frequency pairs referred to the relaxation frequency, at* $u(\varepsilon') = 1 \cdot 10^{-4}$

f_1	f_2	u(φ), %	u(ρ), kg/m³
$0.500 \cdot f_{\mathrm{MW}}$	$2 \cdot f_{\mathrm{MW}}$	0.0546	1.784
$0.500 \cdot f_{\mathrm{MW}}$	$10 f_{\mathrm{MW}}$	0.0414	1.344
$0.500 \cdot f_{\mathrm{MW}}$	$50 \cdot f_{\mathrm{MW}}$	0.0409	1.327
$0.050 \cdot f_{\mathrm{MW}}$	$2 \cdot f_{\mathrm{MW}}$	0.0412	1.354
$0.050 \cdot f_{\mathrm{MW}}$	$10 f_{\mathrm{MW}}$	0.0332	1.085
$0.050 \cdot f_{\mathrm{MW}}$	$50 \cdot f_{\mathrm{MW}}$	0.0329	1.074
$0.005 \cdot f_{\mathrm{MW}}$	$10 f_{\mathrm{MW}}$	0.0331	1.082
$0.005 \cdot f_{\mathrm{MW}}$	$50 \cdot f_{\mathrm{MW}}$	0.0328	1.071

Required resolution of the measuring channel

Because the density interval maps onto a narrow permittivity interval, the conditioning of the problem translates directly into a requirement on the channel. Table 4 gives the propagated uncertainties for the pair 10 kHz and 100 MHz as a function of the resolution in relative permittivity. A resolution of $2 \cdot 10^{-3}$, typical of an uncompensated capacitive channel, would render the density estimate impractical. A resolution of $1 \cdot 10^{-4}$, which corresponds to roughly 40 parts per million of the measured capacitance, reduces the density uncertainty to about 1 kg/m³.

ISSN: 2181-3337 | SCIENTISTS.UZ

Table 4. *Propagated uncertainties versus the resolution of the permittivity channel*

$u(\varepsilon')$	2×10^{-3}	$5 \cdot 10^{-4}$	$2 \cdot 10^{-4}$	1×10^{-4}	$5 \cdot 10^{-5}$	$2 \cdot 10^{-5}$
u(φ), %	0.656	0.164	0.066	0.033	0.016	0.007
u(ρ), kg/m³	21.43	5.36	2.14	1.07	0.54	0.21

Monte Carlo verification of the inversion

The Newton inversion was applied to noisy synthetic readings at three operating points, with 500 realizations each and a channel resolution of $1 \cdot 10^{-4}$. Table 5 reports the outcome. The standard deviations of the estimates agree with the propagated values in Table 4 to within 3%, which confirms that the linearized uncertainty analysis is adequate over this parameter range. The residual bias is two orders of magnitude smaller than the standard deviation and originates in the curvature of the mixture model rather than in the estimator.

Table 5. *Monte Carlo inversion results for 500 realizations per operating point*

φ, %	ρ, kg/m³	Bias in φ, %	Bias in ρ, kg/m³	SD of φ, %	SD of ρ, kg/m³
1.0	810	+0.0028	−0.098	0.0296	0.998
5.0	840	+0.0027	−0.089	0.0328	1.073
10.0	870	+0.0029	−0.092	0.0336	1.067

Tolerance to unknown water conductivity

The relaxation frequency depends on the conductivity of the water phase, which varies with salinity and is rarely known in service. The inversion was therefore run with the nominal value $1 \cdot 10^{-2}\, S/m$ while the synthetic data were generated with conductivities differing from it by up to a factor of three. Table 6 shows that the scheme is robust: a 50% error in the assumed conductivity displaces the density estimate by $0.11\ kg/m^3$ and the water fraction by 0.0034 %, both of which remain well within the noise-driven uncertainty. Only a threefold error produces a displacement comparable with the random component.

Table 6. *Effect of an incorrectly assumed water conductivity on the recovered parameters*

True σi, S/m	$5 \cdot 10^{-3}$	$8 \cdot 10^{-3}$	$1 \cdot 10^{-2}$	$1.5 \cdot 10^{-2}$	$3 \cdot 10^{-2}$
Error in φ, %	+0.0017	+0.0009	0.0000	−0.0034	−0.0217
Error in ρ, kg/m³	−0.057	−0.031	0.000	+0.113	+0.732

Discussion

The principal finding is qualitative before it is quantitative. The determinant of the Jacobian vanishes identically when the two frequencies coincide, so the second frequency is not an accuracy refinement but the condition that makes the estimation problem well-posed. This distinguishes the present treatment from the usual justification of multifrequency dielectric sensing, which appeals to improved discrimination without establishing that single-frequency operation is structurally incapable of the task. The locus in Table 2 makes the point concretely: the readings are not merely similar; they are identical.

The second finding concerns where the informativeness of the frequency axis originates. It does not originate from the mixture rule alone, because a non-dispersive mixture rule would give proportional responses at any two frequencies and a singular Jacobian. Interfacial polarization breaks the proportionality because the low-frequency limit depends on the host permittivity through a simple product with a function of φ, whereas the high-frequency limit couples the two parameters differently. This is why the observability map in Figure 4 is organized around f_{MW} rather than around any property of the electronics, and it explains why the design rule can be stated in units of f_{MW} rather than in hertz.

The third finding is a caution. The condition number of about $1 \cdot 10^5$ means that the problem, although observable, is ill-conditioned, and Figure 3 shows why: the two loci cross at a shallow angle because density modulates the hydrocarbon permittivity only within the narrow interval 2.030–2.173. Any claim of density measurement by this route must therefore be accompanied by a stated channel resolution.

ISSN: 2181-3337 | SCIENTISTS.UZ

Table 4 converts the requirement into a specification, and the specification is demanding: approximately 40 parts per million of the measured capacitance, maintained across the operating temperature range. That level is attainable only with active compensation of the transducer and links the present analysis to the broader design problem of the measurement channel rather than leaving it as an abstract result. The requirement therefore concerns not only instantaneous resolution but also resolution sustained over the verification interval, placing the result within the framework of metrological reliability rather than static accuracy (Sharipov et al., 2022).

The robustness to salinity deserves comment because it is not obvious in advance. One might expect the scheme to be fragile, since the relaxation frequency scales linearly with water conductivity and a salinity error therefore displaces the whole dispersion curve. The computations show otherwise because the design rule places both frequencies far from f_{MW}, in regions where the response has already saturated to its low- and high-frequency limits. Those limits are independent of conductivity. This robustness is therefore a consequence of the frequency-placement rule rather than an accident. It also indicates that operating close to f_{MW}, although it maximizes the dispersion slope, would be the wrong choice.

Several limitations should be stated. The Maxwell–Garnett rule assumes dilute, spherical, non-interacting inclusions; at volume fractions above roughly 0.15, the Hanai (1960) formulation or the integral modification of Qian et al. (2022) would be required, and the numerical values reported here would shift, although the observability argument would not. Droplet-size distribution and non-spherical shape introduce a distribution of relaxation times (Samet et al., 2022; Sillars, 1937), which broadens the transition and reduces the effective dispersion depth. Temperature has been held constant throughout; in service, it acts on both phases and constitutes a third parameter, so a three-parameter observability analysis with an independent temperature reading is the natural continuation of this work. Finally, all results presented here are model-based; experimental confirmation using prepared emulsions of known composition remains to be carried out.

Conclusions and Implications

Water content and hydrocarbon density cannot be separated from a single capacitive reading: the Jacobian of the measurement map is singular at any one frequency, and an entire locus of composition–density pairs produces the same permittivity. Maxwell–Wagner interfacial polarization removes the degeneracy; therefore, a two-frequency scheme is a necessary condition for observability rather than an optional improvement.

Three results are of direct use in instrument design. The frequencies should be placed at or below $0.05\cdot f_{\mathrm{MW}}$ and at or above $10\cdot f_{\mathrm{MW}}$; beyond this separation the gain saturates within 1%, so extreme frequencies are unnecessary. The channel resolution required to make density meaningful is $1\cdot10^{-4}$ in relative permittivity, giving standard uncertainties of 0.033% in water volume fraction and 1.07 kg/m³ in density, values confirmed by Monte Carlo inversion. The scheme tolerates a 50% error in the assumed water conductivity with a density displacement of only 0.11 kg/m³, because the recommended frequencies lie in the conductivity-independent limits of the response.

The resolution requirement is the practical bottleneck and defines the next stage of the work: a capacitive channel with periodic autocalibration against an internal standard and adaptive compensation of influencing quantities, without which the two-frequency scheme remains observable in principle but unusable in practice. Experimental validation using emulsions of certified composition and extension of the observability analysis to include temperature as a third parameter are the two further steps required before the method can be offered for metrological attestation.

REFERENCES

1. Adohi, B. J. P., Vanga Bouanga, C., Fatyeyeva, K., & Tabellout, M. (2009). Application of the Maxwell–Wagner–Hanai effective medium theory to the analysis of the interfacial polarization

relaxations in conducting composite films. *Journal of Physics D: Applied Physics, 42*(1), 015302. https://doi.org/10.1088/0022-3727/42/1/015302

2. Asami, K. (2002). Characterization of heterogeneous systems by dielectric spectroscopy. *Progress in Polymer Science, 27*(8), 1617–1659. https://doi.org/10.1016/S0079-6700(02)00015-1
3. Böttcher, C. J. F. (1973). *Theory of electric polarization* (2nd ed., Vol. 1). Elsevier.
4. Hanai, T. (1960). Theory of the dielectric dispersion due to the interfacial polarization and its application to emulsions. *Kolloid-Zeitschrift, 171*(1), 23–31. https://doi.org/10.1007/BF01520320
5. Joint Committee for Guides in Metrology. (2008). *Evaluation of measurement data—Guide to the expression of uncertainty in measurement (JCGM 100:2008)*. https://doi.org/10.59161/JCGM100-2008E
6. Jumamuratov, B. A., Abduqayumov, A. A., & Eshmuradov, D. E. (2024). Kompozit materiallarning radioshofonligini nazorat qiluvchi vositaning metrologik ta'minoti [Metrological support for a means of controlling the radio transparency of composite materials]. *Milliy Standart*, (3), 1–5.
7. Kaatze, U. (1989). Complex permittivity of water as a function of frequency and temperature. *Journal of Chemical & Engineering Data, 34*(4), 371–374. https://doi.org/10.1021/je00058a001
8. Kalman, R. E. (1963). Mathematical description of linear dynamical systems. *Journal of the Society for Industrial and Applied Mathematics, Series A: Control, 1*(2), 152–192. https://doi.org/10.1137/0301010
9. Maxwell, J. C. (1873). *A treatise on electricity and magnetism* (Vol. 1). Clarendon Press.
10. Qian, J., Yan, S., Li, Z., Yu, L., Wang, X., Zhang, Z., Sun, J., & Han, X. (2022). Modification of the Maxwell–Wagner heterogeneous dielectric model for heterogeneous polymers and emulsions. *Polymers, 14*(13), 2743. https://doi.org/10.3390/polym14132743
11. Samet, M., Kallel, A., & Serghei, A. (2022). Maxwell–Wagner–Sillars interfacial polarization in dielectric spectra of composite materials: Scaling laws and applications. *Journal of Composite Materials, 56*(20), 3197–3217. https://doi.org/10.1177/00219983221090629
12. Sharipov, G. N., Turayeva, N. M., & Eshmuradov, D. E. (2022). Voprosy povysheniya metrologicheskoy nadezhnosti sredstv izmereniy [Issues in improving the metrological reliability of measuring instruments]. In *Proceedings of the International Conference "State and Trends in the Development of Standardization and Technical Regulation in the World"* (pp. 178–184). Tashkent State Technical University.
13. Sihvola, A. (1999). *Electromagnetic mixing formulas and applications*. Institution of Electrical Engineers.
14. Sillars, R. W. (1937). The properties of a dielectric containing semiconducting particles of various shapes. *Journal of the Institution of Electrical Engineers, 80*(484), 378–394. https://doi.org/10.1049/jiee-1.1937.0058
15. Wagner, K. W. (1914). Erklärung der dielektrischen Nachwirkungsvorgänge auf Grund Maxwellscher Vorstellungen. *Archiv für Elektrotechnik, 2*(9), 371–387. https://doi.org/10.1007/BF01657322

ISSN: 2181-3337 | SCIENTISTS.UZ VOLUME 5 ISSUE 8 | AUGUST 2026

REMOTE SENSING AND GIS MONITORING OF WIND EROSION AND DUST EMISSION IN CENTRAL ASIA

Mamatkulov Asliddin[1], Baxodirov Zafar[2], Eshmurodov Sobir[3]
PhD in Agricultural Sciences, Senior Researcher, a.mamatkulov@soil.uz[1]
DSc in Biological Sciences, Senior Researcher, zafarbahodirov@gmail.com[2]
Master's student, sobireshmurodov1@gmail.com,
Soil Science and Agrochemical Research Institute, Tashkent, Uzbekistan[3]

DOI: 10.67620/sai.58a0004

ABSTRACT
Wind erosion and associated dust emission are major drivers of land degradation in arid and semi-arid regions of Central Asia, affecting soil condition, agricultural landscapes, ecosystems, and air quality. The aim of this review is to critically assess current remote sensing and geographic information system (GIS) approaches for monitoring wind erosion, identifying dust-source areas, and characterizing atmospheric dust emissions in Central Asia. The review synthesizes peer-reviewed studies addressing optical and radar satellite observations, unmanned aerial vehicles, GIS analysis, wind-erosion models, aerosol products, meteorological observations, and ground-based measurements. Particular attention is given to the integration of remote sensing with the Revised Wind Erosion Equation (RWEQ), the Wind Erosion Prediction System (WEPS), Google Earth Engine workflows, and atmospheric transport models. The reviewed evidence indicates that optical data are most effective for characterizing vegetation cover, exposed soil, land-cover dynamics, and surface moisture; SAR/InSAR provides complementary information on structural and temporal surface changes; and aerosol products such as AOD and AAI/UVAI describe the atmospheric phase of dust events. However, differences in spatial and temporal resolution, model parameterization, and validation procedures constrain direct comparison among studies. An integrated framework combining remote sensing, GIS, erosion modelling, meteorological observations, UAV surveys, and ground-based aerosol measurements is therefore the most promising direction for operational monitoring of wind erosion and dust emission in Central Asia.

ACCEPTED

03.09.26

Keywords: *wind erosion; remote sensing; GIS; dust emission; Central Asia.*

CC BY

Introduction

Wind erosion is a major geomorphological and soil-degradation process in arid and semi-arid environments. It selectively removes fine and nutrient-rich soil fractions, alters the physical properties of the surface layer, redistributes sediment across landscapes, and can contribute to atmospheric particulate matter. Contemporary research therefore increasingly treats wind erosion and dust emission as linked stages of a continuum extending from soil-surface instability and particle detachment to atmospheric transport and deposition (Alfaro & Gomes, 2001; Jarrah et al., 2020; Borrelli et al., 2021).

Central Asia is particularly vulnerable because extensive arid landscapes coincide with strong seasonal winds, sparse vegetation, soil-surface degradation, irrigation-related land-use change, and a limited density of long-term ground observations. Regional syntheses show that soil-erosion research in Central Asian countries has expanded substantially, while methodological approaches remain heterogeneous in spatial scale, input data, and quantitative assessment procedures (Juliev et al., 2024). Evidence from other dryland regions also demonstrates that anthropogenic land-use and land-cover change can modify wind-erosion patterns (Chi et al., 2019). Climate-driven changes may further modify the spatial and temporal distribution of wind-erodible surfaces and erosion intensity (Li et al., 2020).

The desiccated Aral Sea basin provides one of the clearest examples of the regional importance of aeolian processes. The newly formed Aralkum landscape has become a major source of mineral and saline dust. Regional modelling has identified more than 27,000 km² of potential dust-source areas and estimated mean annual potential dust emission at approximately 80.5 Tg during 2010–2020, with the eastern part of the desiccated basin contributing the largest share (Banks et al., 2022; Chen et al., 2022; Xi & Sokolik, 2016). These findings demonstrate that wind erosion in Central Asia is not only a soil-degradation problem but also an atmospheric and regional environmental issue.

Conventional field methods, including sediment traps, direct measurements of particle transport, meteorological observations, and soil-surface characterization, provide essential measurements for process understanding and model validation. Their principal limitation is spatial representativeness: measurements from a limited number of sites cannot readily describe rapidly changing conditions across millions of hectares. Remote sensing and GIS consequently provide an important means of extending observations from individual sites to regional scales. Recent reviews emphasize the growing role of satellite and UAV observations in identifying erosion-prone surfaces and linking surface characteristics with erosion processes (Lackoóvá et al., 2023; Baxodirov et al., 2022).

The integration of remote sensing with wind-erosion models represents a particularly important development. The original Wind Erosion Equation (WEQ) established an empirical basis for estimating potential wind erosion (Woodruff & Siddoway, 1965), while the Revised Wind Erosion Equation (RWEQ) improved its representation of erosion-driving factors and broadened its practical applicability (Fryrear et al., 2001). More recently, Google Earth Engine has enabled large-scale implementation of RWEQ using long time series of satellite, climatic, soil, and vegetation data. For Central Asia, GEE-RWEQ has been used to generate regional maps of wind-erosion potential at 500 m resolution for 2000–2019 (Wang et al., 2020), and subsequent work has incorporated multi-source remote sensing to assess changes and their climatic and anthropogenic drivers (Yao et al., 2025).

At the atmospheric stage, satellite aerosol products, reanalysis data, ground-based measurements, and transport models provide complementary information. AOD and AAI/UVAI can identify and track aerosol plumes, whereas $PM_{2.5}$ and PM_{10} measurements quantify near-surface particulate loading. Studies of Central Asian dust events demonstrate the value of combining TROPOMI observations with CAMS, MERRA-2, ground observations, and atmospheric transport modelling (Nishonov et al., 2023). This distinction is important because an erosion-potential map describes the susceptibility or potential emission of a surface, whereas atmospheric aerosol measurements describe the resulting airborne phase.

Radar observations provide another complementary information source. Sentinel-1 SAR and multi-temporal InSAR approaches can characterize structural and temporal changes of the land surface under conditions where optical observations are affected by cloud cover or illumination. Recent SBAS-InSAR research in the southern Aral Sea basin identified areas of rapid and slow erosion, stable surfaces, and zones of accumulation, while also demonstrating relationships with soil moisture and wind conditions (Chen et al., 2025).

Despite these advances, an integrated regional monitoring framework that links surface condition, erosion potential, dust emission, atmospheric transport, and impact zones remains insufficiently

ISSN: 2181-3337 | SCIENTISTS.UZ

standardized. Differences in sensor characteristics, temporal coverage, model parameterization, validation methods, and definitions of erosion and dust indicators limit comparability among studies. The objective of this review is therefore to critically synthesize current remote sensing and GIS-based methods for monitoring wind erosion and dust emission in Central Asia, compare their strengths and limitations, and identify priorities for an integrated spatial-temporal monitoring system.

2. Method

This review was designed as a critical synthesis of peer-reviewed literature on remote sensing, GIS, wind-erosion modelling, dust-source identification, and atmospheric aerosol monitoring relevant to Central Asia. The literature base was assembled primarily from Scopus and Web of Science using combinations of the terms “wind erosion”, “dust emission”, “dust storm”, “remote sensing”, “GIS”, “RWEQ”, “WEPS”, “SAR”, “InSAR”, “UAV”, “Central Asia”, “Aral Sea”, and “Aralkum”.

Studies were considered relevant when they addressed at least one of the following: (i) spatial or temporal assessment of wind erosion; (ii) identification or characterization of dust-source areas; (iii) estimation or observation of dust emission; (iv) application of optical, radar, UAV, or aerosol remote sensing; or (v) integration of remote sensing, meteorological, soil, and ground observations with erosion or atmospheric transport models. The selected literature was grouped by data type, analytical method, spatial scale, principal indicators, and methodological limitations.

The synthesis followed three analytical levels. First, surface-oriented approaches were examined, including optical satellite observations, SAR/InSAR, UAV surveys, and GIS-based integration. Second, wind-erosion models were compared with respect to their conceptual basis, data requirements, outputs, and suitability for Central Asian conditions. Third, atmospheric monitoring approaches were evaluated by considering aerosol products, PM measurements, reanalysis datasets, and transport modelling. The final synthesis focused on how these components can be combined into a coherent monitoring chain from soil-surface susceptibility to atmospheric dust and potential impact zones.

Because the study is a review, no primary field or laboratory experiment was conducted. The conclusions are therefore based on the evidence and methodological characteristics reported in the reviewed literature. Particular attention was paid to limitations and validation requirements so that modelled erosion potential would not be interpreted as a direct measurement of sediment flux.

3. Results or Findings

3.1. Wind erosion and dust emission in Central Asia

The reviewed literature indicates pronounced spatial and temporal heterogeneity of wind erosion across Central Asia. Erosion intensity is controlled by interacting meteorological, soil, vegetation, and land-use factors, with the highest susceptibility generally occurring on exposed desert surfaces, degraded lands, and the desiccated Aral Sea bed. Large-scale assessments using RWEQ and remote sensing show that wind speed, vegetation cover, soil moisture, surface condition, and land use are among the dominant controls of spatial variability (Li et al., 2020; Wang et al., 2020). Soil erodibility itself is a critical parameter and requires careful regional characterization because it controls the susceptibility of the surface to detachment and transport (Gao et al., 2022; Webb et al., 2006, 2009).

The Aral Sea basin is a particularly important regional source. Dust-source mapping and emission modelling indicate extensive areas of potentially active surface deflation and substantial annual emissions (Banks et al., 2022; Chen et al., 2022). Earlier analyses using satellite observations also identified the desiccated basin as an active dust source, while later work has emphasized the role of land-use change and desiccation in enhancing anthropogenic and natural dust emissions (Indoitu et al., 2015; Xi & Sokolik, 2016). The magnitude and seasonality of emissions demonstrate why surface erosion monitoring should be connected with atmospheric observations.

Regional studies further indicate that the distribution of erosion-prone areas can shift seasonally and interannually. Changes in wind regime, snowmelt, vegetation dynamics, soil moisture, and land use

may alter the spatial pattern of erosion potential (Wang et al., 2020; Yao et al., 2025). Consequently, a static erosion-risk map cannot fully represent the temporal dynamics of Central Asian dust-source activity.

3.2. Remote sensing and quantitative assessment of wind erosion

Optical satellite observations provide the most widely used regional information on vegetation cover, exposed soil, land-cover change, surface reflectance, and moisture-related characteristics. Landsat, Sentinel-2, and MODIS time series can support the identification of erosion-prone surfaces and provide variables required for model parameterization. Their principal limitation is that spectral observations generally describe surface condition rather than directly measuring particle detachment or sediment flux (Lackoóvá et al., 2023).

The combination of satellite observations with GIS and RWEQ substantially expands the spatial and temporal scope of wind-erosion assessment. Wang et al. (2020) demonstrated that GEE-RWEQ can produce monthly maps of wind-erosion potential across Central Asia at 500 m spatial resolution for 2000–2019. Such workflows reduce the computational burden of processing multi-year, multi-source datasets and make regional comparisons more feasible. More recent work in the Aral Sea region has further linked RWEQ outputs with multi-source remote sensing and factor attribution (Yao et al., 2025).

The results of the reviewed studies also support the use of independent indicators such as dust-storm indices, AOD, and AAI/UVAI for evaluating the spatial and temporal consistency of modelled erosion potential. However, agreement between a modelled erosion index and an aerosol indicator should be interpreted as complementary evidence rather than direct validation of sediment flux. Independent field measurements remain necessary to quantify actual particle transport and to constrain model uncertainty (Borrelli et al., 2021).

Table 1

Comparative characteristics of remote sensing and GIS methods for wind erosion and dust emission monitoring

Method / data source	Key parameters / indicators	Main application	Advantages and limitations
Optical satellite data (Landsat, Sentinel-2, MODIS)	NDVI; surface reflectance; bare-soil indicators; land-cover change; moisture-related indices	Vegetation and exposed-soil assessment; identification and temporal monitoring of erosion-prone areas	Large-area coverage and long archives; repeated observations. Cloud effects and mainly indirect characterization of erosion.
Satellite aerosol products (TROPOMI, MODIS)	AOD; AAI/UVAI; aerosol-plume characteristics	Detection and tracking of dust events and atmospheric aerosol transport	Regional-to-continental coverage. Limited ability to directly quantify individual ground sources; retrieval uncertainty.
SAR / InSAR (Sentinel-1)	Radar backscatter; temporal coherence; surface deformation/displacement	Detection of surface changes associated with erosion, sediment removal, and accumulation	Independent of daylight and comparatively resistant to cloud cover. Interpretation is complex and requires ancillary data.
UAV remote sensing (RGB, multispectral, photogrammetry)	High-resolution imagery; vegetation indices; DSM/DTM; surface morphology	Detailed mapping of erosion features, exposed soil, vegetation gaps, and local dust-source areas; field validation	Very high spatial resolution and flexible acquisition. Limited coverage, weather dependence, and additional processing.
GIS-based spatial analysis	Soil properties; land cover; terrain; wind; moisture; erosion-risk factors	Integration and spatial analysis of remote sensing, soil, meteorological, and field data; erosion-risk mapping	Integrates heterogeneous datasets and supports decision-making. Does not independently measure erosion and depends on input-data quality.
Integrated RS–GIS modelling (RWEQ, GEE-RWEQ)	Wind speed; soil erodibility; vegetation; roughness; climate; satellite-derived variables	Quantitative spatial-temporal assessment of erosion potential and high-risk areas	Suitable for regional assessment and long-term monitoring. Model uncertainty, parameter sensitivity, and need for field validation.

ISSN: 2181-3337 | SCIENTISTS.UZ

Table 1 shows that the methods are complementary rather than interchangeable. Optical observations primarily characterize surface and vegetation conditions, aerosol products describe the atmospheric phase, SAR/InSAR adds information on structural and temporal surface change, and UAV surveys provide localized high-resolution observations. GIS acts as the integration environment, while RWEQ-based approaches translate heterogeneous observations into spatially explicit estimates of erosion potential. The most robust regional strategy is therefore a multi-source workflow supported by independent field validation (Lackoóvá et al., 2023; Baxodirov et al., 2022).

3.3. Comparison of wind-erosion models

Wind-erosion models differ in conceptual structure, data requirements, temporal representation, and intended application scale. The original WEQ was developed as an empirical equation for estimating potential wind erosion using factors such as soil erodibility, surface roughness, climatic conditions, field length, and vegetation cover (Woodruff & Siddoway, 1965). RWEQ retained a comparatively accessible structure while improving the representation of erosion-driving conditions and has become suitable for GIS-based regional assessments (Fryrear et al., 2001; Seo et al., 2020).

WEPS represents a more process-oriented modelling framework with continuous daily simulation of weather, soil, vegetation, hydrology, management, and erosion processes. Its detailed process representation is advantageous for field-scale management and event analysis, but the model requires a comparatively large and well-parameterized input dataset (Hagen, 1991, 2004; Wagner, 2013). Reviews of wind-erosion models emphasize that model selection should reflect the target scale, available data, and required process detail rather than a simple assumption that a more complex model is always preferable (Jarrah et al., 2020).

For Central Asia, GEE-RWEQ is particularly promising because it combines a relatively tractable erosion model with large-scale satellite and climate datasets. Nevertheless, its output should be interpreted as modelled erosion potential rather than direct sediment flux. Soil erodibility, vegetation dynamics, wind forcing, and satellite-derived parameters must be regionally evaluated and, where possible, calibrated against field observations (Wang et al., 2020; Yao et al., 2025).

Table 2

Comparison of wind-erosion models and their applicability to Central Asian conditions

Model / approach	Concept and main inputs	Main outputs / scale	Applicability to Central Asia
WEQ	Empirical equation using soil erodibility, roughness, climate, field length, and vegetation	Potential annual erosion; mainly field-scale assessment	Simple and historically important; limited representation of temporal dynamics and heterogeneous regional surfaces.
RWEQ	Empirical/semi-mechanistic approach incorporating wind, soil erodibility, vegetation, crust, and surface condition	Potential soil loss; field-to-regional assessment	Well suited to GIS-based regional mapping; requires local parameterization and validation.
WEPS	Process-based continuous simulation of weather, soil, vegetation, hydrology, management, and erosion	Soil loss/deposition; saltation, creep, suspension, PM_{10}; field scale	Detailed process representation; high data requirements and need for locally appropriate inputs.
SWEEP	Single-event implementation of the WEPS erosion submodel	Soil loss and transport for individual wind events	Useful for strong-event and experimental analysis; less suited to regional long-term monitoring.
GEE-RWEQ / RS–GIS integration	RWEQ integrated with Google Earth Engine, satellite, climate, soil, vegetation, and wind datasets	Multi-temporal regional maps of erosion potential and risk zones	Strongest regional option among reviewed approaches; represents potential rather than direct sediment flux and requires independent validation.

ISSN: 2181-3337 | SCIENTISTS.UZ

The comparison indicates that model applicability depends on the spatial-temporal scale of the question and on data availability. WEQ is historically important, RWEQ is comparatively practical for regional GIS applications, WEPS provides detailed process simulation, and SWEEP is useful for individual events. For Central Asia, the most scalable pathway is the integration of RWEQ with remote sensing and GIS, complemented by field measurements and atmospheric observations (Seo et al., 2020; Jarrah et al., 2020).

3.4. SAR/InSAR and high-resolution surface monitoring

SAR observations complement optical data because radar acquisition is independent of daylight and less affected by cloud cover. Sentinel-1 time series and InSAR methods can provide information on structural and temporal changes of exposed surfaces. In the southern Aral Sea basin, SBAS-InSAR has been used to distinguish areas of rapid and slow erosion, stable surfaces, and accumulation, with soil moisture identified as an important controlling factor and wind speed linked to material transport (Chen et al., 2025).

InSAR should not be interpreted as a universal direct measure of wind-erosion intensity. Radar-derived changes may reflect several interacting processes, including moisture variation, surface roughness, sediment redistribution, and other deformation mechanisms. Its strongest value is therefore achieved when SAR/InSAR is integrated with optical data, soil-moisture information, digital terrain data, meteorological observations, and erosion models.

3.5. Dust storms and atmospheric aerosol monitoring

Atmospheric monitoring represents a different analytical level from surface erosion assessment. TROPOMI/UVAI, AOD, $PM_{2.5}$, PM_{10}, CAMS, and MERRA-2 can characterize aerosol loading, plume extent, and atmospheric conditions associated with dust events. Satellite aerosol products are especially valuable for regional-scale event detection, while ground-based PM measurements provide local quantitative information required for validation.

A study of strong dust storms in Central Asia using TROPOMI, CAMS, and MERRA-2 demonstrated that combined satellite and reanalysis information can reproduce the spatial and temporal structure of dust events, while also revealing differences among reanalysis products in $PM_{2.5}$ estimation (Nishonov et al., 2023). Analysis of the November 2021 extreme dust event in Uzbekistan further showed the value of combining satellite observations, ground aerosol measurements, and Lagrangian transport modelling for event reconstruction (Nishonov et al., 2023).

At the source-to-atmosphere level, dust emission modelling and atmospheric transport should be linked. Studies of the Aral Sea region demonstrate that combining surface erosion modelling with transport modelling can connect potential source areas, estimated emissions, and downwind pathways (Chen et al., 2022; Banks et al., 2022). Global aerosol research further confirms the usefulness of AOD for characterizing the atmospheric dust burden, although satellite retrievals require careful interpretation under heterogeneous surface and atmospheric conditions (Voss & Evan, 2020).

3.6. Integrated monitoring framework

The synthesis supports a multi-level monitoring chain: soil and vegetation condition → surface susceptibility → wind erosion → particle transport → dust emission → atmospheric aerosol → dust storm → spatial extent and impact. Each stage is best represented by different observations and models, while GIS provides the spatial environment for their integration. This conceptual framework is consistent with the broader methodological transition from isolated monitoring products toward integrated geospatial assessment (Baxodirov et al., 2022).

Figure 1 summarizes the proposed integration of optical satellite observations, SAR/InSAR, aerosol products, UAV data, meteorological and soil information, GIS processing, erosion models, and field validation. The principal analytical advantage is that it preserves the distinction between surface erosion

ISSN: 2181-3337 | SCIENTISTS.UZ

potential and atmospheric dust while allowing the two stages to be linked through source identification and transport analysis.

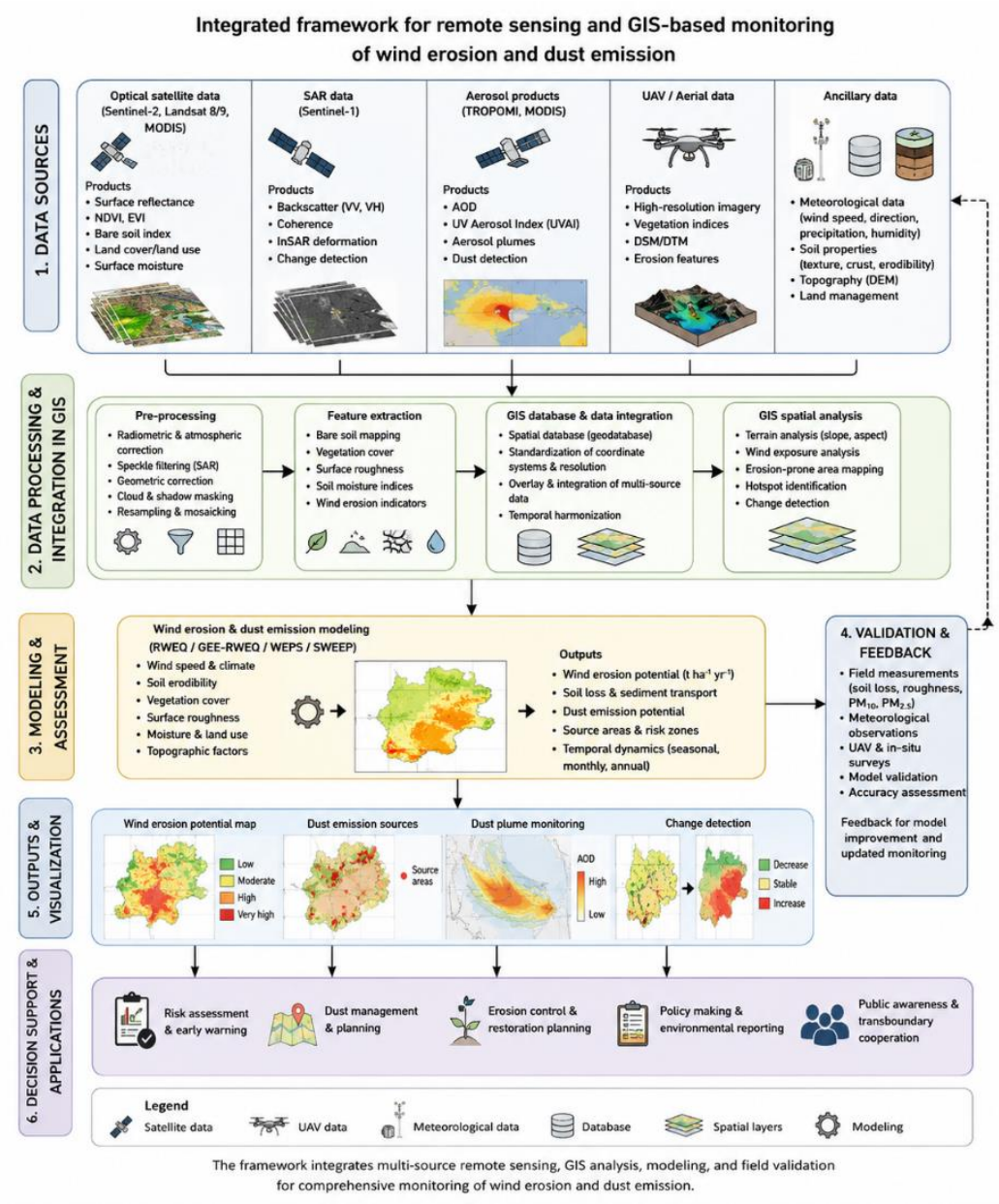


Figure 1. Integrated framework for remote sensing and GIS-based monitoring of wind erosion and dust emission

4. Discussion

4.1. Comparative performance of current monitoring methods

The evidence reviewed indicates that the principal difference among monitoring approaches lies in the type of information they provide. Field measurements are closest to the physical process and are indispensable for validation, but their spatial coverage is limited. Optical remote sensing provides repeated regional observations of surface condition, whereas SAR/InSAR supplies complementary information on structural and temporal surface change. UAVs bridge the scale gap by enabling detailed surveys of selected sites. GIS provides the analytical framework for combining these datasets.

The most important methodological limitation is the tendency to interpret a surface indicator as a direct measure of erosion. Vegetation indices, bare-soil indices, moisture indicators, and radar backscatter describe environmental conditions associated with erosion susceptibility, but they do not by themselves quantify the amount of soil removed. This distinction is particularly important in heterogeneous Central Asian landscapes, where the same spectral or radar response may arise from different combinations of soil texture, roughness, moisture, crusting, and vegetation.

ISSN: 2181-3337 | SCIENTISTS.UZ

Model-based approaches improve quantitative interpretation but introduce parameter and structural uncertainty. GEE-RWEQ is highly suitable for regional screening because it can process long satellite and climate records, while WEPS offers greater process detail at smaller scales. A rational regional strategy is therefore hierarchical: use remote sensing and GEE-RWEQ to identify and monitor broad risk patterns; use UAV and field measurements to validate selected hotspots; and use detailed process-based or event-scale models where management or event reconstruction requires greater physical detail.

4.2. Source-to-atmosphere integration

A critical implication of the literature is that wind erosion and atmospheric dust should be monitored as connected but analytically distinct stages. Surface-oriented models and remote sensing can identify where erosion is likely to occur, whereas aerosol products and PM observations indicate whether and where airborne dust is present. Atmospheric transport models then provide the link between source regions and downwind exposure.

This distinction is particularly important for the Aral Sea region. Potential source mapping alone does not quantify atmospheric exposure, while an aerosol plume alone does not uniquely identify its surface origin. The strongest evidence is obtained when source susceptibility, meteorological forcing, emission estimates, aerosol observations, and transport trajectories converge. Such integration can improve source attribution and help distinguish local dust generation from transported regional aerosol.

Figure 2. Conceptual relationship between wind erosion, dust emission and atmospheric dust monitoring in Central Asia

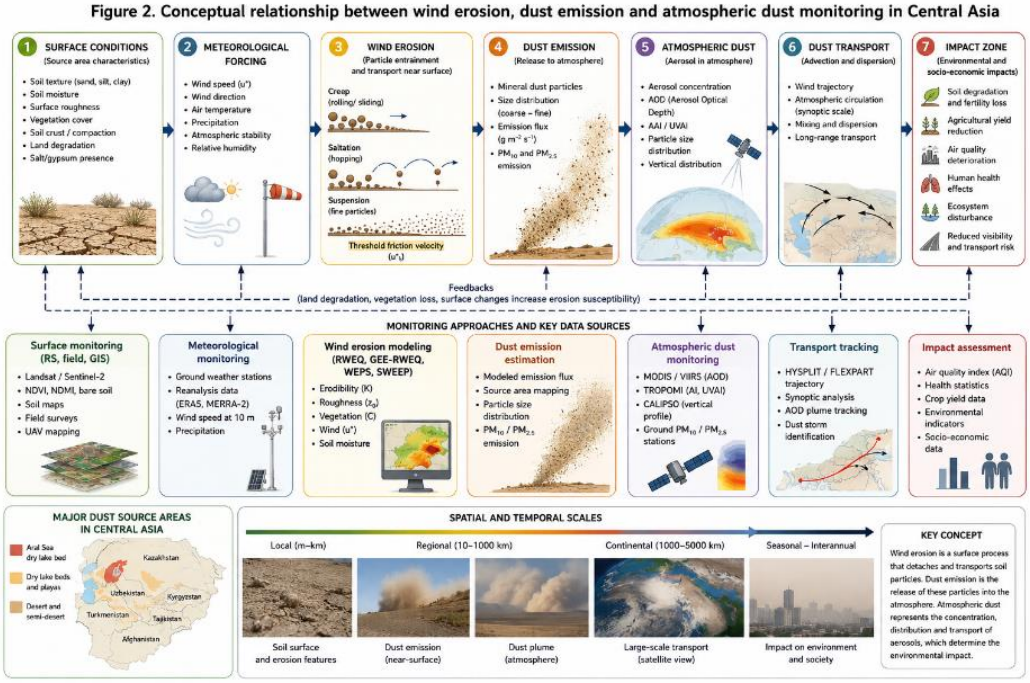


Figure 2. Conceptual relationship between wind erosion, dust emission and atmospheric dust monitoring in Central Asia

Figure 2 conceptualizes the physical sequence from soil-surface destabilization to atmospheric dust. Wind speed and direction interact with soil moisture, texture, roughness, and vegetation cover to control particle detachment and transport by creep, saltation, and suspension. The finest fraction contributes to atmospheric particulate matter and may be transported over long distances. Accordingly, $PM_{2.5}/PM_{10}$, AOD, and AAI/UVAI characterize the atmospheric stage, while surface remote sensing and erosion models are primarily used to characterize source susceptibility and potential emission. The framework highlights the need to combine both stages rather than treating either one as a complete representation of the dust cycle (Alfaro & Gomes, 2001; Voss & Evan, 2020).

4.3. Methodological gaps and priorities for Central Asia

Four methodological gaps are particularly important. First, results from different studies are difficult to compare because spatial and temporal resolutions, model formulations, threshold definitions, and validation criteria vary. Second, field validation remains insufficient relative to the spatial extent of

ISSN: 2181-3337 | SCIENTISTS.UZ

arid landscapes. Third, many studies address only one stage of the process—surface condition, erosion potential, or atmospheric aerosol—without integrating the complete chain. Fourth, the uncertainty associated with soil erodibility, moisture, roughness, and meteorological forcing is not always quantified explicitly.

Future regional monitoring should therefore prioritize standardized protocols for field validation, harmonized multi-source datasets, and uncertainty assessment. Optical and radar satellite time series should be linked with meteorological forcing and soil information; UAV surveys should be used strategically for high-resolution validation; and PM observations should be co-located with representative source areas where possible. Machine-learning methods may improve nonlinear relationships between remotely sensed variables and measured erosion or dust indicators, but such approaches should remain physically interpretable and independently validated.

A practical Central Asian monitoring architecture should operate at several spatial scales. Regional satellite and GIS products can identify candidate source areas; field and UAV observations can characterize surface properties and validate model outputs; event-scale observations can capture strong wind episodes; and aerosol and transport products can track downwind dispersion. Such a hierarchy is more realistic than attempting to use a single universal sensor or model for all stages of the process.

4.4. Implications for soil protection and environmental monitoring

From a soil-science perspective, integrated monitoring can support early identification of surfaces with increasing susceptibility to deflation, enabling targeted measures for vegetation restoration, surface stabilization, and erosion control. From an environmental perspective, linking source maps with atmospheric observations can improve assessment of dust exposure and regional air-quality risks. The combination is particularly relevant to degraded agricultural and desert landscapes of Uzbekistan and neighboring Central Asian countries.

The practical value of the proposed framework lies not in replacing field measurements but in using them more strategically. Remote sensing can identify where measurements are most needed, models can estimate where risk is likely to increase, and atmospheric observations can determine whether source activity translates into measurable aerosol loading. This feedback can support adaptive monitoring and more efficient allocation of field resources.

5. Conclusion and Implications

The critical review demonstrates that remote sensing and GIS have become central components of modern monitoring of wind erosion and dust emission in Central Asia. Optical satellite data are particularly effective for characterizing vegetation cover, exposed soil, land-cover dynamics, and moisture-related surface properties; SAR/InSAR adds complementary information on structural and temporal surface changes; UAVs provide high-resolution local observations; and aerosol products and ground-based PM measurements characterize the atmospheric stage of the dust process.

Among the reviewed erosion models, RWEQ and its GEE-integrated implementations offer a practical basis for regional screening and long-term spatial-temporal assessment, whereas WEPS provides greater process detail for field-scale applications and SWEEP is useful for individual events. None of these approaches should be interpreted as a complete substitute for field measurements. Their reliability depends on input-data quality, parameterization, spatial-temporal scale, and independent validation.

The main methodological conclusion is that wind erosion and atmospheric dust should be treated as linked but distinct stages. A robust monitoring system should connect soil and vegetation condition, meteorological forcing, erosion potential, source identification, dust emission, atmospheric aerosol observations, and transport analysis within a GIS-based framework. This integrated approach is especially relevant to the Aral Sea basin and other degraded arid landscapes of Central Asia, where large dust sources and limited ground-observation networks create a strong need for spatially extensive monitoring.

ISSN: 2181-3337 | SCIENTISTS.UZ

Future work should focus on standardized field-validation protocols, improved regional parameterization of erosion models, integration of optical and SAR observations, systematic UAV validation, machine-learning-assisted risk mapping, and operational linkage of source models with aerosol and atmospheric transport products. Such developments can provide a methodological basis for early identification of high-risk areas, more effective soil-protection measures, and improved assessment of the environmental consequences of dust storms in Central Asia.

REFERENCES

1. Alfaro, S. C., & Gomes, L. (2001). Modeling mineral aerosol production by wind erosion: Emission intensities and aerosol size distributions in source areas. Journal of Geophysical Research: Atmospheres, 106(D16), 18075–18084. https://doi.org/10.1029/2000JD900339
2. Banks, J. R., Heinold, B., & Schepanski, K. (2022). Impacts of the desiccation of the Aral Sea on the Central Asian dust life-cycle. Journal of Geophysical Research: Atmospheres, 127, e2022JD036618. https://doi.org/10.1029/2022JD036618
3. Borrelli, P., Alewell, C., Alvarez, P., Ayach Anache, J. A., Baartman, J., Ballabio, C., et al. (2021). Soil erosion modelling: A global review and statistical analysis. Science of the Total Environment, 780, 146494. https://doi.org/10.1016/j.scitotenv.2021.146494
4. Chen, Z., Gao, X., & Lei, J. (2022). Dust emission and transport in the Aral Sea region. Geoderma, 428, 116177. https://doi.org/10.1016/j.geoderma.2022.116177
5. Chen, Z., Gao, X., & Lei, J. (2025). Monitoring of wind erosion in the southern Aral Sea using SBAS-InSAR technology. International Soil and Water Conservation Research, 13(3), 551–563. https://doi.org/10.1016/j.iswcr.2025.05.005
6. Chi, W., Zhao, Y., Kuang, W., & He, H. (2019). Impacts of anthropogenic land use/cover changes on soil wind erosion in China. Science of the Total Environment, 668, 204–215. https://doi.org/10.1016/j.scitotenv.2019.03.015
7. Fryrear, D. W., Chen, W., & Lester, C. (2001). Revised Wind Erosion Equation. Annals of Arid Zone, 40(3). https://doi.org/10.56093/aaz.v40i3.65816
8. Gao, G., Yin, X., Ding, G., Zhao, Y., Sun, G., & Wang, L. (2022). Soil erodibility for wind erosion: A critical review. Science of Soil and Water Conservation, 20(1), 143–150. https://doi.org/10.16843/j.sswc.2022.01.019
9. Hagen, L. J. (1991). A wind erosion prediction system to meet user needs. Journal of Soil and Water Conservation, 46(2), 106–111. https://doi.org/10.1080/00224561.1991.12456588
10. Hagen, L. J. (2004). Evaluation of the Wind Erosion Prediction System (WEPS) erosion submodel on cropland fields. Environmental Modelling & Software, 19(2), 171–176. https://doi.org/10.1016/S1364-8152(03)00119-1
11. Indoitu, R., Kozhoridze, G., Batyrbaeva, M., Vitkovskaya, I., Orlovsky, N., Blumberg, D., & Orlovsky, L. (2015). Dust emission and environmental changes in the dried bottom of the Aral Sea. Aeolian Research, 17, 101–115. https://doi.org/10.1016/j.aeolia.2015.02.004
12. Jarrah, M., Mayel, S., Tatarko, J., Funk, R., & Kuka, K. (2020). A review of wind erosion models: Data requirements, processes, and validity. CATENA, 187, 104388. https://doi.org/10.1016/j.catena.2019.104388
13. Juliev, M., Kholmurodova, M., Abdikairov, B., & Abuduwaili, J. (2024). A comprehensive review of soil erosion research in Central Asian countries (1993–2022) based on the Scopus database. Soil and Water Research, 19(4), 244–256. https://doi.org/10.17221/82/2024-SWR
14. Lackoóvá, L., Lieskovský, J., Nikseresht, F., Halabuk, A., Hilbert, H., Halászová, K., & Bahreini, F. (2023). Unlocking the potential of remote sensing in wind erosion studies: A review and outlook for future directions. Remote Sensing, 15(13), 3316. https://doi.org/10.3390/rs15133316

15. Li, J., Ma, X., & Zhang, C. (2020). Predicting the spatiotemporal variation in soil wind erosion across Central Asia in response to climate change in the 21st century. Science of the Total Environment, 709, 136060. https://doi.org/10.1016/j.scitotenv.2019.136060
16. Baxodirov, Z. A., Mamatkulov, A. R., & Nurmatov, R. Sh. (2022). Noveyshie metody monitoringa vetrovoy erozii pochv [Latest methods for monitoring soil wind erosion]. Science and Innovation, 6, 38–46. https://doi.org/10.5281/zenodo.7086755; https://doi.org/10.5281/zenodo.13908141
17. Nishonov, B. E., Kholmatjanov, B. M., Labzovskii, L. D., Rakhmatova, N., Shardakova, L., Abdulakhatov, E. I., Yarashev, D. U., Toderich, K. N., Khujanazarov, T., & Belikov, D. A. (2023). Study of the strongest dust storm occurred in Uzbekistan in November 2021. Scientific Reports, 13, 20042. https://doi.org/10.1038/s41598-023-42256-1
18. Seo, I. W., Lim, C. S., Yang, J. E., Lee, S. P., Lee, D. S., Jung, H. G., Lee, K. S., & Chung, D. Y. (2020). An overview of applicability of WEQ, RWEQ, and WEPS models for prediction of wind erosion in lands. Korean Journal of Agricultural Science, 47(2), 381–394. https://doi.org/10.7744/kjoas.20200028
19. Tatarko, J., Sporcic, M. A., & Skidmore, E. L. (2013). A history of wind erosion prediction models in the United States Department of Agriculture prior to the Wind Erosion Prediction System. Aeolian Research, 10, 3–8. https://doi.org/10.1016/j.aeolia.2012.08.004
20. Van Pelt, R. S., Zobeck, T. M., Potter, K. N., Stout, J. E., & Popham, T. W. (2004). Validation of the wind erosion stochastic simulator (WESS) and the revised wind erosion equation (RWEQ) for single events. Environmental Modelling & Software, 19(2), 191–198. https://doi.org/10.1016/S1364-8152(03)00122-1
21. Voss, K. K., & Evan, A. T. (2020). A new satellite-based global climatology of dust aerosol optical depth. Journal of Applied Meteorology and Climatology, 59(1), 83–102. https://doi.org/10.1175/JAMC-D-19-0194.1
22. Wagner, L. E. (2013). A history of wind erosion prediction models in the United States Department of Agriculture: The Wind Erosion Prediction System (WEPS). Aeolian Research, 10, 9–24. https://doi.org/10.1016/j.aeolia.2012.10.001
23. Wang, W., Samat, A., Ge, Y., Ma, L., Tuheti, A., Zou, S., & Abuduwaili, J. (2020). Quantitative soil wind erosion potential mapping for Central Asia using the Google Earth Engine platform. Remote Sensing, 12(20), 3430. https://doi.org/10.3390/rs12203430
24. Webb, N. P., McGowan, H. A., Phinn, S. R., & McTainsh, G. H. (2006). AUSLEM (AUStralian Land Erodibility Model): A tool for identifying wind erosion hazard in Australia. Geomorphology, 78(3–4), 179–200. https://doi.org/10.1016/j.geomorph.2006.01.012
25. Webb, N. P., McGowan, H. A., Phinn, S. R., McTainsh, G. H., & Leys, J. F. (2009). Simulation of the spatiotemporal aspects of land erodibility in the northeast Lake Eyre Basin, Australia, 1980–2006. Journal of Geophysical Research: Earth Surface, 114, F01013. https://doi.org/10.1029/2008JF001097
26. Woodruff, N. P., & Siddoway, F. H. (1965). A wind erosion equation. Soil Science Society of America Journal, 29(5), 602–608. https://doi.org/10.2136/sssaj1965.03615995002900050035x
27. Xi, X., & Sokolik, I. N. (2016). Quantifying the anthropogenic dust emission from agricultural land use and desiccation of the Aral Sea in Central Asia. Journal of Geophysical Research: Atmospheres, 121, 12270–12281. https://doi.org/10.1002/2016JD025556
28. Yao, F., Ding, J., Bao, A., & Li, J. (2025). Attribution and risk assessment of wind erosion in the Aral Sea regions using multi-source remote sensing and RWEQ on GEE. Remote Sensing, 17(16), 2788. https://doi.org/10.3390/rs17162788

ISSN: 2181-3337 | SCIENTISTS.UZ VOLUME 5 ISSUE 8 | AUGUST 2026

REVERSE OSMOSIS MEMBRANES UNDER DUTY-CYCLED OPERATION: COMPACTION, SCALING, BIOFILM REGROWTH AND PERMEATE TRANSIENTS IN PHOTOVOLTAIC-DRIVEN BRACKISH DESALINATION

Kuralov Murodbek[1], **Akhatov Jasurjon**[2]
PhD student, Corresponding author. makuralov@gmail.com[1]
Doctor of Technical Sciences, Professor[2]
S. A. Azimov Physical-Technical Institute, Academy of Sciences of the Republic of Uzbekistan, Tashkent, Uzbekistan

DOI: 10.67620/sai.58a0005

ABSTRACT

Photovoltaic-driven reverse osmosis is the dominant architecture for decentralised brackish-water supply in arid regions, yet it violates the condition under which almost all membrane performance data are obtained: steady pressure, steady flux and continuous operation. This review assembles the evidence on how the polyamide membrane itself, considered as a mechanical and biological object, responds to duty cycling, and reconciles findings that disagree in sign rather than merely in magnitude. Primary studies published between 2006 and 2026 were coded against a purpose-built parameterisation of non-steady operation comprising duty cycle, stop duration, cycle count, ramp rate, fluctuation amplitude and frequency, minimum-flux floor, idle-state fluid, flush protocol and buffering. Four membrane-side consequences are examined: irreversible compaction and creep recovery across repeated pressurisation; scaling induction time relative to residence time at peak supersaturation; biological regrowth during idle intervals; and permeate-quality transients on restart. Reported outcomes span a permeability loss exceeding fifty per cent after seven days of cycling and no measurable degradation after 1,568 start-stop cycles. Three variables reconcile most of that disagreement: idle-state chemistry, spontaneous osmotic backwash on depressurisation, and the partition between reversible compaction of the active layer and irreversible compaction of the support. No located study varies shutdown duration as a controlled independent variable against a biological endpoint on a membrane, and an experimental design closing that gap is specified.

ACCEPTED

03.09.26

Keywords: *Reverse osmosis; Intermittent operation; Membrane compaction; Biofouling; Photovoltaic desalination.*

CC BY

1. Introduction

Membrane-based systems have become the default technology for decentralised water supply where grid electricity and centralised treatment do not reach (Yin & Huang, 2026). For brackish groundwater in arid regions the dominant architecture is reverse osmosis driven by photovoltaic power, and Central Asia holds an early place in its record: a photovoltaic-powered reverse-osmosis pilot was

operated in Uzbekistan more than fifteen years ago (Aybar et al., 2010), preceded by solar direct-osmosis experiments in the same country (Khaydarov & Khaydarov, 2007). The engineering case for the architecture is settled. What is not settled is the condition of the membrane inside it: a photovoltaic system runs when the sun allows, stops at night, may stand idle for days, and delivers whatever flux the irradiance permits, not the flux at which the membrane was characterised.

Almost everything known about that membrane was measured under the opposite regime. The evidence base of membrane science rests on coupons of 5-45 cm² held at constant pressure and constant recovery, fed with synthetic solutions, over hours or days. This is not a shortcoming of individual studies but a constitutive property of the corpus. An audit conducted for this review of thirty-nine review articles published between 2019 and 2026 (1,090 typeset pages, roughly 800,000 words and 5,621 references in their combined bibliographies) found standardised testing protocols treated in none of them, long-term stability in three, and pilot- or field-scale evidence in seven. The mismatch between how membranes are characterised and how photovoltaic-driven systems make them operate is therefore not a gap in any one literature; it is a property of the literature as a whole.

Unsteady and cyclic desalination has recently been mapped at the level of process configurations, feed-channel hydrodynamics and data-driven control (Liang & Li, 2026), and batch-type configurations have been reviewed separately (Kim et al., 2025). The membrane's own response to that duty cycle, however, has not been substantively reviewed: irreversible compaction and creep recovery across repeated pressurisation-depressurisation cycles, rejection loss accumulated over cycles, and biological regrowth during idle intervals. Systematic reviews of solar-driven reverse osmosis continue to treat the membrane as a permeability coefficient and to address intermittency only as a generation-side problem (Almetwally et al., 2025). This review therefore takes the membrane - as a mechanical and biological object - rather than the process configuration as its unit of analysis.

A distinction is drawn throughout between *designed* cycling, in which the cycle is chosen and optimised as part of the process - batch, semi-batch and closed-circuit operation, and feed-flow reversal - and *imposed* cycling, in which the cycle is a disturbance dictated by the energy resource and must simply be survived. Existing treatments of fouling under cyclic operation address the former (Burlace 2022); the latter is the subject of this review. In photovoltaic-driven desalination the imposed cycle is diurnal and non-negotiable: the system stops every night, whatever the state of the membrane.

What that survival costs is not settled even in sign. Under seven days of daily cycling without a pre-shutdown flush, a brackish-water membrane retained less than half of its initial permeability, against more than seventy per cent when antiscalant dosing and a clean-water flush were applied (Freire-Gormaly & Bilton, 2019b). Under a comparable schedule observed by optical coherence tomography, intermittency protected rather than harmed: continuous operation lost 24% of flux where intermittent operation lost 8.9-10.4%, because the fouling layer collapsed from 21.2 µm to 7.5-8.4 µm at every shutdown (S. Lee et al., 2023). The variable separating these outcomes is what the membrane rests in, deionised water or feed, and where that has been varied directly it proves decisive (Yang et al., 2022). The full-scale record divides the same way: the longest intermittent record located, fourteen years at roughly nine hours per day, shows a permeability loss of about half, with specific energy consumption rising from 1.82 to 2.21 kWh m^{-3} (Ruiz-García 2020), while a seawater plant cycled hourly showed no structural degradation at autopsy after 1,568 start-stop events in four months (Carta et al., 2025).

This review organises the evidence around four membrane-side consequences of duty-cycled operation. The first is mechanical: polyamide composite membranes compact under load and recover incompletely, and the only located compaction study with an explicit cycle count reports the irrecoverable fraction growing cycle on cycle (Ding et al., 2024; Wu et al., 2025). The second is physicochemical: whether scaling occurs depends on how long the membrane resides at peak supersaturation relative to the nucleation induction time, a framing under which cycling has been found both protective (Warsinger et al.,

2018) and aggravating (T. Lee et al., 2019), a dispute treated here as the analytical core. The third is biological: regrowth during the idle interval, for which a surface endpoint has been measured under duty cycling (Freire-Gormaly 2019b), but in no located study with idle duration itself as the swept variable. The fourth is permeate quality on restart, where the literature conflates three phenomena that must be separated before results can be compared across studies: a recoverable hydrodynamic transient (Park et al., 2012), an unrecoverable loss of integrity accumulated over pressure cycles (Torii et al., 2019), and an instantaneous driving-force depression during low-power operation (Park et al., 2011).

The contribution intended here is not new data but reconciliation. Three variables already present in the primary literature, and assembled by no single source, account for most of the disagreement in sign: the chemistry of the idle state; the spontaneous osmotic backwash generated by depressurisation itself; and the partition of compaction into a reversible component in the active layer and an irreversible component in the support. A fourth, the scale and horizon of observation, accounts for much of the remainder. Section 2 states the search protocol and introduces a ten-field parameterisation of non-steady operation (Table 1), proposed as the reporting scheme the field currently lacks. Section 3 maps the evidence across the four consequences; Section 4 develops the reconciling variables; Section 5 ranks the resulting research priorities, the first of which is specified to the level of a full experimental design.

2. Method

This work is presented as an evidence map rather than as a systematic review. Bibliographic databases requiring institutional subscription were not accessible during the search, and the retrieval could not be re-executed under identical conditions; the protocol is therefore reported for transparency rather than as a reproducible procedure, and no PRISMA compliance is claimed. Records were located through Crossref, OpenAlex, Semantic Scholar, PubMed and publisher pages, supplemented by backward and forward citation tracking from four anchor studies (Freire-Gormaly & Bilton, 2018, 2019b; Ruiz-García & Nuez, 2020; Warsinger et al., 2018). Every bibliographic record reported here was confirmed against the publisher deposit; no publication year, volume or author list was inferred from an article identifier.

The corpus assembled under this protocol comprises sixty-nine bibliographic records. Eight are review articles, which delimit the surrounding territory without contributing evidence; four are industry standards and manufacturer technical bulletins, treated throughout as practitioner documentation rather than as peer-reviewed sources; the remaining fifty-seven are primary studies and constitute the evidence base mapped in Table 2. Eligibility required experimental observation of a reverse-osmosis or nanofiltration membrane under some form of non-steady operation: imposed start-stop duty cycling, resource-driven variable flux, repeated pressurisation, deliberately designed cyclic operation, or storage and stagnation between periods of service. One adjacent body of evidence was admitted deliberately. Studies of stagnation in drinking-water distribution and premise plumbing do not involve membranes, but they are the only systems located in this search in which idle duration is swept as a controlled independent variable against biological endpoints; they are used in Section 3.4 to define the shape of the response a membrane experiment should anticipate, not as evidence about membranes themselves.

Each primary study was coded against the ten descriptors of non-steady operation defined in Table 1: duty cycle, stop duration, cycle count, ramp rate, fluctuation amplitude and frequency, minimum-flux floor, idle-state fluid, flush protocol and buffering. No shared scheme of this kind was found in the literature, and its absence is consequential: blank cells in Table 2 were retained and never imputed, because what primary studies do not report is itself a finding. Figure 1 projects the coded corpus onto a matrix of non-steady mode against observation scale; the 43 studies shown are those whose observation scale could be verified, with modelling studies, re-analyses of existing datasets and the non-membrane stagnation studies excluded from the projection.

A terminological observation is itself a finding of this review. Querying "intermittent operation" alone recovers well under half of the relevant primary work, because the field is distributed across

ISSN: 2181-3337 | SCIENTISTS.UZ

vocabularies that do not cite one another. The productive alternative terms are "renewable energy powered membrane technology", "solar irradiance fluctuation", "osmotic backwash", "wave-driven pressure fluctuation", "transient membrane transport parameters", "salinity cycling", "compaction and relaxation", and "feed flow reversal". Searches confined to a single vocabulary will systematically under-represent the evidence base.

The fragmentation of vocabulary has an institutional counterpart on the side of standards. Standardisation in this field exists only on the feedwater side. A recent critical review of membrane autopsies cites eighteen ASTM standards, every one of them a method for analysing the feed - silt density index, modified fouling index, Langelier and Stiff-Davis saturation indices, chlorine, iron, silica and oxidation-reduction potential - and none a method for testing the membrane or the element (Philibert et al., 2024). The single ASTM method addressing element-level performance, D4194-23, prescribes measurement under standardised steady-state conditions and makes no provision for cyclic, intermittent or transient operation (ASTM International, 2023). The terminology standard for the field, D6161-19, defines no term for standby, lay-up, idle period, duty cycle, or cycle-count-based service life (ASTM International, 2019).

Table 1.

Proposed parameterisation scheme for non-steady reverse-osmosis operation

#	Parameter	Unit / form of record	Example	Rationale
1	Duty cycle	h operation / h idle per day	8/16; 9/15	Sets the ratio of filtration to stagnation
2	Stop duration	h or d of uninterrupted idleness	overnight; weekend; seasonal	Governs residence time at peak supersaturation relative to the nucleation induction time, and the interval available for biological regrowth
3	Cycle count	number of start-stop events per study	1,568 over 4 months	The only variable found to correlate with accumulated rejection loss
4	Ramp rate	kPa s^{-1} or LMH s^{-1} at start-up	soft start vs. step	Hydraulic shock and mechanical load on the element
5	Fluctuation amplitude	fraction of nominal flux	0.3-1.0	Amplitude of the diurnal irradiance excursion
6	Fluctuation frequency	h^{-1} or spectrum	cloud transients vs. diurnal cycle	Separates fast from slow disturbances
7	Minimum-flux floor	LMH below which the system idles	cut-in threshold	Below the floor: concentration polarisation without production
8	Idle-state fluid	contents of the element at rest	feed / permeate / DI / preservative	The decisive variable: determines the sign of the idle-period effect
9	Flush protocol	presence, timing and volume	permeate flush before shutdown	The best-evidenced mitigation in the corpus
10	Buffering	energy or water storage	permeate tank / battery / supercapacitor	Converts an energy-side problem into membrane protection

3. Results

3.1. The corpus at a glance

Table 2 maps the fifty-seven primary studies against the parameterisation of Table 1. Figure 1 projects the corpus onto a matrix of non-steady mode against observation scale, and its empty cells are findings in their own right. Three are consequential. Biological endpoints are absent above bench scale: no located study measures regrowth on an element or in a full plant with idle duration under experimental control. Compaction is absent under resource-driven flux: every measurement retrieved was made under stepped or programmed pressure, none under an irradiance-shaped profile. And the mechanical integrity of spiral-wound elements under repeated start-stop (hydraulic shock, telescoping, abrasion) has no located peer-reviewed literature, although it is a standing practitioner concern. The temporal profile of the corpus

ISSN: 2181-3337 | SCIENTISTS.UZ

(Figure 2) underlines how recently the field has begun to treat non-steadiness as a subject in its own right: half of all sixty-nine records (35) were published in 2022 or later. The four subsections that follow take the four membrane-side consequences in turn.

Table 2.

Evidence map of primary experimental studies under non-steady operation

Authors (Year)	Non-steady mode	Scale	Feed	Duration / cycles	Key finding
Imposed start-stop, coupon and bench					
Freire-Gormaly & Bilton (2019b)	Daily cycling, 8 h d^{-1}, 16 h idle	Bench + pilot element	Brackish groundwater	7 d	Antiscalant + flush retained >70% of initial permeability; <50% without flush; surface ATP quantified at autopsy
Zhang et al. (2019)	6, 12, 24 h d^{-1} schedules	Element (domestic)	Real tap water	90-180 d	Fouling-layer thickness grew with daily operating time; 6 h d^{-1} outperformed continuous; biofouling detectable at 7 d
Yang et al. (2022)	Two idle periods, fixed 3 h	Bench	$CaSO_4$ + colloidal silica	2 cycles	Benefit of intermittency governed by idle-state chemistry: DI recirculation restored flux, feed recirculation did not
S. Lee et al. (2023)	4/2 h and 8/16 h cycles; feed vs. DI at rest	Coupon (OCT in situ)	NaCl + humic acid	40 h over 5 d	Continuous lost 24% flux vs. 8.9-10.4% intermittent; fouling layer collapsed from 21.2 to 7.5-8.4 µm per shutdown
Dimitriou et al. (2025)	Steady vs. solar vs. cloudy-day profiles	Coupon	about 32 g L^{-1} NaCl	3 x 8 h d per scenario	Cloudy profile without rinse: −37% permeability, −18% rejection (combined compaction and fouling, not separated)
Sarker et al. (2025)	8 h d^{-1} cycling; end-of-day rinse	Bench	Gypsum-prone synthetic	6 d	End-of-day rinsing as a maintainability intervention
Imposed start-stop, full scale					
Ruiz-García & Nuez (2020)	About 9 h d^{-1} with pre-shutdown flush	Full plant, 416 m^3 d^{-1}	Real brackish groundwater	14 y	About 50% permeability loss; SEC 1.82 to 2.21 kWh m^{-3}; fouling acceleration from about day 500
Carta et al. (2025)	1 h on / 1 h off, continuous	Full plant, 100 m^3 d^{-1}	Real seawater	1,568 cycles / 4 mo	No structural degradation at autopsy; recovery improved by 0.12%
Kim et al. (2023)	Intermittent BWRO	Pilot	Brackish water	-	Biofouling under intermittent operation examined at pilot scale
Resource-driven variable flux					
Park et al. (2011)	Wind-driven fluctuating power incl. sub-threshold excursions	Pilot element	Synthetic brackish	h-scale runs	Flux and rejection track power non-linearly; rejection loss concentrated in low-power excursions
Park et al. (2012)	6 on-off cycles h^{-1}; stops 0.5-3 min	Prototype element	2,750-5,500 mg L^{-1} NaCl	1-h test periods	Restart salinity spike resolved against stop duration; sharper for shorter stops
Richards et al. (2015)	Irradiance fluctuation, 400-1,200 W m^{-2}	Bench PV-RO	Brackish	Event-scale	Irradiance steps of 100 W m^{-2} disrupt the polarisation layer via induced osmotic backwash
Cai et al. (2024)	Ramp rates 0.17-2 bar s^{-1}; up to 1,000 shut-downs	Bench crossflow	Synthetic	≤1,000 events	No significant deterioration at the highest ramp rate or cycle count; integrity loss only under forced permeate backpressure of 2-4 bar
Pressure cycling					
Torii et al. (2019)	Repeated pressurisation, household regime	Element + flat sheet	Virus-spiked water	10,000 cycles	About 4 $\log_{10}$ phage removal to 3,000-4,000 cycles, then collapse; replacement interval argued in cycles, not time
Sitterley et al. (2022)	Sinusoidal feed pressure, 500-900 psi	Pilot element	NaCl	About 1,770 h	7.4% irreversible permeability loss

ISSN: 2181-3337 | SCIENTISTS.UZ

Das et al. (2024)	Sinusoidal vs. rectified-sinusoidal waveforms	Element (SWRO)	Seawater	Multi-run	Waveform shape, not variability per se, governs damage; rectified waveform raised permeate salinity
Sitterley et al. (2025)	Trapezoidal ramps, ΔP 100-400 psi, 4-60 s	Pilot element	Dechlorinated tap + NaCl	28 dynamic conditions	A and B are not constants under transient pressure; transient parameters predict flux substantially better
Li (2026)	Dynamic and cyclic RO	Pilot (re-analysis of NREL datasets)	-	-	Counter-claim: permeability constant; apparent change is hysteresis of channel history
Designed cycling					
Warsinger et al. (2018)	Salinity cycling in batch RO	Bench + model	$CaSO_4$, $CaCO_3$, silica; real concentrates	Runs to 36 h	Residence at peak supersaturation 3-4 orders shorter than continuous RO; gypsum recovery limit rises from about 54 to above 90%
T. Lee et al. (2019)	Semi-batch vs. steady-state at matched recovery	Pilot element	Gypsum-supersaturated	Multi-run	Contrarian: semi-batch more scaling-prone; nucleation responds to peak, not time-averaged, supersaturation
Hosseinipour et al. (2023)	Free-piston batch RO	Element, 41 m^2	8 brackish compositions, LSI 1.7-2.6	>100 h / 96 tests	Zero scaling at calcite SI 2.6 without antiscalant; osmotic backwash 3.1-4.6 L per cycle as active cleaning
Tow et al. (2025)	Batch RO with flexible bladder	Pilot, to 5 $m^3\ d^{-1}$	Real concentrate, gypsum SI 0.63	885 cycles / 1 wk	No observable fouling at 82.6% recovery on supersaturated brine
Compaction and relaxation					
Ding et al. (2024)	Creep-recovery cycling, 8/16 h x 7	Coupon (DMA + EIS)	DI and model water	7 cycles; 10 loops	4.2% irrecoverable compaction per cycle, growing with each cycle
Wu et al. (2025)	TMP switching, 10-50 bar	Coupon	-	Stepped	Reversible compaction in the polyamide; irreversible in the support
Idle state and stagnation					
Ma et al. (2026)	Inter-cycle stagnation; 30-s flush at start/stop	Domestic 2-element system	Tap water	24 wk	Permeate TDS below 10 mg L^{-1} with flush vs. above 60 without; recovery 96.5 vs. 93.1% after 24 wk

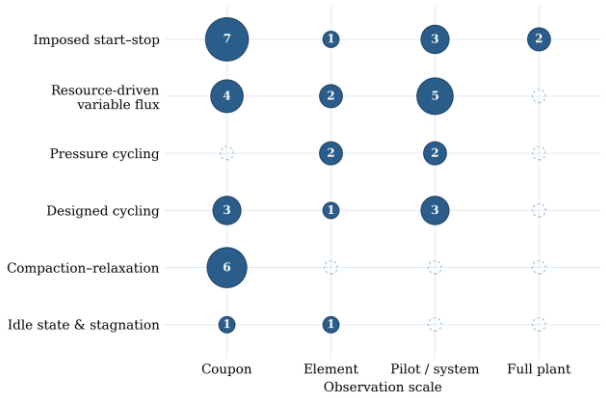


Figure 1. *Coverage of the primary experimental corpus by non-steady mode and observation scale.*

ISSN: 2181-3337 | SCIENTISTS.UZ

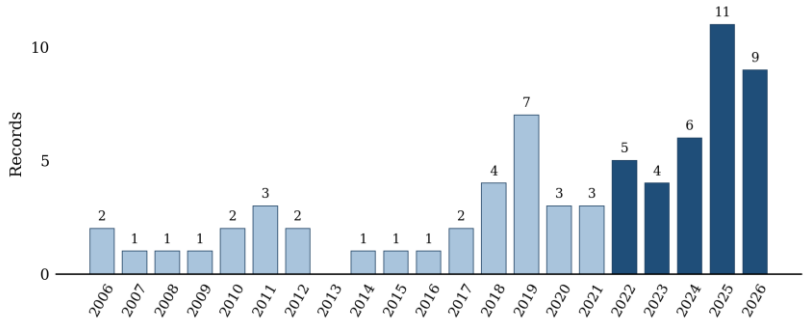


Figure 2. *Publication-year distribution of the corpus*

3.2. Compaction and viscoelastic recovery

The only located compaction study with an explicit cycle count is mechanical, not filtration-based. Under a duty cycle of 8 h load and 16 h recovery repeated seven times, with ten load-unload hysteresis loops and pressure steps to 330 psi, an NF270 membrane showed 15.0% initial compaction of which 10.8% recovered, leaving 4.2% irrecoverable per cycle, and the irrecoverable fraction grew cycle on cycle, which is fatigue in the ordinary materials-science sense of the word (Ding et al., 2024). The RO membrane in the same study compacted 20.9% at 200 psi, and the ratio of creep to instantaneous deformation rose from 8% to 94% across the pressure steps: at operating pressures, most of what the membrane does under load is time-dependent.

Where that deformation resides has been resolved. Compaction scales with transmembrane pressure (up to 30% at 50 bar against under 10% at 10 bar), and switching between high and low pressure does not appreciably change its extent, because the highly cross-linked polyamide recovers on depressurisation while compaction of the polysulfone support is largely irreversible (Wu et al., 2025). Positron annihilation lifetime spectroscopy independently locates the irreversible component outside the selective layer: at 150 bar the support loses about 60% of cross-sectional thickness and up to 95% of surface porosity while the selective layer does not irreversibly compact (Davenport et al., 2020). The polyamide itself is not inert, however: it densifies under load and relaxes only partially, and higher cross-linking buys smaller compaction and better recovery at the price of initial permeability (Wu et al., 2024), a materials lever directly relevant to membranes destined for cyclic duty.

At element scale the phenomenon persists. Some 1,770 h of sinusoidal feed-pressure cycling between 500 and 900 psi left a 7.4% irreversible permeability loss (Sitterley et al., 2022), and compaction under cyclic batch loading carries a measurable energy cost (Patel et al., 2024). Nor is the mechanics confined to the polymer: a gel foulant layer itself exhibits compaction-relaxation hysteresis with distinct time constants for compression and swelling, and oscillating pressure can raise its permeability relative to static load (Epstein & Ramon, 2026), and biofilms compact and relax in the same manner (Valladares Linares et al., 2016). One coupon study emulating photovoltaic profiles reports a 37% permeability loss over three cloudy-day cycles without an end-of-day rinse; the authors attribute the degradation to compaction and fouling jointly and do not separate the two, so the figure is evidence of the combined mechanism only (Dimitriou et al., 2025).

3.3. Scaling: induction time against residence time

A shutdown is, physically, a period of residence at the highest supersaturation the system reaches: permeation stops, the concentration-polarisation layer and the concentrated brine remain, and whether crystals form is then a race against the nucleation induction time. The framing originates in deliberately cyclic operation. Scaling can be prevented by "zeroing" the elapsed nucleation time: interrupting supersaturation before induction completes, demonstrated for calcium sulfate (Pomerantz et al., 2006) and building on the concept of periodic feed-flow reversal introduced by the same group (Gilron et al., 2006). The principle has since been instrumented: flow reversal triggered by ex-situ optical detection of incipient nucleation controlled gypsum scaling in a brackish-water pilot (Uchymiak et al., 2009), and forward-

ISSN: 2181-3337 | SCIENTISTS.UZ

reverse cycles switched by ultrasonic detection of deposit onset avoided the flux decline of continuous forward flow at bench scale (Lu et al., 2012). In these systems the cycle is timed by the chemistry, through a sensor or a schedule set against the induction time. A photovoltaic system executes the same interruption with the timing surrendered to the resource: the sun, not the saturation state, decides when permeation stops.

The batch literature shows how protective the interruption can be when residence times are short. In batch reverse osmosis the residence time at peak supersaturation is three to four orders of magnitude shorter than in continuous operation, so the induction time is never exceeded, and the gypsum-limited recovery ceiling rises from about 54% to above 90% (Warsinger et al., 2018). The prediction has survived severe field tests: 885 cycles in a single week at 82.6% recovery on a real, gypsum-supersaturated concentrate (saturation index 0.63) produced no observable fouling (Tow et al., 2025), and a free-piston batch system desalinating eight brackish groundwater compositions showed zero scaling at calcite saturation indices up to 2.6 without antiscalant, with the depressurisation-driven osmotic backwash of 3.1-4.6 L per cycle identified as an active cleaning mechanism (Hosseinipour et al., 2023). Induction times themselves are becoming predictable, through machine learning grounded in Smoluchowski theory (Abdelkawi et al., 2025) and through a survival-analysis framework for dynamically concentrating systems (Abdelkawi et al., 2026).

The contrarian result defines the boundary of the protection. At matched recovery, semi-batch operation proved more scaling-prone than steady-state reverse osmosis, in both crystal growth rate and scaled area, because nucleation responds to the peak supersaturation the cycle repeatedly visits, not to its time average (T. Lee et al., 2019). Cycling therefore protects only while the excursion above saturation stays shorter than induction; a cycle that repeatedly samples high peak supersaturation can be worse than the steady state it replaces. Under imposed cycling the corpus is thinner but consistent with the frame, much of it produced on a rig purpose-built to impose intermittency (Freire-Gormaly & Bilton, 2017): real-time imaging resolves scale formation on the membrane surface under intermittent operation (Sarker & Bilton, 2021), a pre-shutdown clean-water flush with antiscalant preserved more than 70% of initial permeability where its absence left less than 50% (Freire-Gormaly & Bilton, 2019b), and end-of-day rinsing has been advanced as a maintainability intervention for photovoltaic systems (Sarker et al., 2025).

3.4. Biological regrowth during idle intervals

What has been measured on membranes is quickly stated. Surface adenosine triphosphate was quantified at autopsy after seven days of duty cycling, with the shutdown interval fixed at 16 h by the 8 h d^{-1} schedule (Freire-Gormaly & Bilton, 2019b). Daily schedules of 6, 12 and 24 h have been compared over 90-180 days on real tap water, with biofouling detectable by day 7, fouling-layer thickness growing with daily operating time, and the 6 h d^{-1} schedule outperforming continuous operation (Zhang et al., 2019), but the comparison varies operating time and idle time together. The one study that varies the resting state directly holds idle duration fixed at 3 h and makes no biological measurement at all (Yang et al., 2022). Biofouling under intermittent operation has been examined at pilot scale in a brackish-water system (Kim et al., 2023). The steady-state biofouling literature, by contrast, is mature (Hoek et al., 2022), which is precisely what makes the idle interval the untreated variable.

Biological endpoints have been measured on reverse-osmosis membranes under duty-cycled operation - surface adenosine triphosphate in the case of Freire-Gormaly and Bilton (2019b) - but in every located study the shutdown interval is fixed by the application's diurnal or demand cycle rather than swept as a controlled independent variable. What is varied instead is the state of the membrane at rest: lay-up chemistry (Yang et al., 2022) or end-of-shift rinsing (Sarker et al., 2025). Where idle duration has been swept against biological endpoints, the systems are not membranes but drinking-water distribution and premise plumbing, in which the response proves markedly non-linear: thresholds are reported at two and four hours (Ren et al., 2025), and attenuation rates are resolvable per hour of stagnation (Elliott et al.,

ISSN: 2181-3337 | SCIENTISTS.UZ

2011). The coupling between idle duration and biological regrowth on a polyamide membrane is therefore not quantified, even where biofouling under intermittent operation has been examined at pilot scale (Kim et al., 2023).

The non-membrane evidence indicates what a membrane experiment should expect. With stagnation swept from 0.25 to 10 h, microbial diversity falls and *Legionella pneumophila* rises significantly beyond thresholds at 2 and 4 h, driven by accelerating chlorine decay (Ren et al., 2025). Overnight stagnation alone raises cell counts two- to three-fold and adenosine triphosphate two- to eighteen-fold (Lautenschlager et al., 2010); after roughly six days, counts climb from 10^3 to 7.8×10^5 cells mL^{-1} (Ling et al., 2018); intervals up to 168 h have been resolved against total and intact cell counts across seasons (Zlatanović et al., 2017). Idle time is not uniformly hostile: in household slow sand filters, virus attenuation proceeds at up to 0.061 $\log_{10}$ per hour of idle time, and the effect vanishes when microbial activity is suppressed, a microbially mediated benefit of standing still (Elliott et al., 2011). In these systems idle duration is the controlled variable and the response is non-linear with thresholds at the scale of hours, in the diurnal range of a photovoltaic plant; Figure 3 places the located studies on this axis.

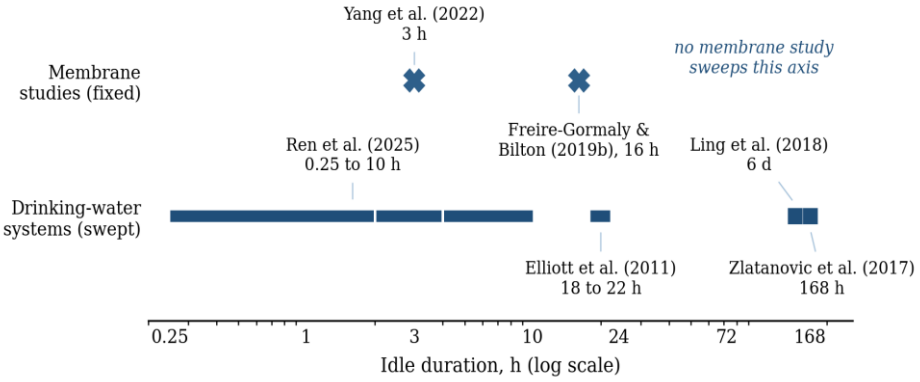


Figure 3. *Idle duration as an experimental variable: ranges swept in drinking-water systems against fixed values in located membrane studies.*

3.5. Permeate quality on restart

The literature conflates three distinct phenomena that this review separates. The first is the transient conductivity excursion during and immediately after a restart, which is hydrodynamic and recoverable, and which has been resolved against shutdown duration only once (Park et al., 2012). The second is the cumulative loss of rejection with cycle count, which is a matter of membrane integrity and is not recoverable (Torii et al., 2019). The third is the depression of rejection during low-power operation, which is a driving-force effect and is instantaneous (Park et al., 2011). No prior source distinguishes them, and conclusions drawn about "permeate quality under intermittent operation" are not comparable across studies until they are separated.

The single resolution of the first phenomenon against stop duration yielded a counter-intuitive result: across six on-off cycles per hour, the permeate salinity spike on restart was sharper after stops of 0.5-1 min than after stops of 1-3 min (Park et al., 2012). The transient also responds to mitigation over long horizons: in a domestic two-element system cycled for 24 weeks, a 30-s flush at start and stop held permeate total dissolved solids below 10 mg L^{-1} against above 60 mg L^{-1} in the unflushed control, and recovery after 24 weeks stood at 96.5% against 93.1%; stagnation accelerates long-term degradation as well as the restart excursion (Ma et al., 2026). The second phenomenon has a cycle count attached: over 10,000 pressurisation cycles emulating household duty, removal of the φX-174 bacteriophage held near 4 $\log_{10}$ for the first 3,000-4,000 cycles and then collapsed, with even *Escherichia coli* penetrating by 10,000; the damage localised near the membrane surface, and the authors argue that replacement intervals should be set in cycles, not calendar time (Torii et al., 2019). Intermittency has since been examined against

ISSN: 2181-3337 | SCIENTISTS.UZ

membrane integrity directly: across feed-pressure ramp rates of 0.17-2 bar s^{-1} and up to 1,000 shut-down events, no significant performance deterioration was observed, and integrity loss appeared only when a permeate backpressure of 2-4 bar was applied to force the backwash (Cai et al., 2024). For the third phenomenon, the shape of the disturbance matters as much as its size: rejection loss under wind-driven power concentrates in low-power excursions (Park et al., 2011), and at element scale a rectified-sinusoidal waveform raised permeate salinity where a smooth sinusoid of equal variability behaved like the steady-state reference (Das et al., 2024). Whether any of this reflects a change in the membrane's own transport properties is disputed in print: transient, pressure-dependent water and salt permeability coefficients predict flux substantially better than constant ones (Sitterley et al., 2025), against the counter-claim that permeability is constant and the apparent change is hysteresis of the flow channel's history (Li, 2026). Null results bound the problem from above: unsteady power did not measurably affect product water quality in long-term field operation (Schäfer et al., 2018), solute rejection proved resilient across membranes under irradiance fluctuation (Boussouga et al., 2021) as under battery-less photovoltaic operation on real brackish groundwater (Richards et al., 2008), resilient operating windows have been mapped for photovoltaic-membrane systems under transient solar conditions (Ogunniyi & Richards, 2026), and the hourly-cycled seawater plant improved its recovery by 0.12% over 1,568 cycles (Carta et al., 2025).

3.6. Five axes of disagreement

Read together, the corpus disagrees in sign along five axes, collected in Table 3: bench-scale harm against bench-scale protection; full-scale degradation over fourteen years against a full-scale null over four months; scaling suppressed by cycling against scaling aggravated by it; rejection collapse with cycle count against unchanged product quality; and transport properties that vary under transient pressure against a constant-permeability counter-claim. None of these is a contradiction to be adjudicated by majority vote. Each is resolved, or in one case delimited, by a variable the primary studies already contain, and that resolution is the subject of the following section.

Table 3.

Disagreements in sign across the evidence base and their reconciling variables

Axis	Study A: finding (sign)	Study B: finding (sign)	Reconciling variable
1. Coupon and bench scale	Freire-Gormaly & Bilton (2019b): <50% of initial permeability after 7 d of cycling without a pre-shutdown flush (harmful)	S. Lee et al. (2023): 24% flux loss under continuous operation vs. 8.9-10.4% under intermittent; fouling layer collapses from 21.2 to 7.5-8.4 μm per shutdown (protective)	Idle-state chemistry: DI vs. feed water (Yang et al., 2022)
2. Full scale, different horizons	Carta et al. (2025): no structural degradation after 1,568 start-stop cycles in 4 months; recovery improved by 0.12% (neutral)	Ruiz-García & Nuez (2020): about 50% permeability loss over 14 years at about 9 h d^{-1}; SEC 1.82 to 2.21 kWh m^{-3} (harmful)	Observation horizon: fouling acceleration begins near day 500, after the four-month window
3. Scaling under cycling	Warsinger et al. (2018); Tow et al. (2025): residence at peak supersaturation 3-4 orders of magnitude shorter than continuous RO; 885 cycles at gypsum SI 0.63 with no observable fouling (protective)	T. Lee et al. (2019): semi-batch RO more scaling-prone than steady-state at matched recovery (harmful)	Nucleation responds to peak, not time-averaged, supersaturation
4. Permeate quality	Torii et al. (2019): rejection collapse after 3,000-4,000 pressure cycles (harmful)	Schäfer et al. (2018); Carta et al. (2025): unsteady power did not measurably affect water quality; recovery even improved (neutral)	Three conflated phenomena: restart transient, integrity loss, driving-force depression (Section 3.5)
5. Transport properties vs.	Sitterley et al. (2025): A and B are not constants under transient	Li (2026): permeability constant; apparent change is hysteresis of	Interpretive framework applied to

ISSN: 2181-3337 | SCIENTISTS.UZ

channel history	pressure; transient parameters predict flux substantially better (properties change)	channel history (properties constant)	the same pilot-scale data; unresolved dispute in print

4. Discussion

None of the five axes of Table 3 is settled by weighing studies against one another. Each disagreement dissolves once a variable already present in the primary data, but assembled by no single source, is made explicit. Four such variables organise this section, and Figure 4 locates each of them on the anatomy of a single start-stop event; two closing subsections address a terminological collision with the nearest prior review and the relation between the scholarly and the practitioner literatures.

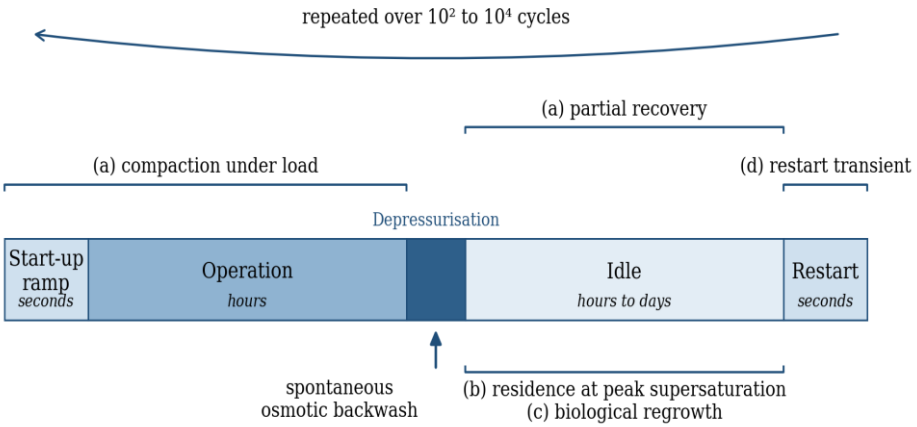


Figure 4. *Phases of a start-stop event and the membrane-side consequences (a)-(d). Time axis not to scale.*

4.1. The chemistry of the idle state

The bench-scale contradiction of axis 1 is not a contradiction but two different experiments. In the study that found harm, the membrane rested in the scaling-prone feed it had been concentrating all day (Freire-Gormaly & Bilton, 2019b); in the study that found protection, every shutdown collapsed the fouling layer and the resting fluid differed (S. Lee et al., 2023). The one study that varies the resting state directly, at fixed idle duration, finds the benefit of intermittency governed by exactly this: deionised-water recirculation restored flux, feed recirculation did not (Yang et al., 2022). The same gradient is visible within a single experiment: intermittent operation resting in deionised water lost 8.9% of flux against 10.4% resting in feed (S. Lee et al., 2023). The practical corollary inverts the usual reading of the pre-shutdown flush. It is not housekeeping; it is the variable that sets the sign of the idle-period effect, which is why its presence or absence separates retention of more than 70% of initial permeability from less than 50% (Freire-Gormaly & Bilton, 2019b; Figure 5) and why end-of-day rinsing is the intervention proposed for photovoltaic systems specifically (Sarker et al., 2025), the measured penalty having already been carried into design guidance for such systems (Freire-Gormaly & Bilton, 2019a). What none of these studies measures is biology at rest: idle-state chemistry resolves the mineral and colloidal side of axis 1 and leaves its biological side inside the gap of Section 3.4.

ISSN: 2181-3337 | SCIENTISTS.UZ

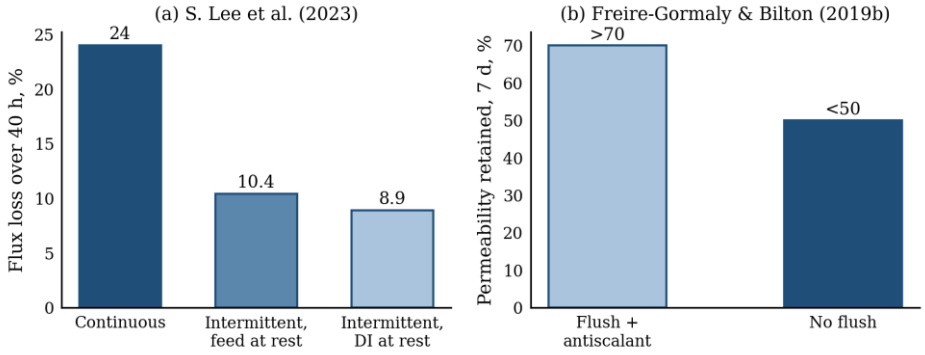


Figure 5. *Idle-state fluid and pre-shutdown flushing set the sign of the idle-period effect: (a) flux loss by resting fluid; (b) permeability retained with and without a pre-shutdown flush.*

4.2. Spontaneous osmotic backwash

The second variable explains why stopping can clean. When permeation ceases and pressure falls, the osmotic gradient across the membrane briefly reverses the water flux, lifting deposited material off the surface. The mechanism was identified under fluctuating irradiance, where steps as small as 100 W m^{-2} disrupt the concentration-polarisation layer through naturally induced osmotic backwash (Richards et al., 2015), and has since been resolved into its direct and spontaneous forms (Cai & Schäfer, 2020), characterised against mineral scaling (Cai et al., 2021), and traced mechanistically to the adhesive energetics between membrane and organic matter (Cai et al., 2022), with its bearing on membrane integrity under intermittency examined in the same series (Cai et al., 2024). In batch operation the depressurisation-driven backwash is measured in litres per cycle and identified as an active cleaning mechanism (Hosseinipour et al., 2023). The synthesis none of these sources draws is that every shutdown of a photovoltaic system performs, without design effort, what batch configurations engineer deliberately. The first two variables then act in sequence: the backwash operates over the seconds of depressurisation, the idle-state chemistry over the hours that follow; a shutdown that begins with a cleaning event can still end in a scaled or colonised membrane if the element is left standing in concentrate.

4.3. The partition of compaction and a hypothesis

The third variable reconciles short and long observations of the same mechanics. Compaction partitions into a reversible component in the polyamide active layer and a largely irreversible component in the polysulfone support (Wu et al., 2025; Davenport et al., 2020), and the irrecoverable fraction accumulates cycle on cycle (Ding et al., 2024). A single depressurisation therefore shows little, because the reversible component masks the irreversible one, while a multi-day cycle accumulates damage; experiments differing only in horizon will disagree in sign with no error on either side.

No study located in this review measured compaction under resource-driven variable flux, and no study of photovoltaic-powered operation measured compaction. The proposition advanced here - that reversible compaction and its incomplete relaxation account for part of the flux hysteresis currently attributed to fouling in the photovoltaic reverse-osmosis literature - is therefore a hypothesis this review advances rather than a finding it reports, and it is labelled as such throughout.

Two pieces of arithmetic, offered as such and not as evidence, mark the size of the open question (Figure 6). A batch pilot executed 885 cycles in a single week (Tow et al., 2025); the only explicit fatigue measurement reports 4.2% irrecoverable compaction per cycle under an 8/16 h duty (Ding et al., 2024). These numbers do not meet: the loading profiles differ by orders of magnitude (seconds-scale depressurisation against sixteen-hour holds), and no located study bridges them, which is itself an argument for reporting ramp rate and duty cycle as Table 1 prescribes. The second: 1,568 start-stop events in four months produced no measurable change at full scale (Carta et al., 2025). Whether coupon-scale fatigue fails to express at element scale, or expresses on horizons longer than four months, is precisely what the corpus cannot yet say.

ISSN: 2181-3337 | SCIENTISTS.UZ

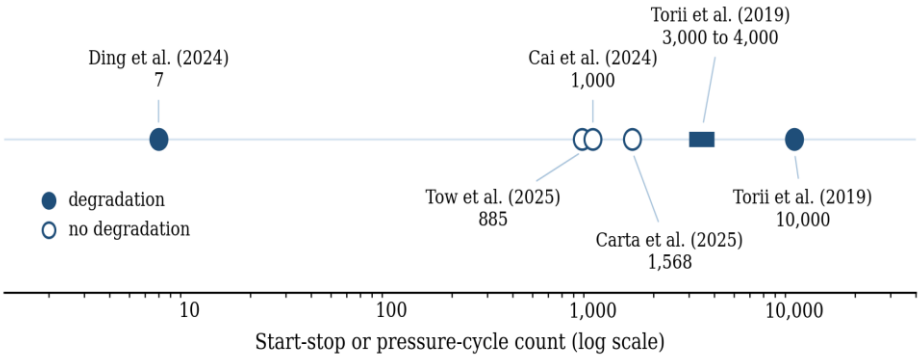


Figure 6. *Reported start-stop and pressure-cycle counts with associated outcomes. Cycle definitions differ between studies.*

4.4. Scale and horizon of observation

The fourth variable is the observation itself. Axis 2 sets a four-month full-scale null (Carta et al., 2025) against a 50% permeability loss over fourteen years (Ruiz-García & Nuez, 2020). The two are consistent with a single degradation curve, since fouling acceleration in the fourteen-year record begins near day 500, beyond the entire window of the four-month study; but consistency is not demonstration: no located data resolve the shape of that curve between four months and fourteen years, and the claim is left as the weaker one. Axis 5 is delimited rather than resolved. Transient, pressure-dependent transport coefficients predict flux substantially better than constants at element scale (Sitterley et al., 2025); the counter-claim holds permeability constant and attributes the apparent variation to the hysteresis of the flow channel's history (Li, 2026). The claims are not symmetric: one estimates parameters from element-scale transients, the other relocates the phenomenon upstream of the membrane. Deciding between them requires an experiment that separates membrane from channel, which is exactly the separation the reporting scheme of Table 1 makes expressible. The dispute is in print, current, and open.

4.5. A terminological collision

A terminological distinction should be noted. The "cycle-to-cycle salt accumulation" identified as a research gap by Liang and Li (2026) refers to salt accumulating in the recirculating brine between cycles, a mass-balance and flushing phenomenon at the process level. It is distinct from the accumulated loss of salt rejection by the membrane material that is examined here, which is a property of the active layer, not of the fluid inventory.

The same review's reported membrane-life extension exceeding 100% is a result of machine-learning-based control demonstrated at industrial scale, not a materials-level analysis, and does not bear on the membrane-side questions treated here.

4.6. The practitioner literature and its missing counterpart

A large practitioner literature governs the idle state, and it has no scholarly counterpart. Manufacturers prescribe preservation for any shutdown exceeding forty-eight hours, specify one to one and a half per cent sodium metabisulfite, cap pressurisation and depressurisation at ten pounds per square inch per second, and state plainly that elements allowed to dry after service may lose water permeability irreversibly. None of these thresholds is derived from a published experiment. The asymmetry is illustrated by the peer-reviewed literature itself: a study of preservation chemistry published in this field's principal materials journal cites a manufacturer's technical service bulletin as the source of its chemistry (Tu et al., 2014).

The peer-reviewed counterpart is confined to a handful of studies: a comparative assessment of non-oxidising biocides against sodium metabisulfite (Majamaa et al., 2011) and the preservation-chemistry study already named, which found permeability rising 10-20% after storage while boron and sodium rejection losses exceeded the permeability change in magnitude (Tu et al., 2014). A recent review of

ISSN: 2181-3337 | SCIENTISTS.UZ

membrane drying addresses preservation of membranes as stored artefacts, adjacent to but distinct from the repeated wet-idle cycling of membranes in service (Van Buggenhout et al., 2025). The nearest located test touches one threshold from below: at bench scale, feed-pressure ramp rates up to 2 bar s^{-1}, nearly three times the 0.7 bar s^{-1} practitioner cap (Hydranautics, 2019), produced no membrane damage (Cai et al., 2024); whether the cap is conservative or protective at spiral-wound element scale is exactly the untested proposition. Every quantitative threshold in service today, from the forty-eight-hour rule (DuPont Water Solutions, 2026) to the ramp-rate cap and the biocide concentrations, still awaits its first published experiment at the scale it governs.

5. Conclusion and Implications

Five research priorities follow, in order of leverage.

First, no located study isolates idle duration as the controlled independent variable for biological regrowth on a reverse-osmosis membrane; the shutdown interval is everywhere fixed by the application while the resting state is varied instead. Closing this gap requires a factorial design in which idle duration is the primary independent variable, swept across at least four levels spanning the diurnal range from one hour to seventy-two hours, crossed with idle-state fluid (feed, permeate, deionised water) and with feed biological loading. Endpoints must be biological - adenosine triphosphate, quantitative PCR of total and viable cells, and extracellular polymeric substance quantification - and must be measured on the membrane surface rather than in the bulk. The design should anticipate a non-linear rather than a monotonic response, since threshold behaviour at intervals of two to four hours has been reported in analogous stagnant systems (Ren et al., 2025).

Second, compaction hysteresis under a photovoltaic-representative duty cycle remains unmeasured in the retrieved corpus; until one does, the hypothesis of Section 4.3, that part of the flux hysteresis now attributed to fouling is viscoelastic, remains open in both directions.

Third, no peer-reviewed study was located on hydraulic transients, water hammer, or mechanical damage at the spiral-wound element scale under start-stop operation, although practitioner documentation caps ramp rates numerically; the distance between a prescribed threshold and a published experiment is short here, and closable.

Fourth, the field has no shared reporting standard for non-steady operation, and the blank cells of Table 2 price that absence; the ten-field scheme of Table 1 is proposed as that standard; the most recent accelerated-ageing protocol for spiral-wound elements takes accumulated exposure, not the number of transitions, as its dose variable (Alkhouzaam & Khraisheh, 2026), which is exactly the quantity the scheme adds.

Fifth, the retrieved corpus contains no field data from the gypsum-prone brackish groundwaters of Central Asia, although the region hosts some of the earliest photovoltaic desalination work (Aybar et al., 2010; Khaydarov & Khaydarov, 2007) and the induction-time framework of Section 3.3 is directly computable for its water compositions. That field campaign is the natural next work of the present authors.

Acknowledgment

This work was supported by grant FL-9024093713 from the Physical-technical Institute named after S.A. Azimov, Academy of Sciences of the Republic of Uzbekistan.

REFERENCES

1. Abdelkawi, A. A., Lindsey, J. L., & Wright, N. C. (2025). Prediction of gypsum induction time to inform scaling kinetics using machine learning and Smoluchowski theory. *Desalination, 616*, Article 119288. https://doi.org/10.1016/j.desal.2025.119288
2. Abdelkawi, A. A., Lindsey, J. L., & Wright, N. C. (2026). A survival analysis framework for predicting gypsum scaling risk in dynamically concentrating desalination systems. *Water Research, 304*, Article 126345. https://doi.org/10.1016/j.watres.2026.126345

3. Alkhouzaam, A., & Khraisheh, M. (2026). Field-realistic accelerated aging protocol for spiral-wound reverse osmosis membranes: Multi-scale diagnostics and end-of-life criteria. *Desalination, 628*, Article 120071. https://doi.org/10.1016/j.desal.2026.120071
4. Almetwally, E. M., Elazab, M., Kabeel, A., Yasser, Y., & Elgebaly, A. (2025). Solar powered reverse osmosis desalination: A systematic review of technologies, integration strategies and challenges. *Desalination, 615*, Article 119228. https://doi.org/10.1016/j.desal.2025.119228
5. ASTM International. (2019). *Standard terminology used for microfiltration, ultrafiltration, nanofiltration, and reverse osmosis membrane processes* (ASTM D6161-19). ASTM International.
6. ASTM International. (2023). *Standard test methods for operating characteristics of reverse osmosis and nanofiltration devices* (ASTM D4194-23). ASTM International. https://doi.org/10.1520/D4194-23
7. Aybar, H. S., Akhatov, J. S., Avezova, N. R., & Halimov, A. S. (2010). Solar powered RO desalination: Investigations on pilot project of PV powered RO desalination system. *Applied Solar Energy, 46*(4), 275-284. https://doi.org/10.3103/S0003701X10040080
8. Boussouga, Y.-A., Richards, B. S., & Schäfer, A. I. (2021). Renewable energy powered membrane technology: System resilience under solar irradiance fluctuations during the treatment of fluoride-rich natural waters by different nanofiltration/reverse osmosis membranes. *Journal of Membrane Science, 617*, 118452. https://doi.org/10.1016/j.memsci.2020.118452
9. Burlace, L., & Davies, P. (2022). Fouling and fouling mitigation in batch reverse osmosis: Review and outlook. *Desalination and Water Treatment, 249*, 1-22. https://doi.org/10.5004/dwt.2022.28103
10. Cai, Y.-H., Boussouga, Y.-A., & Schäfer, A. I. (2024). Renewable energy powered membrane technology: Impact of intermittency on membrane integrity. *Desalination, 580*, 117504. https://doi.org/10.1016/j.desal.2024.117504
11. Cai, Y.-H., Burkhardt, C. J., & Schäfer, A. I. (2021). Renewable energy powered membrane technology: Impact of osmotic backwash on scaling during solar irradiance fluctuation. *Journal of Membrane Science, 619*, 118799. https://doi.org/10.1016/j.memsci.2020.118799
12. Cai, Y.-H., Gopalakrishnan, A., Deshmukh, K. P., & Schäfer, A. I. (2022). Renewable energy powered membrane technology: Implications of adhesive interaction between membrane and organic matter on spontaneous osmotic backwash cleaning. *Water Research, 221*, 118752. https://doi.org/10.1016/j.watres.2022.118752
13. Cai, Y.-H., & Schäfer, A. I. (2020). Renewable energy powered membrane technology: Impact of solar irradiance fluctuation on direct osmotic backwash. *Journal of Membrane Science, 598*, 117666. https://doi.org/10.1016/j.memsci.2019.117666
14. Carta, J. A., Cabrera, P., Melián-Martel, N., & Arenas-Urrea, S. (2025). Experimental investigation of the effect of intermittent operation on membranes in wind-powered SWRO plants, focusing on frequent start-stop scenarios. *Energy Conversion and Management: X, 25*, Article 100848. https://doi.org/10.1016/j.ecmx.2024.100848
15. Das, T. K., Folley, M., Lamont-Kane, P., & Frost, C. (2024). Performance of a SWRO membrane under variable flow conditions arising from wave powered desalination. *Desalination, 571*, Article 117069. https://doi.org/10.1016/j.desal.2023.117069
16. Davenport, D. M., Ritt, C. L., Verbeke, R., Dickmann, M., Egger, W., Vankelecom, I. F. J., & Elimelech, M. (2020). Thin film composite membrane compaction in high-pressure reverse osmosis. *Journal of Membrane Science, 610*, Article 118268. https://doi.org/10.1016/j.memsci.2020.118268
17. Dimitriou, E., Loukatos, D., Arvanitis, K. G., & Papadakis, G. (2025). Experimental evaluation of the performance of a flat sheet reverse osmosis membrane under variable and intermittent operation emulating a photovoltaic-driven desalination system. *Water, 17*(24), Article 3576. https://doi.org/10.3390/w17243576

ISSN: 2181-3337 | SCIENTISTS.UZ

18. Ding, W., Ma, K., & Childress, A. E. (2024). Compaction of pressure-driven water treatment membranes: Real-time quantification and analysis. *Environmental Science & Technology, 58*(41), 18404-18413. https://doi.org/10.1021/acs.est.4c05865
19. DuPont Water Solutions. (2026). *Reverse osmosis - Handling, preservation and storage* (Technical manual excerpt, Form No. 45-D03716-en, Rev. 11). DuPont de Nemours.
20. Elliott, M. A., DiGiano, F. A., & Sobsey, M. D. (2011). Virus attenuation by microbial mechanisms during the idle time of a household slow sand filter. *Water Research, 45*(14), 4092-4102. https://doi.org/10.1016/j.watres.2011.05.008
21. Epstein, J. A., & Ramon, G. Z. (2026). Characterizing the permeability of a foulant layer under a transient applied pressure. *Journal of Membrane Science, 738*, Article 124683. https://doi.org/10.1016/j.memsci.2025.124683
22. Freire-Gormaly, M., & Bilton, A. (2017). An experimental system for characterization of membrane fouling of solar photovoltaic reverse osmosis systems under intermittent operation. *Desalination and Water Treatment, 73*, 54-63. https://doi.org/10.5004/dwt.2017.20391
23. Freire-Gormaly, M., & Bilton, A. M. (2018). Experimental quantification of the effect of intermittent operation on membrane performance of solar powered reverse osmosis desalination systems. *Desalination, 435*, 188-197. https://doi.org/10.1016/j.desal.2017.09.013
24. Freire-Gormaly, M., & Bilton, A. M. (2019a). Design of photovoltaic powered reverse osmosis desalination systems considering membrane fouling caused by intermittent operation. *Renewable Energy, 135*, 108-121. https://doi.org/10.1016/j.renene.2018.11.065
25. Freire-Gormaly, M., & Bilton, A. M. (2019b). Impact of intermittent operation on reverse osmosis membrane fouling for brackish groundwater desalination systems. *Journal of Membrane Science, 583*, 220-230. https://doi.org/10.1016/j.memsci.2019.04.010
26. Gilron, J., Waisman, M., Daltrophe, N., Pomerantz, N., Milman, M., Ladizhansky, I., & Korin, E. (2006). Prevention of precipitation fouling in NF/RO by reverse flow operation. *Desalination, 199*(1-3), 29-30. https://doi.org/10.1016/j.desal.2006.03.136
27. Hoek, E. M. V., Weigand, T. M., & Edalat, A. (2022). Reverse osmosis membrane biofouling: Causes, consequences and countermeasures. *npj Clean Water, 5*, Article 45. https://doi.org/10.1038/s41545-022-00183-0
28. Hosseinipour, E., Harris, E., El Nazer, H. A., Mohamed, Y. M. A., & Davies, P. A. (2023). Desalination by batch reverse osmosis (RO) of brackish groundwater containing sparingly soluble salts. *Desalination, 566*, Article 116875. https://doi.org/10.1016/j.desal.2023.116875
29. Hydranautics. (2019). *Membrane start-up, shutdown, and preservative flushing guidelines* (Technical Service Bulletin TSB118.16). Nitto Group. https://membranes.com/wp-content/uploads/Documents/TSB/TSB118.pdf
30. Khaydarov, R. A., & Khaydarov, R. R. (2007). Solar powered direct osmosis desalination. *Desalination, 217*(1-3), 225-232. https://doi.org/10.1016/j.desal.2007.03.004
31. Kim, G., Song, Y., Hwang, T.-M., Park, Y.-G., Davies, P. A., & Park, K. (2025). Practical implementation and challenges of current batch-type RO systems and future potential: A review. *Desalination, 616*, Article 119404. https://doi.org/10.1016/j.desal.2025.119404
32. Kim, H.-W., Choi, W., Suh, D., Baek, Y., Cho, K., & Jeong, S. (2023). Pilot study of biofouling occurrence in a brackish water reverse osmosis system using intermittent operation. *Journal of Cleaner Production, 425*, 139097. https://doi.org/10.1016/j.jclepro.2023.139097
33. Lautenschlager, K., Boon, N., Wang, Y., Egli, T., & Hammes, F. (2010). Overnight stagnation of drinking water in household taps induces microbial growth and changes in community composition. *Water Research, 44*(17), 4868-4877. https://doi.org/10.1016/j.watres.2010.07.032

34. Lee, S., Cho, H., Choi, Y., & Lee, S. (2023). Application of optical coherence tomography (OCT) to analyze membrane fouling under intermittent operation. *Membranes, 13*(4), Article 392. https://doi.org/10.3390/membranes13040392
35. Lee, T., Choi, J. Y., & Cohen, Y. (2019). Gypsum scaling propensity in semi-batch RO (SBRO) and steady-state RO with partial recycle (SSRO-PR). *Journal of Membrane Science, 588*, Article 117106. https://doi.org/10.1016/j.memsci.2019.05.030
36. Li, M. (2026). Do membrane transport properties vary under dynamic and cyclic RO? Evidence for constant permeability and hysteresis from channel history. *Desalination, 620*, Article 119644. https://doi.org/10.1016/j.desal.2025.119644
37. Liang, Y. Y., & Li, M. (2026). Unsteady-state dynamics and AI in membrane desalination: Challenges and emerging opportunities. *Desalination, 618*, Article 119507. https://doi.org/10.1016/j.desal.2025.119507
38. Ling, F., Whitaker, R., LeChevallier, M. W., & Liu, W. T. (2018). Drinking water microbiome assembly induced by water stagnation. *The ISME Journal, 12*(6), 1520-1531. https://doi.org/10.1038/s41396-018-0101-5
39. Lu, X., Kujundzic, E., Mizrahi, G., Wang, J., Cobry, K., Peterson, M., Gilron, J., & Greenberg, A. R. (2012). Ultrasonic sensor control of flow reversal in RO desalination-Part 1: Mitigation of calcium sulfate scaling. *Journal of Membrane Science, 419-420*, 20-32. https://doi.org/10.1016/j.memsci.2012.05.027
40. Ma, M., Huang, B., Mei, L., Huang, K., Xing, K., & Liao, L. (2026). Development of a zero-stagnant-water purification system based on smart series-parallel control of dual RO membranes. *Membranes, 16*(5), Article 155. https://doi.org/10.3390/membranes16050155
41. Majamaa, K., Bertheas, U., Finlayson, F., & Levy, R. B. (2011). Preservation of reverse osmosis membranes with non oxidizing biocides - comparison with SMBS. *Water Supply, 11*(3), 342-351. https://doi.org/10.2166/ws.2011.041
42. Ogunniyi, E. O., & Richards, B. S. (2026). Renewable energy powered membrane technology: Resilient operating windows of a photovoltaic-powered desalination system operating under transient solar conditions. *Desalination, 625*, Article 119942. https://doi.org/10.1016/j.desal.2026.119942
43. Park, G. L., Schäfer, A. I., & Richards, B. S. (2011). Renewable energy powered membrane technology: The effect of wind speed fluctuations on the performance of a wind-powered membrane system for brackish water desalination. *Journal of Membrane Science, 370*(1-2), 34-44. https://doi.org/10.1016/j.memsci.2010.12.003
44. Park, G. L., Schäfer, A. I., & Richards, B. S. (2012). The effect of intermittent operation on a wind-powered membrane system for brackish water desalination. *Water Science and Technology, 65*(5), 867-874. https://doi.org/10.2166/wst.2012.912
45. Patel, C. G., Joshi, M., & Swaminathan, J. (2024). Membrane compaction in batch reverse osmosis operation and its impact on specific energy consumption. *Desalination, 592*, 118132. https://doi.org/10.1016/j.desal.2024.118132
46. Philibert, M., Villacorte, L. O., Ekowati, Y., Abushaban, A., & Salinas-Rodriguez, S. G. (2024). Fouling and scaling in reverse osmosis desalination plants: A critical review of membrane autopsies, feedwater quality guidelines and assessment methods. *Desalination, 592*(C), Article 118188. https://doi.org/10.1016/j.desal.2024.118188
47. Pomerantz, N., Ladizhansky, Y., Korin, E., Waisman, M., Daltrophe, N., & Gilron, J. (2006). Prevention of scaling of reverse osmosis membranes by "zeroing" the elapsed nucleation time. Part I. Calcium sulfate. *Industrial & Engineering Chemistry Research, 45*(6), 2008-2016. https://doi.org/10.1021/ie051040k

ISSN: 2181-3337 | SCIENTISTS.UZ

48. Ren, A., Dai, Z., Li, X., van der Meer, W., Rose, J. B., & Liu, G. (2025). Temperature-dependent microbial dynamics in touchless sensor faucets during short-term stagnation. *Environmental Science and Ecotechnology, 28*, Article 100624. https://doi.org/10.1016/j.ese.2025.100624
49. Richards, B. S., Capão, D. P. S., Früh, W. G., & Schäfer, A. I. (2015). Renewable energy powered membrane technology: Impact of solar irradiance fluctuations on performance of a brackish water reverse osmosis system. *Separation and Purification Technology, 156*, 379-390. https://doi.org/10.1016/j.seppur.2015.10.025
50. Richards, B. S., Capão, D. P. S., & Schäfer, A. I. (2008). Renewable energy powered membrane technology. 2. The effect of energy fluctuations on performance of a photovoltaic hybrid membrane system. *Environmental Science & Technology, 42*(12), 4563-4569. https://doi.org/10.1021/es703157n
51. Ruiz-García, A., & Nuez, I. (2020). Long-term intermittent operation of a full-scale BWRO desalination plant. *Desalination, 489*, Article 114526. https://doi.org/10.1016/j.desal.2020.114526
52. Sarker, N. R., & Bilton, A. M. (2021). Real-time computational imaging of reverse osmosis membrane scaling under intermittent operation. *Journal of Membrane Science, 636*, Article 119556. https://doi.org/10.1016/j.memsci.2021.119556
53. Sarker, N. R., Cherukupally, P., Sodhi, R., & Bilton, A. M. (2025). End-of-the-day rinsing for improved maintainability of intermittently operated small-scale photovoltaic-powered reverse osmosis systems. *Desalination, 599*, 118439. https://doi.org/10.1016/j.desal.2024.118439
54. Schäfer, A. I., Shen, J., & Richards, B. S. (2018). Renewable energy-powered membrane technology in Tanzanian communities. *npj Clean Water, 1*(1), Article 24. https://doi.org/10.1038/s41545-018-0026-6
55. Sitterley, K. A., Binger, Z., & Jenne, D. S. (2025). Comparing constant and transient membrane transport parameters for use in wave desalination models. *Membranes, 15*(8), Article 243. https://doi.org/10.3390/membranes15080243
56. Sitterley, K. A., Cath, T. J., Jenne, D. S., Yu, Y.-H., & Cath, T. Y. (2022). Performance of reverse osmosis membrane with large feed pressure fluctuations from a wave-driven desalination system. *Desalination, 527*, Article 115546. https://doi.org/10.1016/j.desal.2022.115546
57. Torii, S., Hashimoto, T., Do, A. T., Furumai, H., & Katayama, H. (2019). Impact of repeated pressurization on virus removal by reverse osmosis membranes for household water treatment. *Environmental Science: Water Research & Technology, 5*(5), 910-919. https://doi.org/10.1039/C8EW00944A
58. Tow, E. W., Wei, Q. J., Abraham, A. R., Chua, K. L., Plumley, M. J., & Lienhard, J. H. (2025). Piloting batch reverse osmosis with a flexible bladder for water recovery from scaling-prone brine. *npj Clean Water, 8*, Article 30. https://doi.org/10.1038/s41545-025-00462-6
59. Tu, K. L., Chivas, A. R., & Nghiem, L. D. (2014). Effects of chemical preservation on flux and solute rejection by reverse osmosis membranes. *Journal of Membrane Science, 472*, 202-209. https://doi.org/10.1016/j.memsci.2014.08.052
60. Uchymiak, M., Bartman, A. R., Daltrophe, N., Weissman, M., Gilron, J., Christofides, P. D., Kaiser, W. J., & Cohen, Y. (2009). Brackish water reverse osmosis (BWRO) operation in feed flow reversal mode using an ex situ scale observation detector (EXSOD). *Journal of Membrane Science, 341*(1-2), 60-66. https://doi.org/10.1016/j.memsci.2009.05.039
61. Valladares Linares, R., Wexler, A. D., Bucs, S. S., Dreszer, C., Zwijnenburg, A., Flemming, H. C., Kruithof, J. C., & Vrouwenvelder, J. S. (2016). Compaction and relaxation of biofilms. *Desalination and Water Treatment, 57*(28), 12902-12914. https://doi.org/10.1080/19443994.2015.1057036
62. Van Buggenhout, S., Verbeke, R., Davenport, D. M., & Vankelecom, I. F. J. (2025). Drying polymer membranes for preservation: A review. *Journal of Membrane Science, 731*, Article 124190. https://doi.org/10.1016/j.memsci.2025.124190

63. Warsinger, D. M., Tow, E. W., Maswadeh, L. A., Connors, G. B., Swaminathan, J., & Lienhard, J. H. (2018). Inorganic fouling mitigation by salinity cycling in batch reverse osmosis. *Water Research, 137*, 384-394. https://doi.org/10.1016/j.watres.2018.01.060
64. Wu, J., He, J., Quezada-Renteria, J. A., Le, J., Au, K., Guo, K., Xiao, M., Wang, X., Dlamini, D., Fan, H., Pataroque, K., Suleiman, Y., Shahbazmohamadi, S., Elimelech, M., Li, Y., & Hoek, E. M. V. (2024). Polyamide reverse osmosis membrane compaction and relaxation: Mechanisms and implications for desalination performance. *Journal of Membrane Science, 706*, Article 122893. https://doi.org/10.1016/j.memsci.2024.122893
65. Wu, J., He, J., Quezada-Renteria, J. A., Xiao, M., Le, J., Au, K., Guo, K., Ye, N., Toma, T., Elimelech, M., Li, Y., & Hoek, E. M. V. (2025). Role of transmembrane pressure and water flux in reverse osmosis composite membrane compaction and performance. *Environmental Science & Technology, 59*(17), 8856-8866. https://doi.org/10.1021/acs.est.5c02618
66. Yang, H., Choi, J., Choi, Y., & Lee, S. (2022). Effect of intermittent operation modes on performance of reverse osmosis (RO) membrane in desalination and water treatment. *Membrane and Water Treatment, 13*(1), 39-49. https://doi.org/10.12989/mwt.2022.13.1.039
67. Yin, Y., & Huang, H. (2026). Membrane-based decentralized water supply systems for rural population: A critical review. *Journal of Environmental Management, 405*, Article 129727. https://doi.org/10.1016/j.jenvman.2026.129727
68. Zhang, B., Jiang, Y., Fang, F., & Zhang, K. (2019). Membrane fouling in reverse-osmosis filters during real drinking water purification: Impact of operation modes and pretreatment. *Desalination and Water Treatment, 159*, 214-223. https://doi.org/10.5004/dwt.2019.24058
69. Zlatanović, L., van der Hoek, J. P., & Vreeburg, J. H. G. (2017). An experimental study on the influence of water stagnation and temperature change on water quality in a full-scale domestic drinking water system. *Water Research, 123*, 761-772. https://doi.org/10.1016/j.watres.2017.07.019

ISSN: 2181-3337 | SCIENTISTS.UZ

ISSN: 2181-3337 | SCIENTISTS.UZ VOLUME 5 ISSUE 8 | AUGUST 2026

MORPHOLOGICAL PARAMETERS IN THE UPSTREAM REACH OF A FLOW CONSTRICTED BY A SPUR DIKE

Bakiev Masharif[1], Kuryozov Otaboy[2], Yakubov Kuvonchbek[3], Khasanov Khojiakbar[4], Khalimbetov Azat[5]

Professor, Head of the Department of Hydrotechnical Structures and Engineering Constructions, Tashkent Institute of Irrigation and Agricultural Mechanization Engineers – National Research University (TIIAME-NRU), Tashkent, Uzbekistan[1]

Independent Researcher, Department of Hydrotechnical Structures and Engineering Constructions, TIIAME-NRU, Tashkent, Uzbekistan[2]

PhD, Associate Professor, Department of Hydrotechnical Structures and Engineering Constructions, TIIAME-NRU, Tashkent, Uzbekistan[3]

Assistant and Independent Researcher, Department of Hydrotechnical Structures and Engineering Constructions, TIIAME-NRU, Tashkent, Uzbekistan[4]

PhD, Associate Professor, Department of Hydrotechnical Structures and Engineering Constructions, TIIAME-NRU, Tashkent, Uzbekistan[5]

DOI: 10.67620/sai.58a0006

ABSTRACT

This paper presents the results of an experimental and theoretical study of the morphological parameters of flow in the upstream reach constricted by a spur dike (solid spur). The experiments were carried out in three flumes measuring40×60×1500 cm,40×60×800 cm, 100×50×800 cm. The first flume had glass walls and a wooden bed, the second had concrete walls and a wooden bed, and the third had concrete walls and a concrete bed. Experiments were carried out under the following flow and spur dike conditions: degree of flow constriction nb=lb sinθ /B; 0.125, 0.2, 0.3, 0.375. Here lb is the length of the spur dike; θ is the installation angle, 60–90°; water discharge from 5 to 25 l/s i_d=0.0001-0,0002. Fr_δ=0.02"–" 0.35 The influence of these factors on the formation of the section of maximum backwater and on the length of the upstream recirculation zone was examined. It was found that as the degree of flow constriction increases, the relative distance to the section of maximum backwater S_1/(B-b_0)decreases from 2.0 to 0.96, while the relative length of the upstream recirculation zone l_b/(B-b_0)increases from 3.0 to 4.55. An increase in the Froude number leads to an expansion of the zone of hydrodynamic influence of the structure and a shift of the maximum-backwater zone upstream. It was experimentally confirmed that as the spur dike installation angle increases, the processes of flow separation and circulatory flow in the upstream reach intensify. To provide a theoretical description of backwater propagation, the momentum equation was used, accounting for the influence of hydrostatic pressure forces, bed and bank resistance, and the redistribution of flow momentum in the zone of local constriction. A comparison of calculated results with the experimental data of K.Sh. Sharapov showed satisfactory agreement, including at a substantial bed slope of 0.004: the calculated backwater length was

ACCEPTED

03.09.26

Keywords: *spur dike (spur), backwater, upstream recirculation zone, degree of constriction, piezometric slope, specific energy, spur dike installation angle, Froude number, momentum equation.*

CC BY

L_p=0.86"–" 0.94 m against an experimental value of L_p=1.0 m. The relationships and calculation approaches obtained can be used in the design of channel-regulating and bank-protection structures, as well as in assessing the hydrodynamic conditions governing the formation of local backwater and recirculation zones in river channels.

Introduction

Channel flows interacting with bank-protection and channel-regulating structures are characterized by a complex spatial hydrodynamic structure, accompanied by velocity redistribution, changes in the free surface of the flow, and the development of recirculation zones and local backwater. A particularly complex flow pattern is observed in the upstream reach of flows constricted by spur dikes and groynes, where the local narrowing of the flow cross-section causes the main high-velocity core to shift, recirculation zones to form, and shear-stress distribution to change markedly. These processes directly affect bank stability, the intensity of local scour, sediment transport, and the reliability of hydraulic structures.

Recent studies show that when flow interacts with spurs and lateral constrictions, complex three-dimensional flows develop, accompanied by the growth of vortex structures and deformation of the free water surface. As a result of installing a spur, the main jet shifts toward the opposite bank, while in the nearshore zone regions of reduced velocity and reverse flow form (Gu et al., 2023; Liu et al., 2021). Near the spur head, high values of turbulent kinetic energy, local shear stresses, and intense turbulent mixing are observed, which leads to the intensification of channel deformation and local scour (Chen et al., 2022; Kang et al., 2023). The formation of the upstream and downstream recirculation zones, characterized by complex circulatory flows and secondary vortex structures, plays a particularly important role in the flow structure.

Significant influence on the hydrodynamic structure of the flow is exerted by the geometric parameters of channel-regulating structures. It has been established that the degree of channel constriction, the length of the spur, its installation angle, and the relative flow depth determine the pattern of displacement of the main high-velocity core, the size of the recirculation zones, and the intensity of free-surface deformation (Kang et al., 2023; Ohtsuki et al., 2024). As the degree of constriction increases, the influence of inertial and transverse velocity gradients grows, leading to stronger momentum redistribution and a change in the flow structure in the upstream reach.

The classical foundations for calculating constricted flows were laid in the works of Rotenburg, Avrova, Seleznev, Sharapov, and Zegzhda. Rotenburg (1960) examined the hydraulic design of bridge crossings over lowland rivers and proposed approaches for determining the position of the section of maximum backwater under significant flow constriction. Avrova (1969) studied the hydraulic calculation of river flow constricted by a cofferdam and showed the need to account for changes in flow structure within the zone of local narrowing. Seleznev (1958) studied the kinematics of flow in the vicinity of semi-dams, which is important for understanding the processes of jet separation and the formation of recirculation zones. Sharapov (1968) investigated the hydraulics of massive spurs and proposed approaches for assessing the influence of spurs on channel-flow structure. Zegzhda (1957) developed approaches for determining hydraulic friction losses in channels and pipelines, which provides an important basis for calculating bed and bank resistance (Avrova, 1969; Rotenburg, 1960; Seleznev, 1958; Sharapov, 1968; Zegzhda, 1957). Rotenburg (1960) also assumed that the piezometric slope along the near-bank streamline is zero, and that the section of maximum backwater has a curvilinear shape described by an elliptical relationship. Our studies have shown that these assumptions hold mainly for flows strongly constricted by bridge embankments.

ISSN: 2181-3337 | SCIENTISTS.UZ

At small degrees of constriction, the flow structure changes substantially. Modern experimental studies show that under conditions of weak lateral constriction, a contracted section forms, displaced downstream relative to the constriction section (Fakhri et al., 2020; Nowroozpour et al., 2022). In this case the flow separates from the protected bank considerably earlier, and in the interaction zone regions of intense turbulent mixing and recirculating flow form (Bakiev et al., 2023, 2024; Khalimbetov et al., 2020; Mulahasan et al., 2021; Mulahasan & Mohammed, 2021). The maximum backwater and the most intense deformation of the free surface are also frequently displaced downstream owing to the redistribution of flow momentum and the development of vortex structures.

Despite considerable progress in modern experimental and numerical research methods, many questions relating to the formation of the morphological parameters of flow in the upstream reach remain insufficiently studied. Most current work addresses local scour, turbulence, and numerical modeling of flow around spurs and bridge crossings, whereas the regularities governing the formation of the section of maximum backwater and the upstream recirculation zone under small degrees of constriction have been studied only to a limited extent. Flows constricted by solid spurs (spur dikes), which are characterized by early separation of the near-bank streamline and a positive piezometric slope along it, have been particularly insufficiently studied.

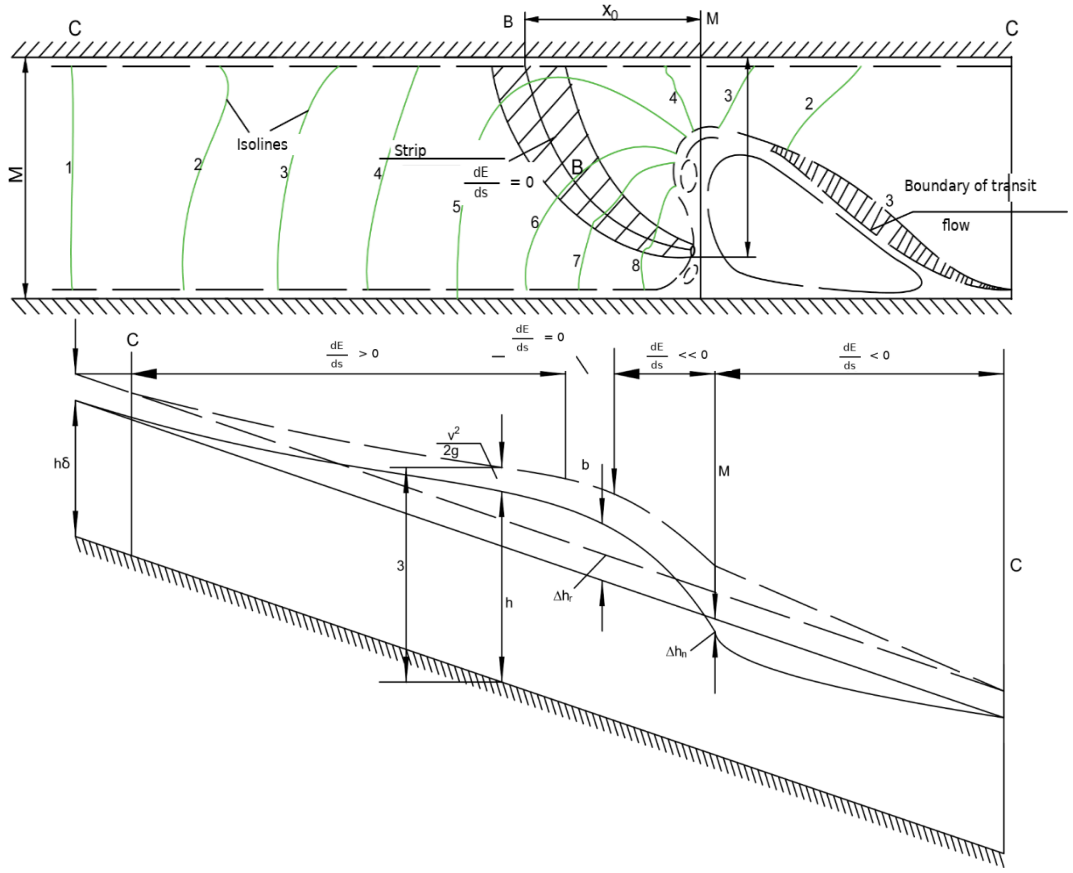


Fig. 1. Diagram of flow constricted by a bridge crossing (after I.S. Rotenburg).

This makes it necessary to further investigate, both experimentally and theoretically, the hydrodynamic features of flow in the upstream reach constricted by a spur dike, taking into account the degree of flow constriction, the spur installation angle, and the Froude number.

The aim of the present study is to determine the regularities governing the formation of the morphological parameters of flow in the upstream reach constricted by a spur dike, and to develop calculation relationships for determining the position of the section of maximum backwater and the length of the upstream recirculation zone as functions of the hydraulic parameters of the flow.

ISSN: 2181-3337 | SCIENTISTS.UZ

Materials and Methods

Experimental Setup

To study the morphological parameters of flow in the upstream reach constricted by a spur dike, laboratory hydraulic experiments were carried out in straight flumes with a non-erodible bed. The use of laboratory flumes made it possible to ensure controlled hydraulic conditions and to exclude the influence of random natural factors typical of field channel processes. This approach enables a detailed analysis of the regularities governing backwater formation, changes in flow structure, and the development of recirculation zones under various flow-constriction regimes.

Scheme of Flow Interaction with the Spur Dike

A spur dike (solid spur), installed at various angles to the flow direction, was used as the channel-regulating element. The main objective of the experiments was to investigate the influence of the spur dike on the redistribution of the hydrodynamic parameters of the flow in the upstream reach.

When the flow interacts with the spur dike, a local narrowing of the flow cross-section occurs, which changes the flow structure. The main flow shifts toward the free part of the channel, a backwater zone forms in front of the structure, and a region of recirculating flow arises in the nearshore area. At the same time, the near-bank streamline separates from the protected bank and an upstream recirculation zone forms.

Unlike flows constricted by bridge crossings, in the case under consideration the streamline separates considerably earlier, and a positive piezometric slope develops along the near-bank streamline:

$$J_s > 0$$

This leads to a change in the position of the line of maximum backwater and a shift of the contracted section downstream relative to the constriction section.

The hydraulic scheme shown in Fig. 2 was used to analyze these processes.

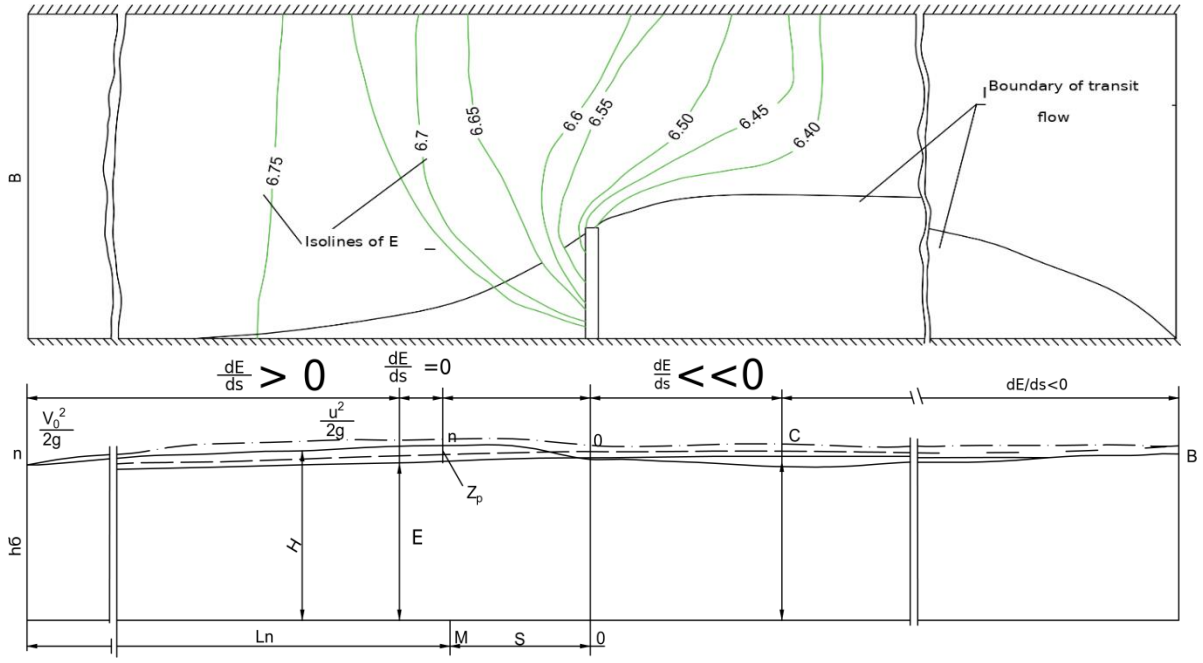


Fig. 2. Diagram of flow constricted by a spur dike (solid spur).

Main Hydraulic Parameters of the Study

To quantitatively describe the processes occurring in the upstream reach of the flow, the principal dimensionless hydraulic parameters were selected. The use of dimensionless characteristics makes it possible to generalize the experimental results and to apply the relationships obtained to channel systems of different scales.

One of the main parameters was the degree of flow constriction:

ISSN: 2181-3337 | SCIENTISTS.UZ

$$n = \frac{b_0}{B}$$

where: b_0— width of the constricted part of the flow; B— full width of the channel.

This parameter characterizes the relative reduction of the flow cross-section caused by installation of the spur dike. A change in the degree of constriction directly affects the intensity of backwater, velocity redistribution, and the development of recirculation zones.

To assess the position of the zone of maximum backwater, the following parameter was used:

$$\frac{S_1}{B - b_0}$$

where: S_1— distance from the spur head to the section of maximum backwater.

The use of a relative form made it possible to exclude the influence of the absolute dimensions of the flume and to analyze the general regularities governing the change in backwater position.

The size of the upstream recirculation zone was assessed using the parameter:

$$\frac{l_b}{B - b_0}$$

where: l_b— length of the upstream recirculation zone.

This parameter characterizes the intensity of the development of recirculating flow in the upstream reach and makes it possible to assess the size of the reverse-flow zone arising from the interaction of the flow with the spur dike.

The hydrodynamic regime of the flow was characterized by the Froude number:

$$Fr_\delta = \frac{V}{\sqrt{gh}}$$

The Froude number is one of the most important criteria of hydraulic similarity and reflects the ratio of inertial to gravitational forces in the flow. A change in this parameter substantially affects the flow structure, the size of the backwater zone, and the intensity of vortex formation.

Method for Determining the Section of Maximum Backwater

To determine the position of the section of maximum backwater, a series of experimental measurements was carried out for various values of the degree of flow constriction, the spur dike installation angle, and the Froude number.

During the experiments, the position of the free-surface line of the flow was measured, and the distance from the spur head to the section at which the maximum rise in water level was observed was recorded. Based on the data obtained, graphical relationships were constructed making it possible to determine the relative position of the section of maximum backwater (Fig.):

The use of graphical relationships is due to the complexity of an analytical description of the spatial flow structure in the zone of local constriction. The experimental approach made it possible to reveal stable regularities in the change of the morphological parameters of the flow.

Method for Determining the Length of the Upstream Recirculation Zone

One of the most important characteristics of the flow in the upstream reach is the length of the upstream recirculation zone. The formation of this zone is associated with separation of the streamline from the protected bank and the development of circulatory motion in the nearshore area.

To determine the length of the recirculation zone, visual observations of the flow trajectory were carried out and the boundaries of the stable recirculating flow were recorded. Based on the experimental results, relationships were constructed (Fig.):

The use of a relative parameter made it possible to exclude the influence of the absolute dimensions of the experimental setup and to obtain more universal relationships.

ISSN: 2181-3337 | SCIENTISTS.UZ

Theoretical Model for Calculating the Backwater Length

To provide a theoretical description of backwater propagation, the momentum equation was used. This approach makes it possible to account for the principal forces acting on the flow in the zone of interaction with the spur dike.

The calculation scheme included:

– hydrostatic pressure forces;
– bed and bank friction forces;
– the influence of the water's own weight;
– the change in flow momentum.

As can be seen from Figs. 1 and 2, the total backwater length L_n is determined as the sum:

$$L_n = l_n + S_1 \tag{1}$$

The distance to the section of maximum backwater S_1 was determined from the graphical relationships by interpolation, while to determine the length $l_n$the momentum equation was applied to the fluid element bounded by sections EB, MB, the bed, and the free surface of the flow (Figs. 1, 2).

The equation is written as follows:

$$\rho Q(\alpha_{o\delta} V_\delta - \alpha_{\text{омп}} V_{\text{мп}}) = \sum P + \sum T - G' \tag{2}$$

where ρ — is the water density; Q— the discharge; $\left.\begin{matrix}\alpha_{o\delta} V_\delta \\ \alpha_{\text{омп}} V_{\text{мп}}\end{matrix}\right\}$— the momentum correction factors and mean velocities, respectively, at the end-of-backwater section (EB) and at the section of maximum backwater; $\sum P = P_n - P_\delta$— the difference in hydrostatic pressure forces acting at sections EB and MB; $\sum T = T_d + 2T_\delta$— the sum of the external friction forces from the bed and the bank; G'— the component of the water's own weight between sections EB and MB.

Here

$$P_n = \frac{\gamma B H^2}{2};\ P_\delta = \frac{\gamma B h_\delta^2}{2}; \tag{3}$$

$$\left.\begin{matrix} T_{\text{д}} = \tau_{\text{д}} l_n B = \rho \frac{\lambda_{\text{д}} V_{\text{ср}}^2}{2} l_n B;\ G' = \gamma B l_n \frac{(H+h_\delta)}{2}\, i_{\text{д}} \\ T_\delta = \tau_{\text{б}} l_n \frac{(H+h_\delta)}{2} = \rho \frac{\lambda_\delta V_{\text{ср}}^2}{2} l_n \frac{(H+h_\delta)}{2} \end{matrix}\right\} \tag{4}$$

Substituting (4) into equation (2), after some transformation we obtain:

$$l_n = \frac{\frac{Q}{g}(\alpha_{\text{об}} V_{\text{б}} - \alpha_{\text{ОМП}} V_{\text{МП}}) - \frac{B}{2}(H^2 - h_{\text{б}}^2)}{\frac{\lambda_{\text{д}}(V_{\text{б}} + V_{\text{МП}})^2 B}{8g} + \frac{\lambda_{\text{б}}(V_{\text{б}} + V_{\text{МП}})^2 (H+h_{\text{б}})}{8g} - \frac{B(H+h_{\text{б}})}{2} i_{\text{д}}} \tag{5}$$

Or, when $\lambda_{\text{д}} = \lambda_{\text{б}} = \lambda$ and $i_{\text{д}} = 0$ a simpler relationship is obtained

$$l_n = \frac{\frac{Q}{g}(\alpha_{\text{об}} V_{\text{б}} - \alpha_{\text{ОМП}} V_{\text{МП}}) - \frac{B}{2}(H^2 - h_{\text{б}}^2)}{\frac{\lambda(V_{\text{б}} + V_{\text{МП}})^2 B}{8g}(B + H + h_\delta)} \tag{6}$$

In formulas (4, 5, 6) the notation is as follows: $\left.\begin{matrix}\tau_{\text{д}}, \lambda_{\text{д}} \\ \tau_{\text{б}}, \lambda_{\text{б}}\end{matrix}\right\}$— shear stresses and the corresponding resistance coefficients of the bed and the bank, respectively $B l_n \frac{H+h_\delta}{2}$— the volume of water between the sections; γ — the unit weight of water; g— the acceleration of gravity; H— the flow depth at section MB.

The remaining notation is clear from Figs. 1 and 2, and the hydraulic friction coefficient is determined from the formula of A.P. Zegzhda.

To improve the accuracy of the calculations, the values of the momentum coefficients were adopted on the basis of the experimental data. This made it possible to achieve satisfactory agreement between the calculated and experimental results.

Results and Discussion

Position of the Section of Maximum Backwater

ISSN: 2181-3337 | SCIENTISTS.UZ

Based on the results of the experimental studies, graphical relationships were obtained that make it possible to determine the position of the section of maximum backwater as a function of the degree of flow constriction, the spur dike installation angle, and the Froude number

The results obtained showed that as the degree of flow constriction increases, *n*the relative distance to the section of maximum backwater decreases. This regularity is explained by the fact that as constriction intensifies, a more intense redistribution of the velocity field occurs in the transverse direction. As a result, the flow adapts more quickly to the changed hydraulic conditions, and the zone of maximum backwater shifts closer to the spur head.

It was also established that an increase in the spur dike installation angle likewise leads to a decrease in the relative distance:

this is because as the installation angle increases, the degree of the structure's effect on the main flow grows, local jet contraction intensifies, and the intensity of momentum redistribution in the upstream reach increases.

The influence of the Froude number is of the opposite character. The experimental results showed that as Fr_δ increases, a certain increase in the relative distance to the section of maximum backwater is observed. This effect is explained by the increase in the inertial forces of the flow. At higher velocities the flow possesses greater kinetic energy, as a result of which the process of its hydrodynamic readjustment occurs over a greater distance upstream.

Thus, the position of the section of maximum backwater is determined by the combined influence of the geometric parameters of constriction and the dynamic characteristics of the flow. The relationships obtained reflect the regularities of pressure redistribution and the change in flow structure in the upstream reach during interaction of the flow with the spur dike.

Table 1. Experimental data used to construct the graph

(n)	(Frδ = 0.06)	(Frδ = 0.20)	(Frδ = 0.35)	a	δ
0.12	2.2	2.08	1.96	0.24	1.9
0.22	1.84	1.76	1.64	0.28	1.75
0.34	1.48	1.46	1.39	0.36	1.5
0.46	1.18	1.22	1.14	0.45	1.3
0.54	1	0.92	0.84		

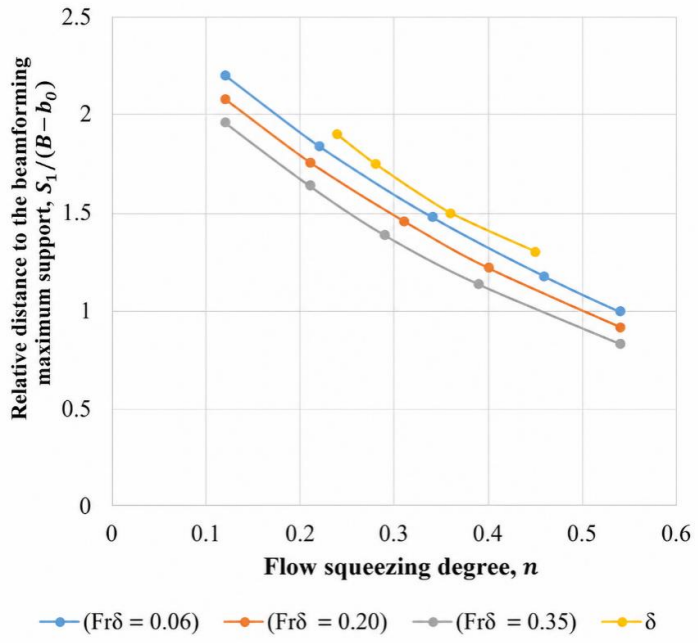


Fig. 3. Relationship between the relative position of the section of maximum backwater and the degree of flow constriction for various values of the Froude number.

ISSN: 2181-3337 | SCIENTISTS.UZ

Formation of the Upstream Recirculation Zone

One of the most characteristic hydrodynamic phenomena arising from the interaction of the flow with the spur dike is the formation of the upstream recirculation zone. The formation of this region is associated with separation of the near-bank streamline from the protected bank and the emergence of a local circulatory flow.

The experimental results showed that the length of the upstream recirculation zone depends substantially on the degree of flow constriction, the spur dike installation angle, and the Froude number (Fig. 4).

It was found that as the degree of flow constriction increases, the relative length of the recirculation zone also increases. This is explained by the fact that under stronger constriction the transverse velocity gradient increases and the process of streamline separation from the bank intensifies. As a result, the size of the recirculation region increases.

A similar regularity is observed with an increase in the spur dike installation angle. At larger angles the intensity of the flow's interaction with the structure increases, which leads to stronger vortex formation and an expansion of the recirculation zone.

The Froude number also has a significant influence on the size of the upstream recirculation zone. As it increases, the relative length of the recirculation zone increases.

This effect is related to the growth of the inertial forces of the flow and the increased stability of the separated streamline. As a result, the recirculating-flow zone extends over a greater distance upstream.

It should be noted that the formation of the upstream recirculation zone has a significant effect on the morphodynamic processes in the channel. Within this region, a decrease in flow velocities, a change in the distribution of shear stresses, and the emergence of local zones of sediment accumulation are observed. The determination of the size of the recirculation zone therefore has important practical significance for the design of bank-protection structures and the prediction of channel deformation.

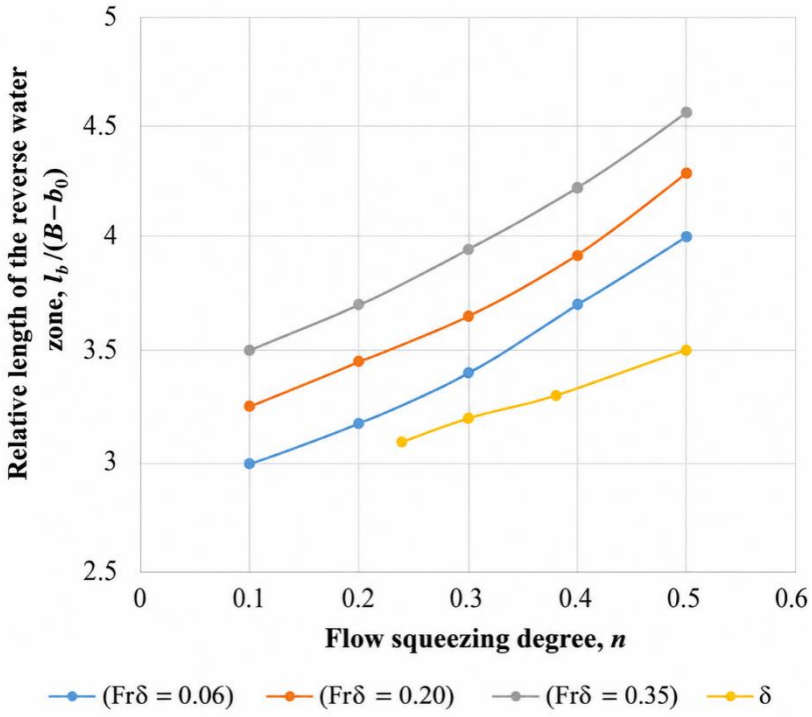


Fig. 4. Relationship between the relative length of the upstream recirculation zone and the degree of flow constriction for various values of the Froude number.

ISSN: 2181-3337 | SCIENTISTS.UZ

Table 2.

Experimental data used to construct the graph

(n)	(Frδ = 0.06)	(Frδ = 0.20)	(Frδ = 0.35)	a	δ
0.1	3	3.25	3.5	0.24	3.1
0.2	3.18	3.45	3.7	0.3	3.2
0.3	3.4	3.65	3.95	0.38	3.3
0.4	3.7	3.92	4.22	0.5	3.5
0.5	4	4.28	4.55		

Comparison of Calculated and Experimental Data

To assess the applicability of the proposed method, calculations of the backwater length were performed and the calculated results were compared with the experimental data of K.Sh. Sharapov (1957)

The calculations were performed for the conditions of a straight flume with a non-erodible bed, for the following hydraulic parameters: water discharge$q = 10$ л/с, mean flow velocity $V = 0.38$ м/с, degree of constriction $n = 0.225$, longitudinal bed slope $i_d = 0.004$

The results obtained showed satisfactory agreement between the calculated and experimental values of the backwater length. The discrepancies between the calculated and experimental data were within acceptable limits, which confirms the validity of the approach used.

Analysis of the results showed that expression (1) essentially determines the overall length of backwater propagation, which in a number of cases may exceed the size of the upstream recirculation zone. This is especially noticeable at small longitudinal channel slopes, typical of lowland rivers.

At

$$i_d < 0.0003$$

the backwater propagates over a considerable distance upstream, so that the backwater length substantially exceeds the size of the recirculation region. At larger slopes, however,

$$i_d \geq 0.004$$

the backwater is localized within a relatively small reach, and the backwater length becomes close to the length of the upstream recirculation zone.

The results obtained confirm that the developed method can be used to assess the morphological parameters of flow in the upstream reach constricted by a spur dike.

Table 3. Comparison of calculated and experimental values of the backwater length.

Test No.	1	2	3
α_b (°)	90	70	50
lb (m)	0.18	0.191	0.234
S1 (m)	0.34	0.37	0.41
H (m)	0.04	0.04	0.04
Vmp (m/s)	0.313	0.313	0.313
λ_d	0.0127	0.0127	0.0127
λ_δ	0.007	0.007	0.007
lp (II-7) (m)	0.6	0.6	0.6
lp (II-4) (m)	0.94	0.9	0.86
lp (II-4) (m)	0.88	0.882	0.9
lp (experiment) (m)	1	1	1

ISSN: 2181-3337 | SCIENTISTS.UZ

Conclusion

As a result of the experimental and theoretical studies carried out, the principal regularities governing the formation of the morphological parameters of flow in the upstream reach constricted by a spur dike have been established. The results obtained made it possible to reveal features of the redistribution of the hydrodynamic characteristics of the flow under local narrowing of the flow cross-section and to determine the influence of the principal hydraulic parameters on the processes of backwater formation and the formation of the upstream recirculation zone.

It has been established that the position of the section of maximum backwater depends substantially on the degree of flow constriction, the spur dike installation angle, and the Froude number. As the degree of constriction and the spur dike installation angle increase, the relative distance to the section of maximum backwater decreases, which is associated with a more intense redistribution of the velocity field and an acceleration of the flow's hydrodynamic readjustment. At the same time, an increase in the Froude number leads to a certain shift of the section of maximum backwater upstream, owing to the growth of the inertial forces of the flow.

It has been experimentally confirmed that the length of the upstream recirculation zone increases with an increase in the degree of flow constriction, the spur dike installation angle, and the Froude number. The formation of this zone is caused by separation of the near-bank streamline from the protected bank and the development of circulatory flow in the nearshore area. The relationships obtained reflect the regularities governing the development of vortex structures and make it possible to assess the size of the recirculation zones in the upstream reach.

Based on the momentum equation, a calculation method for determining the backwater length has been developed. The proposed model accounts for the influence of hydrostatic pressure forces, bed and bank resistance, and the redistribution of flow momentum in the zone of local constriction. A comparison of the calculated results with the experimental data showed satisfactory agreement, which confirms the validity and practical applicability of the developed approach.

The results obtained can be used in the design of channel-regulating and bank-protection structures, as well as in assessing the hydrodynamic conditions governing the formation of local backwater zones and recirculating flow in river and canal channels.

REFERENCES

1. Avrova, T. F. (1969). *Gidravlicheskii raschet rechnogo potoka, stesnennogo peremychkoi* [Hydraulic calculation of river flow constricted by a cofferdam] [Abstract of Candidate of Technical Sciences dissertation, Leningrad Polytechnic Institute named after M. I. Kalinin]. 18 pp.
2. Bakiev, M., Khalimbetov, A., Yakubov, K., Sagin, J., & Asamatdinov, I. (2023). Kinematic parameters of flow constrained by combined dams with through part of tetrahedra in compression region. *E3S Web of Conferences, 401*, 04046. doi:10.1051/e3sconf/202340104046
3. Bakiev, M., Matkarimov, O., Yakubov, K., & Khalimbetov, A. (2024). Study on velocity field of the flow asymmetrically constrained by through spurs. *E3S Web of Conferences, 563*, 02017. doi:10.1051/e3sconf/202456302017
4. Chen, Y., Lu, Y., Yang, S., Mao, J., Gong, Y., Muhammad, W. I., & Yin, S. (2022). Numerical investigation of flow structure and turbulence characteristic around a spur dike using large-eddy simulation. *Water, 14*(19), 3158. doi:10.3390/w14193158
5. Fakhri, A., Ettema, R., Aliyari, F., & Nowroozpour, A. (2021). Large-scale particle image velocimetry for estimating vena-contracta width for flow in contracted open channels. *Water, 13*(1), 31. doi:10.3390/w13010031

ISSN: 2181-3337 | SCIENTISTS.UZ

6. Gu, Z., Cao, X., Cao, M., & Lu, W. (2023). Integrative study on flow characteristics and impact of non-submerged double spur dikes on the river system. *International Journal of Environmental Research and Public Health, 20*(5), 4262. doi:10.3390/ijerph20054262
7. Kang, S. K., Lee, J., Kim, Y., & Khosronejad, A. (2023). Experimental and numerical study on the flow characteristics around spur dikes at different length-to-depth ratios. *Advances in Water Resources, 175*, 104428. doi:10.1016/j.advwatres.2023.104428
8. Khalimbetov, A., Bakiev, M., Shukurova, S., Choriev, J., & Khayitov, K. (2020). Study of submountain river flow patterns constrained by a combined dam. *IOP Conference Series: Earth and Environmental Science, 614*(1), 012053. doi:10.1088/1755-1315/614/1/012053
9. Liu, J. C., Hu, Z. Q., & Zhu, M. Y. (2021). Comparison and analysis of calculation of bridge backwater based on MIKE21 hydrodynamic model. *E3S Web of Conferences, 233*, 03043. doi:10.1051/e3sconf/202123303043
10. Mulahasan, S., Al-Osmy, S., & Alhashimi, S. (2021). Modelling of flow pattern in an open channel with sidewall obstruction. *IOP Conference Series: Materials Science and Engineering, 1090*(1), 012097. doi:10.1088/1757-899X/1090/1/012097
11. Mulahasan, S., & Mohammed, A. Y. (2021). Hydraulic characteristics of flow-through bridge openings. *Applied Engineering Letters, 6*(1), 21–28. doi:10.18485/aeletters.2021.6.1.3
12. Nowroozpour, A., Ettema, R., & Fakhri, A. (2022). A reassessment of contraction scour at bridge waterways. *Journal of Hydraulic Engineering, 148*(12), 06022016. doi:10.1061/(ASCE)HY.1943-7900.0002031
13. Ohtsuki, K., Kono, T., Arikawa, T., Taniwaki, H., & Itsukushima, R. (2024). Spur dike applications for the sustainability of channels in incised steep bend streams. *Water, 16*(4), 575. doi:10.3390/w16040575
14. Rotenburg, I. S. (1960). *Voprosy gidravlicheskogo rascheta i naznacheniia otverstii mostov na perekhodakh cherez ravninnye reki* [Issues of hydraulic calculation and sizing of bridge openings at crossings over lowland rivers]. Saratov University Press.
15. Seleznev, V. M. (1957). *Issledovanie kinematiki potoka v raione poluzaprud* [Investigation of flow kinematics in the area of semi-dams] [Abstract of Candidate of Technical Sciences dissertation]. Leningrad.
16. Sharapov, K. V. (1968). *Issledovanie gidravliki massivnykh shpor* [Investigation of the hydraulics of massive groynes] [Abstract of Candidate of Technical Sciences dissertation, Tashkent Institute of Irrigation and Agricultural Mechanization Engineers]. Tashkent.
17. Zegzhda, A. P. (1957). *Gidravlicheskie poteri na trenie v kanalakh i truboprovodakh* [Hydraulic friction losses in channels and pipelines]. Gosstroyizdat.

ISSN: 2181-3337 | SCIENTISTS.UZ VOLUME 5 ISSUE 8 | AUGUST 2026

IMPROVING THE ALGORITHM FOR CONTROLLING THE CUSTOMS TRANSIT INFORMATION SYSTEM E-TRANSIT OF THE REPUBLIC OF UZBEKISTAN

Musayeva Shoira

Samarkand Institute of Economics and Service
Email: musaeva_shoira@mail.ru

DOI: 10.67620/sai.58a0007

ABSTRACT

This article examines the organization of customs transit and the ongoing development of the customs information system in the Republic of Uzbekistan, with particular attention to the digitalization of transit procedures. The study reviews international experience in customs transit management, especially the practices of developed countries and the European Union's New Computerised Transit System (NCTS). The main stages and functional elements of customs transit information-system algorithms are analyzed in order to identify approaches that may improve the efficiency, transparency, and control of transit operations. Particular attention is given to the processing of transit cargo, information exchange between customs authorities, and the use of digital tools for monitoring the movement and arrival of goods. Based on the comparative analysis, the article proposes a multi-stage customs transit management algorithm for Uzbekistan's E-Tranzit information system. The proposed approach is intended to strengthen customs control, support multimodal transportation, improve the coordination of transit procedures, and create more efficient conditions for foreign trade participants.

ACCEPTED

03.09.26

Keywords: *customs transit, NCTS, control algorithm, E-Tranzit information system, multimodal transportation.*

CC BY

Introduction

In recent years, customs administrations in many countries, landlocked countries are paying particular attention to customs transit issues. A study of the experience of developed countries shows that the path to effective customs transit lies through digitalization and information exchange between customs services of all countries along the international supply chain.people's trade.

For example, the European Union has introduced a new computerized transit system, the New Computerised Transit System (NCTS) was introduced and has been mandatory for all authorised consignees/shippers since 1 April 2006. The following European Free Trade Association countries are also connected to this system: Iceland, Liechtenstein, Norway, Switzerland, Turkey and North Macedonia.

To control transit in Central America, aThe Transit International Merchandise (TIM) system operates in Mexico, Nicaragua, Honduras, El Salvador, Guatemala,Costa Rica and Panama.

In East Africa, a system was established to control goods in transit.The RECTS system was created, uniting Uganda, Rwanda, Burundi,South Sudan, Democratic Republic of the Congo. In the Russian

Federation, there is software that allows for the control of goods transit: AS KTT-2, EAIS TO, KPS “Transit operations”, KPS “Completion of operations”tions”, AS “PP” (Afonin, 2022).

After successful tests in Cambodia, Laos, Malaysia, Singapore, Thailand and Vietnam was officially on November 30, 2023, the ACTS customs transit system for Southeast Asian countries, was launched (Lozinsky & Sazonov, 2022).

Since 2022, customs transit management in the Republic of Uzbekistan has been carried out using the new E-Tranzit information system, which enables decision-making based on the automation of information processes and technologies at all customs posts in the country. The E-Tranzit information system has proven its effectiveness over the course of its operation: over the course of one year, it processed 268,156 transit declarations, 61,176 documents under Book 11, and 182,120 other documents (Mukhtorov et al., 2023). At the same time, an analysis of the system's performance over the past period indicates that there are customs operations not covered by it, which significantly impacts the efficiency of customs authorities. Furthermore, the integration of the E-Tranzit information system with recognized international information systems, such as eTIR, NCTS, and the EAEU information systems, is a pressing issue.

Method

The study employed a systems approach, analysis, and digital metrics. Mass observation methods were used to collect and analyze data from social networks.

Results

The aim of this work was to develop proposals for improving the algorithm of the E-Tranzit information system for managing customs transit, based on the results of a comparative analysis with the information system of the European Union NCTS.

The legal basis of the European common method of transporting goods is based on uniform laws, regulations and standards of the European Union in the field of civil law, tax, banking and insurance legislation, the EU road code, etc. One of the key document is the document for organizing transit is the agreement between the countries of the European Union and the countries of the European Free Trade Association on Trade on a Single Administrative Document for the Transport of Goods (SAD Convention of May 22, 1987). In this regard, cargo transit is divided into the following types: internal, external; general, international, and postal.

"Intrastate customs transit" is a process—a transit system applicable only within a single country or customs territory, in which the departure and destination offices are located within the same territory. Any required security measures apply only to transit movements within the territory controlled by the customs service.

"International customs transit" is a transit movement that is part of a single transit customs operation in the course of which one or more customs borders are crossed in accordance with a bilateral or multilateral agreement. This agreement usually establishes the form of declaration of goods For customs transit And, If This required, guarantee applied in each territory controlled by the parties to this agreement (World Customs Organization, 2017).

As part of the European Union transit system NCTS, the following subsystems are implemented (Aldaniyazov, 2021):

subsystem for generating and transmitting data in the Single Administrative Message (SAM) format. Preliminary notification of customs authorities of countries of departure is being carried out With usingprinciple

"feedback", which allows for faster data transfer and confirmation of the arrival of cargo and transport vehicles to the destination to the destination;

a subsystem for managing a database of lost, stolen, and counterfeit customs seals and stamps used to issue cargo transportation notifications and surety certificates;

product coding subsystem;

ISSN: 2181-3337 | SCIENTISTS.UZ

warning subsystem that allows the transmission of information notification on the transportation of high-risk goods from the customs point of shipment to customs transit points and customs points of destination.

The technology for controlling transit cargo using NCTS includes the following steps.

The customs declaration is submitted to the customs authority of the departure of the cargo in electronic form by the foreign trade participant. The electronic declaration can be prepared independently or through thecash from customs authorities of departure.

The customs declaration must contain all required data and comply with format specifications, since the system controls the reliability of data automatically. If any discrepancy with the approved data is found and the customs declaration does not meet the requirements, NCTS will note this and refuse to accept the customs declaration. In this case, the foreign trade participant must make corrections to accept the customs declaration (Figure 1).

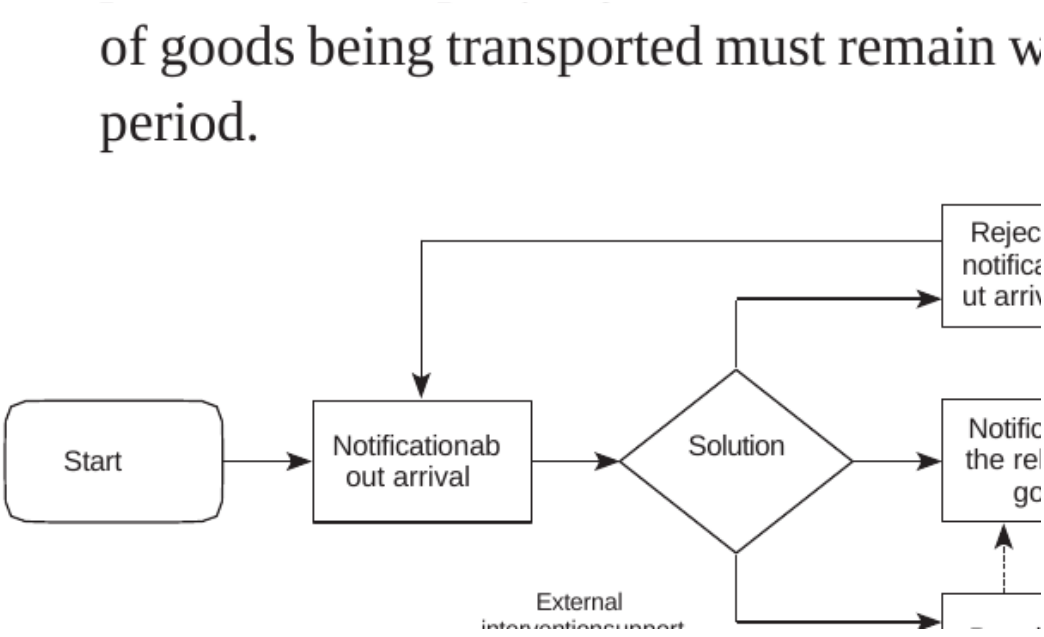
Once a customs declaration is accepted, NCTS registers it and assigns a unique registration number.

After receiving the notification of registration of the NCTS customs declaration, the customs office of departure accepts within 15–30 minutes a decision on conducting customs control in accordance with the recommendations of the risk management system.

After completing the entire customs control process at the customs office of departure the goods will be released in accordance with the transit procedure, and the system will print an accompanying transit document. The accompanying document and the list of goods being transported must remain with the goods throughout the entire transit period.

Figure 1

Flowchart of the NCTS User Interaction Algorithm



Note. Adapted from CTC Traders API Phase 4 Service Guide (HM Revenue & Customs, n.d.).

Simultaneously with the printing of the accompanying transit document, NCTS sends a notification to the designated destination customs office. The message contains information taken from the customs declaration, allowing the destination customs office to inspect the consignment upon its actual arrival.

If the delivery of goods will pass through the customs authority of transit, NCTS also sends a notification about this to all transit customs authorities so that they can monitor their movement.

Upon arrival of the cargo at the transit customs office, the accompanying transit document must be presented to the relevant customs office. Its electronic original will be automatically retrieved in NCTS by entering the unique registration number, after which transit can proceed. Notification of arrival at the transit customs office will be sent to the customs office of departure.

ISSN: 2181-3337 | SCIENTISTS.UZ

Customs office of destination having received prior notification about the cargo, will have all the information about the completed transit transactions and the ability to decide on the required form of control. After applying the required control measures, the destination customs authority; NCTS NCTS will notify the customs office of departure of the control results.

The activities of the customs authorities of the Republic of Uzbekistan have been introduced the E-Tranzit information system. Its development took into account the experience of developed countries and the specifics of national legislation. The E-Tranzit system consists of the following subsystems:

a subsystem for foreign trade participants, which provides submission of a pre-transit declaration prior to arrival at the customs border of the Republic of Uzbekistan(http://cargo.customs.uz);

a subsystem for customs officers to carry out customs procedures such as customs inspection, transport control, etc.;

subsystem for users of related ministries and agencies authorized to license and certify goods and permit their import into the territory of the Republic.

The transit declaration is submitted by the foreign trade participant to the customs authorities through the E-Tranzit information system. Data is entered in four stages, and the document is generated at the 5th stage.

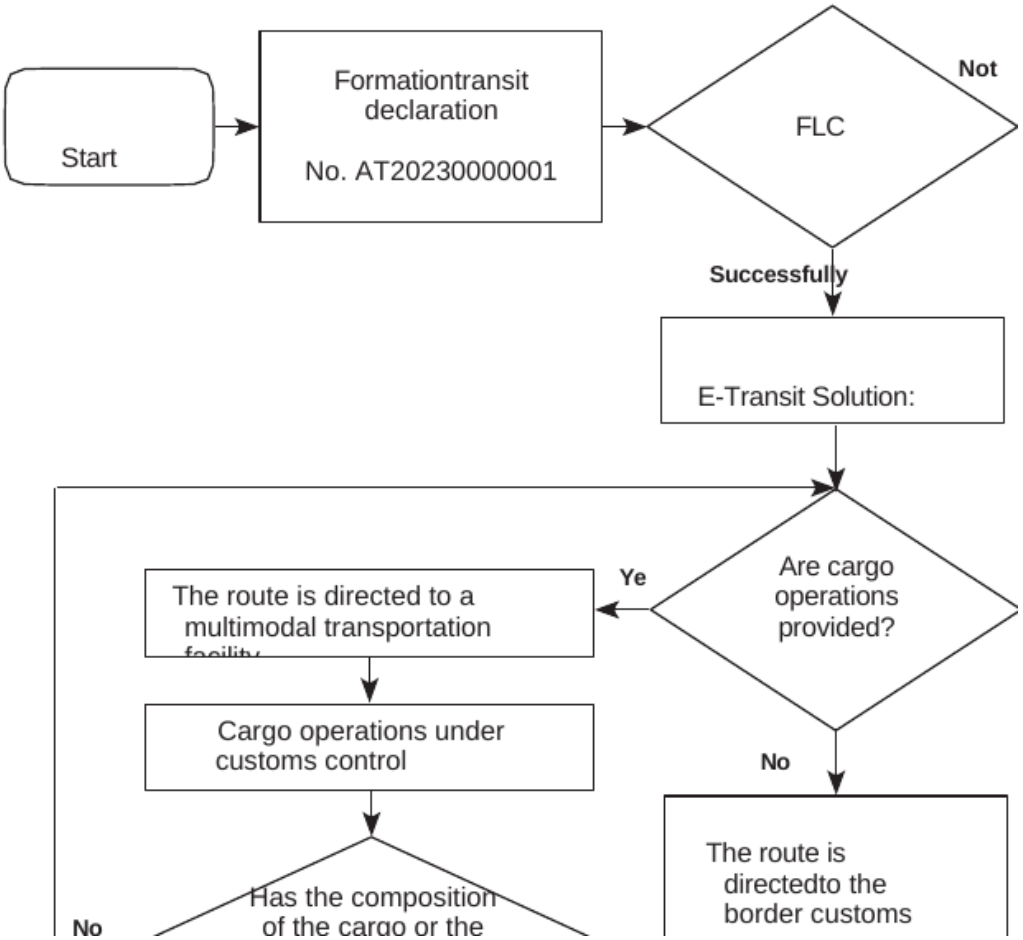
General information:
type of transport;
customs sender;
country where cargo transportation begins;
country where cargo transportation ends.
Transport information:
information about the carrier;
information about transport;
driver data.
Cargo information:
shipping documents for goods;
information about the product;
non-tariff measures to regulate foreign trade.
Warranty and fees:
guarantees;
fees.
Document formation:
in the form of an invoice;
in the form of a transit declaration.

The procedure for submitting a transit declaration by foreign trade participants through the E-Tranzit information system, approved by the decision of the State Customs Committee of the Republic of Uzbekistan and registered by the Ministry of Justice of the Republic of Uzbekistan on August 31, 2022 No. 3382.

ISSN: 2181-3337 | SCIENTISTS.UZ

Figure 2

Flowchart of the Customs Transit Control Algorithm for Multimodal Transport Using the "E-Tranzit" Information System (Author's Design)



One of the features of the E-Tranzit information system is the ability to regulate multimodal transit transportation – control of transit transportation is for consolidated cargo destined for different recipients. The system allows for the registration of cargo operations such as unloading/reloading, change of transport mode, etc., which are carried out under customs control. Flowchart of the customs transit control algorithm for multimodal information transportation.The E-Tranzit system is shown in Fig. 2.

The proposed algorithm is included in the functionality of the E-Tranzit information system as a separate block called

"Cargo Operations." Trial operation of the new version of this system has shown that its new "Cargo Operations" block allows for the management of customs transit in multimodal shipments and creates favorable conditions for participants in foreign trade.

Conclusion

the early version of the "E-Tranzit" information system did not allow for the management of multimodal transport operations and required the submission of a new transit declaration after every cargo-handling operation. Studies on processing times conducted following the implementation of the new version of the "E-Tranzit" system confirm that it helps increase the throughput capacity of customs posts by a factor of 1.5 to 2.

At the same time, operational use of the "E-Tranzit" system highlights the need for further refinement, specifically regarding integration with risk management systems and the targeting of customs transit procedure of integration with the risk management system and the targeting of customs transit.

ISSN: 2181-3337 | SCIENTISTS.UZ

REFERENCES

1. Aldaniyazov, K. (2021). Assessment of Kazakhstan's receipt of observer status of the EU Convention on Common Transit: Report on the results of the study "Trade Facilitation in Central Asia." German Society for International Cooperation. https://www.slideshare.net/KanatAldaniyazov/common-transitrus.pdf
2. Afonin, D. N. (2022). Digital technologies in the product traceability system at customs control: Peculiarities of control for transit in the Russian Federation. In I. R. Begishev, E. A. Gromova, M. V. Zaloilo, I. A. Filipova, & A. A. Shutova (Eds.), Digital technologies and law: Proceedings of the 1st International Scientific and Practical Conference (Vol. 1, pp. 30–34). Poznanie.
3. HM Revenue & Customs. (n.d.). CTC traders API phase 4 service guide. https://developer.service.hmrc.gov.uk/guides/ctc-traders-phase4-service-guide/#api-overview
4. Lozinsky, A. N., & Sazonov, S. L. (2022). New international land–China–ASEAN maritime trade corridor. China in Global and Regional Policy: History and Modernity, 27, 324–338. https://doi.org/10.48647/IFES.2022.88.31.010
5. Mukhtorov, I. M., Dusmukhmedov, A. I., & Saidov, A. A. (2023). Automation of customs transit: From the experience of the European Union to the practice of the Republic of Uzbekistan. Academic Bulletin of the Rostov Branch of the Russian Customs Academy, 2(51), 45–51.
6. Musaeva, S. A. (2025). Customs and security. STAR-SEL LLC.
7. World Customs Organization. (2017). Towards an efficient transit regime: Transit handbook. https://www.wcoomd.org/-/media/wco/public/ru/pdf/topics/facilitation/instruments-and-tools/tools/transit/transit-guidelines-final-ru.pdf?db=web

ISSN: 2181-3337 | SCIENTISTS.UZ VOLUME 5 ISSUE 8 | AUGUST 2026

DETERMINATION OF THE CIRCULATION ZONE WIDTH AT THE JUNCTION OF EARTHEN CANALS

Bobomurodov Furkat[1], Khazratov Alisher[2], Sodikov Jasur[3]
Karshi State Technical University, Karshi, Uzbekistan

DOI: 10.67620/sai.58a0008

ABSTRACT
The junction of open canal flows significantly affects hydraulic conditions, sediment transport, and channel deformation processes. One of the main hydraulic features at canal junctions is the formation of a circulation (vortex) zone near the side bank, which reduces the effective flow cross-section and leads to sediment deposition. This study aims to determine the width and length of the circulation zone formed at the junction of earthen canals. Laboratory and field experiments were conducted, and statistical and regression analyses were applied to establish relationships between flow velocity ratios and cross-sectional parameters. As a result, empirical equations were obtained to predict the width and length of the circulation zone depending on flow conditions and junction angles. Comparison with experimental and existing formula results showed good agreement. The proposed relationships can be used in hydraulic calculations to forecast channel deformation and improve canal design.

ACCEPTED

07.09.26

Keywords: *canal junction, circulation zone, vortex width, open channel flow, sediment transport, hydraulic modeling, regression analysis.*

CC BY

Introduction

The process of flow addition at the junction of the channel joining the main channel negatively affects the operating mode of the channels, leading to changes in the sediment transport process and channel deformations in the channels. Regardless of the scheme of water inflow into the canals from the sides at different angles, the direction of water and sediment movement varies significantly depending on the flow approach conditions.

As a result of the flow addition, as a result of riverbed reformation over time, a specific width, curvature, and depth appear, corresponding to the conditions of the riverbed, and a redistribution of sediments occurs depending on the amount of solid particles flowing in.

The process of transformation of large soil canals, for many reasons, in some cases does not reach equilibrium. These reasons include:

- seasonal and multi-year variability of the flow;
- erosion of the basin surface and accumulation of bottom sediments;
- the occurrence of specific deformation of the flow in the turning zone, etc.

During seasonal changes in the flow rate and the water level in the channels, which change depending on it, the hydraulic parameters of the flow also change and create conditions for channel reformation.

From practice, it is known that in such cases, the reformation of the channel leads to inconveniences for water users. This also leads to a disruption of the natural regime of rivers and canals, as well as a decrease in the water carrying capacity of the riverbed.

The bed of open canals is characterized by the living cross-sectional area and water permeability. When depicted on a plan, this situation takes on a complex appearance. The curvature of the channel bed mainly affects the formation of channel sections under the action of centrifugal forces and secondary flows that affect a number of local processes.

In practice, the disconnection of the flow from the side bank of the canal leads to the formation of vortex fields. This area can be called a vortex zone. Due to the decrease in the velocity of the fluid's translational motion in the vortex zone, sediments accumulate intensively, and the live cross-section of the channel joining the main channel decreases, resulting in coastal deformation. Therefore, determining the dimensions of this vortex zone is one of the important indicators in forecasting channel deformation.

Although a number of researchers have done positive work to find a solution to this problem and have achieved results corresponding to the conditions of their experiments, they have not found a general solution due to the complexity of the problem.

Related hydraulic studies have examined flow separation and redistribution at canal side outlets and junctions (Babazhanov, Babazhanova, et al., 2024; Eshev, Babajanova, et al., 2024), energy losses and vortex behavior in variable-width channels (Babazhanov, Zaripov, et al., 2025; Bobomurodov, Zaripov, et al., 2025), and hydraulic calculations for water-control structures (Eshev, Isakov, et al., 2024; Rakhmatov et al., 2026). Related work on cohesive-soil erosion and soil properties provides additional context for sediment transport and channel deformation (Bobomurodov, Azizov, et al., 2024; Bobomurodov, Khazratov, Dilshodova, et al., 2024; Bobomurodov, Mamatov, et al., 2024; Bobomurodov, Khazratov, Bobomurodov, et al., 2025; Eshev et al., 2022).

Materials and Methods

Experimental studies were conducted in the laboratory "Modeling of Hydraulic Processes" of the Karshi State Technical University to study deformations depending on the size of the vortex field in the channel flow junction zone. For this, we enter the necessary experimental data into Table 1.

We know that there is some kind of relationship between the hydraulic parameters of the flow. We consider that there is a relationship

$$B_b/B_3 = f(v_2/v_3) \quad (1)$$

between the ratios of the flow velocities v_2/v_3 and the ratios of the live-section widths B_b/B_3 that arise during the merging of channel flows. Based on the analysis results, we consider the following proportional relationship for the 2nd connecting channel, located at angles $\theta = 30°$, $\theta = 45°$, and $\theta = 60°$ relative to the main 1st channel:

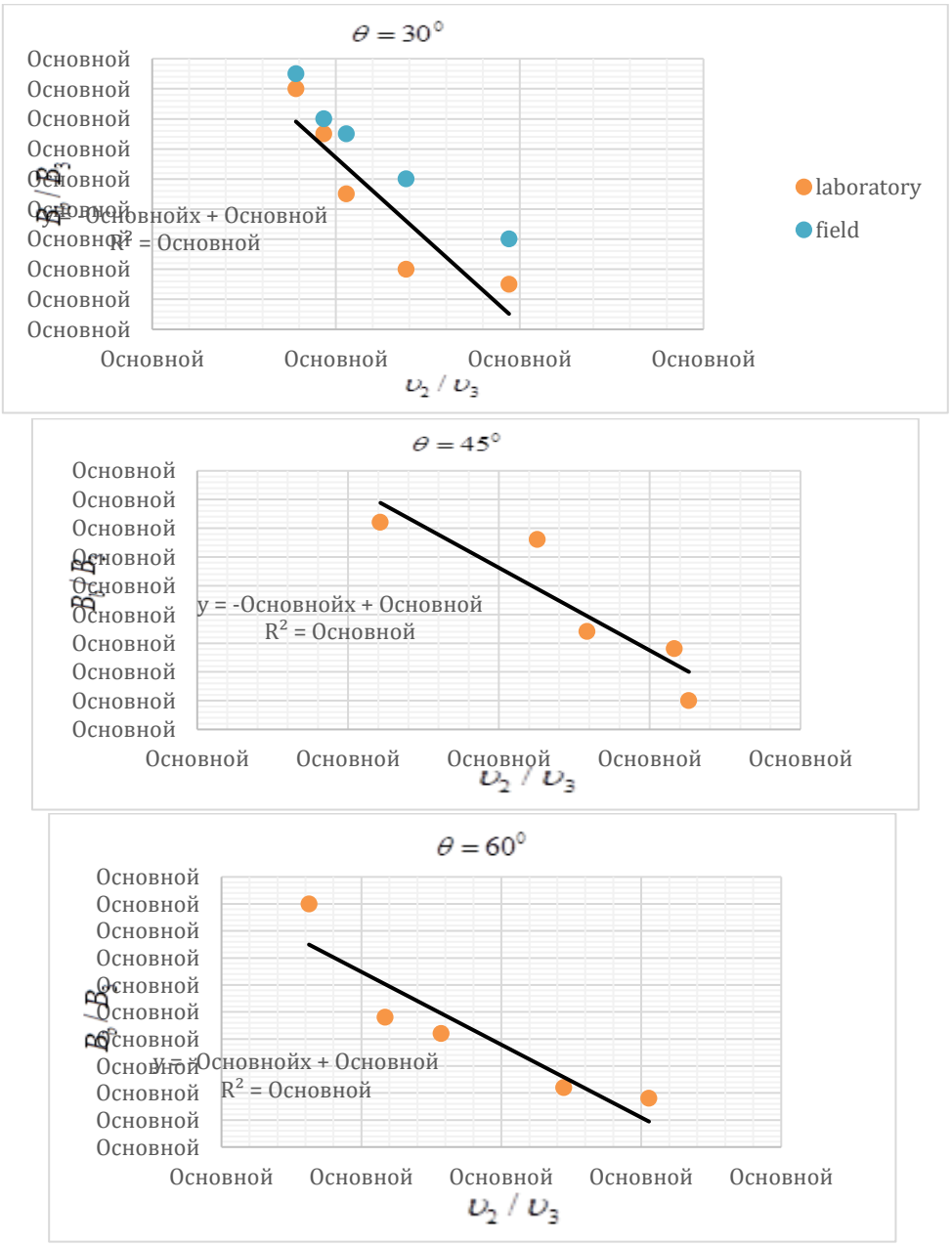
$$B_b/B_3 = \varepsilon(v_2/v_3) \quad (2)$$

As a result of analyzing the data in Table 1 by the method of mathematical statistics, it was established that the values of the proportionality coefficient ε according to the location of the joining 2nd channel relative to the main 1st channel are $\varepsilon = 0.25$, 0.34, and 0.43 for $\theta = 30°$, $\theta = 45°$, and $\theta = 60°$, respectively. Also, based on this view, we will construct a graph of relationship (2) according to the data presented in Table 1 (Figure 1).

ISSN: 2181-3337 | SCIENTISTS.UZ

Figure 1

Relationship Between Width and Velocity Ratios at Junction Angles of 30°, 45°, and 60°



ISSN: 2181-3337 | SCIENTISTS.UZ

Table 1

Laboratory and Field Measurements and Calculated Circulation-Zone Parameters

No. exp.	h_1 (cm)	h_2 (cm)	h_3 (cm)	B_1 (cm)	B_2 (cm)	B_3 (cm)	B_c (cm)	B_b (cm), exp.	B_b (cm), calc.	B_b (cm), Gavr.	L_c (m), exp.	L_c (m), calc.	L_c (m), Gavr.	v_1 (m/s)	v_2 (m/s)	v_3 (m/s)	h_2/h_3	B_v/B_3	v_2/v_3	ε
θ = 30° (laboratory)																				
1	3.7	3.8	4.3	14	18	39	31	8.5	8.8	8.6	18.1	19	19.9	0.75	0.78	0.8	0.98	0.211	0.971	0.216
2	3.9	4.3	4.5	16	20	40	32.2	9.3	9.6	9.5	19	19.4	20.1	0.82	0.85	0.96	1.054	0.212	0.691	0.258
3	4.1	4.5	4.7	19	22	43	34	10	10.3	10.1	17.31	18.2	20.1	1.13	1.11	1.26	1.155	0.217	0.528	0.255
4	4.2	4.7	4.9	21	23	44	34.9	10.1	10.5	10.4	16.99	17.7	18.9	1.29	1.32	1.59	1.157	0.221	0.467	0.268
5	4.6	4.9	5.1	26	24	46	36	11.5	11.8	11.6	15.15	16	16.6	1.52	1.55	1.78	1.258	0.224	0.391	0.274
											17,31									0.284
θ = 30° (field)																				
1	313	323	383	2293	1598	3076	2419	662	690	668	1195	1242	1256	0.75	0.78	0.8	0.949	0.214	0.971	0.22
2	308	324	380	2291	1596	3093	2484	613	632	616	1089	1202	1218	0.74	0.75	0.78	0.951	0.218	0.691	0.21
3	306	322	377	2289	1594	3180	2525	658	691	662	1024	1055	1066	0.83	0.81	0.86	1.056	0.221	0.528	0.209
4	305	321	375	2288	1593	3298	2601	700	716	706	940	968	978	0.82	0.78	0.85	1.059	0.222	0.467	0.235
5	303	319	373	2286	1591	3394	2657	739	754	744	922	944	960	0.91	0.85	0.93	1.153	0.225	0.391	0.252
											1020.6									0.2752
θ = 45° (laboratory)																				
6	4.3	6.6	5.5	13.5	17.9	40	31	9.5	9.8	9.6	17.31	17.6	20.2	0.51	0.55	0.79	1.303	0.23	0.652	0.352
7	4.5	6.8	5.8	15.4	19.2	42	32.2	10.3	10.6	10.5	16.98	18	19.6	0.58	0.59	0.87	1.275	0.239	0.633	0.377
8	4.7	7.1	6	18.1	21.1	44	33.6	11.4	11.6	11.5	17.64	17.9	20.4	0.75	0.84	1.01	1.389	0.242	0.517	0.312
9	4.7	7.4	6.3	19.8	21.7	45	34	12	12.3	12.2	18.92	19.3	21.1	0.81	0.85	1.03	1.38	0.258	0.451	0.325
10	5	7.7	6.5	24.7	23	47	35.5	13	13.3	13.1	20.39	20.7	22.3	0.95	1	1.23	1.493	0.261	0.243	0.347
											16,45									0.362
θ = 60° (laboratory)																				
11	4.1	5.6	6	13	17.7	40	29.3	11.2	11.5	11.4	17.39	18.8	20.4	0.45	0.51	0.77	1.032	0.274	0.611	0.448
12	4.4	5.9	6.3	14.6	18.8	43	31.4	12.1	12.4	12.3	17.48	19	20.8	0.52	0.55	0.82	1.035	0.276	0.489	0.441
13	4.5	6.2	6.5	17.4	20.1	45	32.7	13.3	13.6	13.5	18.85	20.2	21.1	0.65	0.67	0.93	1.152	0.286	0.314	0.444
14	4.6	6.5	6.8	19	20.2	46	33.4	13.6	13.9	13.8	19.92	20.9	22.5	0.68	0.71	0.96	1.154	0.289	0.234	0.426
15	4.8	7	7.1	23.8	22.6	48	34.5	15	15.3	15.1	21.24	21.8	23.7	0.89	0.94	1.16	1.285	0.31	0.125	0.403
											19,17									0.432

Note. exp. = experimental; calc. = calculated; Gavr. = Gavryukhin. The Gavryukhin columns reproduce comparison values carried over from the source manuscript.

ISSN: 2181-3337 | SCIENTISTS.UZ

Using regression analysis, we model the relationship between flow variables, i.e., depth and width, as well as predicted values based on the model.

Results and Discussion

Statistical analysis was carried out within the limits of the obtained data, and as a result, the following equations were obtained (Figure 2):

$$\text{if } \theta = 30°, \quad y = 2.9514x + 1.5144;$$
$$\text{if } \theta = 45°, \quad y = 3.9323x + 1.8037;$$
$$\text{if } \theta = 60°, \quad y = 4.7265x + 2.012. \qquad (3)$$

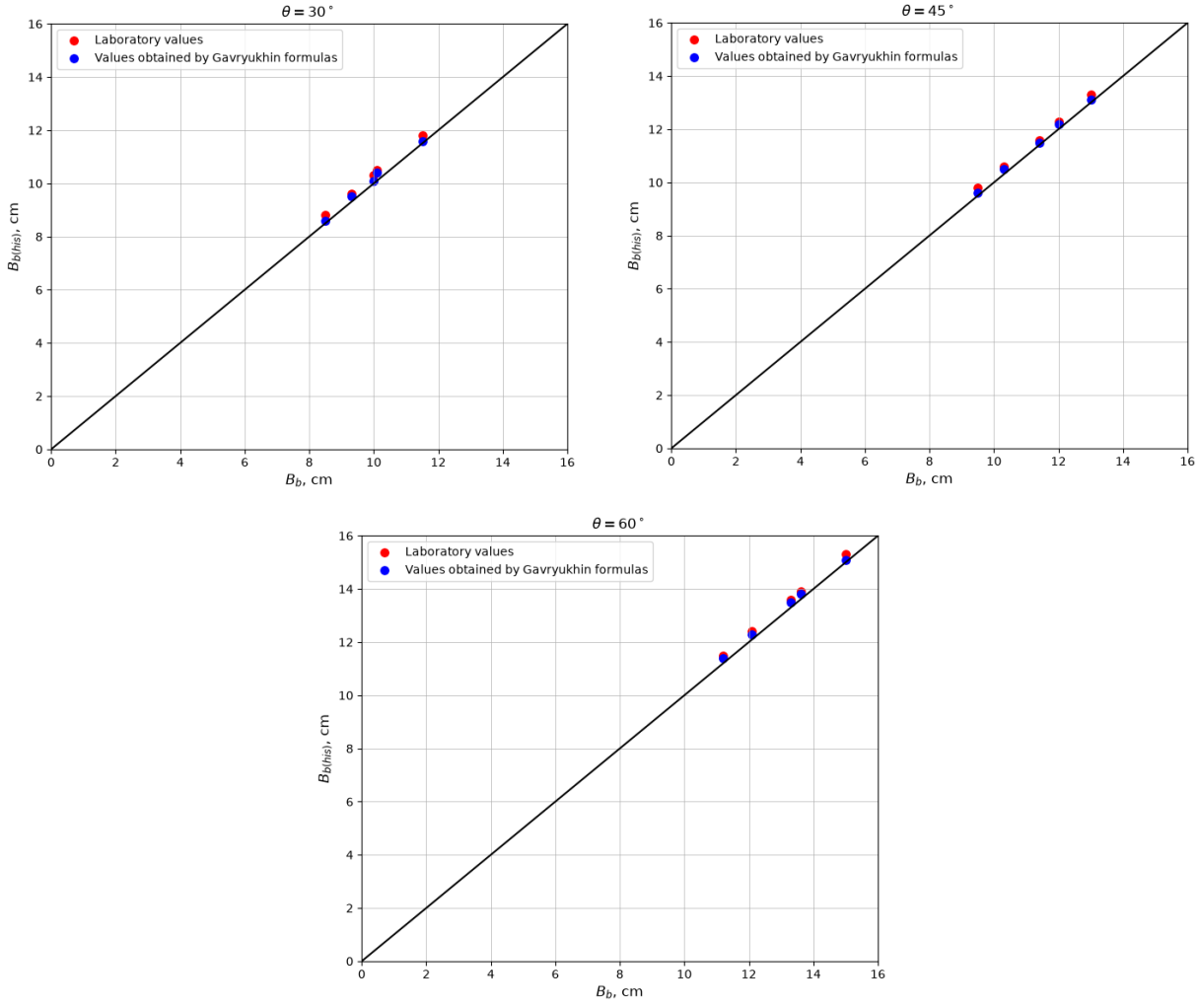
If we introduce the parameters $y = B_b/B_3$, $x = v_2/v_3$, and $\varepsilon = 0.25, 0.34, 0.43$ into these obtained equations (3), then these equations will take the following form, respectively:

$$\text{if } \theta = 30°, \quad B_b = 0.25B_3(2.95v_2/v_3 + 1.51);$$
$$\text{if } \theta = 45°, \quad B_b = 0.34B_3(3.93v_2/v_3 + 1.80);$$
$$\text{if } \theta = 60°, \quad B_b = 0.43B_3(4.73v_2/v_3 + 2.01). \qquad (4)$$

Using equations (4), it is possible to determine the width of the vortex field occurring in the merging zone (main channel 3) for junction angles $\theta = 30°$, $\theta = 45°$, and $\theta = 60°$ of the 2nd merging channel relative to the main channel 1.

Figure 2

Comparison of Calculated Vortex Widths With Laboratory and Gavryukhin Values



Comparison of the calculated values of the vortex width according to the obtained dependence (4) with the data obtained in the field, the values of mathematical modeling, and the values of the Gavryukhin dependence (Table 1) showed their similarity (Figure 2).

ISSN: 2181-3337 | SCIENTISTS.UZ

Now let's consider determining the length of the rotation zone occurring in the flow addition zone. We will analyze the data of the laboratory experiment (Table 1).

From our side, we consider the following relationship between the parameters and velocities of the flow circulation zone, arising in the junction zone in the junction channels. We can express this relationship as follows:

$$B_b/L_c = f(v_2/v_3) \quad (5)$$

Let us construct the graph of this dependence (Figure 4).

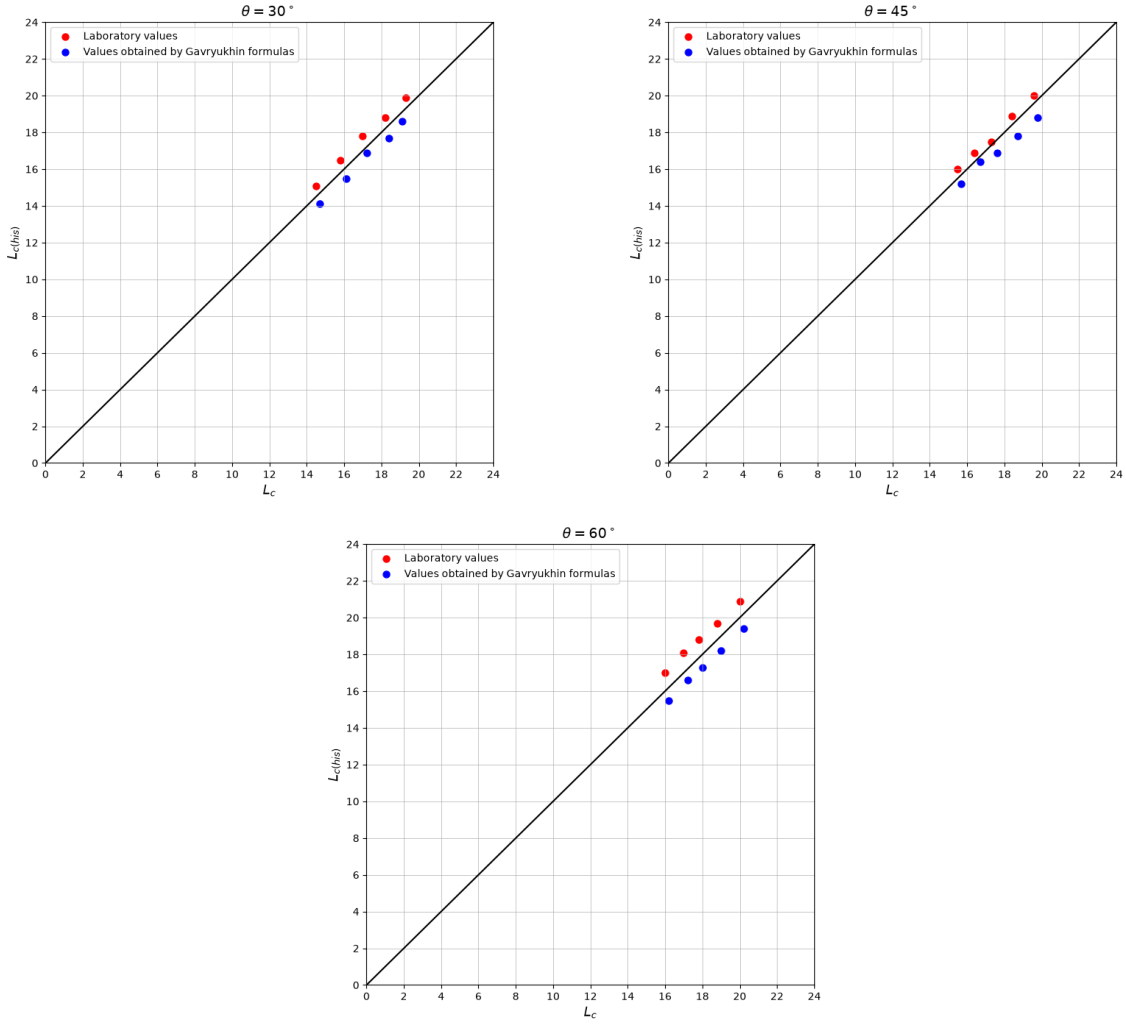
Based on the conducted regression analysis, the following equations for determining the length of the rotation zone were obtained:

$$\begin{aligned} &\text{if } \theta = 30°, \quad L_c = B_3 / (0.27Q_2/Q_3 + 0.25);\\ &\text{if } \theta = 45°, \quad L_c = B_3 / (0.27Q_2/Q_3 + 0.21);\\ &\text{if } \theta = 60°, \quad L_c = B_3 / (0.19Q_2/Q_3 + 0.18). \end{aligned} \quad (6)$$

Comparison of the calculated values of the vortex width according to the obtained dependence (6) with the data obtained in the field, the values of mathematical modeling, and the values of the Gavryukhin dependence (Table 1) showed their similarity (Figure 3).

Figure 3

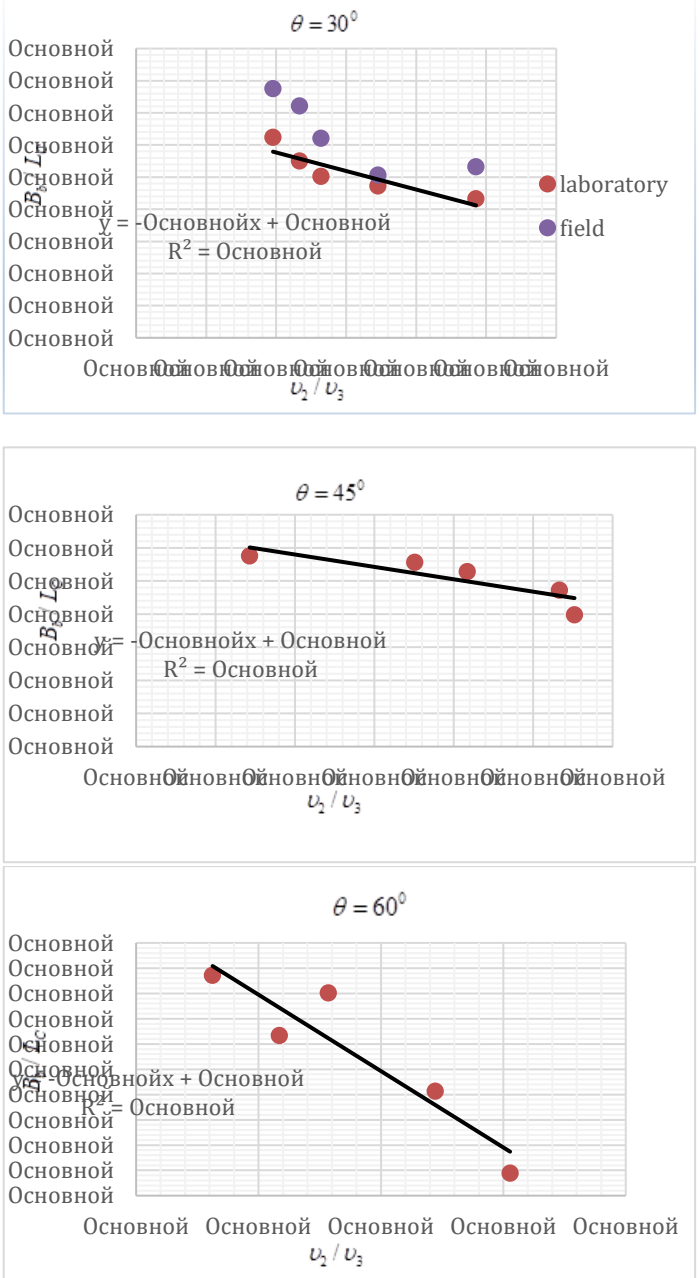
Comparison of Calculated Circulation-Zone Lengths With Laboratory and Gavryukhin Values



ISSN: 2181-3337 | SCIENTISTS.UZ

Figure 4

Relationship Between Circulation-Zone Geometry and the Flow-Velocity Ratio at Junction Angles of 30°, 45°, and 60°



Comparison of the values of the length of the rotation zone, calculated according to this dependence, obtained under laboratory conditions and calculated according to Gavryukhin's formula, shows their similarity.

Conclusions

Flow junctions in earthen canals lead to the formation of a circulation zone that affects sediment transport and channel deformation.

- The width and length of the vortex zone depend on flow velocity ratios and junction geometry.
- Empirical equations were derived using regression analysis based on laboratory and field data.
- The calculated values showed good agreement with experimental results and existing formulas.
- The proposed relationships can be applied in hydraulic design and deformation forecasting of canal junctions.

Consequently, the dependence of the parameters of the circulation zone, i.e., the width and length, on the flow velocity at the junction of open channel flows is important for assessing the hydraulic

ISSN: 2181-3337 | SCIENTISTS.UZ

parameters and deformation properties of the transformed flow. Therefore, when calculating the parameters of the rotation zone occurring in the junction zone of the hydraulics of open channels, dependencies (4) and (6) can be used.

REFERENCES

1. Babazhanov, Y. T., Babazhanova, I. Y., Zaripov, M. B., & Hazratov, A. R. (2024). The problem of fluid flow from a channel with a side outlet. *Journal of Adaptive Learning Technologies, 1*(5), 18–25.
2. Babazhanov, Y. T., Zaripov, M. B., Bobomurodov, F. F., & Dilshodova, D. D. (2025). Flow of liquid in a suddenly expanding channel. *Problems of Architecture and Construction*, (2), 229–230.
3. Bobomurodov, F. F., Azizov, S. A., Khazratov, A. R., & Tuychiyev, J. S. (2024). Calculation of total channel erosion in cohesive soils. *American Journal of Education and Learning, 2*(5), 965–975.
4. Bobomurodov, F. F., Khazratov, A. R., Bobomurodov, F. F., & Jabborova, S. Z. (2025). Analysis of the bonding strength of cohesive soils in stream scour. *American Journal of Education and Learning, 3*(5), 812–820. https://doi.org/10.5281/zenodo.15531371
5. Bobomurodov, F. F., Khazratov, A. R., Dilshodova, D. D., Kulmatov, S. K., & Sattorov, I. O. (2024, May 3). *Evaluating the influence of irrigated soil physical properties on its settling process*. Intellekt. https://dspace.kstu.uz/xmlui/handle/123456789/4334
6. Bobomurodov, F. F., Mamatov, N. Z., Hazratov, A. R., & Xo‘jayorov, S. A. (2024). Bog‘langan gruntli kanallarda umumiy yuvilishni hisoblash [Calculation of total scour in cohesive-soil canals]. *Innovatsion texnologiyalar, 56*(4), 48–54.
7. Bobomurodov, F. F., Zaripov, M. B., Khazratov, A. R., & Kuvvatov, J. Z. (2025). Assessment of energy losses in narrowing channels under conditions of unsteady flow. *Universum: Technical Sciences*, 10(139), 5–10. https://doi.org/10.32743/UniTech.2025.139.10.21018
8. Eshev, S. S., Babajanova, I., Yuldosheva, U., Imomova, M., Khazratov, A., & Eshev, A. (2024). Features of flow parameters in the separation zone of concrete-lined canals. In *Proceedings of the 6th International Conference on Construction Mechanics, Hydraulics and Water Resources Engineering Autumn Season (CONMECHYDRO 2024)* (Vol. 1, pp. 337–343). SciTePress. https://doi.org/10.5220/0013563300004644
9. Eshev, S. S., Bobomurodov, F. F., Isakov, A. N., & Mamatov, N. Z. (2022). Evaluating the effect of cohesive strength on self-leaching in bonded soils. *International Journal of Advanced Research in Science, Engineering and Technology, 9*(8), 19636–19641.
10. Eshev, S. S., Isakov, A. N., Safarov, A. A., & Yuldosheva, U. T. (2024). Calculation of local water behind the lower water mountings. *International Journal of Advanced Research in Science, Engineering and Technology, 11*(2), 21419–21425.
11. Rakhmatov, M., Bobomurodov, F., Khazratov, A., & Payanova, I. (2026). Improving the hydraulic calculation method for water discharge structures. *Innovative Technologies*, 83–90. https://doi.org/10.70769/2181-4732.ITJ.2026-m.10

ISSN: 2181-3337 | SCIENTISTS.UZ VOLUME 5 ISSUE 8 | AUGUST 2026

IMPLEMENTATION OF PARETO ANALYSIS, ABC CUSTOMER CLASSIFICATION, AND CVP MODELLING AT AN INDUSTRIAL MANUFACTURING ENTERPRISE

Musaeva Shoira
Professor at the Samarkand Institute of Economics and Service
Email: musaeva_shoira@mail.ru

DOI: 10.67620/sai.58a0009

ABSTRACT

This study applies Pareto analysis, ABC customer classification, and cost-volume-profit (CVP) modelling to budgeting and financial decision-making at Saturn Metal LLC. Company records for 2023–2025 are used to examine customer concentration, changes in the relative contribution of major customers, and the relationship among revenue, variable costs, fixed costs, and break-even performance. The Pareto and ABC results show that a limited number of customers account for a substantial share of customer-register revenue, while the composition of the highest-contributing group changes markedly across the three years. The analysis therefore draws attention to customer retention, the development of medium-contribution customers, and exposure to individual major buyers. The CVP analysis identifies the break-even level and the margin of safety. The reported figures show a comparatively strong margin of safety in 2024 and a negative margin in 2025, when revenue fell below the break-even point. Taken together, the two analytical approaches provide a practical basis for budgeting, revenue planning, cost control, and risk assessment. Their combined use can support more disciplined managerial decisions while keeping customer concentration and operating risk visible within the budgeting process.

ACCEPTED

07.09.26

Keywords: *enterprise efficiency, ABC customer classification, Pareto analysis, CVP modelling, budgeting, break-even analysis.*

CC BY

Introduction

Effective budgeting and financial control are increasingly important for manufacturing enterprises in Uzbekistan as national development priorities emphasise higher-value production, digitalisation, resource efficiency, and competitiveness. These changes increase the need for financial planning systems that can respond to shifts in sales structure and cost behaviour. For manufacturing firms, budgeting therefore needs to connect customer-related revenue patterns with cost and profitability information so that resources can be allocated more rationally and operating risks identified earlier (Mirziyoyev, 2020, 2021).

Literature review. Budgeting and management accounting are well established in the international and domestic literature. Drury (2016) and Vakhrushina (2014) address core management-accounting concepts, while Uzbek authors discuss management accounting, budgeting, financial planning, and control (Abdusalomova, 2022; Hasanov et al., 2021; Hasanov & Hoshimov, 2011; Tashnazarov et al., 2022; Urazov, 2013).

Musaeva (2022, 2024) also considers marketing communication and research relevant to customer-related managerial decisions. Taken together, the cited works provide the conceptual background for examining customer contribution and cost behaviour. The present study narrows this discussion to the practical application of Pareto analysis, ABC customer classification, and CVP modelling in one manufacturing enterprise.

Research methodology. The study uses a quantitative case-study design based on Saturn Metal LLC records and financial indicators for 2023–2025. Customer-revenue registers are analysed with Pareto analysis and ABC customer classification to examine concentration and year-to-year changes in customer contribution. The financial indicators reported in Table 6 are analysed through cost-volume-profit (CVP) modelling to assess the relationship among revenue, variable costs, fixed costs, contribution margin, the break-even point, and the margin of safety. The two analytical blocks are interpreted separately and then considered together as inputs to budgeting and managerial decision-making.

Results and discussion. For the present case, Pareto analysis is used to examine how customer revenue is concentrated across the customer base and how that concentration changes over time.

Saturn Metal LLC conducts transactions with a large number of customers whose contributions to revenue vary considerably. This makes cash-flow management and revenue budgeting less predictable, particularly when the composition of the following year's customer base changes. Identifying the customers with the greatest effect on sales and revenue therefore helps focus managerial attention on economically important relationships and provides a clearer basis for revenue planning.

Customer classification also supports the review of the customer portfolio, accounts receivable, and financial-planning priorities by distinguishing customers according to their relative economic importance.

In this paper, ABC customer classification is used alongside Pareto analysis to group customers according to their relative contribution to revenue. The term ABC is used here as a customer-segmentation classification rather than as a reference to activity-based costing or activity-based budgeting.

For the present analysis, the groups are interpreted as follows:

Group A contains the largest and most important customers. Together, they typically account for approximately 60–80% of revenue, although the group contains relatively few customers.

Group B contains customers of intermediate importance. Their individual contribution is lower than that of Group A customers, but the group remains significant to the overall revenue structure.

Group C contains customers with small individual shares. Their combined contribution may nevertheless remain material when the group is considered as a whole.

The following analysis applies Pareto analysis and ABC customer classification to Saturn Metal LLC's customer-revenue registers for 2023–2025.

Table 1.

Pareto Analysis of Top Clients for 2023

No.	Top Clients	Sum	Share	Group
1	MIRANKUL CONSTRUCTION MATERIALS LTD	1,200,000,000.00	7.9%	A
2	Shashlik Uz	1,196,703,250.00	7.9%	A
3	JAVOHIR BAKERY SHOP	1,000,000,002.16	6.6%	A
4	ENTER ENGINEERING	860,530,000.00	5.6%	A
5	WOODLANDS	857,360,000.00	5.6%	A
6	SHOXRUXJON SERVICE	798,387,000.00	5.2%	A
7	INNOCRAFT	732,760,000.00	4.8%	A
8	MIXT ROYAL PALACE MCHJ	600,000,000.00	3.9%	A
9	Stainless Steel Samarkand	516,935,001.62	3.4%	A
10	SABRINA VISOL SERVICE	429,650,000.02	2.8%	A
11	XUDOYORXON SHAMS XK	400,000,000.00	2.6%	A

ISSN: 2181-3337 | SCIENTISTS.UZ

12	GRAND SAMARKAND SUPERIOR	311,860,000.00	2.0%	A
13	ENTER ENGINEERING PTE.LTD	302,980,000.00	2.0%	B
14	GASHSAN-LAZIZ	300,000,000.00	2.0%	B
15	TA`MINOT SERVIS BUXORO	299,635,000.00	2.0%	B
16	SHAXZOD PLAZA	284,760,000.00	1.9%	B
17	ENTER ENGINEERING PTE. LTD.	249,190,000.00	1.6%	B
18	MIRONKUL GROUP TOWER	238,400,000.00	1.6%	B
19	GENESIS EDUCATION	211,000,000.00	1.4%	B
20	NAVOBOD NASLLI PARRANDA	183,000,000.00	1.2%	B
21	MCHJ INNOCRAFT	160,703,357.95	1.1%	B
22	SAMARQAND MINTAQAVIY YO`LLARGA BUYURTMACHI XIZMATI	157,000,000.00	1.0%	B
23	MCHJ TOSH-ARIQ QURILISH SERVICE	150,000,000.00	1.0%	B
24	AFROSIYAB CHOYHONASI	150,000,000.00	1.0%	B
25	YAPP UBK AUTO SYSTEM	120,000,000.00	0.8%	B
26	BUNYOD CAPITAL INVEST SERVICE	112,970,000.00	0.7%	B
27	BOYOVUT TECHNO CLUSTER	112,130,000.00	0.7%	B
28	MCHJ 7-SONLI MEXANIZASIYALASHGAN KO`CHMA KOLONNA	112,000,000.00	0.7%	B
29	SPB Parliament	110,160,000.00	0.7%	B
30	PULSAR GROUP BREWERY	108,468,000.00	0.7%	B
	Other:	2,967,710,555.07	19%	C
	Result:	15,234,292,166.82	100%	

For this case study, the reported classification combines the classic 80/20 principle with a modified 60/40 grouping. Table 1 shows that, in 2023, the 12 largest customers accounted for approximately 60% of Saturn Metal LLC's customer-register revenue and were classified as Group A. Group B, shown in yellow, comprised 18 customers and accounted for more than 22% of the reported total. Group C comprised the remaining customers, each with a share below 0.6%. There were 76 such customers in 2023, and their combined contribution was 19%, so the group remained material in aggregate.

The 2023 classification identifies the customer relationships that warrant the closest managerial attention within the reported revenue structure.

Extending the Pareto–ABC analysis across several years reveals changes in the customer-revenue structure. It shows which customers remain in Group A, which lose relative importance and move to Groups B or C, and which move from lower-contribution groups into the highest-contributing category.

The same procedure was applied to the reported data for 2024 and 2025:

Table 2.

Pareto Analysis of Top Clients for 2024

No.	Top Clients	Sum	Share	Group
1	QORAKO`L STROY GROUP	1,500,007,872.00	16.8%	A
2	SAMARQAND XOLIS FAYZ SAVDO	1,500,000,000.00	16.8%	A
3	INTERACTIV PLANET	800,000,000.00	9.0%	A
4	HENGYUAN CEMENT	429,122,000.00	4.8%	A
5	DILKASH-SHIRIN-TAOM	353,300,000.00	4.0%	A
6	REIKARTZ U	335,050,500.00	3.8%	A
7	MEBEL-D	325,301,040.00	3.6%	A
8	SCHELKOVO AGROHIM-O`ZBEKISTON	314,526,000.00	3.5%	B
9	AZAM JAMSHID TAOMLARI MCHJ	300,000,000.00	3.4%	B
10	SOLOMON	288,205,000.00	3.2%	B
11	Shashlik Uz	228,333,333.00	2.6%	B

ISSN: 2181-3337 | SCIENTISTS.UZ

12	SILK ROAD K OILAVIY KORXONA	200,000,000.00	2.2%	B
13	HAVAND-BEGZAD-KUNGRAD	185,000,000.00	2.1%	B
14	SUNNY VILLAGE	175,800,000.00	2.0%	B
15	NARPAYTEX	125,664,000.00	1.4%	B
16	Stainless Steel Samarkand	111,916,400.22	1.3%	B
17	SAMARKAND TOURISTIC CENTER MCHJ	109,539,997.94	1.2%	B
18	ZAMIN-TRAVEL	104,880,000.00	1.2%	B
19	MARKAZIY BANK SAMARQAND VILOYAT BOSH BOSHQARMASI	99,770,006.00	1.1%	B
20	NARZIKULOV DJURABEK MEBELLARI	70,000,000.00	0.8%	B
21	SHAXZOD PLAZA	60,000,000.00	0.7%	B
22	CHET EL KAPITALI ISHTIROKIDAGI "HAMKORBANK	53,500,000.00	0.6%	B
23	OQDARYO PLANKTON	53,000,000.00	0.6%	B
24	GO`SHT-SIFAT	52,362,000.00	0.6%	B
25	GENESIS EDUCATION	50,000,000.00	0.6%	B
26	FIBREGLASS	42,450,000.00	0.5%	B
27	SAM DILFIN	42,000,000.00	0.5%	B
28	SAMARKAND DIYORA LUX	40,000,000.04	0.4%	B
29	SAM VERO GROUP 999	40,000,000.00	0.4%	B
30	PURI AUTHENTIC GEORGIA BAKERY	35,900,000.00	0.4%	B
	Other:	908,309,109.01	10.2%	C
	Result:	8,933,937,258.21	100%	

The composition of Group A changed substantially from year to year, indicating considerable turnover among the highest-contributing customers (see Table 2).

In 2024, the top-customer group differed markedly from that reported for 2023. Mirankul Construction Materials, Shashlik Uz, and Javohir Bakery Shop held the leading positions in 2023, whereas Qorakol Stroy Group, Samarqand Xolis Fayz Savdo, and Interactiv Planet occupied the leading positions in 2024. Only a small number of customers recorded in 2023 also made purchases in 2024. These recurring customers are presented in Table 3.

Table 3.

Comparative analysis of the company's top clients and changes in their ABC groups in 2023–2024

		2023	2024	2023	2024	2023	→	2024
No.	Top Clients	Sum	Sum	Share	Share	Group		Group
1	Shashlik Uz	1 196 703 250	228 333 333	7.9%	2.6%	A		B
2	Stainless Steel Samarkand	516 935 002	111 916 400	3.4%	1.3%	A		B
3	SHAXZOD PLAZA	284,760,000	60,000,000	1.9%	0.7%	B		B
4	GENESIS EDUCATION	211,000,000	50,000,000	1.4%	0.6%	B		B
5	SAM VERO GROUP 999	29,250,000	40,000,000	0.2%	0.4%	C		B
6	ENTER ENGINEERING	860,530,000	34,000,000	5.6%	0.4%	A		C
7	DAKA-INTEX	21,000,000	17,882,000	0.1%	0.2%	C		C
8	MIRANKUL FOODS	48,825,000	17,175,000	0.3%	0.2%	C		C
9	CENTRAL ASIAN STAR	13,700,000	8,000,000	0.1%	0.1%	C		C

Table 3 identifies recurring customers and shows how their relative importance changed between 2023 and 2024. Shashlik Uz and Stainless Steel Samarkand moved from Group A to Group B. Their reported purchase values also declined, while larger customers appeared in the 2024 ranking. Enter Engineering, another major customer in 2023, recorded a substantial reduction in purchases and moved from Group A to Group C in 2024.

ISSN: 2181-3337 | SCIENTISTS.UZ

Shaxzod Plaza and Genesis Education remained in Group B, while Daka-Intex, Mirankul Foods, and Central Asian Star remained in Group C with relatively small contributions to sales. Sam Vero Group 999 was the only recurring customer shown in Table 3 to move upward, from Group C to Group B.

Table 4.

Pareto Analysis of Top Clients for 2025

No.	Top Clients	Sum	Share	Group
1	SADRIDDIN	1,848,350,000.00	31%	A
2	NAVOBOD NASLLI PARRANDA	300,000,000.00	5%	A
3	STDHEALTHMED	278,990,000.00	5%	A
4	SANEG MART	264,000,000.00	4%	A
5	SAKINA RAXMON XAYOT	247,715,000.00	4%	A
6	RADIUS SERVICE	247,715,000.00	4%	A
7	SAMYAK	185,000,000.00	3%	A
8	REGISTON PLAZA	181,609,000.00	3%	A
9	SUNNY VILLAGE	169,810,000.00	3%	B
10	ZAMIN-TRAVEL	151,003,000.00	3%	B
11	ALEXANDER HOTEL	132,000,000.00	2%	B
12	NURSHOD OSHXONASI	125,500,000.00	2%	B
13	DIDI GROUP FOODS	125,000,000.00	2%	B
14	TOLIB BOBO AKT	108,790,000.00	2%	B
15	MAXSUS SUV QURILISH INVEST	105,397,300.00	2%	B
16	SAM-FERRE	102,250,580.00	2%	B
17	MALAXIT PLUS	100,000,000.00	2%	B
18	JIZZAX KELAJAK MAKTABI	98,560,000.00	2%	B
19	Stainless Steel Samarkand	96,934,000.00	2%	B
20	DILKASH-SHIRIN-TAOM	82,000,000.00	1%	B
21	NET PRODUKT LUX	80,700,000.00	1%	B
22	OHANGARON RISING SCHOOL	60,000,000.00	1%	B
23	HMC U	51,025,000.00	1%	B
24	XATAMOVA FAYYOZA UKTAM QIZI	50,000,000.00	1%	B
25	YAKUBOVICH PRODUCTS	47,120,000.00	1%	B
26	OLIY SIFAT PROM STROY	47,000,000.00	1%	B
27	MO'MINJON MA'RUFJON	39,000,000.00	1%	B
28	SHAMPOOR	33,075,000.00	1%	B
29	QADIROV MAMUR KARIMOVICH	33,000,000.00	1%	B
30	YUSUPOV TEHRON AZIZJON O'G'LI	33,000,000.00	1%	B
	Other:	576,443,920.00	9.6%	C
	Result:	6,000,987,800.00	100%	

The 2025 analysis again shows substantial turnover among the highest-contributing customers. Sadriddin became the largest customer and accounted for 31% of the reported total. This represents a pronounced concentration in a single customer, while the remaining customers recorded substantially smaller individual shares and purchase values.

ISSN: 2181-3337 | SCIENTISTS.UZ

Table 5.

Comparative analysis of the company's top clients and changes in their ABC groups in 2024–2025

		2024	2025	2024	2025	2024	→	2025
No.	Top Clients	Sum	Sum	Share	Share	Group		Group
1	SUNNY VILLAGE	175,800,000	169,810,000	2.0%	2.8%	B		B
2	ZAMIN-TRAVEL	104,880,000	151,003,000	1.2%	2.5%	B		B
3	Stainless Steel Samarkand	111 916 400	96,934,000	1.3%	1.6%	B		B
4	DILKASH-SHIRIN-TAOM	353,300,000	82,000,000	4.0%	1.4%	A		B
5	EL-AZIZ	20,000,000	28,238,000	0.2%	0.5%	C		C
6	SOLOMON	288,205,000	26,000,000	3.2%	0.4%	B		C
7	ISTIQBOLLI TA'LIM	28,800,000	19,200,000	0.3%	0.3%	C		C
8	SAMARKAND QUALITY PRINT	2,050,000	6,050,000	0.0%	0.1%	C		C
9	ZILOL BAXT	28,775,600	5,520,000	0.3%	0.1%	C		C
10	SAMARKAND TOURIST CENTER	109,539,998	4,800,000	1.2%	0.1%	B		C
11	MUMIN OTA 1954	10,650,000	3,048,000	0.1%	0.1%	C		C

Of the 143 customers that made purchases in 2024, only 11 made repeat purchases in 2025. Most of these recurring customers remained in their previous ABC categories, although several moved between groups (see Table 5).

Dilkash-Shirin-Taom moved from Group A in 2024 to Group B in 2025. Solomon and Samarkand Tourist Center moved from Group B to Group C, reflecting substantial declines in their relative contributions.

These findings show how ABC customer classification can support budgeting by identifying the customers that contribute most to recorded revenue and by tracking changes in their relative importance. The results can therefore inform account review, customer-concentration monitoring, and the revenue assumptions used in budgeting.

From a managerial perspective, Group A customers warrant close monitoring because they account for the largest share of customer-register revenue. Retention initiatives may be considered for major one-off buyers, while Group B customers can be reviewed for opportunities to deepen commercial relationships. These are managerial implications of the observed customer structure rather than effects tested directly in the present study.

CVP modelling

Cost-volume-profit (CVP) modelling relates revenue, variable costs, fixed costs, and profit and is used to identify the break-even point (Drury, 2016). In budgeting, the model provides a structured basis for assessing the revenue required to cover costs and for evaluating the margin of safety.

Within the CVP framework, revenue first covers variable costs. The remainder is the contribution margin, which is available to cover fixed costs; profit is generated once total contribution exceeds fixed costs.

The model is first expressed in unit terms through the break-even condition:

$$P \times Q - VC_{unit} \times Q - FC = 0$$

where P is the unit selling price,

Q is the quantity of products sold,

VC_{unit}– variable cost per unit of output,

FC represents fixed costs.

Rearranging in terms of the contribution margin gives:

$$Q \times (P - VC_{unit}) - FC = 0$$

The break-even point in units can therefore be expressed as:

$$Q_{bep} = \frac{FC}{P - VC_{unit}}$$

ISSN: 2181-3337 | SCIENTISTS.UZ

The model can then be expressed in monetary terms:

$$CMR = ((P - VC_{unit}) / P) = ((Revenue - VC_{total}) / Revenue)$$

$$S_{BEP} = FC / CMR$$

Here, CMR is the contribution margin ratio; the second line gives the break-even sales value in monetary terms.

The financial indicators reported by Saturn Metal LLC for 2023–2025 are used to calculate the critical CVP values shown in Table 6. These figures provide the basis for assessing the company's position relative to the break-even point in each year.

Table 6.

Calculation of the Break-Even Point and Margin of Safety of Saturn Metal LLC for 2023–2025

Indicator	2023	2024	2025
1. Revenue (S), thousand soums	**7,255,707.00**	**13,613,929.00**	**7,971,075.00**
2. Variable costs (VC), thousand soums	**6,423,656.00**	**12,463,398.00**	**7,196,327.00**
3. Fixed costs (FC), thousand soums	**750,206.00**	**913,223.00**	**786,643.00**
4. Contribution margin (CM), thousand soums	**832,051.00**	**1,150,531.00**	**774,748.00**
5. Contribution margin ratio (CMR)	**11.47%**	**8.45%**	**9.72%**
6. Break-even point, thousand soums	**6,541,996.74**	**10,805,926.21**	**8,093,457.94**
7. Margin of safety (MOS), %	**10.91%**	**25.99%**	**-1.51%**

In 2024, the break-even point increased sharply from 6,541,996.74 to 10,805,926.21 thousand soums. This change was associated with fixed costs of 913,223 thousand soums and a contribution margin ratio of 8.45%. Nevertheless, reported revenue in 2024 remained above the break-even point, producing a margin of safety of 25.99%.

Saturn Metal LLC operated above the break-even point in 2023 and 2024. In 2025, however, the margin of safety became negative (-1.51%), indicating that reported revenue fell below the break-even point by approximately 122,382.94 thousand soums (122,382,940 soums).

The CVP analysis shows how the reported revenue position changed in relation to the break-even threshold across the three years. The negative margin of safety in 2025 makes the break-even relationship particularly relevant to budgeting. CVP modelling can therefore support income and expenditure, cost-optimisation, and sales budgets by making the required operating threshold explicit.

Conclusion

Pareto analysis, ABC customer classification, and CVP modelling provide complementary views of Saturn Metal LLC's budgeting position. The customer analysis shows pronounced year-to-year changes among the highest-contributing accounts and continued concentration of recorded revenue in a relatively limited number of customers. The CVP results show that the company's position relative to break-even also changed across the period, with the margin of safety becoming negative in 2025. Considered together, these findings support closer monitoring of customer concentration, customer continuity, cost behaviour, and break-even performance when budgets are prepared.

The study is limited to one enterprise and to the three-year period covered by the supplied records. The findings should therefore be interpreted as case-specific and should not be generalised beyond the analysed company without additional evidence.

ISSN: 2181-3337 | SCIENTISTS.UZ

REFERENCES

1. Abdusalomova, N. B. (2022). *Boshqaruv hisobiga kirish* [Introduction to management accounting]. Tashkent State University of Economics.
2. Drury, C. (2016). *Upravlencheskiy i proizvodstvennyy uchet: Vvodnyy kurs* [Management and production accounting: An introductory course]. UNITY-DANA.
3. Hasanov, B. A., Hashimov, A. A., Muhametov, A. B., & Abduvohidov, A. A. (2021). *Buxgalteriya hisobi* [Accounting]. Iqtisodiyot Dunyosi.
4. Hasanov, B. A., & Hoshimov, A. A. (2011). *Boshqaruv hisobi* [Management accounting]. Sharq.
5. Mirziyoyev, S. M. (2020). *Milliy tiklanishdan - milliy yuksalish sari* [From national revival to national progress] (Vol. 4). O‘zbekiston NMIU.
6. Mirziyoyev, S. M. (2021). *Yangi O‘zbekiston strategiyasi* [Strategy of New Uzbekistan]. O‘zbekiston.
7. Musaeva, S. A. (2022). *Integrated marketing communications*. Mahorat.
8. Musaeva, S. A. (2024). *Marketing research*. STAR-SEL.
9. Tashnazarov, S. N., Urazov, K. B., & Toshnazarova, D. S. (2022). *Boshqaruv hisobi: Oliy o‘quv yurtlari ta’lim yo‘nalishlari uchun darslik* [Management accounting: Textbook for higher education programmes]. Samarkand Institute of Economics and Service.
10. Urazov, K. B. (2013). *Buxgalteriya moliyaviy hisobi* [Financial accounting]. Samarkand Institute of Economics and Service.
11. Vakhrushina, M. A. (2014). *Upravlencheskiy uchet-1* [Management accounting-1]. Institute of Professional Accountants and Auditors of Russia. https://www.ipbr.org/developments/methodical-collection/2014/3767-upravlencheskij-uchet-1/

ISSN: 2181-3337 | SCIENTISTS.UZ VOLUME 5 ISSUE 8 | AUGUST 2026

NUMERICAL EVALUATION OF GROUNDWATER-LEVEL EFFECTS ON THE SEISMIC RESPONSE OF A MULTISTORY BUILDING–SOIL SYSTEM USING PLAXIS 3D

Yuldashev Sharafitdin[1], Boytemirov Muxamadbobir[2], Abdunazarov Akbarjon[3], Yuldashev Faxriddin[4], Vahobov Boburkhon[5]

Doctor of Technical Sciences, Professor[1]
PhD in Technical Sciences, Associate Professor[2]
PhD Student[3]
PhD in Technical Sciences[4]
PhD in Technical Sciences[5]

DOI: 10.67620/sai.58a0010

ABSTRACT

Groundwater conditions can alter the effective stress state and mass characteristics of foundation soils and thereby influence seismic soil–structure interaction. This study evaluated the effect of groundwater level (GWL) on the seismic response of a multistory building–soil system using three-dimensional finite-element modeling in PLAXIS 3D. The computational domain comprised three soil layers extending from the ground surface to a depth of 50 m and represented by the Mohr–Coulomb constitutive model under drained conditions. Two controlled models were analyzed with GWLs of −50 m and −3 m. Geometry, material properties, the building model, finite-element mesh, monitoring locations, and the same 0–10 s real earthquake accelerogram were held constant so that groundwater level was the only intentionally varied condition. Horizontal displacement, velocity, and acceleration time histories were compared at a soil monitoring node and at the first and ninth floors. The maximum downward vertical displacement was −48.37 mm and was concentrated within the foundation influence zone. At the soil node, several velocity and acceleration peaks were larger for GWL = −3 m, whereas horizontal displacement histories were nearly coincident. First-floor responses were similar between cases, while ninth-floor acceleration exceeded first-floor acceleration. The findings indicate that groundwater level should be treated as an independent variable in seismic soil–structure interaction analyses and that acceleration and velocity may be more sensitive to groundwater changes than displacement under the modeled conditions.

ACCEPTED

07.09.26

Keywords: *groundwater level, seismic response, soil–structure interaction, PLAXIS 3D, finite-element analysis.*

CC BY

Introduction

Numerical Evaluation of Groundwater-Level Effects on the Seismic Response of a Multistory Building–Soil System Using PLAXIS 3D

The seismic performance of buildings in earthquake-prone regions depends not only on the characteristics of the structural system but also on the physical, mechanical, and hydrogeological conditions of the foundation soil (Abdunazarov et al., 2026; Ismailov et al., 2025; Savutov et al., 2026; Yuldashev et al., 2025). During an earthquake, ground motion propagates through the soil to the foundation and subsequently into the superstructure (Il'ichev et al., 1999; Ismoilov et al., 2025; Yuldashev et al., 2026). Soil density, stiffness, stratification, porosity, and groundwater level can therefore influence both the amplitude and the temporal characteristics of the seismic signal reaching the structure (Abdunazarov & Soliev, 2020; Mirsaidov et al., 2021; Yuldashev et al., 2023).

Natural soil is a multiphase medium consisting of a solid mineral skeleton, pore water, and air. When groundwater is deep, much of the soil domain remains unsaturated. As the water table rises, the degree of saturation, bulk mass density, and effective stress state change. Because water is substantially less compressible than air, increasing saturation can alter the bulk response of the soil, while pore-water pressure affects the effective stress carried by the soil skeleton (Abdunazarov, 2022a; Abdunazarov, 2023; Kholmirzayev et al., 2022; Yuldashev & Abdunazarov, 2023). Consequently, groundwater-level changes need not influence displacement, velocity, and acceleration in the same manner (Yuldashev et al., 2022).

A controlled numerical comparison is necessary to isolate the groundwater-level effect. The geometry, constitutive parameters, structural model, finite-element mesh, and seismic input should remain unchanged between the cases being compared (Abdunazarov, 2022c; Yuldashev & Abdunazarov, 2024a). When these quantities are held constant, differences in the computed response can be associated more directly with the hydrogeological condition (Abdunazarov, 2022b; Yuldashev & Abdunazarov, 2024c). This approach is particularly important for a real earthquake accelerogram because the response evolves over time, and a single maximum displacement value cannot fully describe the dynamic behavior of a soil–structure system (Yuldashev & Abdunazarov, 2024b, 2024d).

Accordingly, the objective of this study was to compare two three-dimensional PLAXIS models of the same multistory building–soil system with groundwater levels of −50 m and −3 m under an identical real earthquake accelerogram. The analysis focused on how the hydrogeological condition affected horizontal displacement, velocity, and acceleration at a soil monitoring node and at different elevations of the building (Yuldashev & Abdunazarov, 2024e).

Method

Seismic-Wave Parameters and Dynamic Soil Properties

For an equivalent single-phase elastic medium, the velocities of compressional (P) and shear (S) waves depend on bulk stiffness, shear stiffness, and mass density. The relationships used to describe these dependencies are

$$V_p = \sqrt{[(K + 4G/3)/\rho]} \quad (1)$$

$$V_s = \sqrt{(G/\rho)} \quad (2)$$

where K is the bulk modulus, G is the shear modulus, and ρ is mass density. Rayleigh-wave velocity is generally close to S-wave velocity and may be estimated as $V_r \approx (0.87–0.95)V_s$. Because groundwater-level variations alter density, effective stress, and the stiffness state of the soil skeleton, the conditions governing seismic-wave transmission may also change (Ismailov et al., 2025; Savutov et al., 2026; Yuldashev et al., 2025).

Wavelength (λ) is related to wave velocity (V) and frequency (f) by

$$\lambda = V/f \quad (3)$$

A real earthquake accelerogram contains multiple frequency components. Consequently, changes in dynamic soil properties and wave velocity can modify the time-dependent response. No separate frequency-domain or modal analysis was performed in this study; the results were therefore interpreted directly from computed time histories and their approximate extreme values.

ISSN: 2181-3337 | SCIENTISTS.UZ

Groundwater Level and Effective Stress

For soil below the groundwater table, the relationship between total and effective stress follows Terzaghi's effective stress principle:

$$\sigma' = \sigma - u \quad (4)$$

where σ′ is effective stress, σ is total stress, and u is pore-water pressure. Raising the groundwater level changes the initial hydrostatic condition and the unit weight of the soil below the water table. These changes can modify both the deformation field beneath the foundation and the transmission of dynamic motion. In the present study, the effects were evaluated from displacement, velocity, and acceleration time histories.

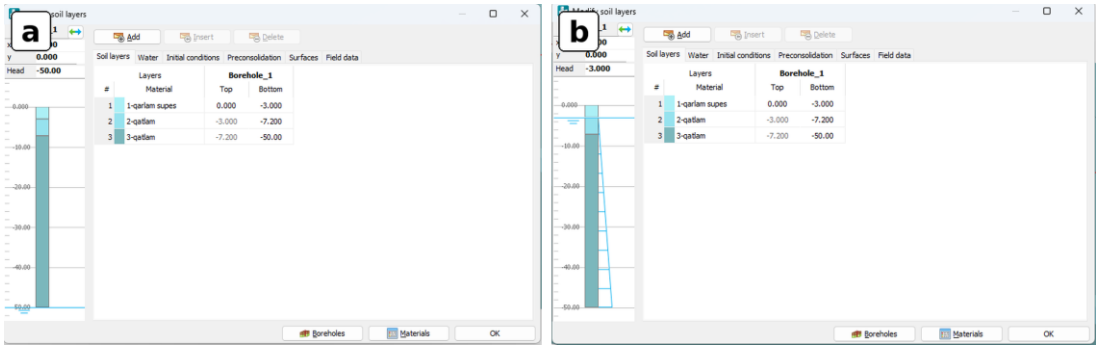
Numerical Model and Analysis Procedure

Soil Profile and Groundwater Scenarios

The computational domain comprised a three-layer soil mass extending to a depth of 50 m. Layer 1 occupied the interval from 0 to −3.0 m, Layer 2 from −3.0 to −7.2 m, and Layer 3 from −7.2 to −50.0 m. Two hydrogeological cases were modeled. In Case 1, the groundwater level was placed at −50 m; in Case 2, it was placed at −3 m. Thus, in Case 2, the soil below −3 m was below the water table, while all other geometric and mechanical conditions were unchanged. Figure 1 illustrates the two groundwater-level scenarios.

Figure 1

Groundwater-Level Scenarios for the Layered Soil Profile



Note. (a) GWL = −50 m; (b) GWL = −3 m. GWL = groundwater level.

The basic physical and mechanical properties of the soil layers are summarized in Table 1, and the porosity and wave-velocity parameters are provided in Table 2.

Table 1

Basic Physical and Mechanical Properties of the Soil Layers

Layer	Depth (m)	γunsat (kN/m³)	γsat (kN/m³)	Eref (MPa)	ν	c′ (kPa)	φ′ (°)
Layer 1	0 to −3.0	17	18	12	0.35	1	31
Layer 2	−3.0 to −7.2	18	19	30	0.30	24	18
Layer 3	−7.2 to −50.0	19	20	90	0.30	0	33

Note. All soil layers were modeled using the Mohr–Coulomb model under drained conditions, with a dilatancy angle ψ = 0°. γunsat = unsaturated unit weight; γsat = saturated unit weight; Eref = reference Young's modulus; ν = Poisson's ratio; c′ = effective cohesion; φ′ = effective friction angle.

Table 2

Porosity and Wave-Velocity Parameters

Layer	einit	ninit	Vs (m/s)	Vp (m/s)	Constitutive model
Layer 1	0.5000	0.3333	50.64	105.4	Mohr–Coulomb
Layer 2	0.5000	0.3333	79.30	148.4	Mohr–Coulomb
Layer 3	0.5000	0.3333	133.7	250.1	Mohr–Coulomb

Note. einit = initial void ratio; ninit = initial porosity; Vs = shear-wave velocity; Vp = compressional-wave velocity.

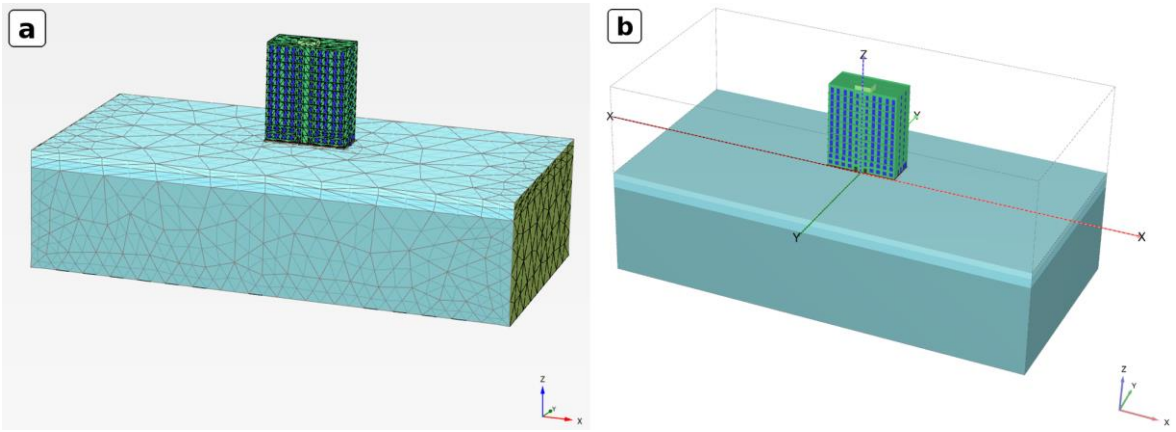
ISSN: 2181-3337 | SCIENTISTS.UZ

Building–Soil System and Finite-Element Mesh

The multistory building and the soil mass were modeled as a unified three-dimensional finite-element system. For both hydrogeological cases, building geometry, soil stratification, material parameters, finite-element mesh, and the overall computational scheme were kept identical. All technical settings of the dynamic analysis were likewise held constant. This controlled design allows differences in response to be attributed primarily to groundwater-level variation. Figure 2 shows the model mesh and overall geometry.

Figure 2

Three-Dimensional Numerical Model of the Multistory Building–Soil System



Note. (a) Finite-element mesh; (b) overall geometry of the soil layers and building.

Seismic Input, Analysis Cases, and Monitoring Points

The same real earthquake accelerogram, covering the interval from 0 to 10 s, was applied to both models. Monitoring nodes were selected in the soil, at the first floor, and at the ninth floor of the building. At these locations, time histories of horizontal displacement (u_x), velocity (v_x), and acceleration (a_x) were obtained. The comparison considered extreme values, the temporal form of the response curves, the locations of prominent peaks, and the variation of response with building height. Table 3 summarizes the two analysis cases.

Table 3

Comparison of the Numerical Analysis Cases

Parameter	Case 1: Deep GWL	Case 2: Shallow GWL
Groundwater level	−50 m	−3 m
Unit weight	γunsat	γsat below groundwater level
Soil model	Mohr–Coulomb, drained	Mohr–Coulomb, drained
Geometry and mesh	Identical	Identical
Seismic input	Same real accelerogram, 0–10 s	Same real accelerogram, 0–10 s
Monitoring	Soil node; 1st and 9th floors	Soil node; 1st and 9th floors

Note. GWL = groundwater level. The geometry, mechanical properties, mesh, monitoring points, and seismic input were identical between cases.

Results and Discussion

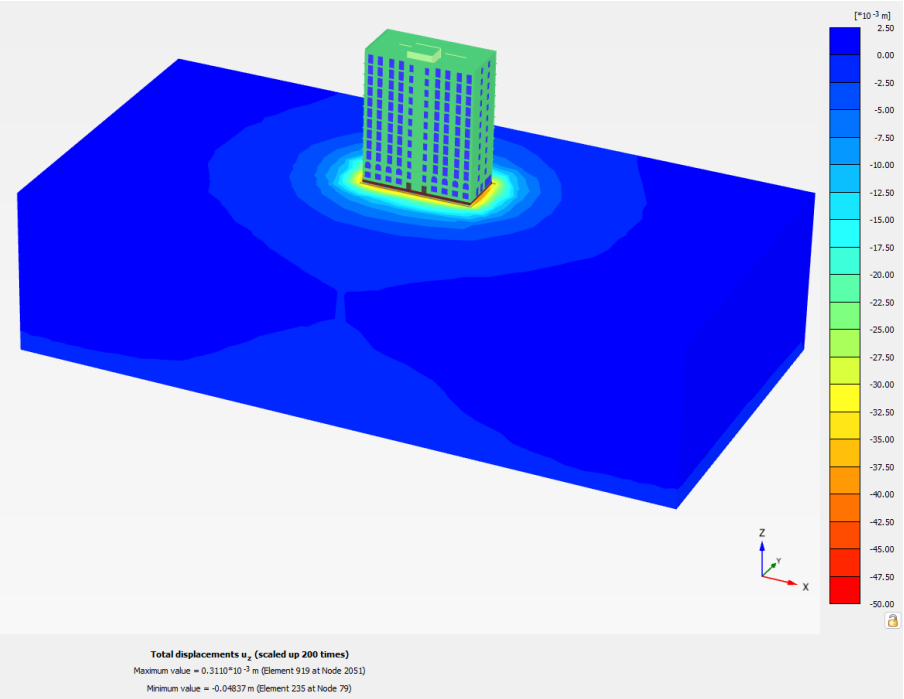
Vertical Displacement Field

The numerical results showed that the largest vertical displacements were concentrated around the building foundation. The contour field decreased outward from the area beneath the foundation. The maximum upward displacement was 0.311 mm, whereas the maximum downward displacement reached −48.37 mm. This distribution indicates that vertical deformation was concentrated within the soil–structure interaction zone adjacent to the foundation (Figure 3).

ISSN: 2181-3337 | SCIENTISTS.UZ

Figure 3

Vertical Displacement Field of the Building–Soil System



Response at the Soil Monitoring Node

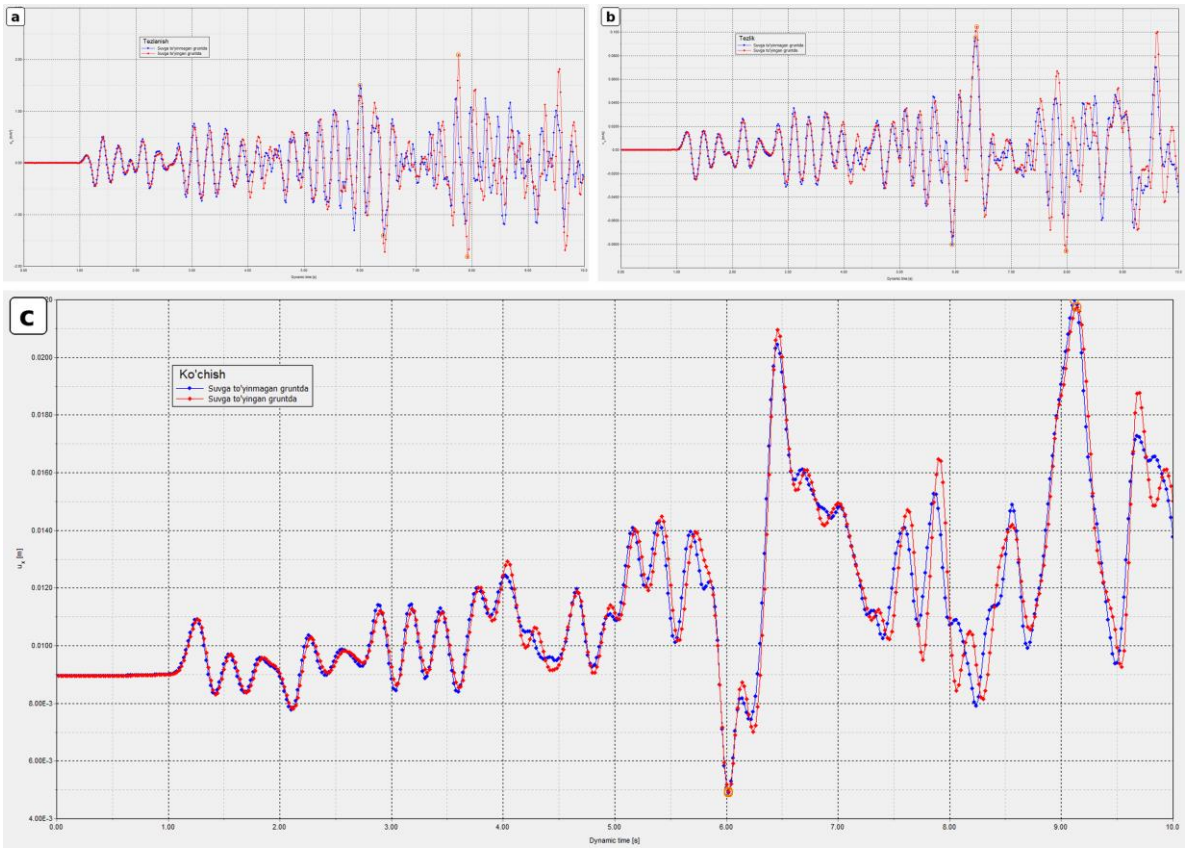
Acceleration, velocity, and horizontal-displacement time histories at the soil monitoring node were compared for the two hydrogeological cases (Figure 4). The response curves were close during the initial portion of the record, whereas differences between several peaks became more pronounced during later strong pulses. Based on the graph scale, the GWL = −3 m case reached an approximately +2.1 m/s² positive acceleration peak and a −1.8 m/s² negative peak; the corresponding extrema for GWL = −50 m were approximately +1.5 and −1.4 m/s². Thus, for several portions of the selected seismic record, the shallower groundwater condition was associated with a larger acceleration response at the soil monitoring node.

In the velocity history, the GWL = −3 m case reached approximately +0.105 m/s and −0.086 m/s, slightly exceeding the corresponding values for the GWL = −50 m case. By contrast, the horizontal-displacement histories were nearly coincident, with a maximum value close to 0.022 m. Under the conditions of the present model and accelerogram, groundwater-level variation was therefore more evident in velocity and especially in acceleration than in displacement.

ISSN: 2181-3337 | SCIENTISTS.UZ

Figure 4

Time Histories at the Soil Monitoring Node



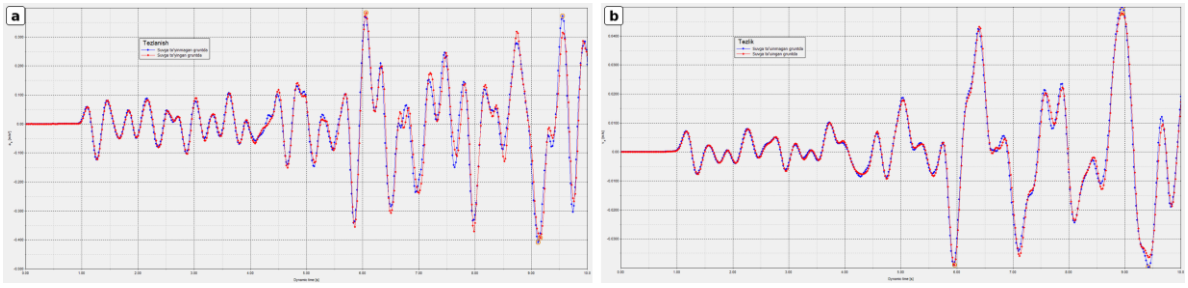
Note. (a) Acceleration a_x; (b) velocity v_x; (c) horizontal displacement u_x. In the source plots, blue represents GWL = −50 m and red represents GWL = −3 m.

First-Floor Response

At the first-floor monitoring node, acceleration and velocity time histories had similar forms for the two groundwater-level cases (Figure 5). From the plot scale, acceleration varied approximately from −0.41 to +0.38 m/s² and velocity from −0.040 to +0.049 m/s. Although small differences appeared at several local peaks, the overall amplitude ranges and temporal responses remained close. Under the selected computational conditions, the influence of groundwater-level variation on the first-floor kinematic response was therefore more limited than at the soil monitoring node.

Figure 5

Time Histories at the First Floor of the Building



Note. (a) Acceleration; (b) velocity.

Ninth-Floor Acceleration Response

Acceleration amplitude at the ninth floor was greater than at the first floor, reaching approximately −0.63 to +0.92 m/s² according to the graph scale. The overall forms of the time histories remained similar for the two groundwater-level cases, although individual peak amplitudes differed: GWL = −50 m produced the larger value at some positive maxima, whereas GWL = −3 m produced the larger absolute value at some negative maxima. This result indicates that seismic response was not distributed uniformly with building height and that dynamic amplification occurred at the upper floor. Because no separate modal

ISSN: 2181-3337 | SCIENTISTS.UZ

analysis was performed, the observed amplification was not assigned to a specific vibration mode (Figure 6).

Figure 6

Acceleration Time History at the Ninth Floor of the Building

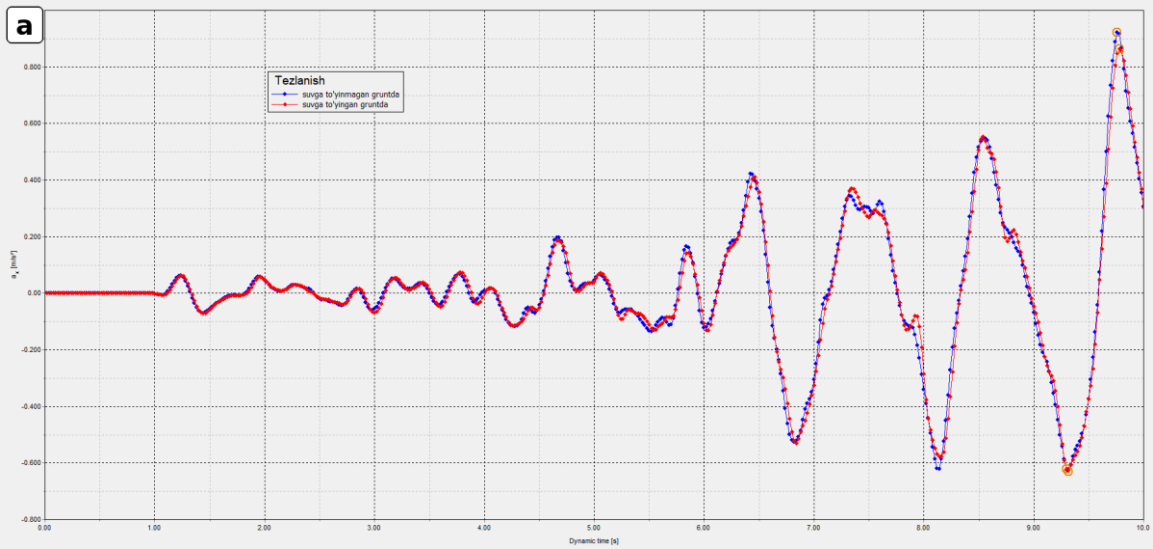


Table 4 summarizes the approximate extreme values read from the time-history plots. These values should be interpreted as plot-based estimates rather than direct numerical exports.

Table 4

Approximate Extreme Values Read From the Time-History Plots

Monitoring point	Parameter	GWL = −50 m	GWL = −3 m	Main observation
Soil	a_x (m/s²)	≈ −1.4 to +1.5	≈ −1.8 to +2.1	Several peaks are higher for GWL = −3 m
Soil	v_x (m/s)	≈ −0.080 to +0.095	≈ −0.086 to +0.105	Small but noticeable increase for GWL = −3 m
Soil	u_x (m)	≈ 0.0048 to 0.0220	≈ 0.0049 to 0.0219	Curves are nearly coincident
1st floor	a_x (m/s²)	≈ −0.41 to +0.38	≈ −0.39 to +0.38	Amplitudes are similar
1st floor	v_x (m/s)	≈ −0.040 to +0.049	≈ −0.039 to +0.048	Difference is very small
9th floor	a_x (m/s²)	≈ −0.61 to +0.92	≈ −0.63 to +0.87	Amplitude exceeds that at the 1st floor

Note. Values are approximate because several extrema were read from the graph scales rather than exported directly from PLAXIS Output. GWL = groundwater level.

Interpretation of Groundwater-Level Effects

The findings show that the groundwater-level effect depends on both the kinematic parameter and the location of observation. At the soil node, GWL = −3 m produced larger acceleration and velocity peaks, while horizontal displacement remained almost unchanged. Differences between the two cases were small at the first floor, whereas acceleration amplitude at the ninth floor was larger than at the first floor. Evaluating the groundwater effect from a single maximum displacement value would therefore provide an incomplete description of the system's dynamic behavior.

Because the same real accelerogram was imposed in both hydrogeological cases, the observed response differences can be associated with the changed initial hydrogeological condition and the resulting equivalent dynamic response of the soil. At the same time, the broadly similar forms of most time histories indicate that the principal temporal structure of the input motion was transmitted through both models. No fast Fourier transform, response-spectrum, or modal analysis was conducted; therefore, the observed amplitude differences cannot be assigned to a specific frequency band or structural vibration mode.

Limitations and Reliability Considerations

The soil layers were represented by the Mohr–Coulomb model under drained conditions. This formulation is appropriate for a controlled comparison of the two hydrogeological cases, but it does not fully represent the nonlinear dependence of soil stiffness on strain level and effective stress. For a more detailed investigation of small-strain dynamic behavior, an advanced constitutive formulation such as HSsmall can account explicitly for small-strain stiffness parameters such as G_{0}^{ref} and $\gamma_{0.7}$ (Yuldashev et al., 2023, 2026).

The present Mohr–Coulomb, drained results should not be interpreted as a complete representation of cyclic excess pore-water-pressure accumulation or liquefaction in saturated soil. In addition, because several extreme values reported in this paper were read from plot scales, the quantitative conclusions should be verified using direct numerical exports from PLAXIS Output (Abdunazarov, 2023; Yuldashev & Abdunazarov, 2023; Yuldashev et al., 2022). Sensitivity analyses with several mesh densities and time-step sizes would further strengthen confidence in numerical stability (Abdunazarov, 2022a).

Future work should investigate intermediate groundwater levels, multiple real earthquake accelerograms, direct comparisons between Mohr–Coulomb and HSsmall soil models, time-history responses of pore-water pressure and effective stress, and frequency-domain measures such as fast Fourier transforms and response spectra.

Conclusion

Two three-dimensional multistory building–soil models with groundwater levels of −50 m and −3 m were compared in PLAXIS 3D under the same real earthquake accelerogram while geometric, physical-mechanical, and computational conditions were kept identical. The results demonstrate that groundwater-level changes did not affect displacement, velocity, and acceleration to the same degree. The most pronounced differences occurred in velocity and acceleration at the soil monitoring node, where several extreme values were higher for GWL = −3 m. Horizontal-displacement histories, however, were almost coincident. Under the conditions of the selected model and input record, velocity and acceleration were therefore more sensitive to groundwater-level variation than displacement.

The maximum downward vertical displacement was −48.37 mm, and the principal deformation was concentrated in the soil–structure interaction zone near the foundation. Velocity and acceleration responses at the first floor were similar between hydrogeological cases, whereas ninth-floor acceleration amplitude exceeded that at the first floor. These findings indicate that the groundwater-level effect is not manifested uniformly throughout the soil and building and that seismic response can be amplified with building height.

The results do not support a general assumption that increased soil saturation will always reduce or always increase seismic vibration. The response of the building–soil system is governed jointly by soil stiffness, mass density, effective stress, groundwater level, the time-dependent characteristics of the accelerogram, and the dynamic behavior of the structure. Groundwater level should therefore be treated as an independent variable in seismic soil–structure interaction analyses. Future studies should evaluate several groundwater levels and multiple earthquake records and should assess displacement, velocity, and acceleration comprehensively in both the soil and the structure.

REFERENCES

1. Abdunazarov, A. (2022a). Analyses on improving measures to determine and reduce the impact of vibrations generated by vehicle movement on buildings. *Science and Innovation, 1*(A5), 372–375. https://doi.org/10.5281/zenodo.7066624
2. Abdunazarov, A. (2022b). Improving measures to determine and reduce the impact of vibrations on buildings. *Science and Innovation, 1*(A5), 380–384.
3. Abdunazarov, A. (2022c). Improving measures to determine and reduce the impact of vehicle-induced vibrations on buildings using local raw material (reed). *Science and Innovation, 1*(A5), 380–385.

4. Abdunazarov, A. S. (2023). Analysis of deformation and seismic-wave propagation in water-saturated loess soils along highways. *Construction and Education, 1*(3), 60–65.
5. Abdunazarov, A., & Soliev, N. (2020). Study of the performance of frameless construction structures under the influence of vertical stresses of ultra-submerged loess soils. *Student Bulletin*, (28-3), 39–40.
6. Abdunazarov, A., Yuldashev, S., Boytemirov, M., Karabayeva, M., & Yuldashev, F. (2026). Seismic surface-wave protection of the administrative building of Namangan State Technical University using a tire-filled barrier. *Vibroengineering Procedia, 62*, 668–674. https://doi.org/10.21595/vp.2026.26127
7. Il'ichev, V. A., Yuldashev, S. S., & Matkarimov, P. Z. (1999). Forced vibrations of an inhomogeneous planar system with passive vibrational insulation. *Soil Mechanics and Foundation Engineering, 36*(2), 50–54. https://doi.org/10.1007/BF02469084
8. Ismailov, V. A., Rakhmatov, A. R., Xusomiddinov, A. S., Yadigarov, E. M., & Bozorov, J. Sh. (2025). Assessment of the soil seismic condition through microseismic measurements: A case study of Bukhara. *News of the National Academy of Sciences of the Republic of Kazakhstan, Series of Geology and Technical Sciences, 5*(473), 131–145. https://doi.org/10.32014/2025.2518-170X.554
9. Ismoilov, V. A., Khusomiddinov, A. S., Mukhammadkulov, N. M., Yadigarov, E. M., Khayriddinov, B. B., Rakhmatov, A. R., Jumaev, D. D., Bozorov, J. Sh., Isroilov, X. B., & Mansurov, A. F. (2025). Assessment of landslide dynamics based on microseismic parameters. *Seismic Instruments, 61*, 346–353. https://doi.org/10.3103/S0747923925700446
10. Kholmirzayev, S., Akhmedov, I., Khamidov, A., Umarov, I., Axmedov, A., & Abdunazarov, A. (2022). Prospects for the development of reinforced concrete structures in Uzbekistan. *Science and Innovation, 1*(A8), 1052–1057.
11. Mirsaidov, M., Boytemirov, M., & Yuldashev, F. (2021). Estimation of the vibration waves level at different distances. In *Proceedings of FORM 2021: Construction—The Formation of Living Environment* (pp. 207–215). Springer. https://doi.org/10.1007/978-3-030-79983-0_19
12. Savutov, R., Shamuratov, A., Ismailov, V., Yodgorov, S., & Abdunazarov, A. (2026). Assessing the seismic vulnerability of single-family residential buildings in the Khorezm region. *Vibroengineering Procedia, 62*, 189–194. https://doi.org/10.21595/vp.2026.26187
13. Yuldashev, S. S., & Abdunazarov, A. S. (2023). Identification of seismic surface waves affecting a building and their reduction using a seismic barrier (polyurethane foam). In *Science and Innovation–2023: Development and Priority Directions: Republican Scientific-Practical Conference* (pp. 198–201).
14. Yuldashev, S. S., & Abdunazarov, A. S. (2024a). Advantages of circular and rectangular seismic barriers. *Journal of Transport, 1*(3), 91–93.
15. Yuldashev, S. S., & Abdunazarov, A. S. (2024b). Determining the effectiveness of seismic barriers by changing their height. *Science and Innovation, 3*(A8), 48–56. https://doi.org/10.5281/zenodo.13623022
16. Yuldashev, S. S., & Abdunazarov, A. S. (2024c). Determining the effectiveness of seismic barriers by changing their thickness. *Science and Innovation, 3*(A8), 27–34. https://doi.org/10.5281/zenodo.13350631
17. Yuldashev, S. S., & Abdunazarov, A. S. (2024d). Determining the effectiveness of distance placement of a seismic barrier in protecting buildings from seismic waves. *Journal of Transport, 1*(3), 124–126.
18. Yuldashev, S. S., & Abdunazarov, A. S. (2024e). Determining the efficiency of seismic barriers based on their horizontal and vertical positioning. *Science and Innovation, 3*(A8), 40–47. https://doi.org/10.5281/zenodo.13386720
19. Yuldashev, S. S., Boytemirov, M. B., Yuldashev, F. S., & Abdunazarov, A. S. (2022). Effect of vehicle-traffic-induced vibration on buildings. *Mechanics and Technology, 4*(9), 19–29.

20. Yuldashev, S. S., Alimov, X. L., Abdunazarov, A. S., Yuldasheva, G., & Xakimov, X. A. (2023). Effect of groundwater level on the propagation of seismic surface waves. In *Innovations in Construction and Seismic Safety of Buildings and Structures: International Scientific and Technical Conference* (pp. 314–318).
21. Yuldashev, S., Abdunazarov, A., Jumaboyeva, S., Boytemirov, M., & Tillaboyev, Y. (2025). Attenuation of seismic surface waves affecting the building using various barriers. *AIP Conference Proceedings*, *3265*, 030016. https://doi.org/10.1063/5.0265304
22. Yuldashev, S. S., Boytemirov, M. B., & Abdunazarov, A. S. (2026). Evaluation of the effectiveness of strengthening the foundation soil of multistory buildings using a soil cushion and deep soil mixing technology in reducing seismic effects. *Science and Innovation*, *5*(6), 33–42. https://doi.org/10.5281/zenodo.20697242

ISSN: 2181-3337 | SCIENTISTS.UZ VOLUME 5 ISSUE 8 | AUGUST 2026

MEDICAL AND PEDAGOGICAL SIGNIFICANCE OF RADIATION BACKGROUND IN THE USE OF NUCLEAR POWER REACTORS

Sayfullayev Ramziddin
Independent Researcher, Oriental University

DOI: 10.67620/sai.58a0011

ABSTRACT

This study examines the medical and pedagogical significance of radiation background associated with nuclear power reactors and evaluates a case-study approach for teaching radiation safety to medical students. The central argument is that radiation literacy should be treated not only as knowledge of physical dose and biological effect, but also as a patient-safety and risk-communication competency. International radiological protection frameworks emphasize justification, optimization, and dose limitation, while evidence on very low-dose health effects remains subject to uncertainty. Against this scientific background, a classroom comparison was conducted with 31 students at Samarkand State Medical University: 15 students received case-based instruction and 16 received a traditional lecture. The case-study group achieved a mean grade of 4.27 (SD = 0.70) and learning efficiency of 85.4%, compared with 3.69 (SD = 0.87) and 73.8% in the control group. The difference was 11.6 percentage points. An exploratory reanalysis of the reported grade distribution produced Welch's t(28.39) = 2.04, p = .051, with Hedges' g = 0.71, indicating a potentially meaningful effect that requires replication in a larger, better-controlled sample. The findings support integrating authentic radiation-safety cases into medical curricula while avoiding overstatement of low-dose risks.

ACCEPTED

07.09.26

Keywords: *nuclear energy, radiation background, medical education, radiation protection, radiological literacy, risk communication, case-based learning.*

CC BY

Introduction

Nuclear energy is increasingly discussed as part of low-carbon electricity systems, but public acceptance and safe implementation depend on more than engineering performance. Radiation-related questions are also medical and educational questions because physicians are frequently expected to interpret health risks, communicate uncertainty, and respond to public concern. In countries considering expansion of nuclear energy, including Uzbekistan, this responsibility makes radiation literacy relevant to both clinical training and public health education.

Radiation safety education should therefore be treated as a clinical competency rather than as a narrow physics topic. Future physicians need to distinguish routine environmental exposure from accident scenarios, understand the difference between deterministic tissue reactions and stochastic cancer risk, apply the principles of radiological protection, and explain risk without either minimizing legitimate hazards or amplifying radiophobia. International guidance places protection within the framework of justification, optimization, and dose limitation (International Atomic Energy Agency [IAEA], 2014; International Commission on Radiological Protection [ICRP], 2007).

This paper argues that case-based learning is particularly suitable for this task because it requires students to connect radiation quantities and biological mechanisms with clinical judgment, regulatory standards, and patient communication. The study evaluates whether a structured case-study lesson can improve short-term learning outcomes compared with a traditional lecture and interprets the findings in light of current radiation-protection and medical-education literature.

Literature Review

Low-Dose Radiation and Radiological Protection

The adverse effects of moderate and high doses of ionizing radiation are well established, whereas quantitative risk estimation at very low doses is more uncertain. Brenner et al. (2003) concluded that direct epidemiological evidence is strongest above the very-low-dose range and supported linear extrapolation as a practical method for estimating cancer risk when direct evidence becomes difficult to obtain. The National Research Council (2006) similarly used a linear no-threshold approach for population risk assessment, while emphasizing uncertainty at low doses. More recent reviews by the United Nations Scientific Committee on the Effects of Atomic Radiation (UNSCEAR, 2022) synthesize biological mechanisms relevant to low-dose and low-dose-rate exposure and reinforce the need to distinguish evidence, inference, and uncertainty.

This distinction is pedagogically important. A scientifically responsible course should not teach students that every detectable radiation level is immediately dangerous, nor should it imply that low-dose exposure is risk-free. Instead, students should learn why radiological protection uses prudent assumptions and why decisions depend on dose, dose rate, exposure pathway, population, and context. ICRP (2007) and the IAEA (2014) provide a coherent protection framework for translating this evidence into practice.

Radiation Background and Nuclear Power

Environmental radiation around nuclear facilities must be understood through source terms, release pathways, monitoring, dose assessment, and comparison with other radiation sources. Cooper et al. (2003) describe the principles governing environmental radioactivity, radionuclide transport, measurement, and dose assessment. At the international level, UNSCEAR (2017) compared radiation exposures associated with electricity-generation technologies and documented methods for evaluating public and occupational exposure across the nuclear fuel cycle. These sources support a teaching approach based on measured dose and exposure pathways rather than on generalized fear of the word radiation.

For medical students, the key educational issue is not to defend or oppose nuclear energy as a policy position. It is to develop the ability to evaluate health claims using dose-based evidence, recognize the limits of current knowledge, and communicate proportionate protective actions. This approach is consistent with public-health risk communication guidance, which emphasizes transparency, uncertainty, trust, and communication adapted to the audience (World Health Organization [WHO], 2018).

Radiation Literacy and Case-Based Learning in Medical Education

Radiation-protection knowledge among medical trainees is often incomplete. Faggioni et al. (2017) found important gaps in knowledge of radiation protection and imaging dose levels among medical students, radiography students, and radiology residents, supporting the need for stronger undergraduate and postgraduate education. Radiation literacy is therefore relevant even outside nuclear medicine and radiology because physicians may order imaging, counsel patients, or participate in public-health responses.

Case-based learning offers a mechanism for integrating scientific knowledge with clinical reasoning. A systematic review by Thistlethwaite et al. (2012) found that learners and educators generally value case-based learning for engagement and linking theory to practice, although comparative evidence was heterogeneous. A later meta-analysis of eight studies involving 939 medical students reported improvements in academic performance and case-analysis ability with case-based learning (Cen et al.,

2021). These findings justify testing a radiation-safety case in a medical curriculum, while also requiring cautious interpretation of results from small local samples.

Method

Design and Participants

The study used a small classroom comparison with experimental and control groups. The pedagogical experiment was conducted at Samarkand State Medical University in a course setting associated with Medical Biology and General Genetics or Medical Physics. A total of 31 students participated. The experimental group included 15 students and the control group included 16 students. Because the source study does not document random assignment, the design is best interpreted as quasi-experimental rather than as a randomized controlled trial.

Instructional Procedures

The experimental group studied the topic "Radiation Background of Nuclear Reactors and Its Medical Consequences" using a case-study method. Students were presented with a realistic medical-ecological scenario, such as evaluating the annual radiation dose of a population living near a nuclear facility and considering reported disease statistics. They worked through relevant medical norms and radiation-safety principles, discussed alternative interpretations, made decisions, and defended their conclusions.

The control group received the same general topic through a conventional lecture and reproductive-question format. The instructor presented the material using a board and presentation slides, students took notes, and questions were answered at the end of the lesson. Both groups then completed 10 problem-based test and control questions described in the source study as equivalent in difficulty.

Outcome Measures and Statistical Analysis

Student performance was evaluated on the 5-point grading scale used in the source study (5 = excellent, 4 = good, 3 = satisfactory, 2 = unsatisfactory). Learning efficiency was calculated as the group mean divided by the maximum grade of 5 and multiplied by 100. The original study reported grade frequencies, mean scores, and percentage-based learning efficiency.

For this revised manuscript, the reported grade distributions were additionally reanalyzed to provide a more informative estimate of the between-group difference. Means and sample standard deviations were calculated from the published grade counts, Welch's independent-samples t test was used because equal variances were not assumed, and Hedges' g was calculated as a small-sample standardized effect size. These inferential statistics are exploratory because of the small sample, the absence of documented random assignment, and the lack of a pretest.

Results

The case-study group showed higher performance across the main descriptive outcomes. Six of 15 students in the experimental group received a grade of 5, compared with 3 of 16 students in the control group. No student in the case-study group received an unsatisfactory grade, whereas one student in the control group did. Table 1 summarizes the grade distribution and the calculated learning efficiency.

ISSN: 2181-3337 | SCIENTISTS.UZ

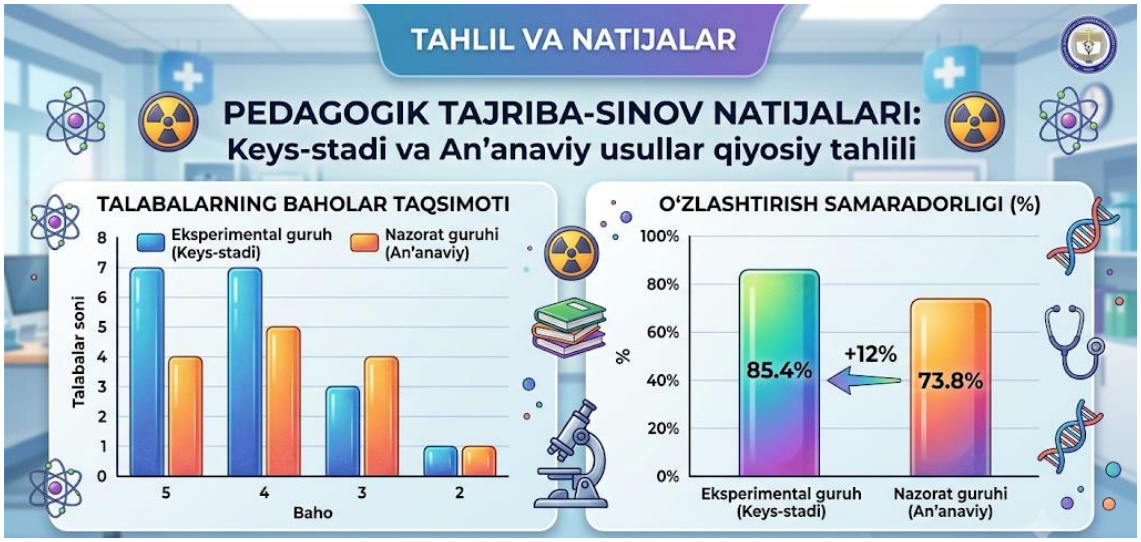
Table 1

Comparison of Learning Outcomes by Instructional Method

Outcome	Case-study (n = 15)	Traditional (n = 16)	Difference
Grade 5 (excellent)	40.0% (6)	18.75% (3)	+21.25 pp
Grade 4 (good)	46.7% (7)	37.50% (6)	+9.2 pp
Grade 3 (satisfactory)	13.3% (2)	37.50% (6)	-24.2 pp
Grade 2 (unsatisfactory)	0% (0)	6.25% (1)	-6.25 pp
Mean grade (SD)	4.27 (0.70)	3.69 (0.87)	+0.58
Learning efficiency	85.4%	73.8%	+11.6 pp

Note. Learning efficiency = mean grade / 5 x 100. pp = percentage points.

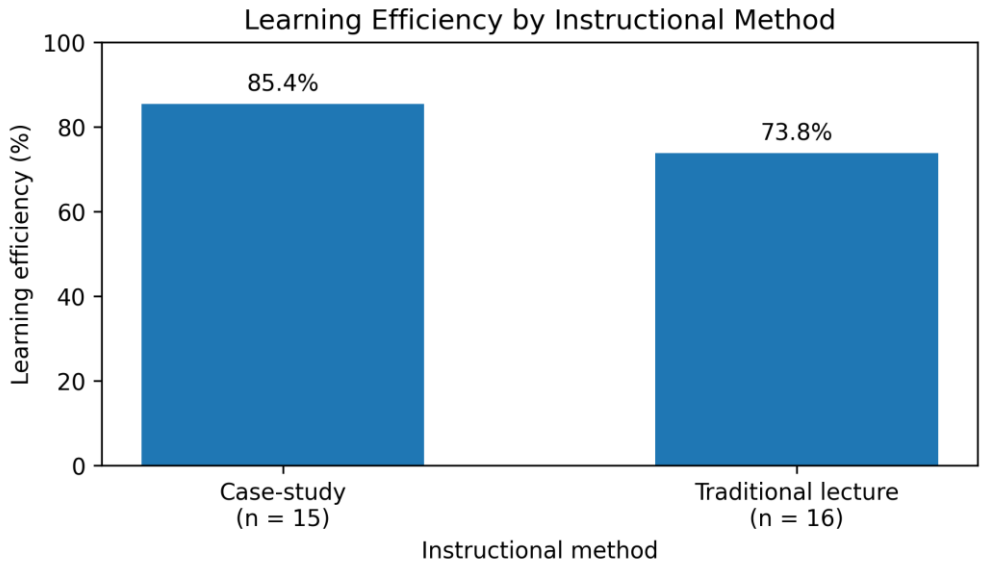
The mean grade was 4.27 (SD = 0.70) in the case-study group and 3.69 (SD = 0.87) in the traditional group, corresponding to learning efficiencies of 85.4% and 73.8%, respectively. The absolute difference in learning efficiency was 11.6 percentage points. The exploratory Welch test yielded t(28.39) = 2.04, p = .051. Hedges' g was 0.71, a standardized difference consistent with a moderate-to-large educational effect, although the p value narrowly exceeded the conventional .05 threshold and the confidence around the estimate is necessarily wide in a sample of 31 students.



ISSN: 2181-3337 | SCIENTISTS.UZ

Figure 1

Learning Efficiency by Instructional Method



Note. Learning efficiency = mean grade / 5 x 100.

Discussion

The results provide preliminary support for the paper's central argument: when radiation safety is taught through an authentic clinical-environmental problem, students may engage more effectively with the material than when the same topic is delivered primarily as a lecture. The 11.6-percentage-point difference is educationally meaningful, and the standardized effect estimate (Hedges' g = 0.71) suggests that the observed advantage is not trivial. At the same time, the exploratory p value of .051 cautions against presenting the finding as definitive statistical proof. The appropriate conclusion is that the case-study approach shows a promising signal that should be tested in a larger and more rigorous design.

This interpretation is consistent with the broader medical-education literature. Cen et al. (2021) reported improved academic performance and case-analysis ability in a meta-analysis of case-based learning, while Thistlethwaite et al. (2012) emphasized that the strength of comparative evidence varies across studies. The present result therefore contributes a small, topic-specific example rather than establishing a universal superiority of case-based teaching.

The pedagogical value of the intervention extends beyond test scores. Radiation-related decisions frequently require interpretation of uncertainty. Students must understand that low-dose risk estimation is not the same as direct observation of harm at every small dose, while also recognizing that radiological protection deliberately uses conservative principles to reduce avoidable exposure (Brenner et al., 2003; ICRP, 2007; National Research Council, 2006; UNSCEAR, 2022). A case that requires students to compare doses, identify exposure pathways, apply protection principles, and explain conclusions to a simulated patient or community member can integrate scientific literacy with communication competence.

This integration is important because insufficient radiation knowledge can produce two opposite errors: unjustified reassurance and disproportionate fear. Evidence that medical trainees have gaps in dose and radiation-protection knowledge (Faggioni et al., 2017) supports explicit curriculum time for the subject. WHO (2018) guidance also indicates that effective risk communication depends on transparency, trust, and acknowledgment of uncertainty. For this reason, radiation education in medical schools should teach both what is known and how confidently it is known.

Limitations

The study has several limitations. First, the sample was small and drawn from a single institution, limiting generalizability. Second, random assignment was not documented, so pre-existing differences between groups cannot be excluded. Third, no pretest was reported, which prevents direct measurement of

ISSN: 2181-3337 | SCIENTISTS.UZ

individual learning gain. Fourth, the outcome was an immediate post-lesson assessment and does not establish long-term retention, transfer to clinical behavior, or improvement in public communication. Fifth, the 5-point grading scale is relatively coarse. Future research should use validated radiation-literacy measures, pretest-posttest designs, larger samples, and delayed follow-up assessments.

Conclusion and Recommendations

Radiation background associated with nuclear power should be taught in medical education as a combined problem of radiobiology, protection, clinical judgment, and risk communication. International evidence supports a cautious, dose-based approach: health effects at higher doses are established, low-dose risk estimation contains uncertainty, and radiological protection relies on structured principles rather than fear-based interpretation. Within that framework, the present classroom comparison suggests that case-based instruction can improve immediate learning outcomes and may produce a practically meaningful educational effect.

The evidence is not strong enough to claim definitive superiority from a single 31-student experiment, but it is strong enough to justify curriculum development and a larger confirmatory study. The following recommendations follow from the findings and literature:

- Integrate authentic radiation-safety cases into medical physics, radiology, biology, and public-health courses, emphasizing dose, exposure pathways, and protection principles.
- Add risk-communication tasks in which students explain low-dose uncertainty and protective actions to patients or community members.
- Use larger pretest-posttest studies with standardized outcomes and delayed retention testing.
- Avoid alarmist or dismissive framing; distinguish established evidence, modeled risk, and uncertainty.

REFERENCES

1. Brenner, D. J., Doll, R., Goodhead, D. T., Hall, E. J., Land, C. E., Little, J. B., Lubin, J. H., Preston, D. L., Preston, R. J., Puskin, J. S., Ron, E., Sachs, R. K., Samet, J. M., Setlow, R. B., & Zaider, M. (2003). Cancer risks attributable to low doses of ionizing radiation: Assessing what we really know. *Proceedings of the National Academy of Sciences of the United States of America, 100*(24), 13761-13766. https://doi.org/10.1073/pnas.2235592100
2. Cen, X.-Y., Hua, Y., Niu, S., & Yu, T. (2021). Application of case-based learning in medical student education: A meta-analysis. *European Review for Medical and Pharmacological Sciences, 25*(8), 3173-3181. https://doi.org/10.26355/eurrev_202104_25726
3. Cooper, J. R., Randle, K., & Sokhi, R. S. (2003). *Radioactive releases in the environment: Impact and assessment*. John Wiley & Sons.
4. Faggioni, L., Paolicchi, F., Bastiani, L., Guido, D., & Caramella, D. (2017). Awareness of radiation protection and dose levels of imaging procedures among medical students, radiography students, and radiology residents at an academic hospital: Results of a comprehensive survey. *European Journal of Radiology*, *86*, 135-142. https://doi.org/10.1016/j.ejrad.2016.10.033
5. International Atomic Energy Agency. (2014). *Radiation protection and safety of radiation sources: International basic safety standards (General Safety Requirements Part 3)*. https://doi.org/10.61092/iaea.u2pu-60vm
6. International Commission on Radiological Protection. (2007). The 2007 recommendations of the International Commission on Radiological Protection (ICRP Publication 103). *Annals of the ICRP, 37*(2-4).
7. National Research Council. (2006). *Health risks from exposure to low levels of ionizing radiation: BEIR VII Phase 2*. The National Academies Press. https://doi.org/10.17226/11340

8. Thistlethwaite, J. E., Davies, D., Ekeocha, S., Kidd, J. M., MacDougall, C., Matthews, P., Purkis, J., & Clay, D. (2012). The effectiveness of case-based learning in health professional education: A BEME systematic review, BEME Guide No. 23. *Medical Teacher*, *34*(6), e421-e444. https://doi.org/10.3109/0142159X.2012.680939
9. United Nations Scientific Committee on the Effects of Atomic Radiation. (2017). *Sources, effects and risks of ionizing radiation: UNSCEAR 2016 report to the General Assembly, with scientific annexes*. United Nations.
10. United Nations Scientific Committee on the Effects of Atomic Radiation. (2022). *Sources, effects and risks of ionizing radiation: UNSCEAR 2020/2021 report, volume III, scientific annex C: Biological mechanisms relevant for the inference of cancer risks from low-dose and low-dose-rate radiation*. United Nations.
11. World Health Organization. (2018). *Communicating risk in public health emergencies: A WHO guideline for emergency risk communication policy and practice*.

ISSN: 2181-3337 | SCIENTISTS.UZ VOLUME 5 ISSUE 8 | AUGUST 2026

DEVELOPMENT OF A NEW SEEDER FOR RESTORING DESERT AND SEMI-DESERT AREAS IN UZBEKISTAN

Farmonov Erkin[1], Mirzaeva Shakhnoza[2], Xodjaqulova Nodira[3]
Department of Engineering Systems Management, Faculty of Agricultural Mechanization,
"Tashkent Institute of Irrigation and Agricultural Mechanization Engineers"
National Research University, Tashkent, Uzbekistan[1,2,3]

DOI: 10.67620/sai.58a0012

ABSTRACT
This study developed and evaluated a specialized seeder for restoring degraded desert and semi-desert pastures in Uzbekistan through mechanized sowing of native drought-resistant plants. Saxaul (Haloxylon spp.), cherkez (Salsola spp.), and izen (Kochia prostrata) were selected because of their adaptation to arid conditions and their potential to stabilize sandy soils and improve pasture productivity. Laboratory and field investigations assessed seed quality, seed-flow behavior, and the operational performance of an experimental seeder equipped with cone-shaped seed-mixture loosening elements. Seed purity ranged from 20% to 25%, and germination capacity ranged from 40% to 45%. Experimental results showed that increasing the operating parameter of the cone-shaped working element increased the quantity of sown seeds while maintaining a relatively low number of wingless seeds. The loosening mechanism reduced seed bridging and clogging, supported continuous seed flow, and improved the uniformity and stability of seed distribution compared with manual sowing. Field trials conducted in 2025 confirmed the practical suitability of the seeder for sandy and degraded pasture soils. The developed technology offers a technically effective approach for pasture restoration, soil stabilization, and improved establishment of desert forage vegetation.

ACCEPTED

07.09.26

Keywords: *desert, semi-desert, pasture degradation, natural pasture restoration, sandy soils, Haloxylon, izen, desert plants, seeding technology, mechanized sowing.*

CC BY

Introduction

Arid natural pastures, covering millions of hectares and primarily reserved for livestock grazing, contain extensive areas of degradation in almost all regions (Arshad et al., 2022). Approximately 40% of desert pastures have been affected by degradation of varying degrees, resulting in a 20–30% decline in their average productivity (Abd Elsalam & Bahobail, 2016). In the Republic of Uzbekistan, approximately 8.0 million hectares of degraded pastures require improvement (Table 1). Arid and semi-arid regions cover approximately 66.7 million km² worldwide and are home to nearly 2 billion people (Arshad et al., 2022). According to the United Nations (UN), drylands account for approximately 30% of the Earth's land surface across more than 100 countries, and nearly 2 billion people currently live in these areas (Arshad et al., 2022). Considering the current rate of desertification, if the scenario proposed by the UN materializes, by 2025, one in every five people worldwide could be living in territories affected by severe land degradation (Arshad et al., 2022). More than 2 billion hectares of productive land have already been degraded, and an additional 12 million hectares are degraded annually (Anttila et al., 2011). There is a close relationship

between the spatial structure of vegetation and the desertification processes associated with intensive livestock grazing on natural pastures (N. Z. Shamsutdinov et al., 2021). Degradation occurs particularly rapidly and reaches severe levels in pastures used for grazing throughout the year (Shamsutdinova & Shamsutdinov, 2021). Uncontrolled livestock grazing and overgrazing are among the major causes of degradation of pasture vegetation, soil degradation, and the formation and accumulation of wind-blown sand deposits (N. Shamsutdinov et al., 2020). Pasture ecosystems are particularly vulnerable during the dry season, when vegetation cover and soil moisture are significantly reduced (Farmonov et al., 2022). Under conditions of severe and prolonged drought, the processes of land degradation and desertification may develop rapidly, leading to a substantial reduction in vegetation productivity, soil stability, and the ecological resilience of natural pasture ecosystems (Karimova et al., 2012). Therefore, the restoration and sustainable management of degraded arid and semi-arid pastures require scientifically based technologies and effective mechanized methods for establishing native drought-resistant vegetation (Farmonov et al., 2020a).

Table 1

Level of Pasture Degradation Across Regions of the Republic of Uzbekistan

Republic of Uzbekistan	**The area of degraded grasslands, mil. ha**	**Degradation size, %**
Karakalpakstan	1.50	43.4
Navoi	4.10	43.8
Bukhara	1.2	37.6
Surkhandarya	0.20	41.2
Samarkand	0.12	23.6
Kashkadarya	0.18	24.5
Jizzakh	0.17	25.4
Total	7.47	40

At present, extensive degraded areas are found across almost all natural pasturelands of the Republic of Uzbekistan, with their total area reaching approximately 8 million hectares. The distribution and extent of these degraded areas vary among regions. Approximately 40% of desert pastures have undergone degradation of varying degrees, resulting in a 20–30% decline in their average productivity (Table 1). These figures clearly demonstrate that the primary task for ensuring the sustainable development of livestock production and, in particular, pastoral livestock farming in arid regions is the development of effective technologies and technical means for restoring degraded pastures and increasing their productivity (Urinova et al., 2023). At the same time, protecting arid pastures from further degradation is equally important as improving their productivity. Therefore, sustainable pasture management should focus not only on restoring degraded lands but also on preventing further deterioration of vegetation and soil resources. The implementation of scientifically based technologies and appropriate mechanized technical means for the establishment of native drought-resistant vegetation can contribute significantly to the restoration of degraded pastures, stabilization of sandy soils, prevention of desertification, and improvement of the forage base for livestock production in arid regions.

Method

The study was conducted to develop and evaluate a mechanized technology for improving degraded desert and semi-desert territories of the Republic of Uzbekistan through the establishment of native drought-resistant vegetation. The research methodology was based on field observations, laboratory studies, experimental evaluation of seed quality, and field testing of a newly developed desert seeder. The study area included degraded natural pastures and sandy soils characteristic of the arid and semi-arid

ISSN: 2181-3337 | SCIENTISTS.UZ

regions of Uzbekistan (Farmonov et al., 2022). The selection of plant species was based on their natural distribution, adaptation to severe arid conditions, resistance to drought, and potential for restoring degraded pasture ecosystems. The principal plant species selected for the study were saxaul (*Haloxylon spp.*), cherkez (*Salsola spp.*), and izen (*Kochia prostrata*), which are considered promising native desert and semi-desert plants for improving the vegetation cover of degraded lands.

Seed Materials and Quality Assessment

Before sowing, the main physical and biological quality characteristics of the seed material were determined. Particular attention was given to seed purity and germination capacity, since these parameters directly affect the efficiency of mechanized sowing and subsequent plant establishment (Farmonov et al., 2020a). The seed purity of the prepared seed material ranged from 20 to 25%, while germination capacity was determined to be 40–45%.

Seeder Design and Development

A new experimental prototype of a desert seeder was developed for mechanized sowing of saxaul and izen seeds. The design of the seeder was developed taking into account the specific physical and mechanical properties of desert plant seeds, their low flowability, and the technological requirements for sowing on sandy soils (Mirzaev et al., 2021). The seeding system was designed to provide continuous movement, uniform distribution, and controlled placement of seed material while reducing the probability of seed bridging, clogging, and irregular seed flow.

Patented Technology and Experimental Procedures

The proposed seeding technology and the construction of the seeding equipment were developed on the basis of experimental and theoretical studies and are protected by patents of the Republic of Uzbekistan (No. FAP 2670 and No. FAP 3044). Laboratory and field experiments were conducted to assess the operational performance of the seeder and the quality of the sowing process under natural soil and climatic conditions.

Field Trials and Data Analysis

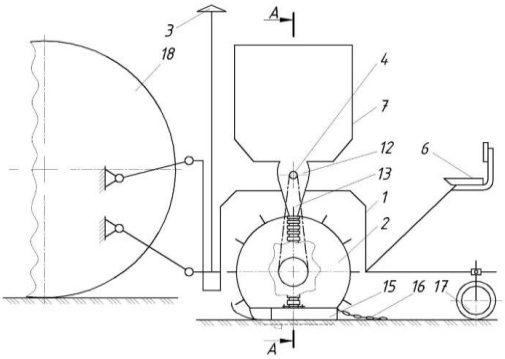
During the field trials, the seeder was evaluated according to the uniformity of seed distribution, stability of the seeding process, and suitability for operation on sandy and degraded pasture soils. The obtained experimental data were analyzed to determine the effectiveness of the proposed technology for restoring degraded desert and semi-desert territories (Farmonov et al., 2020a). The results were used to assess the potential of mechanized sowing of native drought-resistant plants as a practical method for improving pasture vegetation, stabilizing sandy soils, reducing degradation, and increasing the ecological sustainability and productivity of arid pasture ecosystems.

Results

The proposed seeder for sowing the seed heap of desert forage plants (izen) operates as follows (Farmonov et al., 2022). Before starting operation, hopper 7 is filled with the seed mixture. As the seeder, aggregated with a tractor, moves across the field, the ground wheels 2 transmit motion to the left 4 and right 5 horizontal drive shafts. The rotating left 4 and right 5 horizontal shafts, in turn, transmit rotational motion to the seed-mixture loosening devices mounted on bearings 8 in the lower sections of hopper 7. The left horizontal shaft 4 transmits rotation to the two left shafts 9 of the seed-mixture loosening devices, while the right horizontal shaft 5 transmits rotation to the two right shafts 9 of the seed-mixture loosening devices (Fig. 1). The arrangement of the side walls of the quadrangular hopper at an angle of 90° relative to the seed-mixture loosening devices significantly reduces friction between the seed mixture and the walls of hopper 7. This configuration ensures smooth movement of the seed mixture from the upper part toward the lower part of the hopper and onto the surfaces of the conical fingers 10 of the seed-mixture loosening devices (Fig. 2).

Figure 1

Schematic Diagram of the Proposed Unit for Sowing a Seed Heap of Desert Forage Plants (Izen)

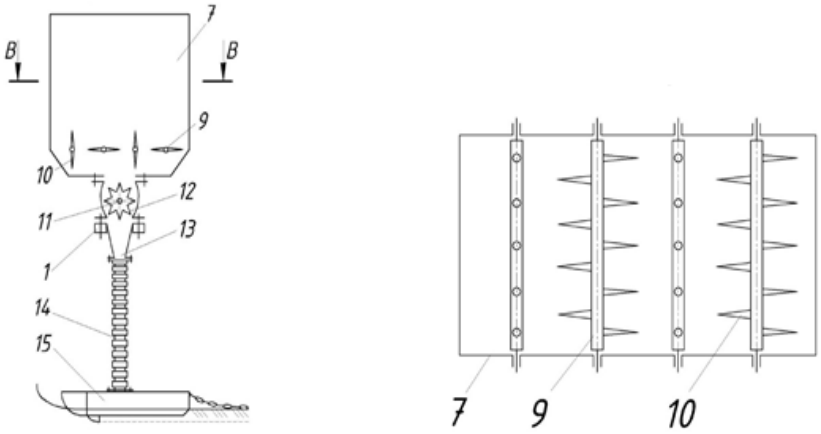


Note. 1 = frame; 2 = support wheels; 3 = marker; 4–5 = left and right horizontal shafts; 6 = seat; 7 = hopper; 8 = bearing; 9 = seed-mixture softeners; 10 = cone-shaped fingers; 11 = drum distributor; 12–13 = seeding apparatus; 14 = seed tube; 15 = coulter; 16 = hedder; 17 = compacting roller; 18 = tractor chassis.

The seeds remain above the surfaces of the fingers 10 of the seed-mixture loosening devices 9 until the fingers are set into motion. The conical fingers 10 prevent the seeds from falling abruptly onto the surfaces of the triangular grooves 12 of the distributing drum 11. As a result, the formation of a seed arch above the grooves is prevented (Fig. 2). The rotation of the seed-mixture loosening devices continuously disturbs and loosens the seed material, thereby maintaining its mobility within the lower part of the hopper. The conical fingers provide a gradual transition of the seed mixture toward the triangular grooves of the distributing drum, preventing localized accumulation and blockage of the seed material.

Figure 2

Seeding Section of the Seed Harrow for Sowing Izen



Note. 1 = frame; 7 = hopper; 9 = seed-mixture softeners; 10 = cone-shaped fingers; 11 = drum distributor; 12 = triangular chute; 13 = seed guide; 14 = seed tube; 15 = coulter.

This operating principle improves the continuity and stability of seed flow and contributes to a more uniform distribution of the seed mixture during the sowing process. Thus, the proposed design makes it possible to maintain a stable flow of the non-free-flowing seed mixture, reduce the risk of bridging and clogging in the hopper, and ensure reliable feeding of the seed material to the distributing drum. This is particularly important for the mechanized sowing of izen seeds, which are characterized by specific physical and mechanical properties and require specialized technological conditions for effective and uniform sowing.

ISSN: 2181-3337 | SCIENTISTS.UZ

Figure 3

Laboratory Bench Used for the Experiments



The following data for the proposed device were determined under laboratory conditions using a DT-2236 B electronic tachometer. The calculated values are presented in Figure 5. Field trials of the seeder were conducted in 2025 at the testing grounds of BMKB-Agromash Joint-Stock Company, located in the Farish district of the Jizzakh region, and also in the Urtachirchik district of the Tashkent region that same year. The seeder is coupled to wheeled tractors of class 0.9–1.4 (T-40, MTZ-80/82) (Fig. 4).

Figure 4

General View of the Experimental Prototype of the Machine

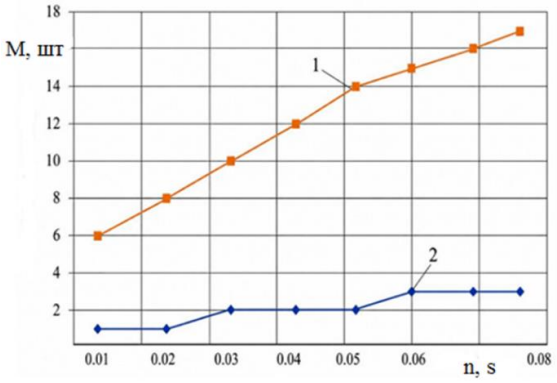


As shown in the figure, with an increase in the rotation parameter from 0.01 to 0.075 s, the quantity of sown seeds increases steadily from approximately 6 to 17 seeds. The most pronounced increase is observed over the range of 0.01–0.05 s, where the number of sown seeds rises from 6 to 14. With a further increase in the parameter, the number of seeds continues to increase, reaching approximately 17 seeds at 0.075 s. In contrast, the number of wingless seeds remains relatively low and stable. At the initial values of the parameter (0.01–0.02 s), approximately 1 wingless seed is observed. At 0.03–0.05 s, this value increases to approximately 2 seeds, and at 0.06–0.075 s it reaches approximately 3 seeds. The obtained relationship indicates that increasing the operating parameter of the cone-shaped working element promotes more intensive loosening and movement of the seed mixture, thereby increasing the amount of seed supplied to the distributing mechanism. At the same time, the relatively small increase in the number of wingless seeds indicates that the working element provides effective separation and controlled movement of the seed mixture. Thus, the results confirm the ability of the proposed cone-shaped working element to ensure a stable and continuous supply of seed material and improve the reliability of the sowing process.

ISSN: 2181-3337 | SCIENTISTS.UZ

Figure 5

Dependence of Seed-Heap Quantity on the Number of Revolutions of the Cone-Shaped Working Element



Note. 1 = sown seeds; 2 = wingless seeds.

In general, the graph confirms the direct dependence of the number of seeds on the number of revolutions and allows us to determine the rational range of operation of the device, which ensures high productivity while maintaining the quality of seeding.

Discussion

The experimental results demonstrate that the proposed planter provides a more uniform and stable sowing process within the established agrotechnical requirements compared with manual sowing (Farmonov et al., 2020a; Farmonov et al., 2020b; Farmonov et al., 2022; Mirzaev et al., 2021). The separation of seeds at a fixed rate and their subsequent placement into the furrow formed in the cultivated sandy soil contributed to a more consistent distribution of seeds along the sowing row. This is particularly important for desert forage plants such as izen, whose seeds are characterized by small size and specific physical and mechanical properties that can complicate their uniform metering and distribution. The observed improvement in sowing uniformity can be attributed to the operating principle of the developed planter. The seed mixture is continuously loosened and directed toward the seed-metering and distributing element, which reduces the probability of seed bridging, clogging, and irregular discharge. In contrast, manual sowing is strongly dependent on the operator and may result in fluctuations in the amount of seed deposited along the row. Such fluctuations can lead to both excessive concentration and insufficient density of plants, which negatively affects the uniformity of plant establishment. The results are especially relevant for sowing on sandy soils after plowing and cultivation by machine-tractor aggregates. Under these conditions, maintaining a stable seed flow and placing seeds uniformly in the prepared furrow are essential for obtaining an even plant stand. The proposed planter combines mechanized seed metering with continuous seed-flow regulation, thereby reducing the influence of human factors and improving the stability of the technological process.

The higher efficiency and productivity observed for the developed planter indicate that its application can reduce the labor requirements associated with manual sowing while simultaneously improving the quality of seed distribution. The obtained results therefore confirm the suitability of the proposed design for mechanized sowing of desert forage plant seeds under sandy-soil conditions. Moreover, the improved uniformity of seed placement may contribute to more consistent emergence and establishment of plants, which is important for the restoration and productive use of degraded desert and pasture lands. Overall, the experimental findings confirm that the developed planter is capable of providing a stable and technologically controlled sowing process within the required range of sowing quality. Its advantages over manual sowing are associated primarily with improved seed distribution uniformity, reduced dependence on operator performance, and higher operational efficiency. These findings support the practical application of the proposed planter for establishing desert forage vegetation in sandy areas.

ISSN: 2181-3337 | SCIENTISTS.UZ

Conclusion and Implications

The experimental results confirm the effectiveness of the developed planter for sowing desert forage plant seeds under sandy-soil conditions. The proposed design ensures a stable and uniform supply of seeds within the required sowing rate and improves the distribution of seeds along the prepared furrow compared with manual sowing. The use of the cone-shaped working element in the seed hopper contributes to continuous loosening of the seed mixture and prevents the formation of bridges and blockages, thereby maintaining a stable seed flow to the seed-metering and distributing mechanism. The developed planter demonstrated higher sowing efficiency and productivity, while reducing the dependence of sowing quality on operator performance. The obtained results indicate that mechanized sowing provides more consistent seed placement and a more stable sowing process than the manual method. This is particularly important for small and lightweight seeds of desert forage plants, for which achieving a uniform sowing rate is technically difficult. The practical implication of the study is that the proposed planter can be used for establishing and restoring desert forage vegetation in sandy and degraded areas. More uniform seed distribution can contribute to a more even plant stand and improve the efficiency of seed utilization. Consequently, the developed technology has potential for application in pasture restoration, prevention of land degradation, and improvement of the productivity of desert grazing areas. From a technological perspective, the results demonstrate that incorporating a cone-shaped seed-mixture loosening element into the hopper is an effective approach to improving the reliability of seed metering for non-free-flowing desert plant seeds. The developed solution can serve as a basis for further improvement of seeders intended for sowing small, irregularly flowing seeds under difficult soil and environmental conditions. In conclusion, the developed planter provides a technically effective alternative to manual sowing by combining improved seed-flow stability, more uniform seed distribution, and higher operational efficiency. Further research should focus on long-term field trials under different soil moisture conditions, operating speeds, and sowing rates, as well as on evaluating seedling emergence, plant survival, and the economic efficiency of large-scale application.

Declarations

Acknowledgments: Not applicable.

Authors' contributions: Erkin Farmonov contributed to the conceptualization of the study, development of the experimental methodology, design and development of the proposed planter, performance of the experiments, analysis and interpretation of the experimental results, and preparation of the manuscript. Shakhnoza Mirzaeva contributed to the development of the research methodology, organization and supervision of the experimental studies, analysis and interpretation of the obtained results, critical revision of the manuscript, and coordination of the manuscript preparation and submission. Both authors read and approved the final version of the manuscript. Nodira Xodjaqulova contributed to the development of the research methodology, organization and supervision of the experimental studies.

Competing interests: The authors declared no potential conflicts of interest with respect to the research, authorship, and/or publication of this article.

Funding: This research did not receive any specific grant from funding agencies in the public, commercial, or not-for-profit sectors.

Ethics approval and consent to participate: Not applicable. This study did not involve human participants, human subjects, or personal data. Therefore, ethical approval and consent to participate were not required.

Note: This article is based on research conducted as part of a doctoral (PhD) dissertation in technical sciences on the development and justification of parameters of a cone-shaped working element in the hopper of a seeder for sowing seeds of desert forage plants (izen).

Publisher's note: Science and Innovation Journal remains neutral with regard to jurisdictional claims in published maps and institutional affiliations.

REFERENCES

1. Abd Elsalam, H. E., & Bahobail, A. S. (2016). Lignin biodegradation by thermophilic bacterial isolates from Saudi Arabia. *Research Journal of Pharmaceutical, Biological and Chemical Sciences, 7*(1), 1413–1424.
2. Anttila, A., Leppänen, A.-P., Rissanen, K., & Ylipieti, J. (2011). Concentrations of 137Cs in summer pasture plants that reindeer feed on in the reindeer management area of Finland. *Journal of Environmental Radioactivity, 102*(7), 659–666. https://doi.org/10.1016/j.jenvrad.2011.03.009
3. Arshad, F., Waheed, M., Harun, N., Fatima, K., Khan, B. A., Fatima, K., Abbas, Z., Jabeen, S., & Majeed, M. (2022). Indigenous farmer's perception about fodder and foraging species of semi-arid lowlands of Pakistan: A case study of District Kasur, Pakistan. *Taiwania, 67*(4), 510–523. https://doi.org/10.6165/tai.2022.67.510
4. Farmonov, E., Ismailova, Z., Abdilaev, T., & Farmonova, F. (2020a). Mechanized sowing of seeds of desert fodder plants. *IOP Conference Series: Materials Science and Engineering, 883*(1), 012096. https://doi.org/10.1088/1757-899X/883/1/012096
5. Farmonov, E., Lakaev, S., Khalilov, R., & Gorlova, I. (2020b). Aeromechanical purification of freshly harvested seed heaps of desert fodder plants. *IOP Conference Series: Materials Science and Engineering, 883*(1), 012097. https://doi.org/10.1088/1757-899X/883/1/012097
6. Farmonov, E. T., Arifjanov, A. M., & Farmonova, F. E. (2022). Experimental seeders for sowing unseeded seeds. *Journal of Physics: Conference Series, 2176*(1), 012057. https://doi.org/10.1088/1742-6596/2176/1/012057
7. Karimova, T. Yu., Lushchekina, A. A., Narantuya, N., Neronov, V. M., Safronova, I. N., & Uchrakhbayar, T. (2012). Changes in state of Mongolian gazelle (*Procapra gutturosa* Pallas 1777) population of Eastern Mongolia: Long-term data analysis. *Arid Ecosystems, 2*(3), 150–155. https://doi.org/10.1134/S2079096112030079
8. Mirzaev, B., Mamatov, F., Tulaganov, B., Sadirov, A., Khudayqulov, R., & Bozorboev, A. (2021). Suggestions on increasing the germination seeds of pasture fodder plants. *E3S Web of Conferences, 264*, 04033. https://doi.org/10.1051/e3sconf/202126404033
9. Shamsutdinov, N., Shagaipov, M., & Sanzheev, V. (2020). Ecological restoration of degraded pasture lands in the Circum-Caspian Sea semi-desert. *E3S Web of Conferences, 222*, 02023. https://doi.org/10.1051/e3sconf/202022202023
10. Shamsutdinov, N. Z., Sanzeev, V. V., & Sh Shamsutdinov, Z. (2021). Ecological restoration of fodder productivity of degraded pastures in the foothill desert zone of Central Asia. *IOP Conference Series: Earth and Environmental Science, 901*(1), 012033. https://doi.org/10.1088/1755-1315/901/1/012033
11. Shamsutdinova, E., & Shamsutdinov, Z. (2021). The fodder shrub—*Halothamnus subaphyllus* (C.A. Mey.) Botsch.: Reproductive biology and seed productivity in the culture. *IOP Conference Series: Earth and Environmental Science, 699*(1), 012028. https://doi.org/10.1088/1755-1315/699/1/012028
12. Urinova, A., Tulaev, J., & Choriev, B. (2023). Determination of distribution areas and reserves for state accounting of Tajik Kavrak (*Ferula Tadshikorum* Pimenov) resources in the flora of Surkhandarya and Kashkadarya provinces, Uzbekistan. *E3S Web of Conferences, 376*, 02011. https://doi.org/10.1051/e3sconf/202337602011

ISSN: 2181-3337 | SCIENTISTS.UZ

CONTENTS

Kurbonov Salohiddin
DEVELOPMENT OF AN OPTIMIZED PERFORMANCE-GRADED (PG) ASPHALT BINDER FOR UZBEKISTAN'S ROAD-CLIMATIC CONDITIONS AND TRAFFIC LOADS: RHEOLOGICAL CHARACTERIZATION AND HYBRID POLYMER MODIFICATION 4

Akbarov Dilshod, Akramov Khusnitdin
DEFORMATION-DECOUPLED CONNECTIONS BETWEEN A PULTRUDED GFRP FRAME AND THREE-LAYER 3D-PRINTED WALLS 14

Eshmuradov Dilshod, Ismailov Otabek, Nizomov Norkhuja
MAXWELL–WAGNER OBSERVABILITY ANALYSIS IN TWO-FREQUENCY CAPACITIVE MEASUREMENT OF WATER CONTENT AND DENSITY IN HYDROCARBON EMULSIONS 30

Mamatkulov Asliddin, Baxodirov Zafar, Eshmurodov Sobir
REMOTE SENSING AND GIS MONITORING OF WIND EROSION AND DUST EMISSION IN CENTRAL ASIA 39

Kuralov Murodbek, Akhatov Jasurjon
REVERSE OSMOSIS MEMBRANES UNDER DUTY-CYCLED OPERATION: COMPACTION, SCALING, BIOFILM REGROWTH AND PERMEATE TRANSIENTS IN PHOTOVOLTAIC-DRIVEN BRACKISH DESALINATION 50

Bakiev Masharif, Kuryozov Otaboy, Yakubov Kuvonchbek, Khasanov Khojiakbar, Khalimbetov Azat
MORPHOLOGICAL PARAMETERS IN THE UPSTREAM REACH OF A FLOW CONSTRICTED BY A SPUR DIKE 69

Musayeva Shoira
IMPROVING THE ALGORITHM FOR CONTROLLING THE CUSTOMS TRANSIT INFORMATION SYSTEM E-TRANSIT OF THE REPUBLIC OF UZBEKISTAN 80

Bobomurodov Furkat, Khazratov Alisher, Sodikov Jasur
DETERMINATION OF THE CIRCULATION ZONE WIDTH AT THE JUNCTION OF EARTHEN CANALS 86

Musaeva Shoira
IMPLEMENTATION OF PARETO ANALYSIS, ABC CUSTOMER CLASSIFICATION, AND CVP MODELLING AT AN INDUSTRIAL MANUFACTURING ENTERPRISE 94

Yuldashev Sharafitdin, Boytemirov Muxamadbobir, Abdunazarov Akbarjon, Yuldashev Faxriddin, Vahobov Boburkhon
NUMERICAL EVALUATION OF GROUNDWATER-LEVEL EFFECTS ON THE SEISMIC RESPONSE OF A MULTISTORY BUILDING–SOIL SYSTEM USING PLAXIS 3D 102

Sayfullayev Ramziddin
MEDICAL AND PEDAGOGICAL SIGNIFICANCE OF RADIATION BACKGROUND IN THE USE OF NUCLEAR POWER REACTORS 112

Farmonov Erkin, Mirzaeva Shakhnoza, Xodjaqulova Nodira
DEVELOPMENT OF A NEW SEEDER FOR RESTORING DESERT AND SEMI-DESERT AREAS IN UZBEKISTAN 119



International Scientific Journal
Science and Innovation Series A
Volume 5 Issue 8

ISSN: 2181-3337

Published: 31.08.2026. Font: “Times New Roman”.

LLC “Science and innovation”
License Mass Media №:1597 27.04.2022
License Publisher №:455168 21.11.2024
Address: 100121, Uzbekistan, Tashkent city, Yakkasaroy district,
Shota Rustaveli Street 150, Vega Business Center, 6th floor, Room 2.
www.scientists.uz, info@scientists.uz, +998901259654

ISSN: 2181-3337